HIGH ASPECT RATIO TRANSMISSION LINES AND FILTERS

A Thesis Submitted to the College of
Graduate Studies and Research
in Partial Fulfillment of the Requirements
for the Degree of Doctor of Philosophy
in the Department of Electrical Engineering
University of Saskatchewan
Saskatoon

by
K.D. Himal C. Jayatilaka

PERMISSION TO USE

In presenting this thesis in partial fulfillment of the requirements for a Postgraduate degree from the University of Saskatchewan, I agree that the Libraries of this University may make it freely available for inspection. I further agree that permission for copying of this thesis in any manner, in whole or in part, for scholarly purposes may be granted by the professor or professors who supervised my thesis work or, in their absence, by the Head of the Department or the Dean of the College in which my thesis work was done. It is understood that any copying or publications or use of this thesis or parts there of for financial gain shall not be allowed without my written permission. It is also understood that due recognition shall be given to me and to the University of Saskatchewan in scholarly use which may be made of any material in my thesis.

Requests for permission to copy or to make other use of material in this thesis in whole or part should be addressed to:

Head of the Department of Electrical Engineering
College of Engineering
University Of Saskatchewan
Saskatoon, Canada
S7N 5A9

- *Dedicated to my beloved family members.*

Abstract

There are a significant number of microwave applications, where improvement of such qualities as manufacturing costs, size, weight, power consumption, etc. have attracted much research interest. In order to meet these requirements, new technologies can be actively involved in fabrication of microwave components with improved characteristics. One such fabrication technology is called LIGA (a German acronym with an English translation of lithography, electroforming, and moulding) that allows fabrication of high aspect ratio (tall) structures, and only recently is receiving growing attention in microwave component fabrication.

The characteristics of high aspect ratio microstrip and coplanar waveguide (CPW) transmission lines are investigated in this thesis. Very low impedance high aspect ratio CPW transmission lines can be realized. A high aspect ratio microstrip folded half wavelength open loop resonator is introduced. Effective configurations for external and bypass gap coupling with open loop resonators are given. Filters with transmission zeros in the stopband, consisting of high aspect ratio single mode open loop resonators are presented to demonstrate the advantages of high aspect ratio structures in realizing lower external quality factors or tight coupling. The transmission zeros are created by novel coupling routings. Some of the filters are fabricated and the filter responses are measured to validate high aspect ratio coupling structures. High aspect ratio diplexers with increased channel isolation are also designed by appropriately combining filters with transmission zeros.

A wideband bandpass filter design method, based on the electromagnetic bandgap (EBG) concept is introduced in this thesis. The wideband filters are miniaturized as a result of using the EBG concept in design. An EBG based wideband filter consisting of unit cells that are realized by using high aspect ratio CPW stepped impedance resonators is also presented. The main advantage of this approach is that the high aspect ratio CPW structures make short unit cells practically realizable, resulting in compact filter structure.

Acknowledgements

I would like to acknowledge my genuine gratitude to my supervising professor, Dr. D.M. Klymyshyn, who has taken every effort to facilitate implementation of this research and has given an valuable support throughout the program and preparation of this thesis.

I am deeply obliged to the Institute for Microstructure Technology (IMT) of Karlsruhe, Germany and its personnel, especially Martin Boerner who fabricated the some of devices given in this thesis. I am also truly grateful to Telecommunications Research Laboratories (TRLabs) Saskatoon and its personnel for providing me with financial assistance, for accordance of a privilege to use its facilities.

Contents

Appendices

Appendices

Appendices

Appendices

Appendices

List of Tables

List of Figures

Chapter 1

Introduction

1.1 Background

Recent advances in RF and microwave technology, dominated by commercial and also defence, national security and scientific research systems such as radar, communications, electronic warfare, and radiometry have occurred in the 1-100 GHz frequency band. There is also massive thrust towards microwave and millimetre-wave frequency bands because of the congestion in lower frequency bands and the other advantages in this regime such as higher bandwidth. With the advent of affordable systems, improved performance with continued affordability is in demand.

The current trend in microwave technology is toward circuit miniaturization, high level integration, improved reliability, low power consumption, cost reduction and high volume applications. Component size and performance are prime factors in the design of certain electronic systems, such as systems for, satellite communications, phased array radar systems and other military applications, while small size and low cost drive the consumer electronic market. The arrival of monolithic microwave integrated circuits (MMIC) that are based on gallium arsenide (GaAs) has made a great impact on meeting above requirements. Extensive research is being carried out for achieving systems-on-a-chip, where the goal is an integrated circuit combining digital and analogue functions with micromechanical components, optical components, and radio transceivers [3], [4], [5].

Presently, in a typical wireless communication system the received signal is directed from the antenna to a low-noise amplifier via a diplexer, and the transmit signal is directed to the antenna through the diplexer. Power leakage between the two amplifiers can cause increased noise figure. High isolation and low insertion loss filters, which comprise the diplexer means power conservation in the transmitter side and minimized noise figure. Typically, diplexer components and signal carrying lines are based on waveguide that could be in planar structure or a three dimensional structure. In satellites, the communication system can consume considerable percent of the total dry mass of a spacecraft. Amplifiers also consist of many capacitors, inductors, and microstrip interconnects in addition of active devices. This heavy use of passive components is a requisite because matching networks are essential in order to achieve usable gain from transistors at microwave frequencies. In a MMIC, these passive components consume a large percentage of the expensive semiconductor substrate and quality monolithic components are difficult to achieve. Hence, it is important to design these passive structures efficiently and effectively.

Filters are widely used in designing diplexers [6]. Microwave filters and diplexers have their planar counterparts for microwave integrated circuits (MICs) and some are realized based on any or a combination of planar transmission structures such as microstrip lines, coplanar waveguide (CPW), slot line, etc. [7]. Many of them are conventionally comprised of quarter wavelength or half wavelength transmission line sections [8], [9]. They consume large space, especially in the lower microwave region (1-20 GHz). There are several common approaches in order to achieve improved electrical performances and/or miniaturization.

Quarter wavelength or half wavelength transmission lines sections are substituted by electrically equivalent shorter transmission line sections cascaded with a shunt capacitive reactance or a series inductive reactance in both ends or in a single end in lumped or distributed forms. These nonuniform quarter wavelength or half wavelength resonant structures cascaded with distributed reactance are called stepped impedance resonators (SIR) [10]. SIRs can have shorter resonant lengths and filters are miniaturized using these SIRs [11],[12]. Stopband performance of filters composed of SIRs is improved by having the first spurious passband at a higher frequency than at twice of the centre frequency.

Microwave filters and diplexers are also designed and fabricated in fully lumped versions for MIC and MMIC applications, especially below 20 GHz [13], [14]. Though lumped element versions bring about miniaturization, associated losses are high. Quality factor (Q factor) is typically below 100 in the range of 5-10 GHz [15], [16]. Low Q factor due to increased losses in lumped elements deteriorates filter performances [17].

Slow wave transmission lines are also being used for miniaturization. Slow wave transmission lines can be obtained by introducing periodic perturbations into the conventional transmission structure itself [18]. These types of periodically loaded transmission lines are used for miniaturization and/or performance improvement of passive microwave devices mentioned in [19],[20], [21]. In general, ohmic losses associated with this type of periodic perturbations due to small dimensions are high. Electromagnetic band gap (EBG) structures have attracted much attention recently and are essentially a slow wave periodic structure. EBG structures have been used in microwave engineering in many ways. EBG typed periodic structures have been used to realize filters with several approaches. Much research has focused on realizing high performance low pass filters directly using the first passband of EBG structures [22],[23]. In this type of low pass filters, passband and out-of-band is coincident with its EBG passband and stopband. The ground plane or the dielectric substrate of conventional planar low pass filters and bandpass filters are EBG engineered to suppress spurious passbands in stopbands [2]. Narrow-band bandpass filters can also be realized using EBG defect resonators where a defect is introduced in the EBG structure to obtain a high Q defect mode [24].

In another approach for improving filter performance, transmission zeros are introduced into the stopband of filters to improve stopband performance where high rejection and sharp skirt characteristics of the stopband are required [25]. Filters with properly located transmission zeros are combined to obtain diplexers with greater channel isolation. These transmission zeros are commonly brought about by cross coupling of non adjacent resonators [26]. Comparatively little research work has been carried out to investigate source/load multi-resonator coupling as an efficient method of bringing additional transmission zeros in microwave filters [27].

Various fabrication techniques are being used in order to create high performance and/or miniaturized microwave filters [28]. Traditional transmission line resonators are increasingly being micromachined in order to reduce losses in them. A four pole micromachined elliptic filter with a Q factor of 500 at 60 GHz has been published in [29]. Low temperature co-fired ceramic technology (LTCC) that allows fabrication of multilayered structures is also used increasingly to design and construct miniaturized high performance filters [30]. The LIGA process (a German acronym with an English translation of lithography, electroforming, and moulding) that allows tall (typically up to 1mm), high-aspect ratio metal structures with optical quality side walls to be very accurately patterned has also been explored. Resonant cavities and acoustic wave resonators, wideband 3 dB co-planar waveguide couplers and also lumped reactive elements such as variable capacitors have been realized using the LIGA process as presented in [31], [32], [33], [34], [35]. Wideband parallel coupled bandpass filters have also been fabricated using LIGA [36], [37]. The tight coupling of tall LIGA parallel coupled lines has been useful for getting wider passband in these filters.

Promising initial research has been done to explore LIGA advantages applied to microwave devices, but comparatively little compared with other micro fabrication techniques. Tall structures on micron and millimeter scales with aspect ratios, as high as 100:1 and also sub-micron scales with precise features as small as 0.1 μm can be achieved. Advantages of high aspect ratio structures to microwave filters are proposed to be further investigated in this work.

1.2 LIGA Process

The LIGA fabrication process uses coherent synchrotron radiation and a PMMA (polymethyl methacrylate) photoresist [38], [39]. A good overview of the typical LIGA process is found in [40]. A thin metal layer (typically Ti or TiOx is applied to a substrate to form a metal seed layer for subsequent electroplating. A thick PMMA resist sheet (typically 100s of μm) is bonded to a substrate typically silicon or alumina. X-ray stop material (typically 20 μm Au) patterned according to the structure required is supported on an X-ray mask membrane. Then, the resist is exposed to X-rays and the exposure time depends on the thickness of the PMMA structure. After the X-ray exposure, the exposed PMMA is removed using a development process and the metal structure is plated into the openings. These metal structures can form the final structures, or can be metal templates for further replication of devices using embossing or injection moulding techniques.

Since the early days of LIGA, the Institut für Mikrostrukturtechnik (IMT), Forschungszentrum Karlsruhe (FZK), has been one of the leading institutes developing the processes and characterizing the structuring capabilities of LIGA [41], [42]. The structures described in this thesis are fabricated at the IMT, and benefit from these years of research into LIGA process and device fabrication.

1.3 Research Objective

The main objective of this research work is to exploit the advantages of high aspect ratio structures of high precision into microwave filters to achieve good performance and miniaturization in novel ways. Various approaches as detailed in Section 1.1, including transmission line segments cascaded with reactive loadings, the use of lumped elements, the use of slow wave periodic structures, the introduction of transmission zeros in the filter stopband, and the use of special fabrication techniques are a few general methods persued for adaptation in order to achieve good performance and/or miniaturization in microwave filters as detailed in Section 1.1.

Characteristics of high aspect ratio microstrip and CPW lines are investigated. High aspect ratio folded half wavelength resonators are also studied. Novel methods of realizing source/load multi-resonator coupling are introduced using high aspect ratio half wave length folded resonators. The advantage of the ability to realize higher capacitive coupling from high aspect ratio structures is also used in introducing the proposed source/load multi-resonator coupling scheme. The performance of a novel objective function for optimizing coupling matrices used in designing these higher order filters is discussed. High aspect ratio diplexers with higher channel isolation are also designed using the above source/load multi-resonator filters.

A novel wideband bandpass filter design technique is presented using the EBG concept. Bandpass filters based on bandpass type EBG structures where the passband and stopband of the filters is coincident with the passband and stopband of the EBG structure, are researched. The use of high aspect ratio low impedance SIRs in EBG based miniaturized bandpass filter design is also investigated.

1.4 Thesis Organization

The details supporting above contributions will be discussed in subsequent chapters. This thesis contains eight chapters.

Chapter 2 presents the fundamentals upon which this thesis is built. Details on filter transfer functions and lowpass prototyped networks are included. An equivalent bandpass filter network with resonators and impedance/ admittance inverters is derived from the prototyped network. The bandpass filter design approach with the knowledge of external quality factors and coupling coefficients between resonators is described. Extraction methods of coupling coefficient and, external and unloaded quality factors is also presented.

In Chapter 3, basic analyzing methods of microstrip and CPW transmission lines are reviewed. Characteristics of high aspect ratio microstrip and CPW lines are presented. Half wavelength high aspect ratio microstrip folded open loop resonators are appreciated as building blocks of filters. External and unloaded quality factors of high aspect ratio half wavelength resonators and their planar versions are compared.

Chapter 4 is devoted to designing second order asymmetrical bandpass filters. The coupling of differently oriented half wavelength open loop resonators is described. Two prototyped asymmetrical filter networks are synthesized from generalized Chebyshev transfer functions. One of these networks has the response with a transmission zero in the upper stopband while the other network has the response with a transmission zero in the lower stopband. Second order high aspect ratio bandpass filters with half wavelength open loop resonators are designed out of these prototyped networks. Source/load multi-resonator coupling is realized in unique ways. The advantage of high aspect ratio structures for realizing the required tight coupling is demonstrated. Experimental results for LIGA fabricated second order filters are also given.

Chapter 5 presents higher order bandpass filters with at least two transmission zeros in their responses. The coupling matrix based filter design technique that is obtained from optimization is described. An effective objective function for the optimization is appreciated. Third order bandpass filter designs using high aspect ratio open loop resonators to create two transmission zeros in the lower stopband, in the upper stopband and in the both stopbands closer to the passbands are presented. Fourth order bandpass filters that create two transmission zeros in the upper stopband and lower stopband are also given in this chapter.

In Chapter 6, some of the previously designed bandpass filters are used to design diplexers. A second order diplexer is designed combining two second order filters, one having a transmission zero in the upper stopband and the other having a transmission zero in the lower stopband. A third order diplexer whose channel responses have two transmission zeros mutually aligned in channel passbands, is also presented.

Chapter 7 is devoted to novel wideband bandpass filters based on the EBG concept. Bandpass type EBG unit cells are introduced. Propagation characteristics of bandpass typed EBG structure made of shunt loaded unit cells and design equations to control bandwidth are given. The performance of a microstrip bandpass filter designed based on this bandpass type EBG concept is compared with a conventional microstrip bandpass filter. A miniaturized CPW wideband filter based on the bandpass typed EBG concept is also designed using SIRs with low impedance segments that are effectively realized by LIGA structures.

Chapter 8 summarizes the work presented in this thesis, suggests improvements for current methods and discusses future work.

Chapter 2

General Filter Design

2.1 Introduction

A passive microwave filter is a circuit consisting of only lumped components (inductors, capacitors) or distributed elements (waveguide sections or other transmission lines) or both, arranged in a particular configuration such that signal frequencies are allowed to pass with minimum signal distortion while undesired signals are attenuated. An ideal filter would have infinite attenuation in the stopband, zero transmission attenuation in the passband, and linear phase response.

The second section of this chapter describes the filter transfer function. The third section is devoted to lowpass prototype networks and extension to bandpass networks. The fourth section describes design of practical microwave filters.

2.2 Transfer Functions

The transfer function of a two port filter network is a mathematical expression of network characteristics which is namely S_{21} (S_{21} is defined in Appendix C) . The amplitude response for microwave networks for a lossless passive filter network is defined by

$$|S_{21}(j\omega')| = |H(j\omega')| = \frac{1}{\sqrt{1 + \epsilon^2 F_n^2(\omega')}} \tag{2.1}$$

where ϵ is a parameter that defines the ripple level in the passband and $F_n(\omega')$ is a n-th order even or odd polynomial of ω' which is the normalized frequency variable. The transfer function of linear time-invariant networks can be defined as a rational function,

$$S_{21}(p) = \frac{N(p)}{D(p)} \tag{2.2}$$

where $N(p)$ and $D(p)$ are polynomials in the complex frequency variable $p = \sigma + j\omega'$. σ and ω' are in a complex plane where the rational function is defined. σ is in the horizontal axis of the complex plane while $j\omega'$ is in the imaginary axis. The characteristics of network response are defined by the poles of $S_{21}(p)$, that is the roots of the denominator $D(p)$. These poles lie in the left half of the complex plane. Roots of $N(p)$ which are responsible for bringing in finite transmission zeros of the filter network can occur anywhere on the entire complex plane.

The order of the filtering function $F_n(\omega')$ is usually determined according to the desired slope of the transition band of the filter response. Filter design begins with selecting a suitable filtering function $F_n(\omega')$ that provides the required network responses. Some commonly used filtering functions are Butterworth (maximally flat), Chebyshev, and elliptic functions [8]. For instance, an ideal filter response can be approximated with a Chebyshev function $C_n(\omega')$ described by

$$C_n(\omega') = \begin{matrix} \cos(n\cos^{-1}\omega') & |\omega'| \leq 1 \\ \cosh(n\cosh^{-1}\omega') & |\omega'| \geq 1 \end{matrix} \tag{2.3}$$

Equation 2.3 must be a polynomial in ω'. $C_n(\omega')$ is expressed as a recursive formula [17]

$$C_{n+1}(\omega') = 2\omega' C_n(\omega') - C_{n-1}(\omega') \tag{2.4}$$

with initial conditions $C_0(\omega') = 1$ and $C_1(\omega') = \omega'$.

2.3 Lowpass Prototype and Bandpass Filters

2.3.1 Lowpass Prototype Filters

Filter synthesis starts with determining $N(p)$ and $D(p)$ from left half plane roots of amplitude-squared functions for specified passband ripple, ϵ. The input impedance function is obtained from the transfer function. The Darlington synthesis procedure may be performed by applying a bit of algebra such as partial fractions to obtain prototype elements [43]. These prototype elements usually produce a so-called lowpass prototype network with a cutoff angular frequency of unity and normalized source and load impedance. A lowpass prototype filter network constructed from prototype elements is shown in Fig. 2.1. The dual network (shunt capacitors replaced with series inductors and series inductors replaced with shunt capacitors) is also a valid lowpass prototype network.

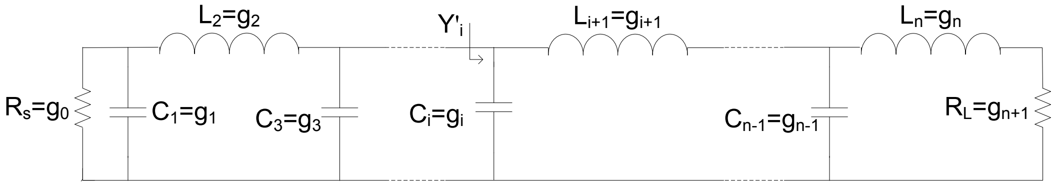

Figure 2.1: Lowpass prototype network.

Since the Darlington procedure is a lengthy process, tabulated lowpass prototype elements for several passband ripple levels (for several ϵ) and filter orders of $n = 1$ to 9 can be found in literature [9],[8]. For evaluating prototype elements for Chebyshev responses when the passband ripple level is not listed in the tables, the following equations can be used [26].

$$
\begin{aligned}
g_0 &= 1 \\
g_1 &= \frac{2}{\gamma}\sin\left(\frac{\pi}{2n}\right) \\
g_i &= \frac{1}{g_{i-1}}\frac{4\sin\frac{(2i-1)\pi}{2n}\sin\frac{(2i-3)\pi}{2n}}{\gamma^2+\sin\frac{(i-1)\pi}{n}} \quad \text{for } i = 2, 3, \cdots, n \\
g_{n+1} &= \left\{\begin{array}{ll} 1 & \text{for } n \text{ odd} \\ \coth^2\left(\frac{\beta}{2}\right) & \text{for } n \text{ even} \end{array}\right\}
\end{aligned}
\tag{2.5}
$$

where

$$
\begin{aligned}
\beta &= \ln\left[\coth\left(\frac{L_{Ar}}{17.37}\right)\right] \\
\gamma &= \sinh\left(\frac{\beta}{2n}\right)
\end{aligned}
$$

and L_{Ar} is given by

$$L_{Ar} = 10(1+\log\epsilon^2).$$

2.3.2 Bandpass Filters

A lowpass prototype filter network can be scaled to any frequency and transformed into any filter type, namely, lowpass, highpass, bandpass or bandstop. To map the lowpass prototype to a bandpass filter, the following transformation is used,

$$\omega' \leftarrow \frac{\omega_c'}{\Delta}\left(\frac{\omega}{\omega_0} - \frac{\omega_0}{\omega}\right) \tag{2.6}$$

where $\Delta = (\omega_2 - \omega_1)/\omega_0$, $\omega_0 = \sqrt{\omega_1\omega_2}$, and ω_c' is the normalized cutoff frequency of the prototype network which is often equal to 1, ω_1 and ω_2 are the lower and upper bandedge frequencies respectively. The above frequency transformation on the circuit in Fig. 2.1 yields a bandpass filter as shown in Fig. 2.2. At microwave frequencies, it is often not practical to construct a filter shown in Fig. 2.2, with alternating occurrence of series and parallel resonant circuits. Tuning different types of resonators is difficult and connecting series and parallel resonators may take more space.

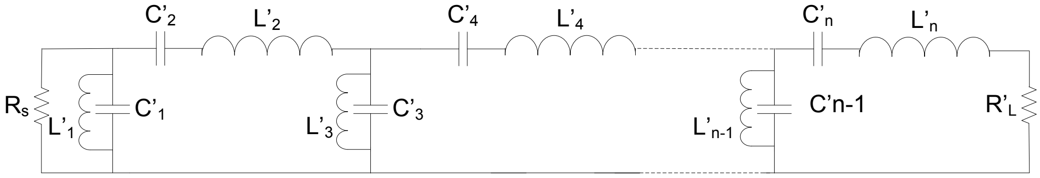

Figure 2.2: A bandpass filter network with series and parallel resonators.

However, it is possible to convert the filter with series tuned elements into an equivalent filter containing only parallel resonant circuits in a cascade connection. In order to design a bandpass filter with only shunt resonators, the lowpass prototype filter illustrated in Fig. 2.1 can be modified into a circuit with only shunt capacitors connected through admittance inverters. Fig. 2.3 depicts a modified lowpass network with only shunt capacitors as reactive elements, accomplished by considering the fact that a shunt capacitance with an admittance inverter on either side looks like a series inductance from the external terminal. Referring

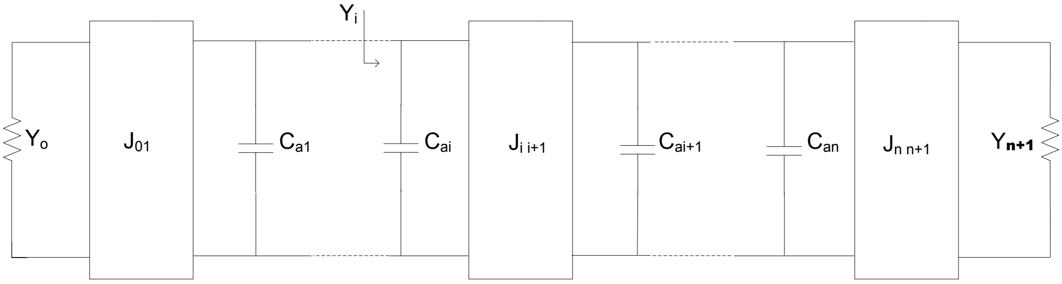

Figure 2.3: A modified prototype lowpass filter network.

to Fig. 2.1, the admittance of the $i^{\mathtt{th}}$ path and $i+1^{\mathtt{th}}$ path is given by

$$Y_i' = j\omega' C_i + \frac{1}{j\omega' L_{i+1}} \tag{2.7}$$

and referring to Fig. 2.3, that of the $i^{\mathtt{th}}$ path and $i+1^{\mathtt{th}}$ path is expressed from

$$Y_i = j\omega' C_{ai} + \frac{J_{ii+1}^2}{j\omega' C_{ai+1}}. \tag{2.8}$$

by multiplying Y_i' by a scaling factor of C_{ai}/C_i, we can equate

$$\begin{aligned} Y_i &= \frac{C_{ai}}{C_i} Y_i' \\ &= j\omega' C_{ai} + \frac{C_{ai}}{j\omega' C_i L_{i+1}}, \end{aligned} \tag{2.9}$$

so long as J_{ii+1} is made equal to

$$\begin{aligned} J_{ii+1} &= \sqrt{\frac{C_{ai}C_{ai+1}}{C_i L_{i+1}}} \qquad \text{for } i = 1 \text{ to } n-1 \\ &= \sqrt{\frac{C_{ai}C_{ai+1}}{g_i g_{i+1}}}. \end{aligned} \tag{2.10}$$

Similarly we can determine,

$$J_{01} = \sqrt{\frac{Y_0 C_{a1}}{g_0 g_1}} \tag{2.11}$$

and

$$J_{nn+1} = \sqrt{\frac{Y_{n+1} C_{an}}{g_n g_{n+1}}}. \tag{2.12}$$

The new element values in the modified prototype circuit, namely Y_0, C_{ai} and Y_{n+1}, can be chosen arbitrarily and the filter response will be identical to that of original network, provided that ideal admittance inverters can be realized as indicated in Equations 2.10 to 2.12.

The frequency transformation given in Equation 2.6 can be performed on the modified lowpass prototype network to obtain a bandpass filter with only shunt parallel resonators since ideal admittance inverter parameters are frequency invariant (actually, a modified lowpass network can be transformed into any other type of filter by applying a suitable frequency translation.).

Parallel resonators are convenient in practice to characterize using susceptance slope parameters. The susceptance slope parameter, b, of any parallel resonator

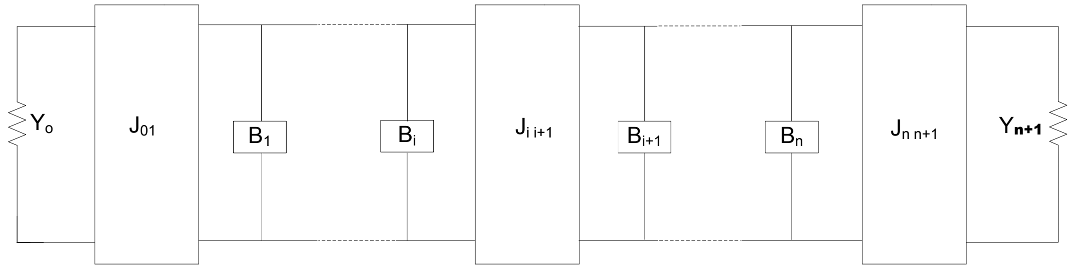

Figure 2.4: Generalized bandpass filter with shunt parallel resonators and admittance inverters.

is given by

$$b = \frac{\omega_0}{2}\frac{dB(\omega)}{d\omega}\Big|_{\omega=\omega_0} \tag{2.13}$$

where B is the susceptance of the resonator. Then, performing the frequency transformation on the modified lowpass prototype network, susceptance B_i of shunt parallel resonators in the generalized bandpass filter shown in Fig. 2.4 given by

$$jB_i = j\frac{\omega_c'}{\Delta}\left(\frac{\omega}{\omega_0} - \frac{\omega_0}{\omega}\right)C_{ai} \tag{2.14}$$

and the susceptance slope parameter of shunt parallel resonator given by

$$b_i = \frac{\omega_0}{2}\frac{d}{d\omega}\left[\frac{\omega_c'}{\Delta}\left(\frac{\omega}{\omega_0} - \frac{\omega_0}{\omega}\right)C_{ai}\right] \tag{2.15}$$

yields

$$C_{ai} = \frac{b_i\Delta}{\omega_c'} \quad \text{for } i = 1 \text{ to } n. \tag{2.16}$$

The admittance inverters of the generalized filter illustrated in Fig. 2.4 can then be represented as,

$$J_{01} = \sqrt{\frac{Y_0\Delta b_1}{\omega_c' g_0 g_1}} \tag{2.17}$$

$$J_{ii+1} = \frac{\Delta}{\omega_c'}\sqrt{\frac{b_i b_{i+1}}{g_i g_{i+1}}} \quad \text{for } i = 1 \text{ to } n{-}1 \tag{2.18}$$

$$J_{nn+1} = \sqrt{\frac{Y_{n+1}\Delta b_n}{\omega_c' g_n g_{n+1}}} \tag{2.19}$$

from Equations 2.10 to 2.12. Now, the bandpass filter shown in Fig. 2.4 can be designed knowing the susceptance slope parameters of arbitrarily selected shunt parallel resonators. Similar design equations can also be obtained for the dual circuit (only series elements) of the bandpass filter in Fig. 2.4.

Admittance inverters can be realized basically in two ways. One way is using quarter wavelength transmission lines and the other way is implementing it with lumped elements. Two common lumped element based admittance inverter topologies are shown in Fig. 2.5 [18], [9]. These inverters are assumed to be ideally frequency independent in the filter design although this is not the case in reality. Admittance inverter parameters of these circuits can be obtained as follows:

$$J = \begin{matrix} \frac{1}{\omega L} & \text{for inductive circuit} \\ \omega C & \text{for capacitive circuit} \end{matrix} \tag{2.20}$$

In terms of phase change, the signs of J of inductive circuits and capacitive circuits are considered as positive and negative respectively.

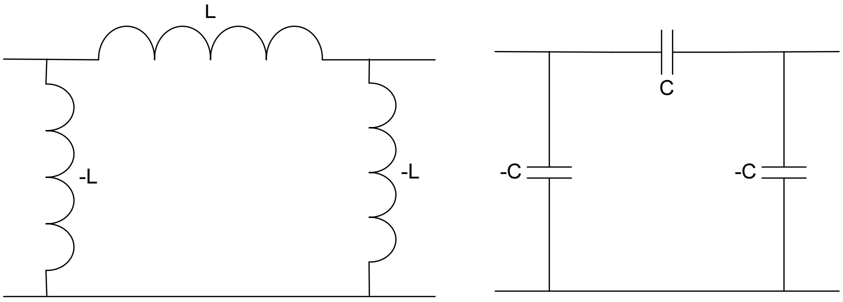

Figure 2.5: Lumped element inverters.

The use of the generalized bandpass filter in Fig. 2.4 with admittance inverters, designed from the lumped element lowpass prototype network through the use of network synthesis and impedance and frequency transformation works well for bandpass filters with simple TEM (transverse electromagnetic- electric and magnetic field are perpendicular to the direction of propagation) transmission line resonators such as half wavelength microstrip resonators and half wavelength CPW resonators. For bandpass filters with complex resonators such as miniaturized half wavelength open loop resonators and non-TEM waveguide resonators (cavity resonators), the approach with the knowledge of only external quality factor Q_e and the coupling coefficient m_{ii+1} (will be detailed in the next section) between each resonator is more convenient. Both of these parameters can be described in terms of the prototype g_i values and the ripple bandwidth Δ.

The coupling coefficient is given by

$$\begin{aligned} m_{ii+1} &= \frac{J_{ii+1}}{\sqrt{b_i b_{i+1}}} \\ &= \frac{\Delta}{\omega_c' \sqrt{g_i g_{i+1}}} \end{aligned} \tag{2.21}$$

where the subsequent equation is obtained using Equation 2.18. The quality factor Q of a parallel resonator with conductance G is given by [8]

$$Q = \frac{b}{G} \tag{2.22}$$

The admittance inverter J_{01} from Fig. 2.4 reflects an admittance of J_{01}^2/Y_0 to the first resonator. The loaded quality factor Q_{L1} of the first resonator can be given by

$$Q_{L1} = \frac{b_1}{J_{01}^2/Y_0 + G}. \tag{2.23}$$

If $G = 0$ (unloaded $Q_{u1} = \infty$), then Q_{L1} is equal to Q_{e1} (because $1/Q_{L1} = 1/Q_{e1} + 1/Q_{u1}$[26]), and

$$\begin{aligned} Q_{e1} &= \frac{b_1}{J_{01}^2/Y_0} \\ &= \frac{\omega_c' g_0 g_1}{\Delta} \end{aligned} \tag{2.24}$$

from Equation 2.17. Similarly the output external quality factor Q_{exn} in the generalized bandpass filter in Fig. 2.4 is given by

$$\begin{aligned} Q_{exn} &= \frac{b_n}{J^2_{nn+1}/Y_{n+1}} \\ &= \frac{\omega'_c g_n g_{n+1}}{\Delta} \end{aligned} \tag{2.25}$$

using Equation 2.19. If lumped element resonators and frequency independent admittance inverters were used in the practical realization of the filter, the above design equations are exact. However, for frequency dependent components such as coupling gaps and for distributed resonators, the above equations are good approximations only over a bandwidth of a few percent of the centre frequency. The assumption that unloaded quality factor $Q_u = \infty$ also contributes to this approximation. Hence coupling coefficient and external quality factors have to be tuned to meet design goals.

2.4 Coupling Coefficient

After determining the bandpass filter design parameters such as coupling coefficient and external quality factor, establishing the relationship of these parameters to physical structure is the pending important task to find the physical parameters of final filter structure for fabrication. A relationship for extracting coupling coefficient from physical parameters is developed, from the definition of it. In general, the coupling coefficient of coupled *RF* or microwave resonators can be defined as the ratio of coupled *EM* energy between resonators to the total stored *EM* energy of both resonators at the resonance.

Capacitively coupled miniaturized half wavelength open loop resonators have been illustrated in Fig. 2.6(a) along with the simplified equivalent circuit shown in Fig. 2.6(b). Synchronously tuned resonators (resonators that resonate at the same frequency) are represented by parallel shunt *LC* resonators and shunt capacitors

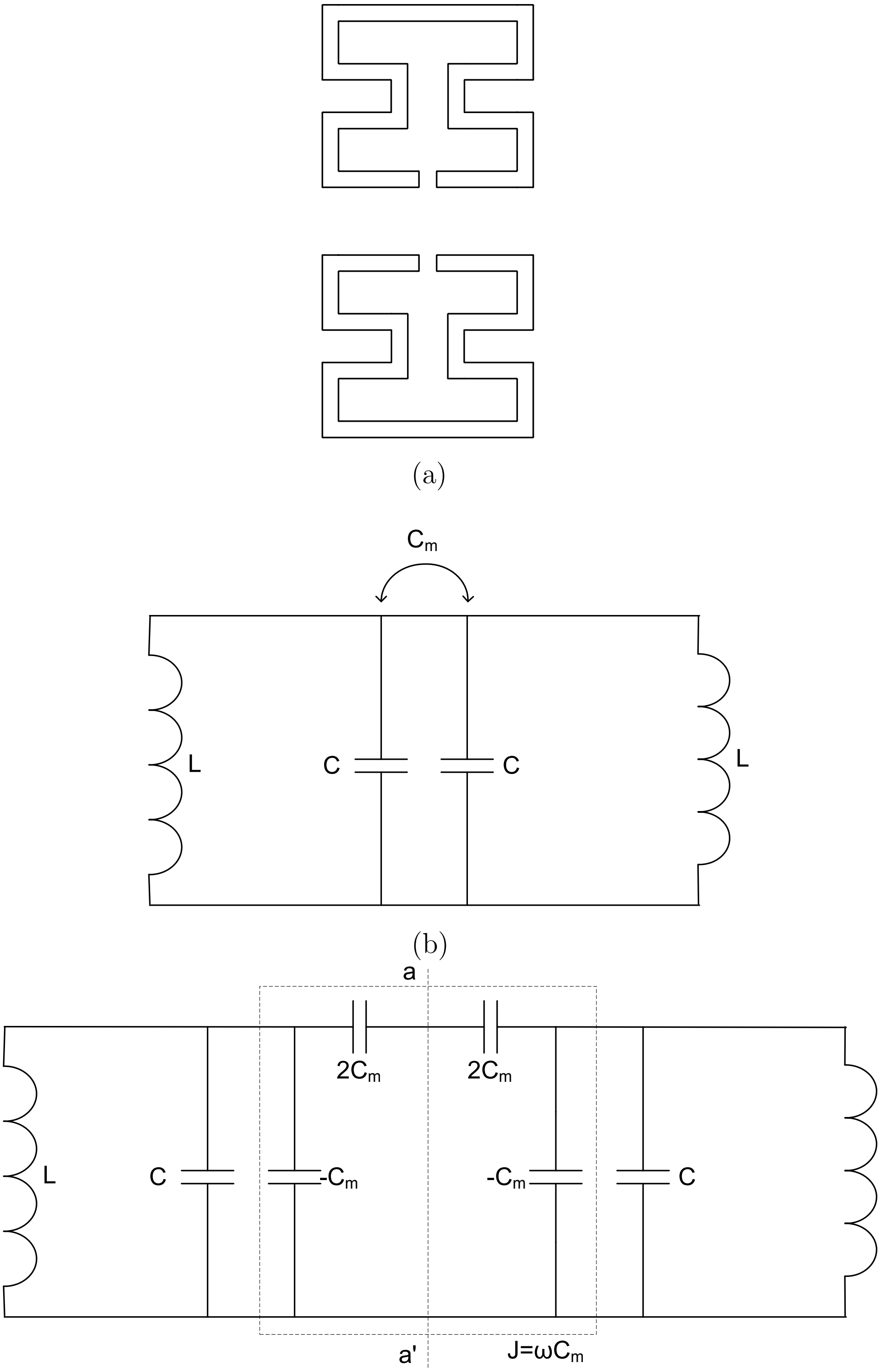

(a)

(b)

(c)

Figure 2.6: (a) Capacitively coupled half wavelength open loop resonators, (b) An equivalent circuit for these resonators; (c) An alternative equivalent circuit with admittance inverter $J = \omega C_m$.

and are coupled together by a mutual coupling capacitor with capacitance of C_m. An alternative form of the above equivalent circuit which is more convenient to deal with can be obtained from network theory and it is depicted in Fig. 2.6(c)[44]. The two port parameters of both circuits are the same. The coupling of parallel shunt resonators is represented by an admittance inverter $J = \omega C_m$ (refer to Equation 2.20). For each loop resonance, there are two oscillation modes, one corresponding to an electric wall or a short circuit surface at the symmetry plane $a - a'$ and the other corresponding to a magnetic wall or open circuit at the symmetry plane. The resonant frequency f_e when the electric wall is inserted, is given by

$$f_e = \frac{1}{2\pi\sqrt{L(C + C_{m)}}} \tag{2.26}$$

while the resonant frequency is given by

$$f_m = \frac{1}{2\pi\sqrt{L(C - C_m)}} \tag{2.27}$$

when a magnetic wall is placed at the symmetry plane. According to the definition of coupling coefficient, $m = C_m/C$ (the ratio of coupled energy to stored energy). The coefficient m can also be obtained by applying Equation 2.21 for two synchronously tuned resonators with shunt capacitance, C coupled with an admittance inverter of $J = \omega C_m$. From Equations 2.26 and 2.27, the coupling coefficient is given by

$$m = \frac{C_m}{C} = \frac{f_m^2 - f_e^2}{f_m^2 + f_e^2}. \tag{2.28}$$

Similar equations can be obtained for magnetic coupled resonators or mixed coupled resonators [26].The uncoupled identical resonators have the same resonant frequency, which depends on the physical lengths of the loops. When resonators are coupled, the resonant mode of each resonator becomes degenerate and the frequencies split as defined by f_e, which shifts lower in frequency due to $C + C_m$ term in 2.26 and f_m which shifts upper in frequency due to $C - C_m$ in 2.27.

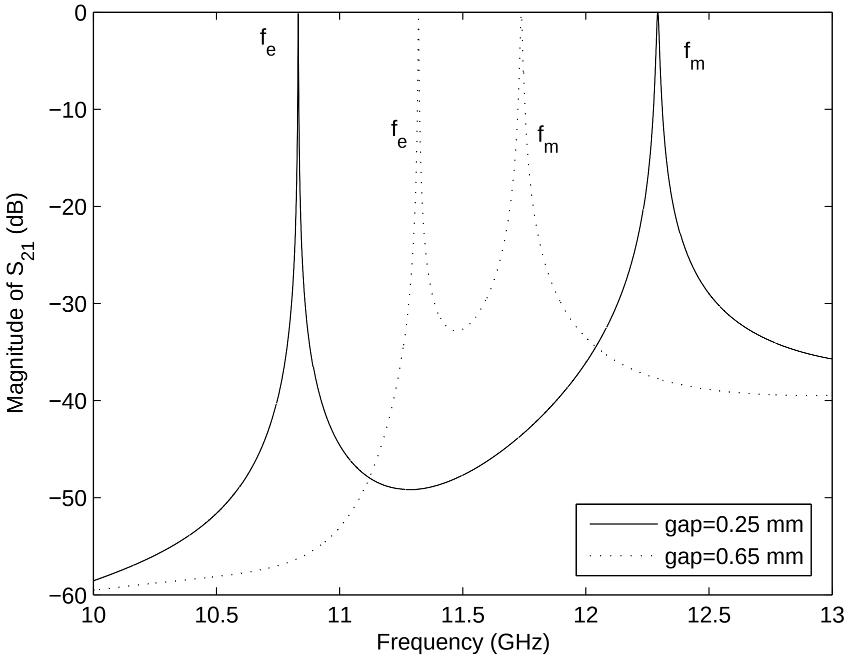

Figure 2.7: Insertion loss curves for open loop resonators illustrated in Fig. 2.6(a): Solid curve corresponds to a coupling gap of 0.25 mm; Dotted curve corresponds to a coupling gap of 0.65 mm

An illustration of insertion loss curves for miniaturized capacitively coupled open loop resonators whose individual resonant frequency is around 11.5 GHz is shown in Fig. 2.7. It demonstrates shifting of poles for different coupling gaps. The mode splitting is illustrated by two peaks at $f_m = 12.3$ GHz and $f_e = 10.83$ GHz for the solid curve which corresponds to a coupling gap of 0.25 mm, and by the other two peaks at $f_m = 11.74$ GHz and $f_e = 11.32$ GHz for the dotted curve which corresponds to a coupling gap of 0.65 mm. Split resonant frequency modes shift above and below the individual resonant frequency. The wider coupling gaps yield weaker coupling.

Now, the coupling coefficient of synchronously tuned resonators may be easily determined from insertion loss curves as shown in Fig. 2.7 using Equation 2.28. In this thesis, the coupling coefficients are obtained from insertion loss curves of resonators loosely coupled to external ports for convenience. The coupling coefficient can also be obtained from the Eigenmode response without loading effect of the external ports.

2.5 Q-Factors

To determine the physical parameters of the external interface to the resonators of a filter, external quality factor is an important design parameter. To establish a relationship with physical parameters, there are two basic methods in the literature for this purpose, namely transmission type extraction and reflection type extraction [45], [46].

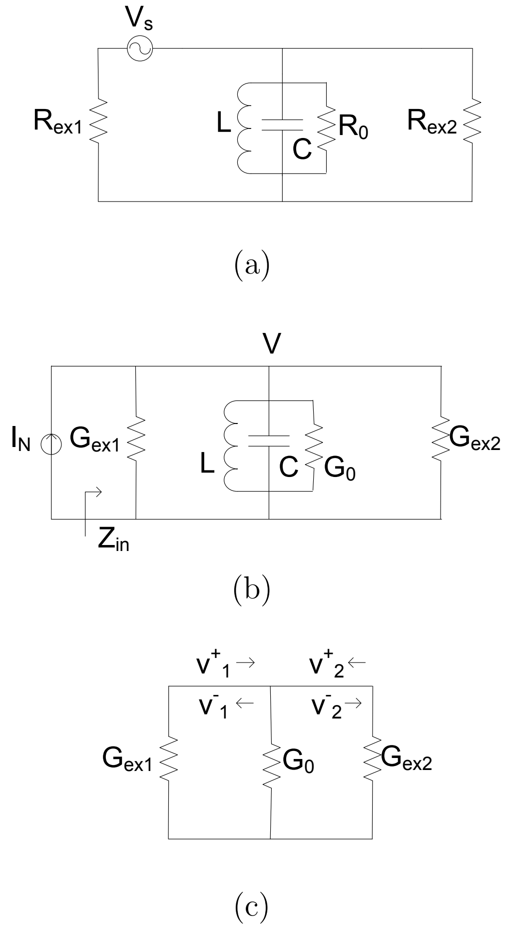

(a)

(b)

(c)

Figure 2.8: (a) Thevenin's equivalent circuit for transmission type Q-factor extraction, (b) Norton's equivalent circuit for figure in (a), (c) Simplified equivalent circuit at resonance.

An illustration of a Thevenin's equivalent circuit of a transmission type Q-factor extraction setup is shown in Fig. 2.8(a). A voltage source with voltage V_s and a internal resistance of R_{ex1} is coupled to a shunt resonator with resistance R_0, inductance L and capacitance C. A load resistance R_{ex2} is also coupled to the resonator. Converting the Thevenin's circuit into a Norton equivalent, Fig.

2.8 (b) is obtained to facilitate derivation of an expression for Q-factor. Average energy stored in the capacitor is $W_e = |V|^2C/4$, where V is the voltage across the shunt resonator. Magnetic energy stored in the inductor is same as W_e. The total power loss is $P_{loss} = |V|^2/(2R)$ where the overall shunt resistance $R = 1/(G_{ex1} + G_0 + G_{ex2})$. Hence, the loaded quality factor is

$$Q = \omega_0 \frac{2W_e}{P_{loss}} = \omega_0 RC. \tag{2.29}$$

where ω_0 is the resonant angular frequency. The overall impedance seen from the source is given by

$$Z_{in} = \left(\frac{1}{R} + \frac{1}{j\omega L} + j\omega C\right)^{-1}. \tag{2.30}$$

Letting $\omega = \omega_0 + \Delta\omega$, where $\Delta\omega$ is small, Equation 2.30 can be written as [8]

$$\begin{aligned} Z_{in} &\simeq \left(\frac{1}{R} + \frac{1 - \Delta\omega/\omega_0}{j\omega_0 L} + j\omega_0 C + j\Delta\omega C\right)^{-1} \\ &\simeq \left(\frac{1}{R} + 2j\Delta\omega C\right)^{-1} \\ &\simeq \frac{R}{1 + 2j\Delta\omega RC} = \frac{R}{1 + 2jQ\Delta\omega/\omega_0}. \end{aligned} \tag{2.31}$$

Z_{in} is a function of frequency and $|Z_{in}|$ drops to $R/\sqrt{2}$ when $\omega = \omega_2$ or ω_1 where $\omega_2 - \omega_1 = 2\Delta\omega$. Hence, loaded quality factor can be determined by

$$Q_L = \frac{\omega_0}{\omega_2 - \omega_1} = \frac{f_0}{f_2 - f_1}. \tag{2.32}$$

Using a relationship of $|S_{21}|$ with f or ω is more practical to find f_2 and f_1 or ω_2 and ω_1 when $|S_{21}|$ drops by 3 dB as shown in Fig. 2.9, since $1/\sqrt{2}$ bandwidth (3 dB bandwidth) is same for $|S_{21}|$ and $|Z_{in}|$. The magnitude of S_{21} at the resonant frequency f_0 is also a useful parameter for evaluating external quality factor and unloaded quality factor. Referring to the simplified circuit at resonance in Fig. 2.8(c), the reflected wave at the input port v_1^- can be written in terms of the

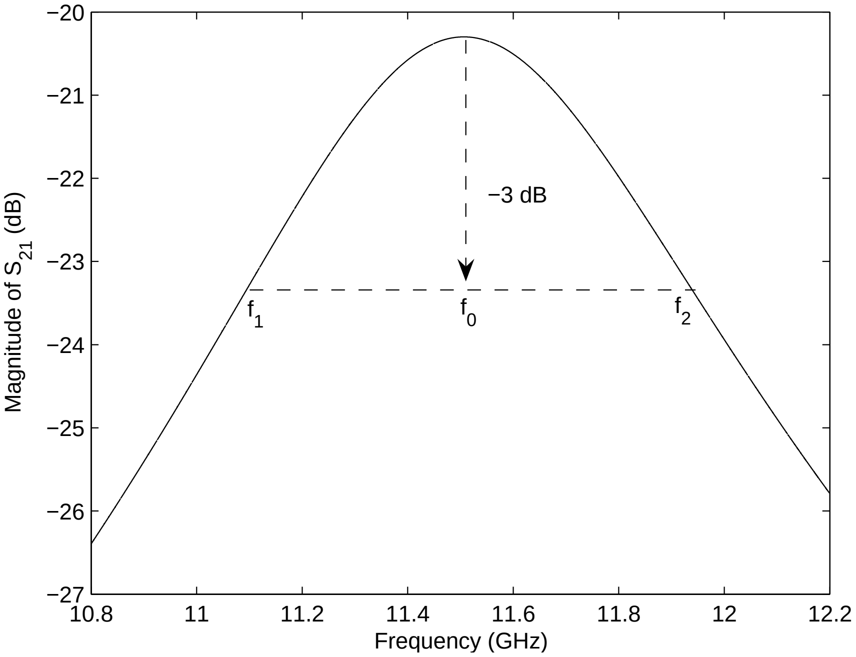

Figure 2.9: Typical insertion loss curves for extracting Q_L

incident wave at the input port and the reflection coefficient Γ, as $v_1^- = v_1^+\Gamma$ where $\Gamma = (G_{ex1} - G_0 - G_{ex2})/(G_{ex1} + G_0 + G_{ex2})$. Since $v_2^- = v_1^+ + v_1^-$, we can obtain the ratio v_2^-/v_1^+ as

$$\begin{aligned}\frac{v_2^-}{v_1^+} &= (1+\Gamma)\\ &= \frac{2G_{ex1}}{G_{ex1}+G_0+G_{ex2}}.\end{aligned} \tag{2.33}$$

Now, insertion loss at resonance can be found in terms of shunt conductance using Equation 2.33 and it is given by

$$\begin{aligned}|S_{21}(f_0)| &= \sqrt{\frac{(v_2^-)^2 G_{ex2}}{(v_1^+)^2 G_{ex1}}} = \frac{2\sqrt{G_{ex1}G_{ex2}}}{G_{ex1}+G_0+G_{ex2}}\\ &= \frac{2\sqrt{\frac{G_{ex1}}{G_0}\times\frac{G_{ex2}}{G_0}}}{1+\frac{G_{ex1}}{G_0}+\frac{G_{ex2}}{G_0}}.\end{aligned} \tag{2.34}$$

The ratio of power dissipated in the external circuit to the power dissipated in the resonator is called external coupling coefficient k [45]. As G_0 , G_{ex1}, and

G_{ex2} have a common voltage, the ratio of powers are proportional to conductance values, and one can therefore define the input and output coefficient as follows:

$$k_1 = \frac{G_{ex1}}{G_0} = \frac{Q_0}{Q_{ex1}} \tag{2.35}$$

$$k_2 = \frac{G_{ex2}}{G_0} = \frac{Q_0}{Q_{ex2}} \tag{2.36}$$

because $Q_{ex1} = 4\omega_0 W_e/(V^2 G_{ex1})$ and Q_0, Q_{ex2} have similar equations in terms of G_0 and G_{ex} respectively. Having expressed coupling coefficient in terms of conductance, one can determine $|S_{21}(f_0)|$ in terms of coupling coefficients using Equations 2.35 and 2.36 as given by

$$|S_{21}(f_0)| = \frac{2\sqrt{k_1 k_2}}{1 + k_1 + k_2}. \tag{2.37}$$

Through a careful design and fabrication procedure, input and output coupling coefficients can be made equal to each other so that $k_1 = k_2$. For such a symmetrical coupling, the ratios of Q_0/Q_{ex1} and Q_0/Q_{ex2} are obtained from Equations 2.35, 2.36 and 2.37 as,

$$\frac{Q_0}{Q_{ex1}} = \frac{Q_0}{Q_{ex2}} = \frac{|S_{21}(f_0)|}{2(1 - |S_{21}(f_0)|)}. \tag{2.38}$$

$|S_{21}(f_0)|$ can be obtained easily from a graph like shown in Fig. 2.9. Q_L, Q_{ex} and Q_0 can be determined separately using Equations 2.32 and 2.38 and considering the fact that $1/Q_L = 1/Q_{ex} + 1/Q_0$ [8].

For the transmission type parameter extraction to be accurate, input and output couplings should be equal to each other. In measurement, one must trust that the mechanical tolerances are tight enough to ensure the equality whereas in simulation, this condition can be met easily. Another important factor to note is that the accuracy reduces when coupling is larger than critical. This happens because $|S_{21}(f_0)|$ approaches unity as the coupling becomes strong and slight error in insertion loss reflects as an amplified error to the left hand side of Equation 2.38.

Chapter 3

LIGA Micromachined Transmission Lines and Resonators

3.1 Introduction

Most transmission systems in microwave integrated circuits (MICs) are planar in configuration. A planar configuration implies that the characteristics of the transmission system can be controlled by dimensions in a single plane. Hence, circuit fabrication can be easily carried out by techniques of photolithography and photoetching of thin films. There are several planar transmission structures commonly used in MICs as shown in Fig. 3.1. Microstrip, slotline, CPW and coplanar strips are among them. These conventional transmission lines fabricated using standard photolithography and photoetching of thin film have certain limitations in achieving certain requirements in microwave and millimetrewave circuits [47]. The LIGA process allows fabrication of novel counterparts of the above transmission lines to achieve certain required properties which cannot be achieved with conventional transmission lines, using the vertical height as a new design parameter without losing the advantages of the lateral configurations of the above conventional transmission line [5], [33], [36].

Among these transmission lines, microstrip line and CPW are most popular, mainly due to the fact that the mode of propagation is approximately transverse

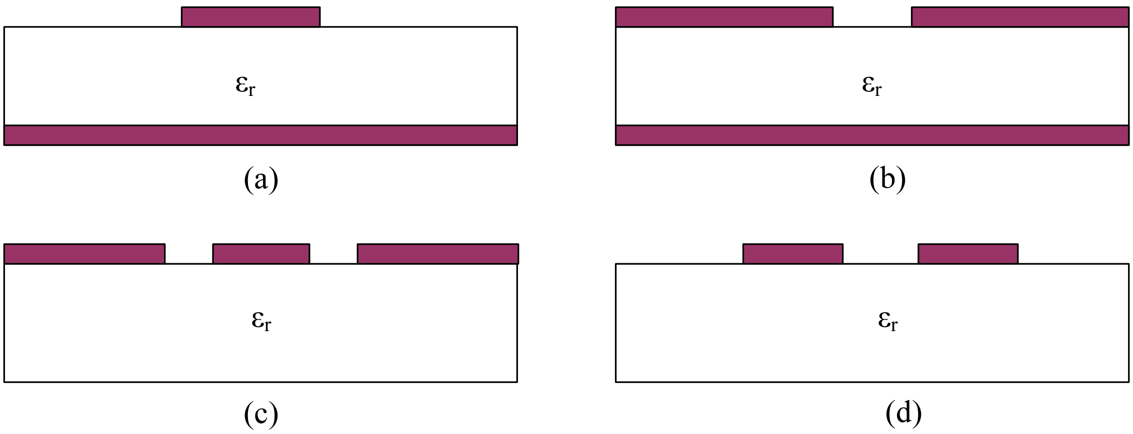

Figure 3.1: Planar Transmission Structures; (a) Microstrip line, (b) Slot line, (c) Coplanar waveguide, (d) Coplanar strips.

(TEM) and convenient element connections are possible. LIGA microstrip transmission lines and CPWs are discussed in this chapter. The characteristics of half wavelength folded open loop resonators are presented.

3.2 LIGA Micromachined Microstrip Transmission Lines

Microstrip is a two conductor transmission line which can be considered to have evolved conceptually from a two wire transmission line. A two wire transmission line system is equivalent to a single wire line in the presence of an infinite perfect conductor which is placed at the half distance of the gap between the original two wires, in the same media as in the original two wire line. Then a dielectric slab is introduced between the wire and infinite perfect conductor. The shape of the wire is changed into the shape of a trace in a microstrip line.

3.2.1 Methods of Microstrip Analysis

The microstrip structure is open at the top. This open configuration makes microstrip lines very convenient for use in MICs where lumped (active or passive) or distributed elements are to be mounted on the circuit. However, it makes the analysis of microstrip lines more difficult.

Extensive literature dealing with the analytical and numerical solutions of microstrip transmission line exists [7]. Of these solutions, the quasi-static approach is perhaps the simplest but has a limited range of validity, while the full-wave technique is complete and rigorous. In the quasi-static approach, the nature of the mode of propagation is considered to be pure TEM (transverse electric and magnetic fields). The transmission line characteristics are determined from the electrostatic capacitances of the structure and these capacitances are evaluated employing conformal transformation methods [7]. Even with the quasi-static approximation, no closed form expressions for transmission characteristics exist. Derivations for thin strip with dielectric have been given by Wheeler in 1965 [48]. Two sets of formulas cover wide and narrow strips. The first-order effect of small thickness is given in the paper based on width adjustment for the cases of wide and narrow strips. As an extreme departure from the thin strip, a square or a circular cross section has been considered by Wheeler in a later paper, in order to approximate the metal thickness of the signal trace of the microstrip structure [49]. In this case also, metal thickness is accounted for by the width adjustment for special cases of narrow strips and wide strips. Modified equations to give higher accuracy for narrow strips are given in [50]. These models are not suitable for LIGA microstrip lines with very thick (100s of microns) conductors and their dimensions varying over a wide range.

The magnetic field and the electric field in the microstrip structure exist both in the air and dielectric regions. Tangential electric and magnetic field components both in air and dielectric and on the air−dielectric interface should be equal since there are no surface currents. To meet this criteria, it can be shown using Maxwell's Equations that longitudinal electric and magnetic field components must exist [7], and thus, microstrip transmission line cannot support a pure TEM wave. So it is necessary to resort to full-wave numerical methods in order to accurately characterize tall microstrip lines. The finite element method (FEM) is a powerful numerical method suitable for analyzing three dimensional complicated structures. In this research work as explained in later Chapters, complex structures will be analyzed using a full-wave technique taking into account the tall metal height of conductors. The finite element method based numerical technique is more suitable to deal with complex three dimensional structures.

In general, FEM contains several basic steps starting from discretizing or meshing the entire solution region into a finite number of small sub−regions or elements. Continuous quantities are approximated with discrete quantities in finite elements. Finally, the set of linear equations is solved after assembling all elements in the solution region. A more profound reference as applied to electromagnetics may be found in [51].

Commercial FEM-based software such as Ansoft `HFSS`™ 3D electromagnetic simulation software [52] is useful to analyze LIGA microstrip lines. It is a full−wave 3D simulation software capable of determining 3D fields and associated currents of passive structures. HFSS takes into account losses, dispersion effect, all propagation modes, and radiation. The software manually or automatically discretizes the solution region into a fine mesh with tetrahedra, and then finds vector fields at vertices. The field inside tetrahedra is interpolated from the field at vertices whose components are along three converging edges of the tetrahedral. HFSS represents Maxwell's Equations as sets of algebraic equations, using discrete nodal fields, and by applying relevant boundary conditions (such as perfect conductor, perfect magnetic, surface impedance, radiation, absorbtion and master− slave) solves them using matrix methods. Generally, a fine mesh is required for better accuracy, however, available computer resources is a limiting factor for the density of the mesh. Therefore, a trade-off between the level of accuracy and mesh density is sought proceeding from availability of computing resources. Generally, the size of elements should be considerably smaller than the wavelength, and should be sufficiently small to interpolate the quantities inside the element with acceptable accuracy. Starting with a course mesh which can be seeded manually if needed, the software may optimize the mesh refining it in the regions with higher error density in each iteration until the stop criteria is met.

3.2.2 Characteristics of High Aspect Ratio Microstriplines

High aspect ratio microstrip lines of different conductor height, h, on a 0.5 mm thick ($t = 0.5$ mm) fused Quartz substrate (relative permittivity, $\epsilon_r = 3.78$) are characterized. Approximately 15000 to 20000 tetrahedral elements are created for the mesh in HFSS for analyzing microstrip structures. Comparison of the magnitude of microstrip electric field distribution for a thin conductor with $h =$ 0.01 mm and tall conductor with $h = 0.22$ mm is illustrated in Fig. 3.2 (a) and (b) respectively (conductor trace width $w = 0.875$ mm). Highest field concentration is located at the bottom outer edges of both lines and the magnitude of field concentration of the thin conductor is higher than that of thick conductor, hence greater conductor loss associated with the thin conductor can be anticipated. Higher electric field intensity above the substrate along the side walls of the tall trace can be observed up to a higher level than with thin conductor.

Fig. 3.3 illustrates the variation of characteristic impedance with the conductor width, w, varied from 0.05 mm to 0.95 mm for different conductor heights of $h = 0.01$mm, $h = 0.22$ mm, $h = 0.4$ mm and $h = 0.8$ mm. For the same conductor width, the characteristic impedance is lower for microstrip lines with tall conductor traces. For instance, the required trace width with $h = 0.01$ mm for realizing a microstrip line with characteristic impedance of 100 Ω is 0.265 mm while the required trace width with $h = 0.22$ mm for realizing the same line is 0.12 mm. This difference is much more significant for microstrip lines with very narrow signal traces as evident from the figure. It indicates that low impedance microstrip lines can be fabricated using the LIGA micromachining technique with relatively narrow conductor strips, potentially resulting in compact structures.

The variation in phase constant of microstrip lines with traces having different

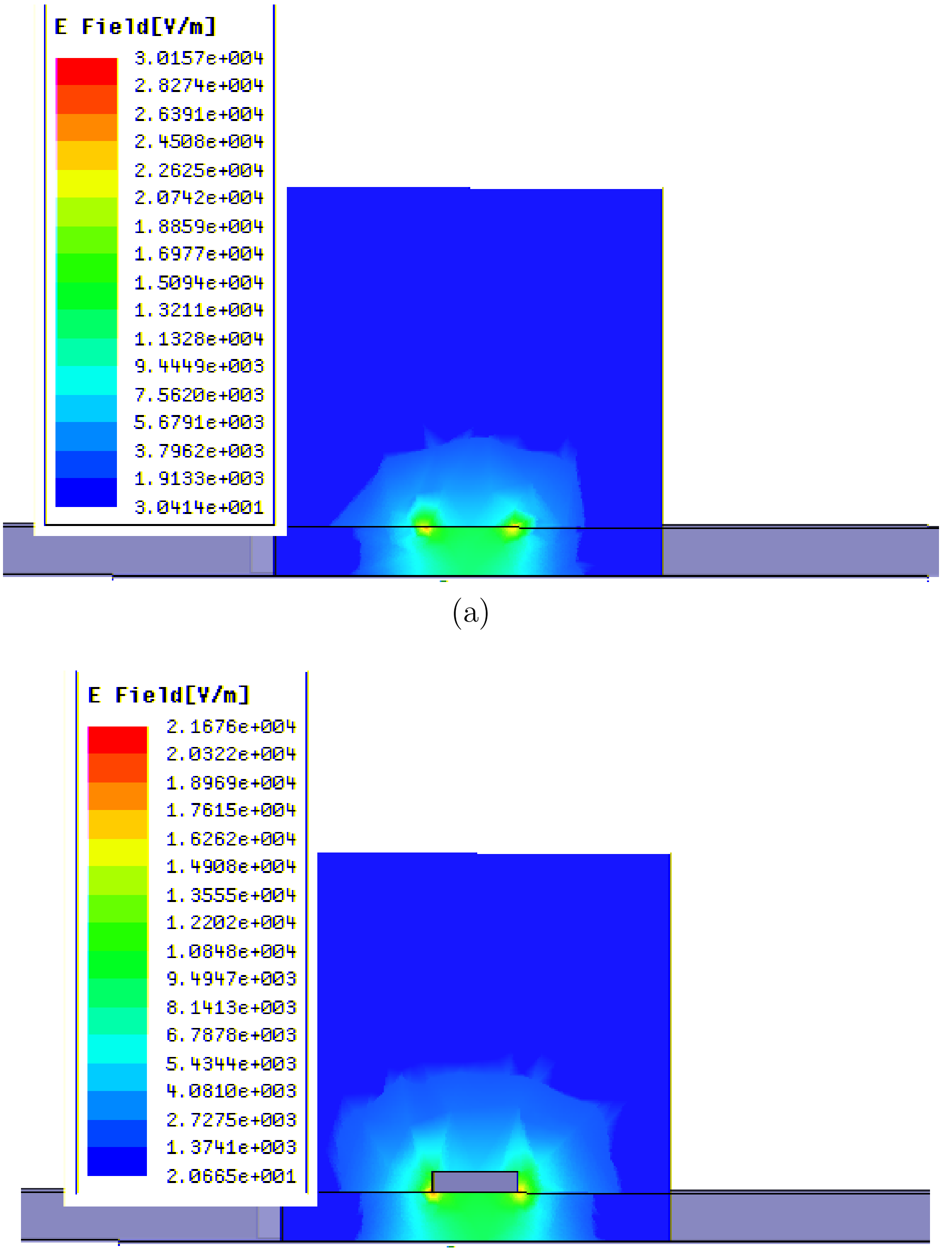

(a)

(b)

Figure 3.2: Electric field pattern of microstrip lines of width $w = 0.875$ mm on fused quartz substrate of $t = 0.5$ mm; (a) Thin microstrip line of height $h = 0.01$ mm, (b) Tall microstrip line of height $h = 0.22$ mm.

heights as in the above case versus trace width is shown in Fig. 3.4. With the increase in trace height, phase constant decreases. It is due to the fact that effective dielectric constant decreases with the increase of trace height because the presence of field in the air above the substrate increases as observed in field distribution diagram in Fig. 3.2. The characteristics of attenuation constant (α) is depicted

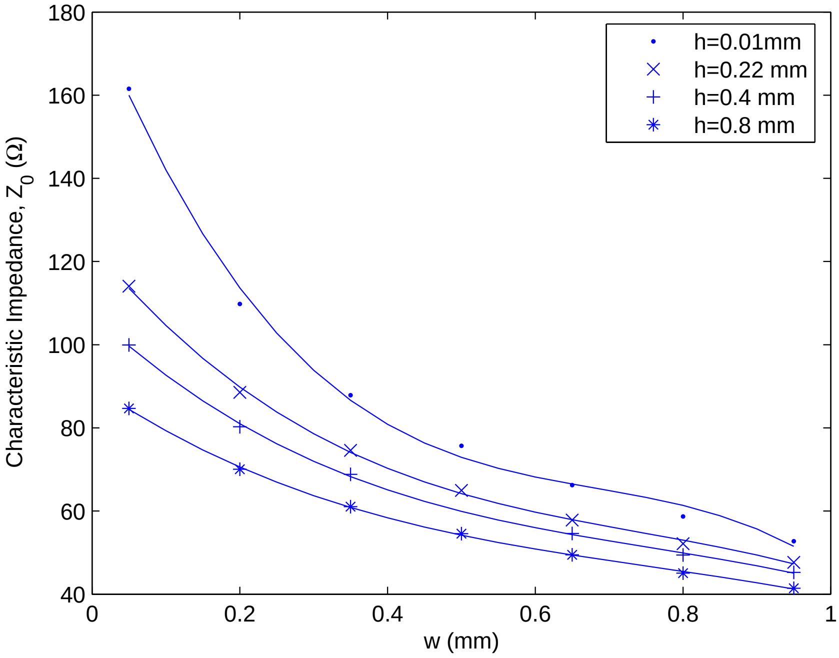

Figure 3.3: Characteristic impedances of microstrip lines vs. conductor width, w, on a 0.5 mm thick fuzed quartz substrate at the frequency of 10.5 GHz.

in Fig. 3.5 for microstrip lines made of gold with height $h = 0.01$ mm, $h = 0.22$ mm and $h = 0.4$ mm at the frequency of 10.5 GHz. Attenuation loss decreases with increase of trace height. There is a significant attenuation loss for narrow thin traces compared to narrow tall traces. It is mainly because higher current density is crowded in a small cross sectional area in the case of thin narrow traces unlike in the case of tall narrow traces. Hence, it is possible to fabricate low loss narrow traces using the LIGA fabrication method.

3.3 LIGA Micromachined Coplanar Waveguide

As shown in Fig. 3.1(c), coplanar waveguide consists of a centre conductor strip with two ground planes parallel to and on the same surface on the dielectric. This waveguide was first proposed by Wen [53] in 1969. Since then, it has become a popular transmission media because of its inherent advantages suitable for MICs.

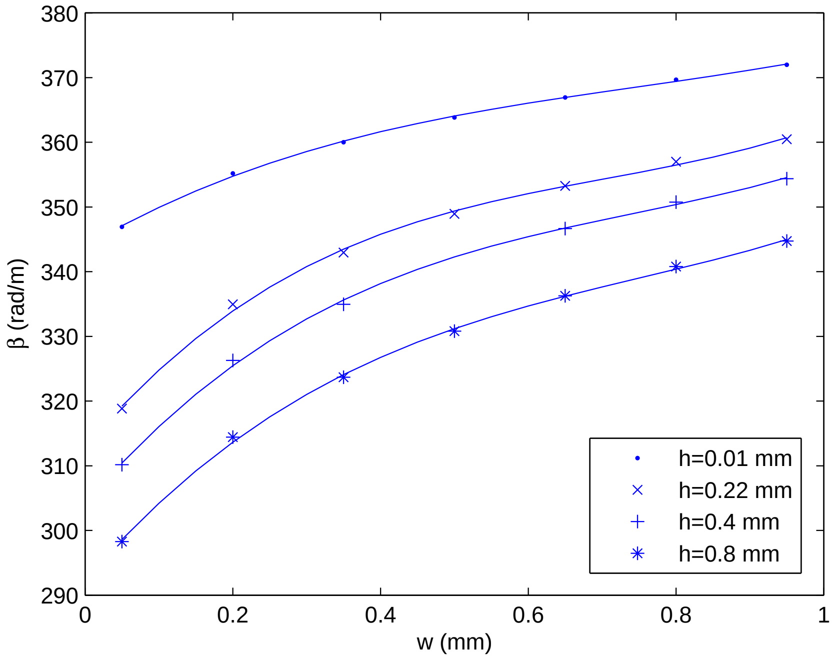

Figure 3.4: Phase constant of microstrip lines vs. conductor width, w, on a 0.5 mm thick fuzed quartz substrate at the frequency of 10.5 GHz.

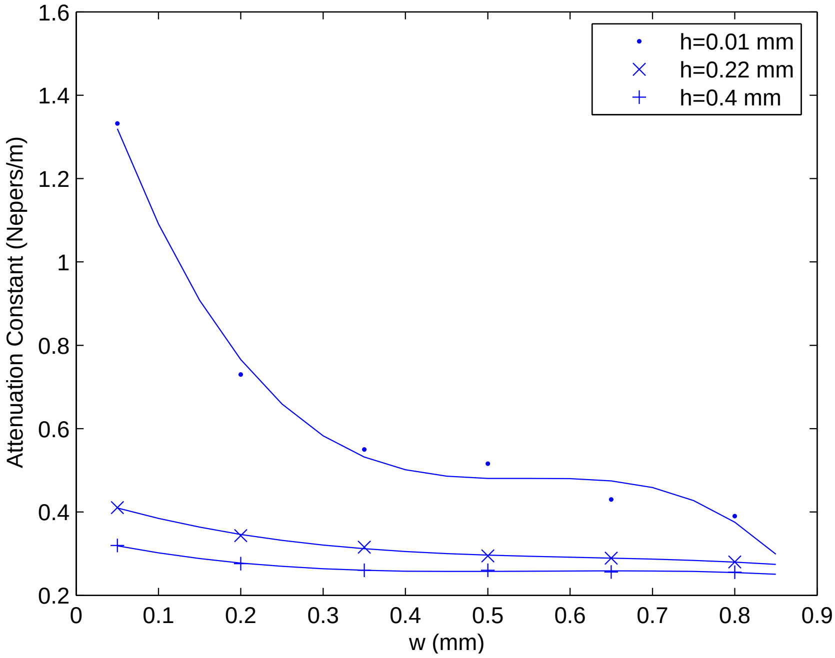

Figure 3.5: Attenuation constant (α) of microstrip lines vs. conductor width, w, on a 0.5 mm thick fuzed quartz substrate at the frequency of 10.5 GHz.

Mounting of lumped components (active or passive) in shunt or series configuration is much easier and avoids drilling holes through the substrate that may cause unwanted resonances and parasitics.

Since CPW generally consists of metal conductors backed by dielectric media, the field propagating along the line is not entirely in a homogeneous media. So making a similar argument as in the case for microstrip line in Section 3.1.1, it can be shown using Maxwell's Equations that longitudinal components of electric field and magnetic field should not be equal to zero in order to meet the boundary conditions at the air dielectric interface. Hence, CPW cannot support pure TEM propagation mode. However, longitudinal field components are small enough to assume that CPW supports quasi-TEM mode.

3.3.1 Analysis of Coplanar Waveguide

Most of the CPW analysis and design methods based on an analytical approach for the sake of obtaining relatively simple formulas are based on assumptions. A rudimentary quasi-static analysis method is available in [7] by using conformal transformation and by making assumptions of negligible metallization thickness and an infinitely thick dielectric. The transformed structure is treated as a parallel plate capacitor. This method has been modified by Davis [54] to account for finite thickness of the dielectric substrate. Schwarz-Cristoffel formulas, a conformal transformation suitable for polygon regions, have been utilized for analyzing CPW with finite conductor thickness. The initial cross section topology is transformed into a rectangular shape to solve the Laplace Equations relatively easily. A case study for analyzing CPWs with a trapezoidal centre conductor has been presented in [55]. However, infinite substrate thickness is assumed in many cases (some references cited in [55]) when conductor thickness is taken into account.

The above mentioned methods based on an analytical approach do not account for dispersion characteristics and the frequency dependance of propagation characteristics. For analyzing complex CPW structures that are encountered in this research work, numerical approaches are required since the above analytical approaches are limited to uniform CPW lines. As in the case of microstrip lines, full wave three dimensional electromagnetic simulation can be used to characterize high aspect ratio CPWs.

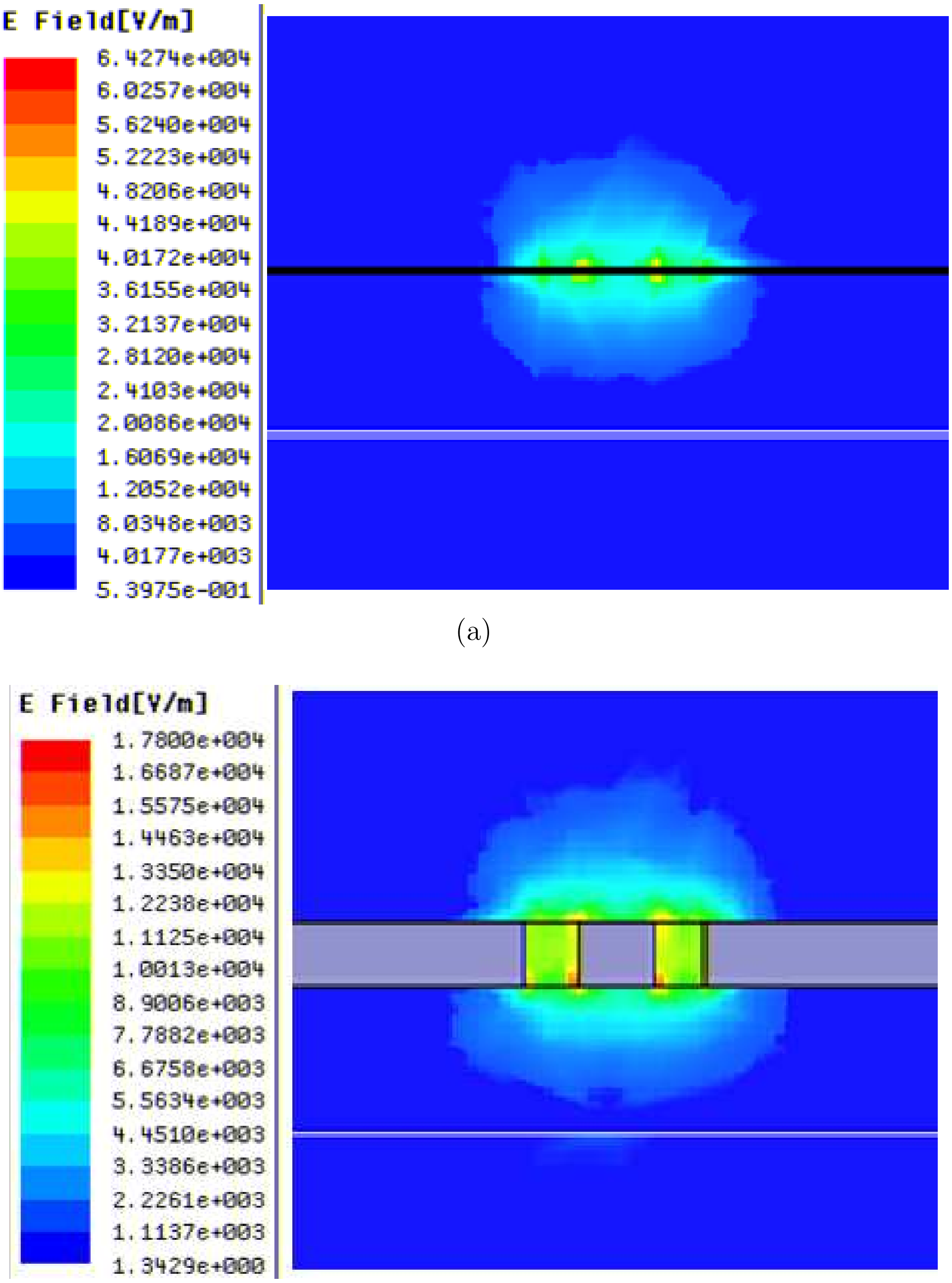

(a)

(b)

Figure 3.6: Electric field patterns for CPW of width $w = 0.25$ mm and ground to trace spacing of $s = 0.17$ mm on fused quartz substrate of $t = 0.5$ mm; (a) Thin CPW of height $h = 0.01$ mm, (b) Tall CPW of height $h = 0.22$ mm.

3.3.2 Characteristics of High Aspect Ratio Coplanar Waveguide

High aspect ratio CPW having different heights h (h=0.01, 0.22, 0.4, 0.8 mm) on fused quartz substrates with a thickness t of 0.5 mm are simulated in order to determine their propagation characteristics. Approximately 15000 to 20000 tetrahedral elements were made to simulate CPWs using HFSS. Comparisons of the magnitude of electric field distribution for CPW with conductor trace width of $w = 0.25$ mm and ground to trace spacing of $s = 0.17$ mm , for thin conductors with $h = 0.01$ mm and tall conductors with $h = 0.22$ mm are illustrated in Fig. 3.6 (a) and (b) respectively. The highest field concentration is located at the top and bottom outer edges of both CPWs and the magnitude of field concentration of the thin conductor is higher than that of thick conductor as in microstrip lines.

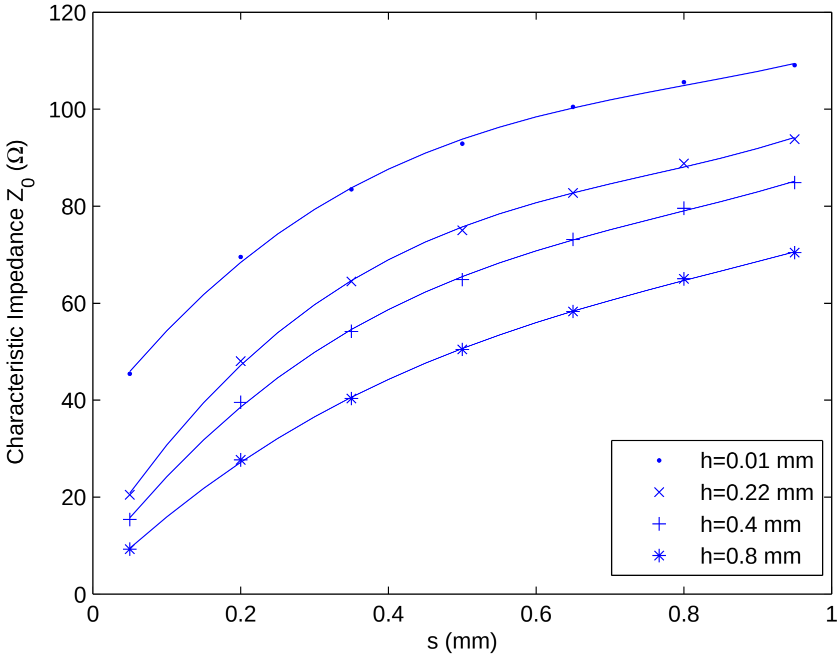

Figure 3.7: Characteristic impedances of CPW vs. ground to trace spacing, s, on a 0.5 mm thick fused quartz substrate at the frequency of 6.67 GHz and $w = 0.5$ mm.

Fig. 3.7 illustrates the variation of characteristic impedance with the signal trace to the ground spacing, s, varied from 0.05 mm to 0.95 mm for different conductor heights of h = 0.01mm, h = 0.22 mm, h = 0.4 mm and h = 0.8 mm. The characteristic impedance of CPW drops significantly with the increase of trace height and the impedance drop is greater for narrow spacing between the trace and the ground. This is due to higher capacitive coupling from the signal trace to the ground. CPW with characteristic impedances as low as 10 Ω which is prohibitive with planar CPW can be realized thanks to the vertical dimension of LIGA CPW as evident from Fig. 3.7, and the practical use of such low impedance lines is unfolded in a later chapter. Their propagation constant is illustrated in Fig. 3.8. The propagation constant decreases with the increase of metal heights of CPWs, especially for narrow ground to trace spacing. It is due to the fact that the effective dielectric constant decreases because much of the electromagnetic field stays above the substrate in air with the decrease of s, as in microstrip lines.

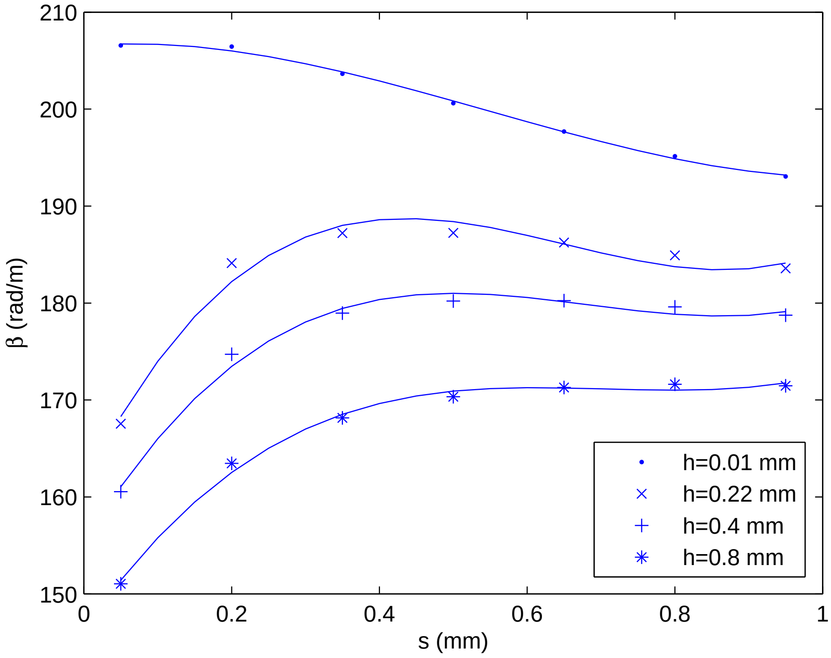

Figure 3.8: Phase constant of CPW vs. ground to trace spacing, s, on a 0.5 mm thick fused quartz substrate at the frequency of 6.67 GHz and w = 0.5 mm.

Fig. 3.9 and Fig. 3.10 show the variation of characteristic impedance and

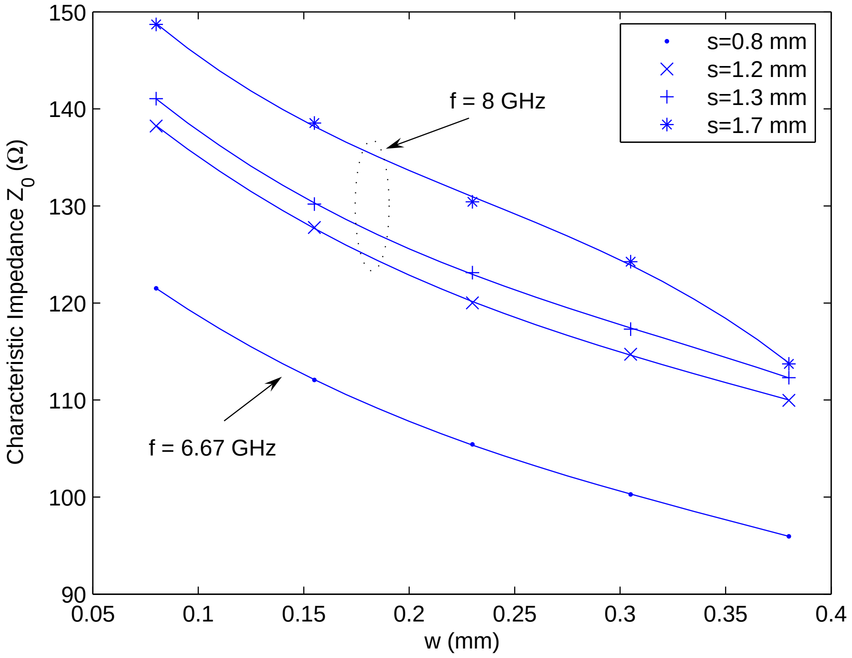

Figure 3.9: Characteristic impedance of CPW vs. trace width, w, on a 0.5 mm thick fused quartz substrate at frequencies of 6.67 GHz and 8 GHz and $h = 0.22$ mm.

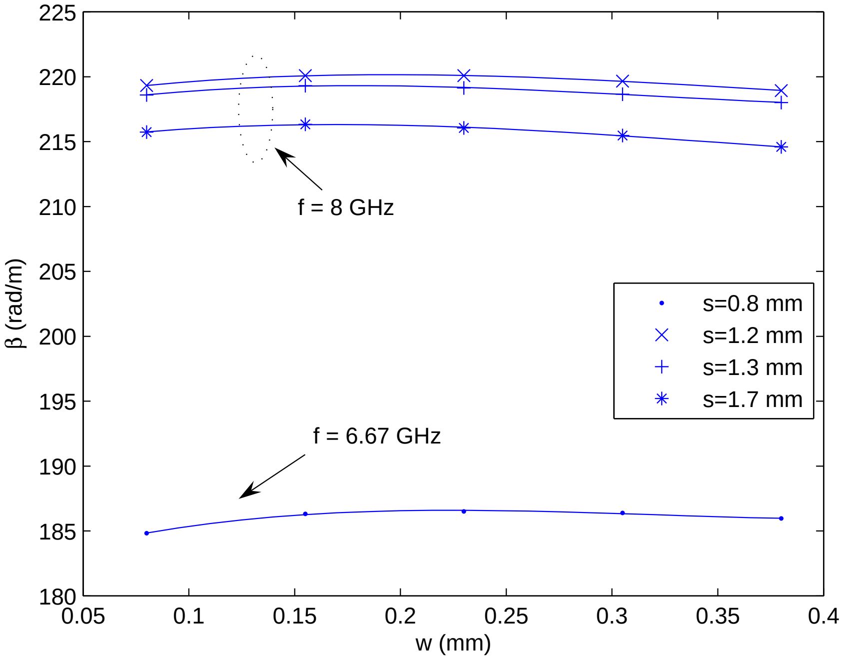

Figure 3.10: Phase constant of CPW vs. trace width, w, on a 0.5 mm thick fused quartz substrate at frequencies of 6.67 GHz and 8 GHz and $h = 0.22$ mm.

phase constant with w for $h = 0.22$ mm and different trace to ground spacing ($s = 0.8$ mm, $s = 1.2$ mm, $s = 1.3$ mm, $s = 1.7$ mm) and for frequencies of 6.67

GHz and 8 GHz, respectively. The phase constant decreases with increase of s, but it has very little dependance on w. These graphs are used for circuit design in later chapters. To appreciate tall CPW, a comparison of attenuation constants

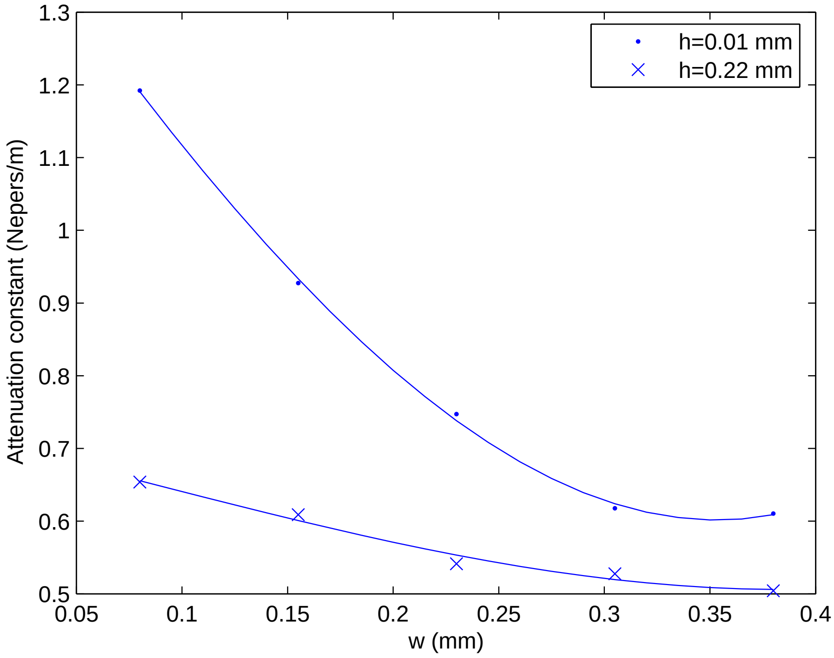

Figure 3.11: Attenuation of CPWs made of gold vs trace width, w, on a 0.5 mm thick fused quartz substrate at the frequency of 8 GHz and $s = 0.17$ mm.

of CPW made of gold with $h = 0.01$ mm and $h = 0.22$ mm and varying with w at 8 GHz is depicted in Fig. 3.11. The difference of attenuation for CPW with narrow traces is very significant as evident from the figure. Attenuation constant of a 50 Ω CPW made of gold with metal height of 0.22 mm is 0.543 Nepers/m while attenuation constant for same CPW with metal height of 0.01 mm is 0.702 Nepers/m.

3.4 Microstrip Open Loop Half Wavelength LIGA Resonators

A resonator is an important building block for microwave filters. Resonators can be made of lumped elements, distributed elements or a combination of both. For designing filters at RF frequencies at the lower end of the microwave frequency band, resonators can be designed using lumped elements such as chip inductors, chip capacitors, and printed inductors. Lumped elements can be implemented easily, and using currently available surface mount components, one can meet size and cost targets in high volume production. However, higher losses associated with these lumped elements, and hence lower unloaded quality factor, especially at higher frequencies, make them prohibitive to use in MIC and MMIC technologies for some wireless applications.

Low quality factor of resonators that are used to designed filters cause higher insertion loss in their passband and the insertion loss of bandpass or bandstop filters at the centre frequency, ΔL_{A0} is quantitatively given by [26]

$$\Delta L_{A0} = 4.343 \sum_{i=1}^{n} \frac{\omega_c'}{\Delta Q_{ui}} g_i \qquad \text{dB} \tag{3.1}$$

where Q_{ui} is the unloaded quality factor of i^{th} resonator. From Equation 3.1, It is evident that low unloaded quality factors of resonators bring about higher losses for narrowband filters than for wideband filters. For instance, consider a lowpass 3^{rd} order Butterworth filter with $g_1 = g_3 = 1$, $g_2 = 2$, and $\omega_c' = 1$, and it is transformed into a bandpass filter with $\Delta = 0.05$. Assuming all resonators have the same unloaded quality factor Q_u, and substituting these data into Equation 3.1 yields $\Delta L_{A0} = 0.347$ dB for $Q_u = 1000$ and $\Delta L_{A0} = 3.47$ dB for $Q_u = 100$ while for a bandpass filter with $\Delta = 0.5$, it yields $\Delta L_{A0} = 0.0347$ dB for $Q_u = 1000$ and $\Delta L_{A0} = 0.347$ dB for $Q_u = 100$. Unloaded quality factor of typical lumped element resonators at microwave frequencies are usually below 100. Hence, resonators built of distributed elements are more often exploited at microwave frequencies despite the disadvantage of consuming larger space.

The half wavelength microstrip resonator is widely used for microstrip bandpass filter design and there are several coupling methods such as capacitive end coupling [8], [9]. The unloaded quality factor of these resonators is given by

$$Q_u = \frac{\beta}{2\alpha}, \tag{3.2}$$

neglecting fringing effect at the ends, where α and β are attenuation constant and phase constant, respectively. According to the above equation, one can envisage higher unloaded quality factor from LIGA half wavelength microstrip resonators since their attenuation constant, α, is less. For an example, phase constants (β) of thin microstrip line with $w = 0.2$ mm and $h = 0.01$ mm, and thick microstrip line with $w = 0.2$ mm and $h = 0.22$ mm obtained from Fig. 3.4 are 354.75 rad/m and 335.48 rad/m, respectively while attenuation constants of same microstrip lines made of gold, obtained from Fig. 3.5 are 0.766 Nepers/m and 0.346 Nepers/m, respectively. Substitution of above data into Equation 3.2 yields unloaded quality factor of a half wavelength resonator made with thin microstrip line as 231.6 and that made of thick microstrip line as 484.8. Hence, LIGA microstrip lines allow realization of microstrip resonators with relatively high quality factor, compared to the planar counterparts.

In addition to the higher quality factor, half wavelength microstrip resonators do not need via hole grounding, unlike with quarter wavelength resonators. Via hole grounding in mass production is itself a complicated process, especially on hard substrates. However, one major disadvantage of half wavelength resonators in microwave filter design is the requirement of large space. Complicated inductive and capacitive inter-resonator coupling is also difficult with straight half wavelength microstrip resonators. A miniaturized microstrip bandpass filter has been reported in [56] using meander line half wavelength resonators that are end-coupled capacitively by interdigital capacitors. Half wavelength microstrip resonators are folded to form hairpin resonators to reduce the size as depicted in Fig. 3.12 by Cristal and Frankel [57]. The hairpin resonator has the additional advantage for complicated coupling, that is, capacitively and inductively as reported by Hong and Lancaster [58].

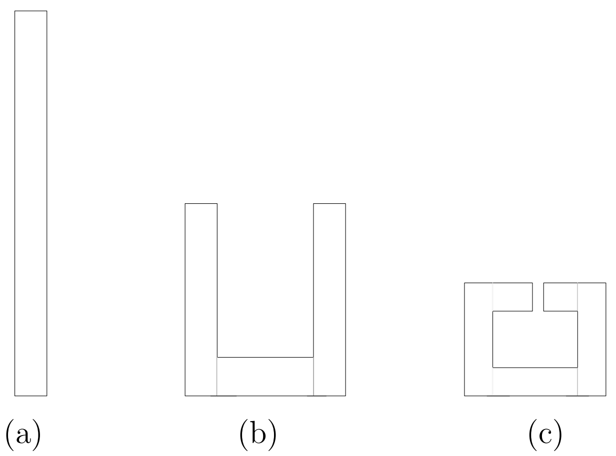

Figure 3.12: Evolution of the microstrip open loop resonator; (a) microstrip half wavelength resonator, (b) microstrip half wavelength hairpin resonator, (c) microstrip half wavelength open loop resonator.

A magnetic wall model based perturbation analysis is given in [59] for analyzing open ring resonators which is a further compact version of hairpin resonators. The square open loop half wavelength resonator shown in Fig. 3.12 (c) is a popular modified version of the open ring resonator because it is more suitable for inter resonator coupling in filter design. The end to end capacitance of the square loop half wavelength resonator is also helpful in shifting its self resonance frequency, resulting in size reduction.

Hong and Lancaster proposed a more compact open loop half wavelength resonator built from a meander line at a frequency of 1.5 GHz in [60]. 50% size reduction is reported. But realizing microstrip mender open loop half wavelength resonators with wide microstrip lines in order to reduce conductor losses is problematic in upper microwave frequencies such as X band since there is not enough resonator lengths to make the folds. In this research, a LIGA folded microstrip open loop half wavelength resonator realized from narrow microstrip lines for X band is proposed as shown in Fig. 3.13. The quality factor of this resonator can be keep high compared to its planar counterpart due to the trace height, even though the trace width is as narrow as 0.2 mm.

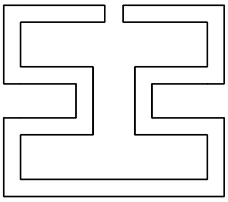

Figure 3.13: Microstrip open loop folded half wavelength resonator.

3.4.1 External Quality Factor of Microstrip Open Loop Resonators

Bandpass filter design equations were expressed in terms of external quality factors and coupling coefficients in the previous chapter. External quality factor is important for determining physical parameters of the interface between external ports and the filter network as mentioned earlier.

The configuration of external coupling of the open loop resonator is not unique and it could be either inductive or capacitive. The knowledge of the current and voltage distribution in the open loop resonator is essential in designing external coupling. Voltage, $V(z)$, and current, $I(z)$, of a TEM open ended transmission line can be expressed as,

$$\begin{aligned} V(z) &= 2V_0^+ \cos\left(\frac{2\pi z}{\lambda_0}\right) \\ I(z) &= \frac{-2jV_0^+}{Z_0} \sin\left(\frac{2\pi z}{\lambda_0}\right) \end{aligned} \tag{3.3}$$

where V_0^+ is the incidence voltage at the open end, z is measured from the open end, and λ_0 is the wavelength at the resonance of the transmission line. The above equation suggests that voltage is higher closer to the open ends of a half wavelength resonator and current is higher closer to the middle of a half wavelength resonator.

For the inductive external coupling, the external signal trace can be directly connected to the middle region of the open loop resonator where the voltage is minimum. The level of coupling can be increased or decreased (ie. Q_{ex} increases or decreases) by increasing or decreasing the length of the connection point from the zero voltage point (the middle point of the open loop resonator). For capacitive external coupling, the external signal trace is kept in close proximity with the open loop resonator. Placing the external trace close to one end of the open loop resonator where the voltage is higher, is desirable to obtain a higher external quality factor.

Fig. 3.14 demonstrates an external coupling configuration (gap coupled) with an open loop resonator. A narrow side arm whose one end connected to the main trace is extended along the loop resonator expecting higher external coupling. However, the coupling configuration in Fig. 3.14 (a) does not provide good coupling with the resonator because the coupled microstrip line of the resonator and external coupled line are analogous to parallel coupled lines whose image impedance appearing in the same ends is imaginary [8]. The other configurations in Fig. 3.14 (b) and (c) provide better external couplings and coupled transmission line sections in them are analogous to parallel coupled lines fed at opposite ends where the image impedance at opposite ends is real [8]. A suitable configuration has to be selected considering the orientation of resonators in the filter network.

Lossless half wavelength open loop miniaturized resonators placed on 0.5 mm fused quartz substrate coupled with external traces as given Fig. 3.14(b) were EM simulated with HFSS for obtaining external quality factors. To extract external quality factors from the relationship between $|S_{21}|$ vs. frequency, Equation 2.32 is used since the loaded quality factor is equal to the external quality factor when the resonator is lossless. A comparison of external quality factors of resonators with 0.2 mm wide conductors and different heights ($h = 0.22$ mm and $h = 0.005$ mm) and the variation of external quality factors with external coupling gap, g_{ex}, is illustrated in Fig. 3.15. The lateral dimensions of both resonators and associated external coupling lines are the same and the resonator dimensions are given by, $l_s = 2.05$ mm, $l_b = 1.92$ mm, $l_n = 0.59$ mm, $l_{gb} = 0.4$ and the resonator

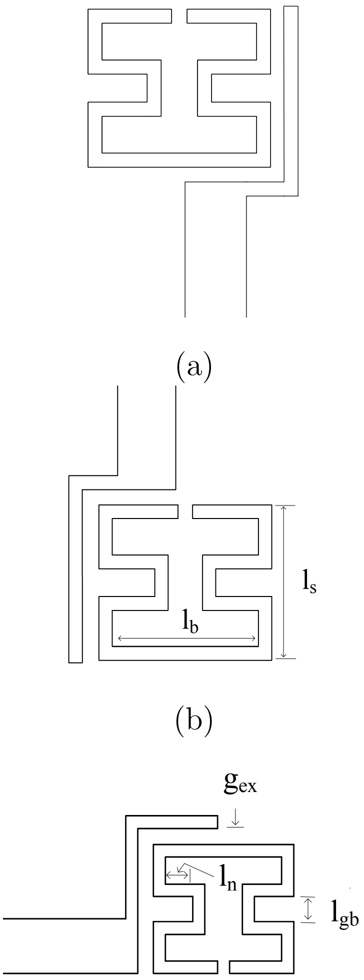

(a)

(b)

(c)

Figure 3.14: Configurations for external coupling: (a) Does not provide good coupling; (b), (c) Provides good coupling.

opening $g_c = 0.2$ mm. The width of the narrow coupling arm connected to the 0.875 mm wide 50 Ω microstrip line is 0.2 mm. Tight coupling to the resonator, in other words lower external quality factor, which is required for filters with wider bandwidth can be realized with the LIGA microstrip structure. According to Fig. 3.15, there is at least 17.5 difference of external quality factor between the structures with $h = 0.005$ mm and $h = 0.22$ mm for the range, 0.2 mm $< g_{ex} <$ 0.32 mm. A lower external quality factor required for narrow band filters can be realized simply by making the coupling gap, g_{ex} larger with LIGA microstrip structures.

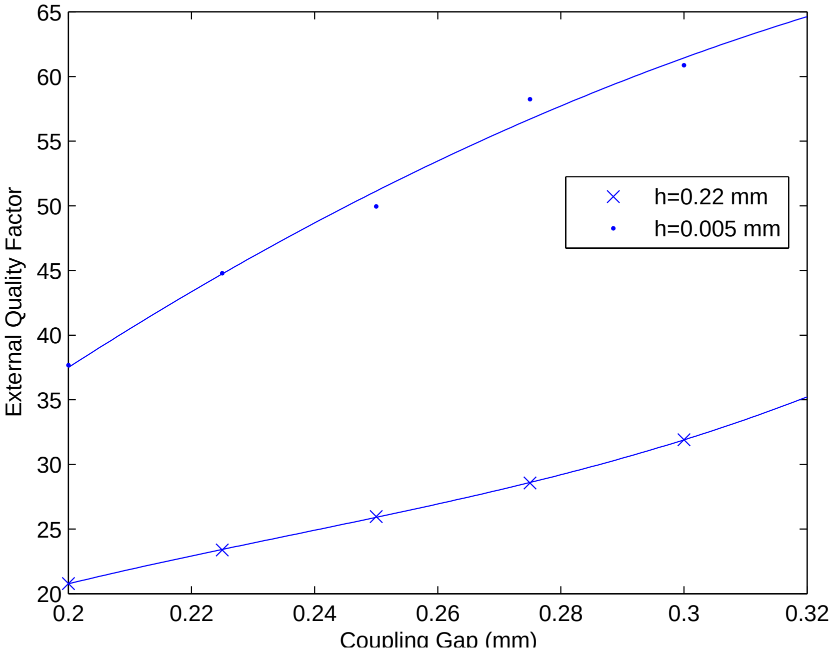

Figure 3.15: External quality factor vs. external coupling gap, g_{ex}, for resonators with $h = 0.005$ mm, $h = 0.22$ mm and with same the lateral dimensions.

3.4.2 Unloaded Quality Factor of Microstrip Half Wavelength Open Loop Resonators

A higher unloaded quality factor is important for keeping passband losses minimum. The unloaded quality factor of miniaturized microstrip open loop half wavelength resonators placed on 0.5 mm high fused quartz substrate are EM simulated using HFSS software. Around 50000 tetrahedral elements are used for EM simulation to extract the quality factors. Transmission type extraction detailed in the previous chapter is used for estimating the Q factor. The open loop resonator identically and moderately coupled to both ports, that was EM simulated for obtaining unloaded quality factor, is shown in Fig. 3.16. The lateral dimensions of the resonator are $l_s = 2.25$ mm, $l_b = 2.2$ mm, $l_n = 0.65$ mm, $l_{gb} = 0.4$ and the resonator opening $g_c = 0.2$ mm. Simulation results for the resonator made of copper with $h = 0.22$ mm give $f_0 = 10.3174$ GHz, $f_1 = 10.2318$ GHz, $f_2 = 10.4053$ GHz and $|S_{21}(f_0)| = -1.79$ dB. Substituting these results into Equations 2.32 and 2.38 yields an unloaded quality factor of the resonator made of copper with

h = 0.22 mm of 319.5. Simulation results for a thin resonator with the same lateral dimensions made of copper with h = 0.005 mm give f_0 = 9.1652 GHz, f_1 = 9.1116 GHz, f_2 = 9.22 GHz and $|S_{21}(f_0)| = -4.18$ dB. From these results and Equations 2.32 and 2.38, the unloaded quality factor of the thin copper resonator is found to be 221.6. The quality factor of a thin resonator that resonates at 10.3 GHz is even lower than 221.6. The high aspect ratio microstrip open loop resonator has higher unloaded quality factor and in this particular resonator with the above lateral dimensions, the unloaded quality factor is over 100 higher than that of its thin counterpart. The quality factor extraction data for the above resonator made of gold with the same lateral dimensions and h = 0.22 mm are f_0 = 10.3107 GHz, f_1 = 10.2161 GHz, f_2 = 10.408 GHz and $|S_{21}(f_0)| = -1.74$ dB. From the above data and Equations 2.32 and 2.38, the unloaded quality factor of this gold resonator is found to be 296.3. Simulation results for a thin resonator with same lateral dimensions made of gold with h = 0.005 mm give f_0 = 9.1678 GHz, f_1 = 9.11345 GHz, f_2 = 9.2242 GHz and $|S_{21}(f_0)| = -4.72$ dB. From these results, the unloaded quality factor of the planar gold resonator is 197.4. The difference of unloaded quality factor between copper resonators and gold resonators is around 25, irrespective of their vertical height, h.

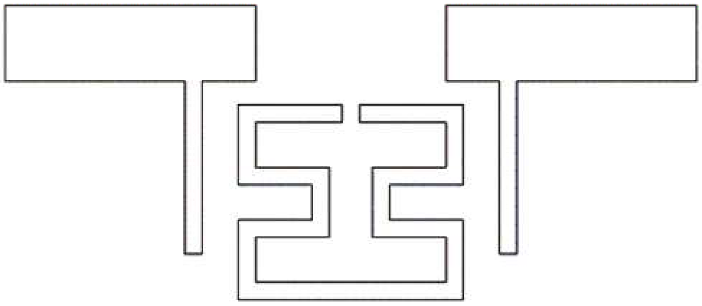

Figure 3.16: Unloaded Q factor extraction.

Based on Equation 3.1, the calculated passband loss of a third order Butterworth bandpass filter, with a 5 percent bandwidth (3 dB bandwidth at $\omega'_c = 1$), that is made of above resonators with h = 0.22 mm and a quality factor of 320 is 1.09 dB while the passband loss of a same filter made of resonators with a quality factor of 220 is 1.58 dB. Similarly, the calculated passband loss of a fifth order Butterworth bandpass filter, with a 5 percent bandwidth (3 dB bandwidth at $\omega'_c = 1$), that is made of above resonators with $h = 0.22$ mm and an quality factor of 320 is 1.76 dB while the passband loss of a same filter made of resonators with a quality factor of 220 is 2.56 dB.

3.5 Measured Unloaded Quality Factor of Open Loop Resonators

3.5.1 Layout Preparation

The first step of the fabrication is preparing a layout which contains the lateral pattern of all devices to be fabricated. The total size of the layout is 20 mm × 60 mm but the usable area is roughly 19 mm × 59 mm. Therefore a 500 μm border is left around the layout. Normal tone is selected for the layout. Therefore closed polygons result in similar metal shapes in the final structures. A 0.5 mm to 1 mm space between microstrip devices that have to be separated for coaxial probing is reserved for dicing. The devices on the layout are arranged in a such a way that dicing on direct lines is possible as shown in Appendix A. As a general rule, devices with small features are kept closer to the centre of the layout and moved out towards the border of the layout with increasingly large devices while keeping symmetry of metal parts as much as possible to have even electroplating. Sharp corners in each device are curved with a radius of 5 μm because sharp corners may cause cracking in thick resist or breaking from the substrate during the LIGA process due to stress.

3.5.2 Measurement

The single resonator device shown in Fig. 3.16 was fabricated using nickel electroplating in the LIGA process. Nickel was selected as the electroplating metal because there are critical issues in electroplating structures as tall as 0.22 mm with other metals with higher electrical conductivity such as gold or copper. Its lateral dimensions are same as the structure with $h = 0.22$ mm, used for obtaining Q factor from simulations in Section 3.4.2. Measured metallic height at the both sides of the resonator opening are 0.221 mm and 0.203 mm. The ground plane of this microstrip device was made of sticky copper foil. Coaxial connectors were mounted for probing. The ground plane of this coaxial connectors was soldered to the ground of the device. The centre pin of coaxial connectors was connected to the microstrip nickel trace using silver epoxy glue. This structure was tested using the Agilent$^{\text{TM}}$ 8722 ES vector network analyzer (VNA). The unloaded quality factor (Q_0) of this nickel structure with an open loop resonator, obtained from measurement is 63.94 while the unloaded quality factor obtained from *EM* simulation for the same nickel structure is 77.74.

Chapter 4

Half Wavelength Open Loop Second Order LIGA Bandpass Filters with Transmission Zeros

4.1 Introduction

Sharp cutoff slopes, symmetric or asymmetric responses, low passband return loss and low power loss are some of good attributes of high performance filters demanded with modern communication systems. Higher order filters can achieve responses with sharp cutoff slopes but at the expense of large circuit size. Power loss of higher order filters is also high. Alternatively, the out-of-band characteristics of bandpass filters can be effectively improved by introducing additional transmission zeros (i.e. attenuation poles) at finite frequencies in the rejection band. Inserting a circuit that becomes open at pole frequencies, using resonators with bandpass typed and bandstop typed resonances and adapting a multi-path structure within the circuit are some common techniques found in literature to obtain additional transmission zeros. A ladder network consisting of series bandpass LC resonators and shunt bandstop LC resonators alternately has been proposed in [61] for obtaining transmission zeros in stopband and it is an example of the above first technique. However, only two transmissions zeros are generated, whatever the order of the network because multiple transmission zeros are overlapped at the same frequencies. Tap-coupled filters are also examples for filters with transmission zeros that contain circuits which become open at pole frequencies

[62]. Parallel coupling and anti-parallel coupling structures are also leveraged for circuits that become open at pole frequencies [11]. A compact microstrip resonant cell proposed in [13] is an example of resonators with bandpass typed and bandstop typed resonances. Resonator configurations in Fig. 4.1 (illustrated with black nodes, while source and load are illustrated with white nodes) are useful for introducing these transmission zeros [63], [64], [65]. Week cross or bypass coupling of non-adjacent resonators (e.g. i^{th} and $i+2^{\text{th}}$ resonators) are shown in Fig. 4.1(a). Usually, the coupling and routing scheme of these filters consists of a main path in which adjacent resonators (i^{th} and $i+1^{\text{th}}$ resonators) are directly coupled with relatively stronger coupling than the cross coupling as depicted in Fig. 4.1(a). Levy presented a synthesis method for these type of filters with transmission zeros at the real or imaginary axis [66]. Both capacitively and inductively coupled parallel coupled line filters that adapt multi-path structures have been proposed in [67].

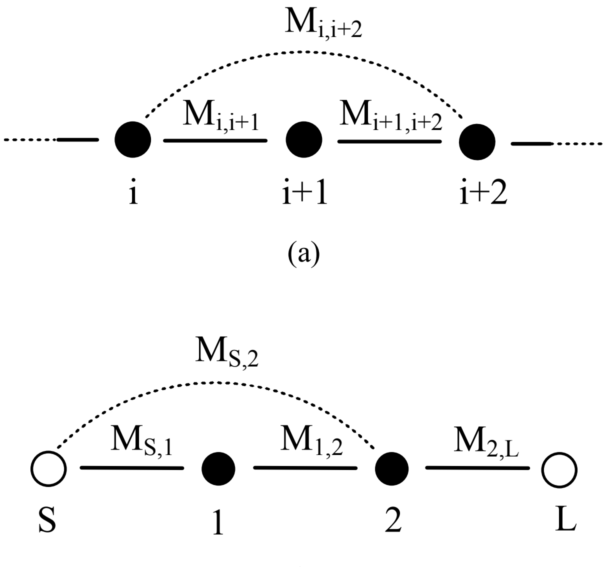

Figure 4.1: Coupling schemes of multi-resonator filters. Black nodes: resonators, White nodes: source/load, $M_{i,i+1}$: Coupling between i^{th} and $i+1^{\text{th}}$ resonators (a) Bypass coupling of non-adjacent resonators, (b) Source coupled to both resonators.

The higher the number of finite transmission zeros in the imaginary axis, the higher the stopband rejection. The number of transmission zeros is also directly related to the topology of the network. There is extensive research work on elliptic and pseudo-elliptic microwave filters whose source and load are coupled to the network through only one resonator [63], [64], [65], [66]. Such filter networks generate a maximum of only $n-2$ transmission zeros where n is the order of the network. Complex coupling schemes or additional modifications can be introduced to the network in order to create more than $n-2$ transmission zeros [68], [69], [70]. In [68] and [69], additional transmission zeros are created by open ended stubs that are used as admittance inverters to connect quarter wavelength resonators. For instance, n transmission zeros can be obtained by introducing additional bypass coupling between source and load [71]. Here, the source and load are capacitively coupled and the signal through the source/load capacitively coupled path interferes destructively with the signal through the inductively coupled open loop resonators creating two transmission zeros at both upper side and lower side of the passband. Additional transmission zeros can also be generated when the source and/or load is coupled to more than one resonator as depicted in Fig. 4.1(b). However, little research has been conducted on filters with source/load-multi-resonator couplings [70], [72], [73], [74]. In some of these examples, both source and load are coupled to more than one resonant node.

Dual mode resonators have been used to implement source/load multi-resonator couplings. Here, resonant modes of the dual mode resonator represent resonant nodes of the coupling routing (i.e. black nodes in Fig. 4.1). Direct couplings between adjacent resonant nodes (i.e. $M_{i,i+1}$) are brought out by the intra coupling of these resonant modes of dual mode resonators. Interface ports, i.e. source and load, are coupled to a nearby dual mode resonator such that both direct coupling of the source and load to the nearby resonant nodes and bypass couplings to non-adjacent resonant nodes in the coupling routing (e.g. $M_{S,1}$ and $M_{S,2}$) are realized. Since the introduction of dual mode filters for space applications in 1970s [70], most of the research effort in this area has been focused on more ingenious ways of achieving the coupling schemes discussed above [75]. However, designing of the physical dual mode structure may require a little more effort. The filter order is often limited to an even number if it is made of dual mode resonators. In this chapter, a novel source/load multi-resonator coupling method for miniaturized microstrip filters with half wavelength open loop resonators is proposed to alleviate difficulties encountered when realizing source/load multi-resonator coupling with dual mode resonators. A narrow side arm connected to the source or load, which is used for obtaining the required external quality factor of the first resonator, is extended up to the second resonator to obtain the coupling of source/load to the second resonator (i.e. $M_{S,2}$ in Fig. 4.1(b)) as depicted in Fig. 4.2. In this figure, coupling structures for two different resonator orientations are shown for the above mentioned coupling schemes. The main advantage with this kind of arrangement is that couplings, $M_{S,1}$ and $M_{S,2}$, can be controlled more independently with relatively little effort.

To show the capability of the proposed coupling method, novel high aspect ratio (HAR) second order open loop microstrip filter structures with one transmission zero in their responses are designed. The HAR structure is useful to avoid extremely narrow capacitive coupling gaps because higher capacitive coupling is created by side walls of the tall conductors. The next section is devoted to describing the coupling responses of differently oriented open square loop resonators. Second order filters with transmission zeros both in upper and lower stopbands are synthesized and synthesis details are given in the third section. The design procedure of the above filters can be found in the fourth section. Physical parameter extraction details, filter implementation, and results are appended in the last section. Prototype filter response and electromagnetic simulated response are verified experimentally.

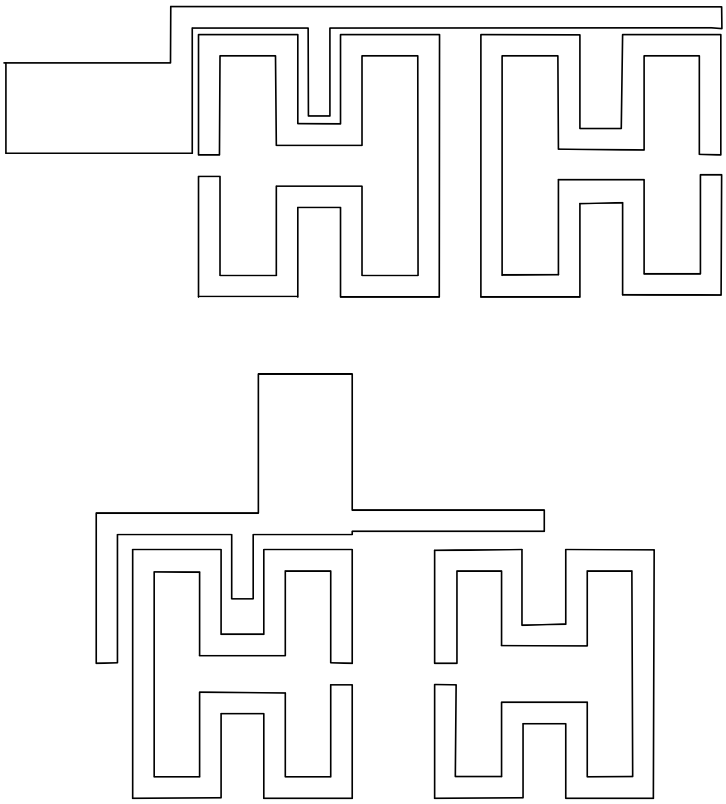

Figure 4.2: External port is coupled to both open loop half wavelength resonators in both configurations

4.2 Typical Coupling Structures and Responses

The coupling of differently oriented open loop square resonators are described. As examples, the coupling responses of electrically and magnetically coupled open loop resonators are demonstrated in this section. For this purpose, microstrip coupling structures illustrated in Fig. 4.3 are employed. Each open loop resonator is essentially a folded half wavelength resonator. These coupling structures result from different orientations of a pair of open loop square resonators separated with coupling gaps. The proximity coupling of these resonators is created by the fringe field. The nature and the strength of the fringe field and the relative location of external ports determine the characteristic of resonator couplings.

Following the reasoning given in Section 3.4.1 for miniaturized open loop half wavelength resonators, one can deduce that at resonance of the fundamental mode,

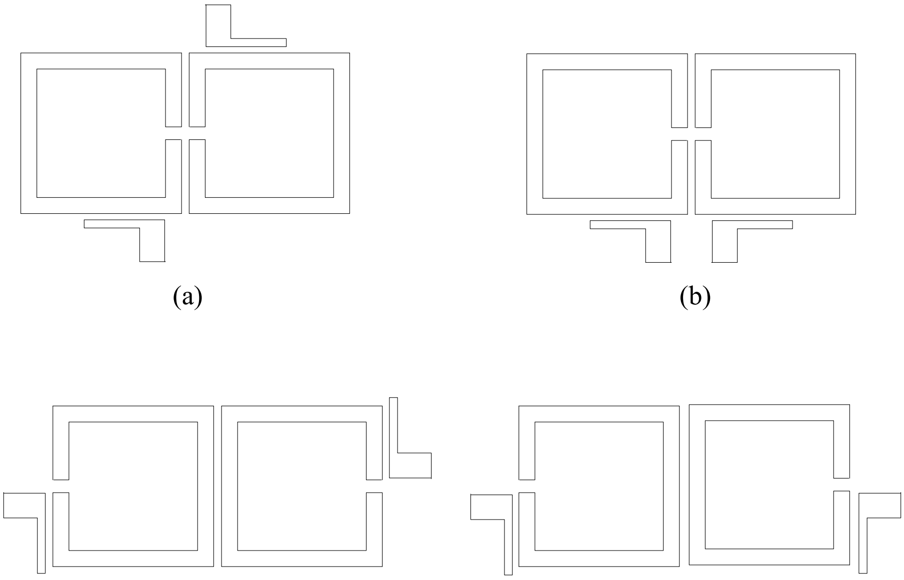

(a) (b) (c) (d)

Figure 4.3: Typical coupling configurations of half wavelength open loop resonators: (a) electric coupling, external ports are in opposite sides; (b) electric coupling, external ports are in same side; (c) magnetic coupling, external ports are in opposite sides; (d) magnetic coupling, external ports are in same side.

each of the open loop resonators has the maximum electric field density at the sides with an open gap, and the maximum magnetic field density at the opposite side. Because the fringe field decays exponentially, the electric fringe field is stronger near the side having the maximum electric field distribution, whereas magnetic field is stronger near the side having the maximum magnetic field distribution. It follows that the electric coupling, which is the capacitive coupling in other words, can be obtained if the open sides of two coupled resonators are proximately placed, as Fig. 4.3(a) shows, and the magnetic coupling, which is the inductive coupling, can be obtained if the sides with the maximum magnetic field of two coupled resonators are proximately placed, as Fig. 4.3(c) shows. The resonator orientations in Fig. 4.3(a) and (b) are same and their typical coupling responses are shown in Fig. 4.4. However, the phase responses are different because the external coupling ports are differently placed. The typical phase responses of magnetically coupled resonators in Fig. 4.3(c) and (d) are illustrated in Fig. 4.5

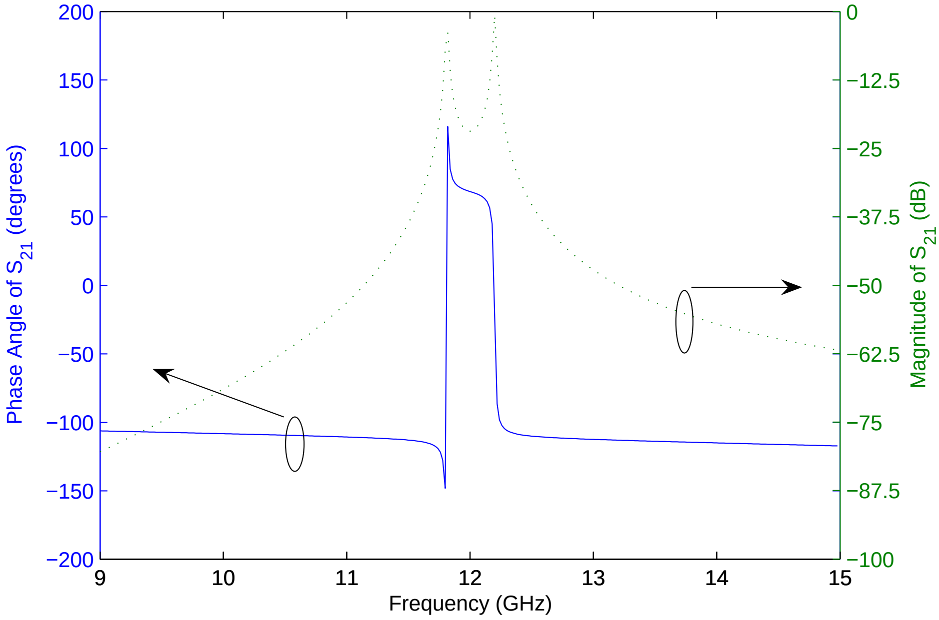

(a)

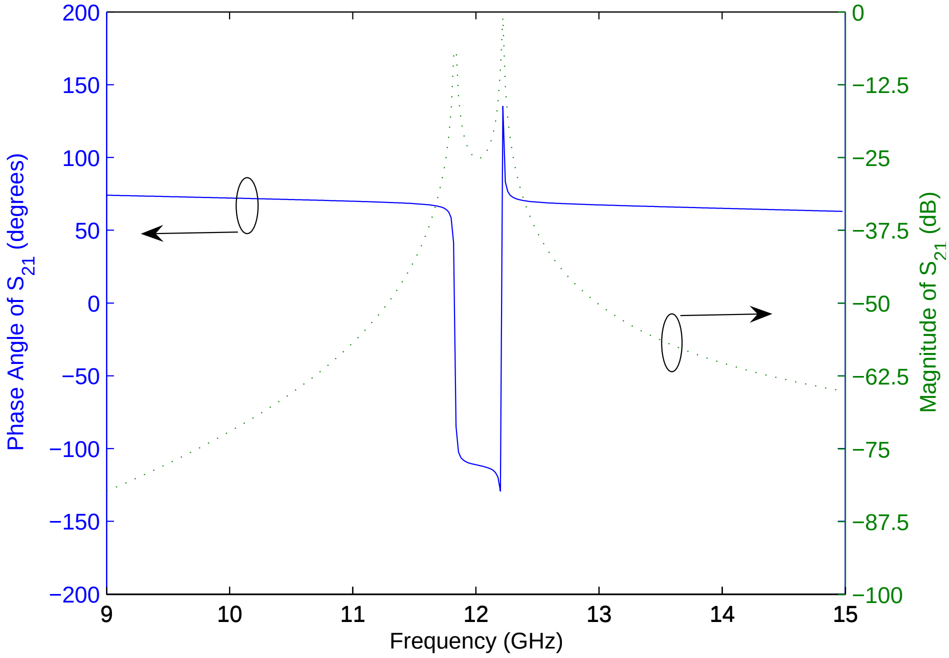

(b)

Figure 4.4: (a) Typical resonance responses of the configuration in Fig. 4.3(a), (b) typical resonance responses of the configuration in Fig. 4.3(b).

and the phase responses are not the same, as the external coupling ports are placed differently as with electrically coupled resonators. The typical phase responses of coupled resonators in Fig. 4.3(a) and (d) take the same shape while typical phase responses of coupled resonators in Fig. 4.3(b) and (c) take the same shape. This information may be useful in designing higher order open loop resonator filters.

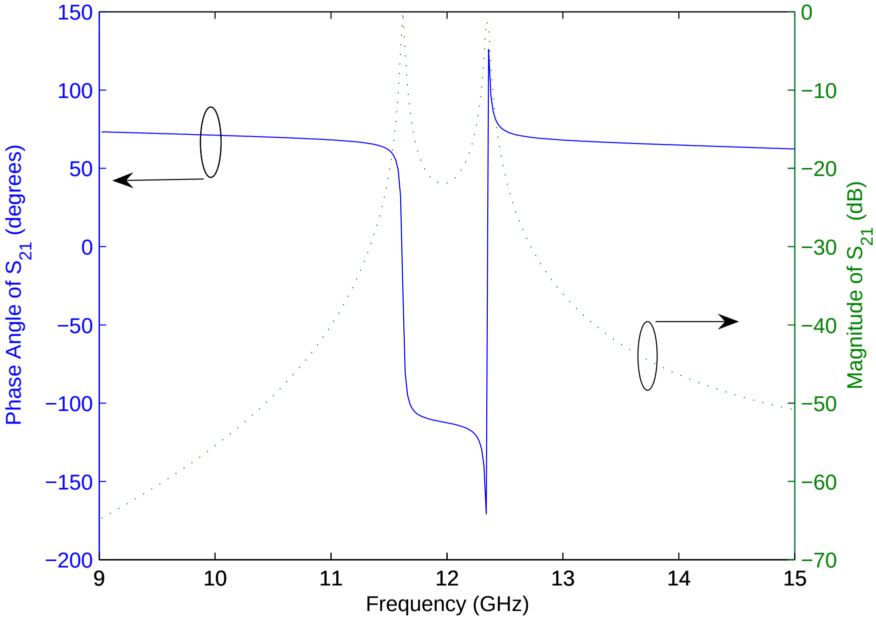

(a)

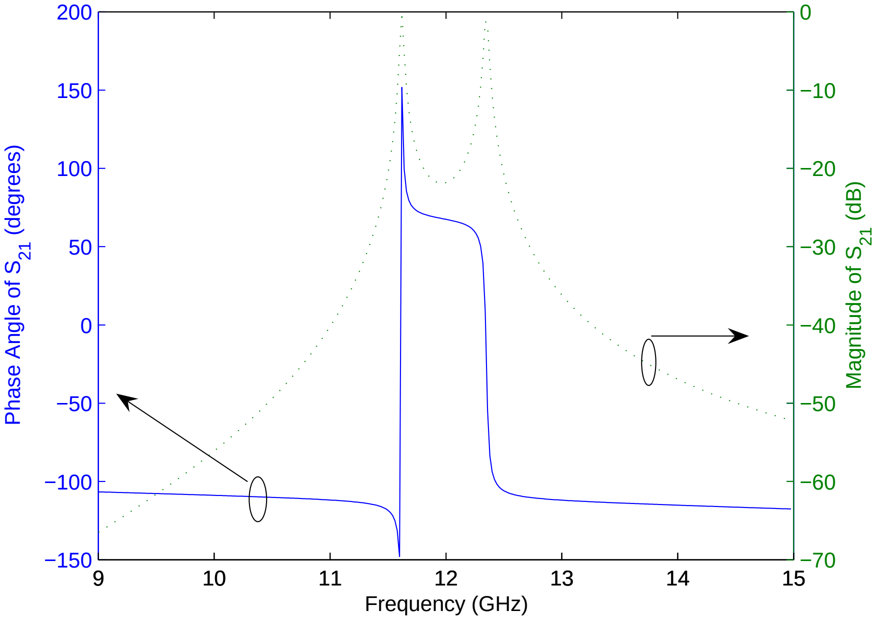

(b)

Figure 4.5: (a) Typical resonance responses of the configuration in Fig. 4.3(c), (b) typical resonance responses of the configuration in Fig. 4.3(d).

4.3 Network Synthesis

The Chebyshev approximation detailed in the second chapter does not posses amplitude characteristics with transmission zeros. However, the generalized Chebyshev approximation provides a filter with equiripple passband amplitude characteristics with arbitrarily placed transmission zeros in the stopband. Both symmetric and asymmetric frequency responses can be generated because the transmission zeros can be placed arbitrarily. Furthermore, the transmission zeros are not restricted to being at real frequencies but may also be located in the complex plane.

In this work, the generalized Chebyshev function, $F_n(\omega')$ where ω' is the normalized angular frequency and n is the order of the generalized Chebyshev function, is used as the filtering function and is defined by

$$F_n(\omega') = \cosh \sum_{k=1}^{k=n} \cosh^{-1}(x_k) \tag{4.1}$$

where $x_k = (\omega' - 1/\omega'_k)/(1 - \omega'/\omega'_k)$, and ω'_k is the k^{th} transmission zero [76]. The transmission coefficient of the lowpass prototype network is given by

$$|S_{21}(j\omega')|^2 = \frac{1}{1 + \epsilon^2 F_n^2(\omega')} \tag{4.2}$$

where ϵ is the constant related to the passband return loss R, by $\epsilon = (10^{R/10} - 1)^{1/2}$. $F_n(\omega')$ is a rational function of the form $F_n(\omega') = P_n(\omega')/D_n(\omega')$ where the denominator $D_n(\omega')$ is given by [76]

$$D_n(\omega') = \prod_{k=1}^{k=n} \left(1 - \frac{\omega'}{\omega'_k}\right). \tag{4.3}$$

The polynomial $P_n(\omega')$ is related by the recursion relation [76]

$$
\begin{aligned}
P_{n+1}(\omega') &= -P_{n-1}(\omega')\left(1-\frac{\omega'}{\omega'_n}\right)^2\left[\frac{1-\frac{1}{\omega'^2_{n+1}}}{1-\frac{1}{\omega'^2_n}}\right]^{1/2} \\
&\quad +P_n(\omega')\left[\omega'-\frac{1}{\omega'_{n+1}}+\left(\omega'-\frac{1}{\omega'_n}\right)\left[\frac{1-\frac{1}{\omega'^2_{n+1}}}{1-\frac{1}{\omega'^2_n}}\right]^{1/2}\right].
\end{aligned}
\tag{4.4}
$$

The polynomials $P_0(\omega')$ and $P_1(\omega')$ are equal to 1 and $\omega' - 1/\omega'_1$ respectively.

4.3.1 Asymmetric Filter with One Transmission Zero in the Higher Stopband

For demonstration, a second order network is synthesized giving an asymmetric response with one transmission zero at infinity and one at $\omega' = 4.42$ with $R = -20$ dB. $F_2(\omega')$ is evaluated for these specifications using the above recursion formulas, in order to express Equation 4.1 in the polynomial form. Then $|S_{11}(j\omega')|^2$, ($|S_{11}(j\omega')|^2 = 1 - |S_{21}(j\omega')|^2$ if the network is lossless), is obtained using Equation 4.2. The denominator of $S_{11}(p)$ is obtained from the left half-plane poles of $|S_{11}(j\omega')|^2$ where $p = j\omega'$. The numerator of $|S_{11}(j\omega')|^2$ is equal to $\epsilon^2 F_2^2(\omega')$. Hence, the numerator of $S_{11}(p)$ is essentially a constant times $F_2(p)$ and the unknown constant is found from Equating $S_{11}(p)$ to unity when $p \to \infty$. The input admittance is formulated from $S_{11}(p)$. Elements in Fig. 4.6(a) are extracted starting from the capacitor, C_1, and subsequently the frequency invariant susceptance (constant susceptance extracted to continue the synthesis process [17]), jB_1, such that the remaining admittance possesses a zero at 4.42 ($jC_2\omega' + jB'_2$), frequency invariant susceptance , jB'_3, and finally the resistive element, r_{02} as detailed in Appendix B. It is usually more practical to convert the network in Fig. 4.6(a) into a cross coupled network that can be realized conveniently. First, the series branch consisting of the capacitor (C_2) in parallel with the frequency invariant susceptance (jB'_2) and in series with the frequency invariant susceptance (jB'_3) is converted into a parallel connection of a inductor in series with

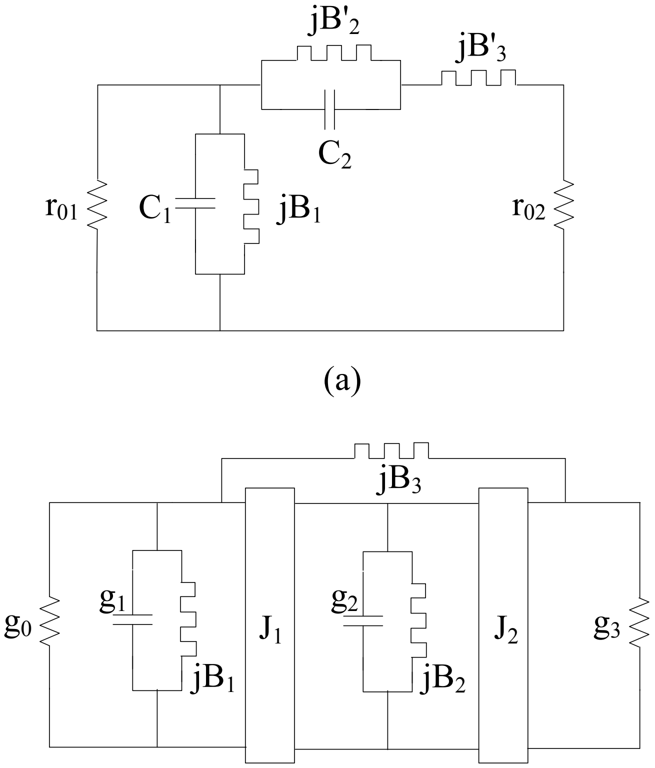

(a)

(b)

Figure 4.6: Generalized Chebyshev filter with $n = 2$ and one transmission zero at a finite frequency; (a) Ladder network, (b) Final cross coupled network.

a frequency invariant reactance, and a frequency invariant susceptance as illustrated in Fig. 4.7. Equating the admittances of the two circuits in Fig. 4.7, we obtain the parameters of the equivalent circuit elements as $B_3 = B'_3$, $L = C_2/B'^2_3$ and $X' = (B'_2/B'^2_3) + 1/B'_3$. Still, the series bandpass resonator resulting from

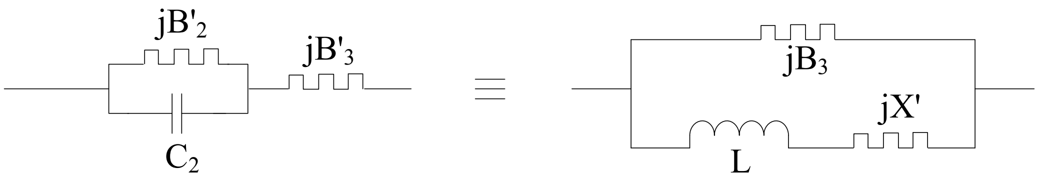

(a)

(b)

Figure 4.7: Equivalent of the series branch in Fig. 4.6(a); (a)series connection, (b) parallel connection.

L and X' in Fig. 4.7(b) when the prototype network is frequency transformed into a bandpass filter, is difficult to realize in microstrip form. The shunt branch consisting of L and X' in Fig. 4.7(b) can be transformed into a cascade of an admittance inverter ($J_1 = 1$), shunt capacitor in parallel with a frequency invariant susceptance, and an admittance inverter of opposite sign ($J_2 = -1$) as illustrated in Fig. 4.6(b), following the reasoning in [77]. The proof of this equivalence is found by analysis of the $ABCD$ matrix of the two circuits. The parameters of the shunt capacitor in parallel with the frequency invariant susceptance centred by admittance inverters in the resulting final cross coupled network (g_2 and jB_2 in Fig. 4.6(b)) are found by equating the parameters of those $ABCD$ matrices, namely $g_2 = L$ and $B_2 = X'$. In the example final cross coupled prototyped network, resistive elements g_0 and g_3, and capacitive elements, g_1 and g_2 are 1, 0.8295, 0.6432 and 0.5474, respectively. Frequency invariant susceptances, B_1, B_2 and B_3 are -0.0368, -0.094 and 0.4296, respectively while admittance inverters, J_1 and J_2 are 1 and -1, respectively.

4.3.2 Asymmetric Filter with One Transmission Zero in the Lower Stopband

A prototyped second order filter network producing an asymmetric filter response with one transmission zero at $\omega' = -4.62$ and a passband return loss of 20 dB is also demonstrated. First, using Equation 4.2, $|S_{21}(j\omega')|^2$ of this network is expressed as a polynomial after obtaining $F_2(\omega')$ from the recursion formulas given in the preceding section. The denominator of $S_{11}(p)$ is formulated using the left half plane poles of $|S_{11}(p)|^2$ while the numerator is formulated from multiplying $F_2(\omega')$ by an unknown constant which is found from equating $S_{11}(p)$ to unity when p approaches to infinity. Having obtained the admittance function from $S_{11}(p)$, the synthesis procedure as described in the previous section is performed until the network depicted in Fig. 4.6(a) is obtained. Next, it is converted into a cross coupled network which is more practical to be realized. The values of resistive elements, g_0 and g_3, in the final cross coupled network are 1 and 0.8288, while

g_1 and g_2 are 0.6450 and 0.5477 respectively. Frequency invariant susceptance, B_1, B_2 and B_3 are 0.0353, 0.0897 and -0.4098, respectively while admittance inverters, J_1 and J_2 are 1 and -1, respectively. The signs of the frequency invariant susceptances of this filter are opposite signs of the previous asymmetric filter with the transmission zero in the higher stopband. Solid curves in Fig. 4.8 show the prototype frequency response of the above filter with the transmission zero in the lower stopband. Dotted curves in same figure depict the frequency response of a similar network with elements of the same values as in the above filter network with the transmission zero in upper stopband, except the signs of the frequency invariant susceptances are opposite. This fact suggests that the transmission zero at finite frequency can be shifted from one side of the passband to the other side by just interchanging the signs of the frequency invariant reactance, in another words, changing the capacitive frequency invariant reactance into inductive frequency invariant reactance and vise versa.

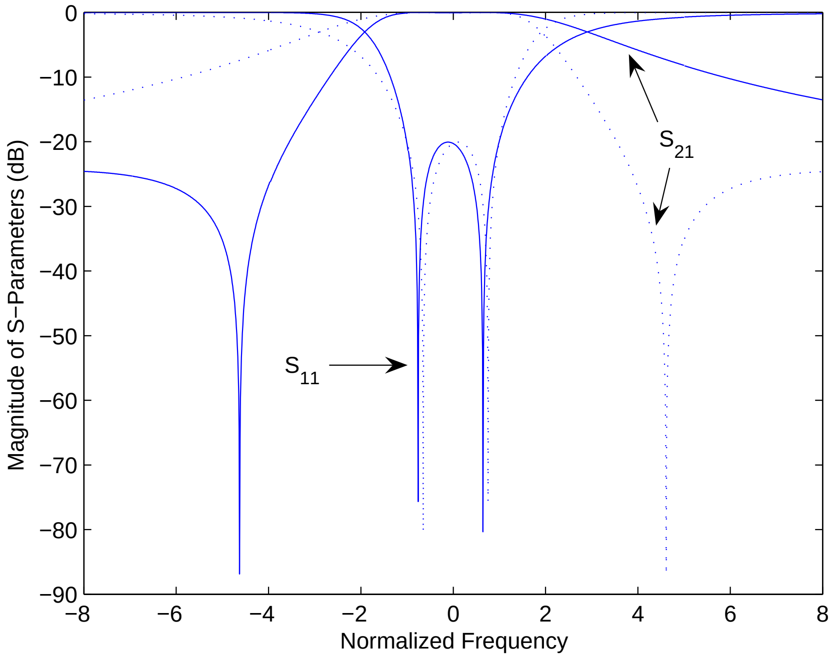

Figure 4.8: Prototype frequency responses; solid curves- Frequency response of network with $g_0 = 1$, $g_3 = 0.8288$, $g_1 = 0.6450$, $g_2 = 0.5477$, $B_1 = 0.0353$, $B_2 = 0.0897$, $B_3 = -0.4098$, $J_1 = 1$ and $J_2 = -1$; dotted curve- same network but the signs of frequency invariant susceptances are opposite.

4.4 Filter Design

Asymmetric bandpass filters with one transmission zero at a finite frequency are designed based on the above synthesized networks using half wavelength miniaturized LIGA open loop resonators. Filter design parameters which are external quality factors and coupling coefficients are estimated from prototype elements. The vertical height of LIGA resonators is used for realizing the required tight resonator couplings with external ports and bypass coupling of external ports.

To transfer lowpass networks to bandpass networks, the lowpass to bandpass frequency transformation given in Equation 2.6 is used. Applying the above frequency transformation, the corresponding transmission zeros at bandpass frequencies can be found by [26]

$$f_{ai} = f_0 \frac{\Delta \cdot \omega_i' + \sqrt{(\Delta \cdot \omega_i')^2 + 4}}{2} \tag{4.5}$$

where f_0 is the midband frequency and f_{ai} is the transmission zero at bandpass frequency corresponding to ω_i'. Shunt nodal capacitances and their associated frequency invariant susceptances of lowpass prototype networks are transformed into shunt bandpass resonators whose equivalent capacitors and inductors are given by C_{ri} and L_{ri} respectively. Using bandpass transformation, C_{ri} and L_{ri} can be related to lowpass elements as,

$$j\omega C_{ri} + \frac{1}{j\omega L_{ri}} = \frac{1}{\Delta}\left(\frac{j\omega}{\omega_0} + \frac{\omega_0}{j\omega}\right) g_i + jB_i. \tag{4.6}$$

Derivation of the above equation with respect to $j\omega$ yields

$$C_{ri} - \frac{1}{(j\omega)^2 L_{ri}} = \frac{1}{\Delta}\left(\frac{1}{\omega_0} - \frac{\omega_0}{(j\omega)^2}\right) g_i. \tag{4.7}$$

The substitution of $\omega = \omega_0$ in above two equations gives

$$\begin{aligned}\omega_0 C_{ri} - \frac{1}{\omega_0 L_{ri}} &= B_i \\ C_{ri} + \frac{1}{\omega_0^2 L_{ri}} &= \frac{1}{\Delta}\left(\frac{2}{\omega_0}\right) g_i.\end{aligned} \tag{4.8}$$

C_{ri} and L_{ri} are found to be

$$\begin{aligned}C_{ri} &= \frac{1}{\omega_0}\left(\frac{g_i}{\Delta} + \frac{B_i}{2}\right) \\ L_{ri} &= \frac{1}{\omega_0}\left(\frac{g_i}{\Delta} - \frac{B_i}{2}\right)^{-1}.\end{aligned} \tag{4.9}$$

Hence, the resonant frequency of the equivalent shunt bandpass resonators (ω_{0i}) can be found as

$$\omega_{0i} = \frac{1}{\sqrt{L_{ri} C_{ri}}} = \omega_0 \sqrt{1 - \frac{B_i}{g_i/\Delta + B_i/2}}. \tag{4.10}$$

Equation 4.10 suggests the effect of shunt frequency invariant susceptances in the lowpass prototype network to the resonant frequency of shunt bandpass resonators of the bandpass filter. The resonant frequency of shunt bandpass resonators of the bandpass filter shifts from the midband frequency, thereby shunt resonators are asynchronously tuned. The susceptance slope parameter of the bandpass resonator is important to determine the external quality factor and the coupling coefficient. Using Equation 2.13, one can find the susceptance slope parameter of the bandpass resonator as,

$$b_i = \omega_{0i} C_{ri} = \frac{\omega_{0i}}{\omega_0}\left(\frac{g_i}{\Delta} + \frac{B_i}{2}\right). \tag{4.11}$$

Now, using the above equation and definitions given in Chapter 2, external quality factors are given by

$$\begin{aligned}Q_{e1} &= \frac{b_1}{g_0} = \frac{\omega_{0i}}{\omega_0 g_0}\left(\frac{g_1}{\Delta} + \frac{B_1}{2}\right) \\ Q_{en} &= \frac{b_n}{g_{n+1}} = \frac{\omega_{0n}}{\omega_0 g_0}\left(\frac{g_n}{\Delta} + \frac{B_n}{2}\right)\end{aligned} \tag{4.12}$$

where n is the order of the filter. Similarly, the coupling coefficient is given by

$$\begin{aligned} M_{ij}\big|_{i\neq j} &= \frac{J_{ij}}{\sqrt{b_i b_j}} \\ & \quad \frac{\omega_0}{\sqrt{\omega_{0i}\omega_{0j}}} \cdot \frac{\Delta J_{ij}}{\sqrt{(g_i + \Delta B_i/2)(g_j + \Delta B_j/2)}}. \end{aligned} \tag{4.13}$$

4.4.1 Design of Bandpass Filter with One Transmission Zero in the Higher Stopband

A bandpass filter with 4.0 percent bandwidth centred at 10.5 GHz was designed using the synthesized cross coupled network shown in Fig. 4.6(b), with the transmission zero in the higher side of the passband. Substituting the above data and parameters of the synthesized network into Equation 4.10, resonant frequencies of the first and second asynchronously tuned resonators are found to be 10.512 GHz and 10.536 GHz respectively. Using Equation 4.13, the inter resonator coupling is determined. The coupling between the first and second resonators is 0.0674. Using Equation 4.12, the evaluated external quality factors of the first and second resonators due to direct couplings are 16.1 and 11.4 respectively.

The bypass coupling of the source or load realized by extending a narrow side arm as described previously in the proposed structure is capacitive. Fortunately, bypass coupling of the source or load in the synthesized network is capacitive for this filter because B_3 is positive. Bypass coupling of the source or load is also expressed as an external quality factor in designing the bandpass network. In order to determine the external quality factor of bypass of the source or load, consider the network in Fig. 4.9 where a resistive load, R, is connected to a shunt resonator with shunt capacitor, C, and inductor, L, through a frequency invariant reactance, X. The total admittance of the network across the resonator is

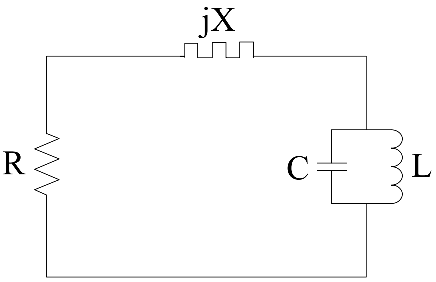

Figure 4.9: Equivalent of the bypass coupling of the source or load.

$$\frac{R}{R^2+X^2} + j\omega C - j\left(\frac{1}{\omega L} + \frac{X}{R^2+X^2}\right). \tag{4.14}$$

Hence, external quality factor of the above network can be determined by

$$Q_{exby} = \frac{\omega'_{01}}{2} \frac{\left(C + \frac{1}{\omega'^2_{01} L}\right)(R^2+X^2)}{R} \tag{4.15}$$

where

$$\omega'_{01} = \frac{\frac{X}{R^2+X^2} + \sqrt{\left(\frac{X}{R^2+X^2}\right)^2 + \frac{4C}{L}}}{2C}. \tag{4.16}$$

Using the above equation, the external quality factor of the first resonator due to the bypass coupling of the second termination is determined and it is found to be 118.2.

The necessary inter resonator coupling is positive and it can be physically realized from a structure similar to the structure illustrated in Fig. 4.3(c). The required external quality factors of shunt resonators are physically realized by placing a narrow arm in close proximity to the resonator, connected to the source or load as shown in Fig. 4.10.

An additional narrow arm with a length of l_{in}, connected to the side arm is inserted into the cave of the folded resonator as shown in Fig. 4.10 to realize a tight coupling with the resonator, in other words to realize a lower external quality factor. The resonant frequency of the resonator changes with coupling gap, g_{ex}. So, for given set of g_{ex}, the variations of resonant frequency and external quality

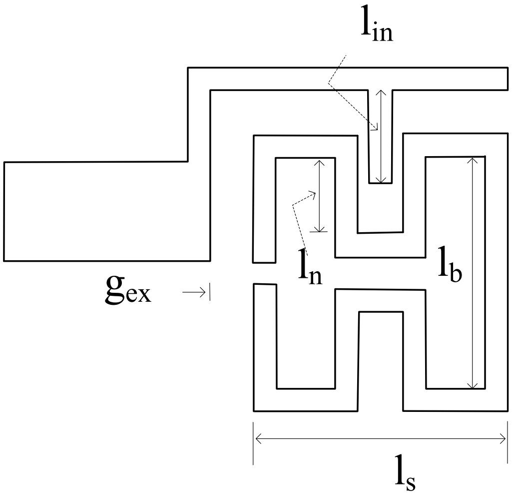

Figure 4.10: Structure for realizing external Q factors of the bandpass filter with a transmission zero in the upper stopband.

factor with l_n are obtained as described in Chapter 2, using *EM* simulated data. Conductor losses and radiation losses are neglected in the simulation for extracting above filter design parameters. Fig. 4.11 shows the variation of resonant frequency and external quality factor with l_n for a coupling structure with $g_{ex} = 0.38$ mm on a 0.5 mm thick fused quartz substrate with dielectric constant of 3.78, with other dimensions being, $l_s = 2.25$ mm, $l_b = 2.05$ mm, $l_{in} = 0.82$ mm, $l_{gb} = 0.4$ mm while the conductor width of the resonator and coupling side arms is 0.2 mm and the width of resonator opening is 0.2 mm. Conductor height, h, is 0.22 mm.

Using a set of graphs for different g_{ex} (one is depicted in Fig. 4.11 for $g_{ex} = 0.38$ mm), graphical relationships of g_{ex} and related l_n with external quality factor are obtained subsequently for required resonant frequencies of shunt resonators (10.512 GHz and 10.536 GHz). The above relationships are shown in Fig. 4.12(a) and (b) for frequencies of 10.512 GHz and 10.536 GHz, respectively.

From Fig. 4.12, the required g_{ex} and l_n of the first and second resonators of the bandpass filter with the transmission zero in upper stopband are found. Next, the variation of coupling coefficient of the above two resonators with the coupling gap, l_{mg} is found again from *EM* simulations. Since these resonators are asynchronously tuned, Equation 2.28 cannot be used to extract the coupling

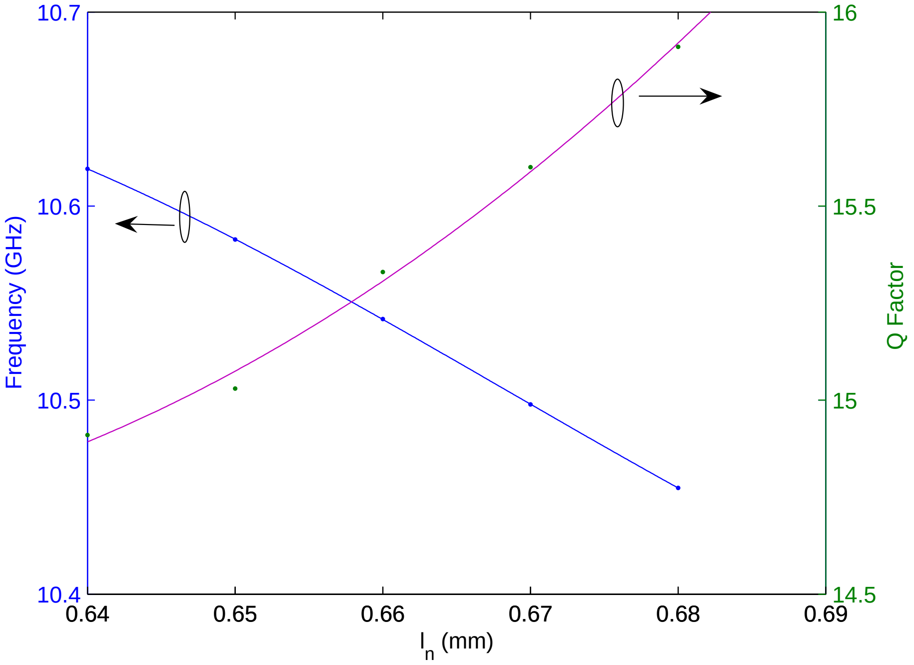

Figure 4.11: Variation of resonant frequency and external quality factor with l_n when $g_{ex} = 0.38$ mm for a structure shown in Fig. 4.10.

coefficient as described in Chapter 2. The coupling coefficient of asynchronously tuned resonators is extracted from $|S_{21}|$ using,

$$m = \pm\frac{1}{2}\left(\frac{f_{02}}{f_{01}} + \frac{f_{01}}{f_{02}}\right)\sqrt{\left(\frac{f_{p2}^2 - f_{p1}^2}{f_{p2}^2 + f_{p1}^2}\right)^2 - \left(\frac{f_{02}^2 - f_{01}^2}{f_{02}^2 + f_{01}^2}\right)^2} \tag{4.17}$$

where f_{p2} and f_{p1} correspond to the resonant peaks of the coupled structure while f_{02} and f_{01} are individual resonant frequencies of the coupled resonators. Fig. 4.13 shows the variation of coupling coefficient with coupling gap for the inductively coupled structure with the first and second resonators selected before for the above filter. Now, the necessary coupling gap is determined for the required coupling coefficient from the graph in Fig. 4.13.

Having found inter resonator coupling gaps, coupling gaps of the external ports, and parameters of the resonators, the physical parameters of the bypass coupling path of the filter with the transmission zero in higher stopband are obtained. Fig. 4.14 shows this bypass coupling structure in which the second

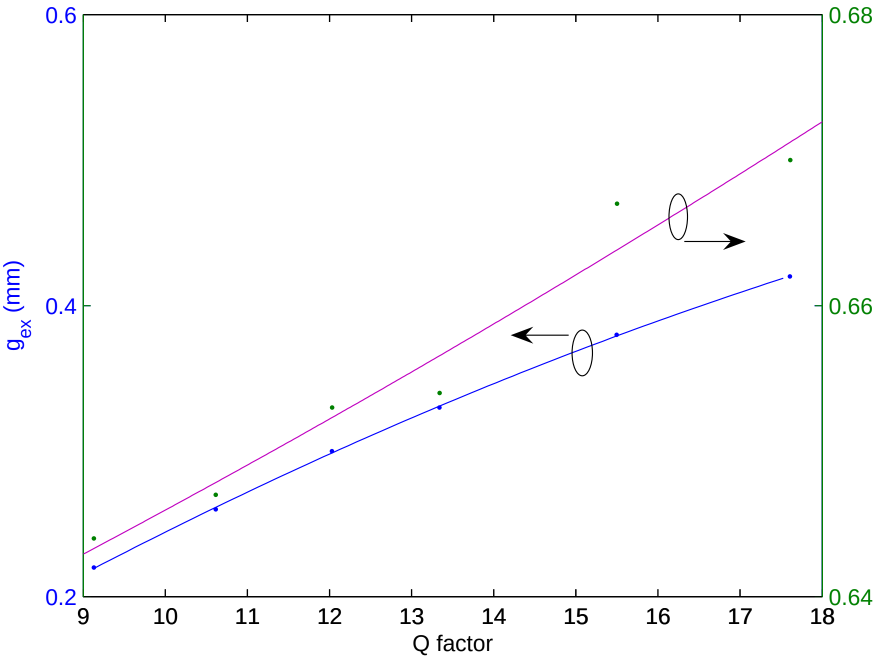

(a)

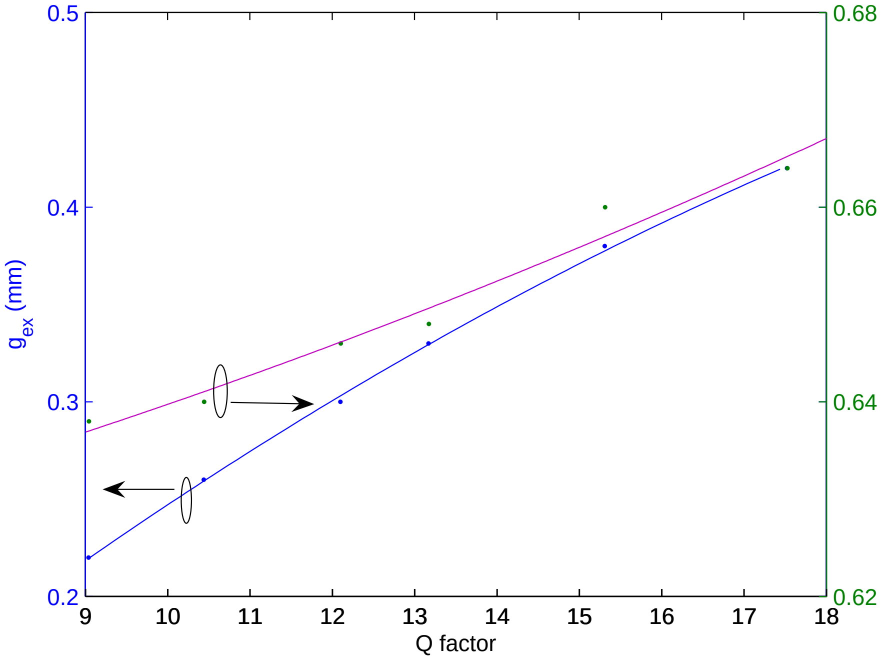

(b)

Figure 4.12: Graphical relationships of g_{ex} and related l_n with external quality factor, Q factor, for the structure in Fig. 4.10, (a) for the frequency of 10.512 GHz, (b) for the frequency of 10.536 GHz.

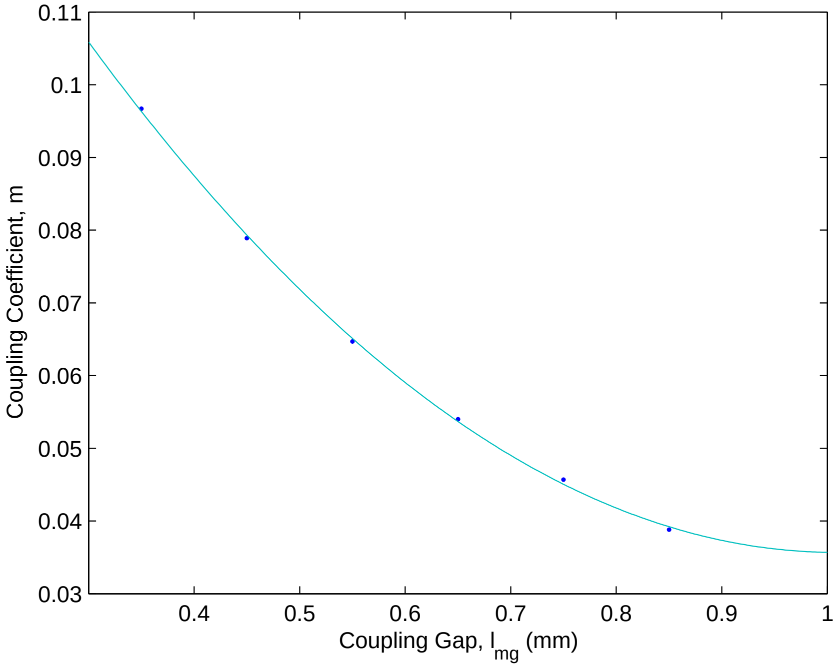

Figure 4.13: Variation of coupling coefficient with coupling gap of inductively coupled resonators required for the filter with the transmission zero in the upper stopband.

termination is coupled with the first resonator. The variation of external quality factor of the bypass coupling path with g_{sg} is depicted in Fig. 4.15 for the above structure with dimensions $l_s = 2.25$ mm, $l_b = 2.05$ mm, $l_{in2} = 0.82$ mm, $l_{gb} = 0.4$ mm, $l_{n2} = 0.644$mm, $l_{mg} = 0.53$mm, $g_{ex2} = 0.284$ mm. From this figure, g_{sg} is obtained for the required bypass coupling.

4.4.2 Design of Bandpass Filter with One Transmission Zero in the Lower Stopband

An asymmetric bandpass filter with 3.6 percent bandwidth centred at 11.6 GHz and a transmission zero located in lower side of its stopband was also designed in order to test the proposed source/load bypass coupling method. The related lowpass prototype network is transformed into a bandpass network applying the

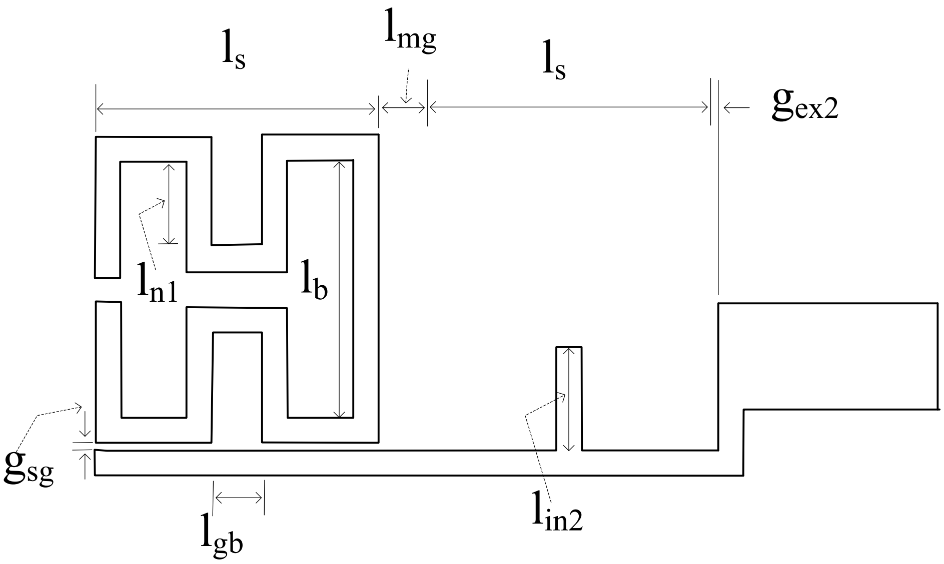

Figure 4.14: Bypass coupling structure of the bandpass filter with the transmission zero in higher stopband.

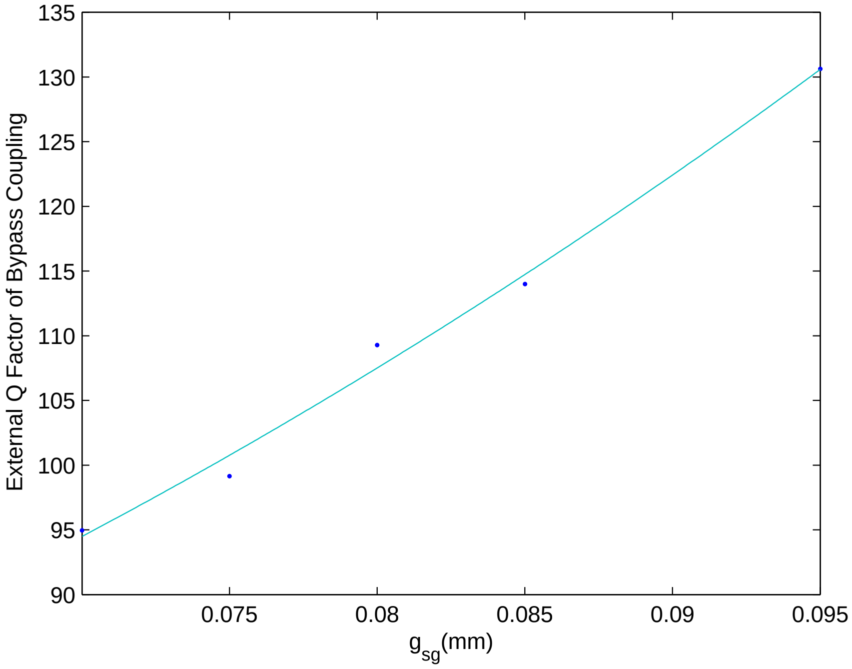

Figure 4.15: Variation of external Q factor of the bypass coupling path illustrated in Fig. 4.14.

bandpass transformation. Substituting the above filter requirements and parameters of the lowpass network into Equation 4.9, resonant frequencies of the first and second asynchronously tuned resonators are found to be 11.588 GHz and 10.565

GHz respectively. Equation 4.13 gives the inter resonator coupling of the first and second resonator as 0.0623. Using Equation 4.12, the external quality factors of the first and second resonators due to direct couplings are evaluated and they are equal to 17.4 and 12.9. respectively. The external quality factor of the first resonator due to the bypass coupling of the second termination is determined using Equation 4.15, and it is equal to 146.5. This bypass coupling is inductive (positive) as B_3 is negative in the prototype network. The inter resonator coupling of the prototype network which is parallel to the bypass path, is also positive (inductive). However, the bypass coupling of the second termination is capacitive in the proposed structure.

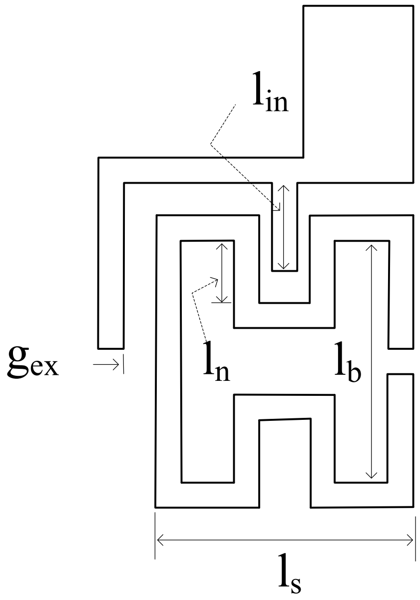

Figure 4.16: Structure for realizing external Q factors of the bandpass filter with a transmission zero in the lower stopband.

Hence, both the bypass coupling and the inter resonator coupling of the final filter structure which are in parallel are realized from capacitive couplings (negative) without changing the magnitude of the filter response. This allows to realize the bypass coupling using the proposed coupling method.

Hence, the necessary inter resonator coupling for this filter after switching the

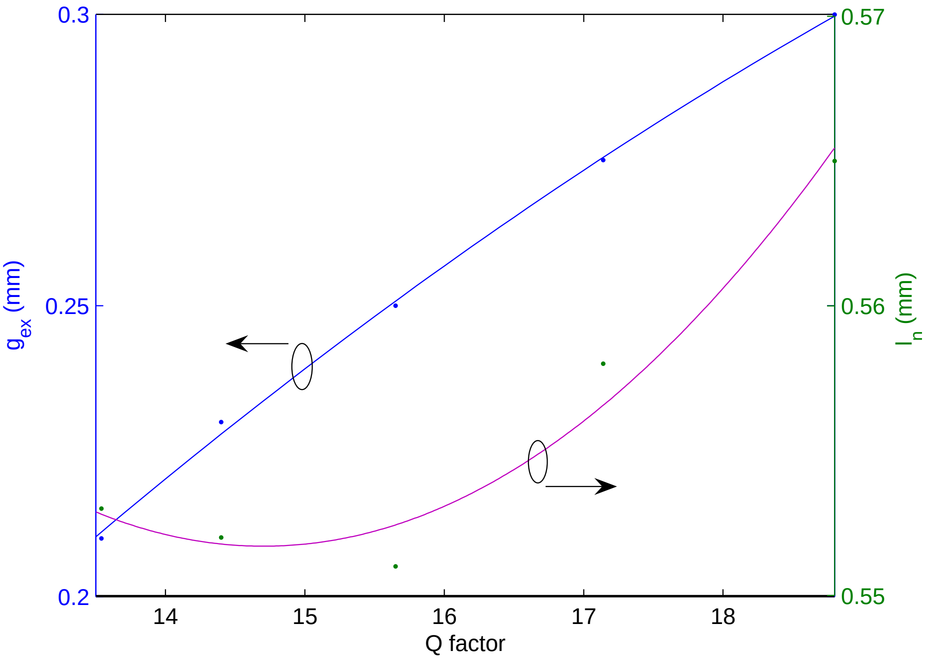

(a)

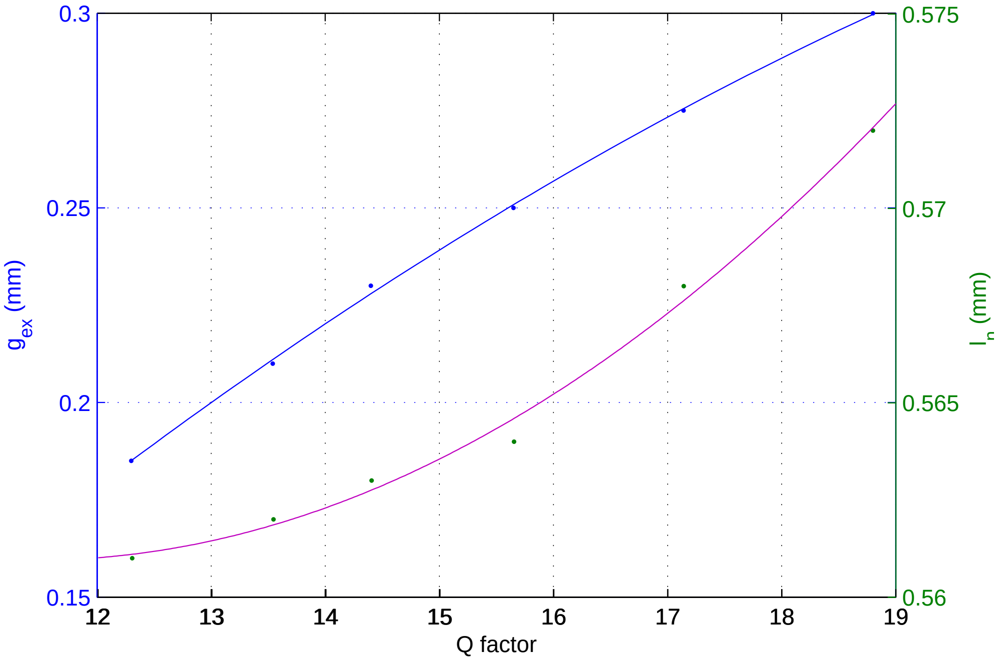

(b)

Figure 4.17: Graphical relationships of g_{ex} and related l_n with external quality factor, Q factor, for the structure in Fig. 4.16, (a) for the frequency of 11.588 GHz, (b) for the frequency of 11.565 GHz.

signs of coupling of parallel paths is negative (capacitive) and it can be physically realized from a structure similar to the structure illustrated in Fig. 4.3(a). The required external quality factors of shunt resonators are physically realized by placing a narrow arm in close proximity to the resonator, connected to the source or load as shown in Fig. 4.16. An additional narrow arm with a length of l_{in}, connected to the side arm is inserted into the cave of the folded resonator as shown in Fig. 4.16 to realize a tight coupling with the resonator as in the previous filter. For given set of g_{ex}, the graphs of variations of resonant frequency and external quality factor with l_n are obtained as in the previous section. From these graphs, graphical relationships of g_{ex} and related l_n with external quality factor are obtained for the required resonant frequencies of shunt resonators at 11.588 GHz and 11.565 GHz. The above relationships are shown in Fig. 4.17(a) and (b) for a coupling structure on a 0.5 mm thick fused quartz substrate with dielectric constant of 3.78, with other dimensions being, $l_s = 2.05$ mm, $l_b = 2$ mm, $l_{in} = 0.7$ mm, $l_{gb} = 0.4$ mm while the conductor widths of the resonator and coupling side arms are 0.2 mm and the width of resonator opening is 0.2 mm. The conductor height is 0.22 mm.

From Fig. 4.17, required g_{ex} and l_n of the first and second resonators of the bandpass filter with the transmission zero in lower stopband are found. These resonators are capacitively coupled to obtain negative inter resonator coupling as mentioned earlier. The necessary coupling gap is determined for the required coupling coefficient from the graph in Fig. 4.18 which depicts the variation of coupling coefficient with coupling gap for the capacitively coupled structure with the first and second resonators selected before for the above filter.

The bypass coupling structure of the filter with the transmission zero in the lower stopband, in which the second termination is coupled with the first resonator is shown in Fig. 4.19. The variation of external quality factor of the bypass coupling path with g_{sg} is depicted in Fig. 4.20 for the above structure with dimensions $l_s = 2.05$ mm, $l_b = 2.00$ mm, $l_{in2} = 0.6$ mm, $l_{gb} = 0.4$ mm, $l_{n2} =$

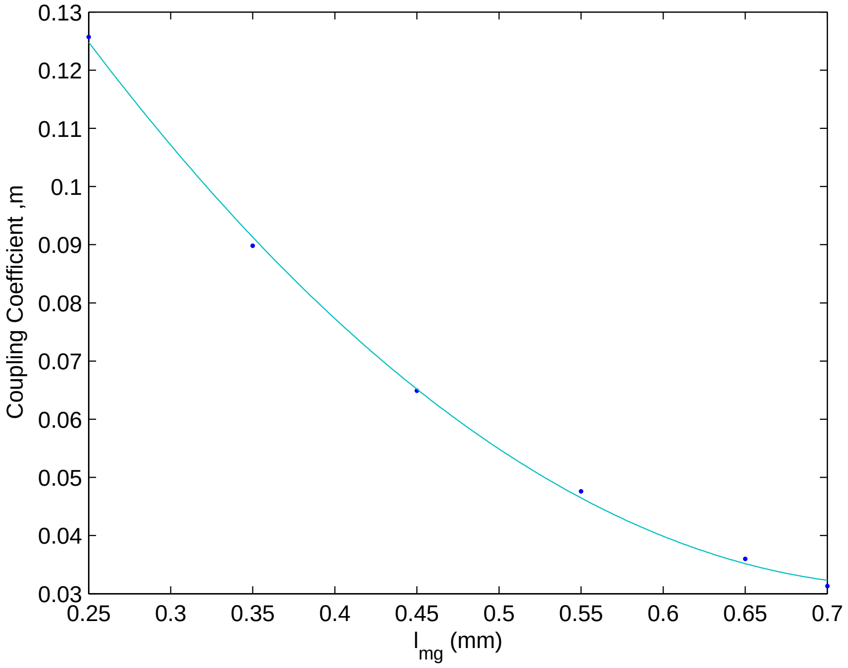

Figure 4.18: Variation of coupling coefficient with coupling gap of capacitively coupled resonators required for the filter with the transmission zero in the lower stopband.

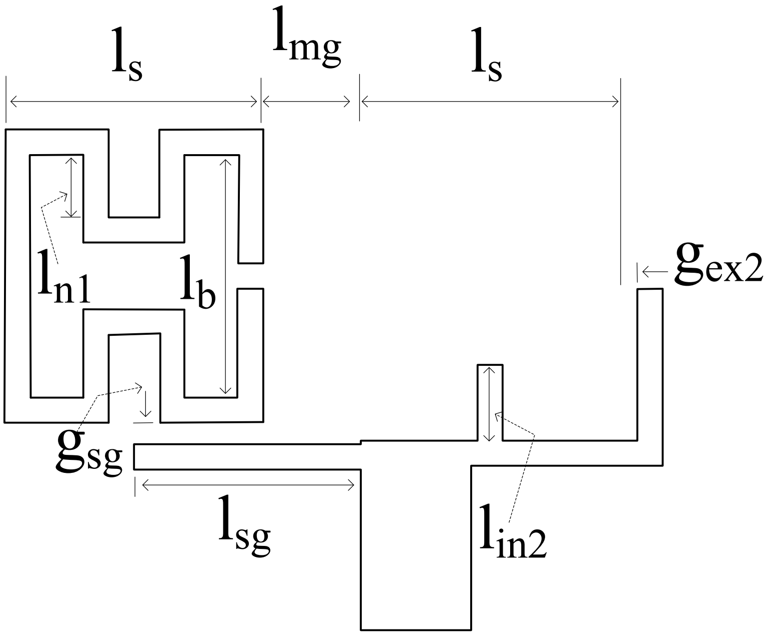

Figure 4.19: Bypass coupling structure of the bandpass filter with the transmission zero in the lower stopband.

0.561mm, $l_{mg} = 0.46$mm, $g_{ex2} = 0.197$ mm and $l_{sg} = 1.48$ mm. From this figure, g_{sg} is obtained for the required bypass coupling.

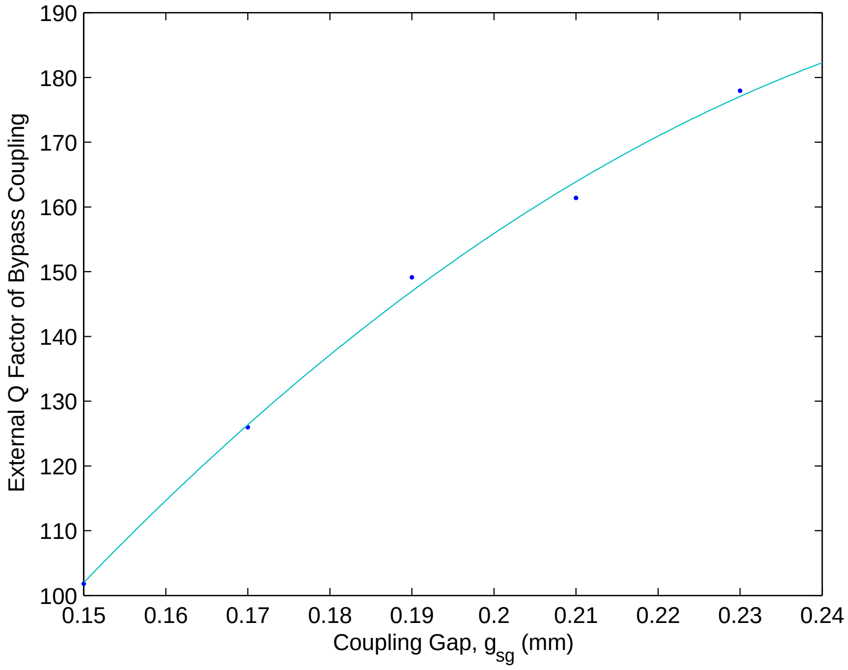

Figure 4.20: Variation of external Q factor of the bypass coupling path illustrated in Fig. 4.19.

4.5 Implementation and Results

For the above designed filters, microstrip structures on a 0.5 mm thick fused quartz substrate with dielectric constant of 3.78, as illustrated in Fig. 4.21, were designed and analyzed using EM full wave finite element simulator HFSS. Physical parameters, in the final circuits, which were extracted graphically and individually in the previous section, were optimized from *EM* simulation to obtain intended filter responses. The proposed bypass couplings of the second termination with the first resonator were achieved by extending a narrow arm up to the first resonator as described in previous sections and shown in Fig. 4.21 avoiding difficulties associated with implementation of those filters with dual mode resonators. Here, the designer can enjoy the degrees of freedom of independently controlling the length of the extended arm and the gap of it with the first resonator while maintaining the required coupling with second resonator.

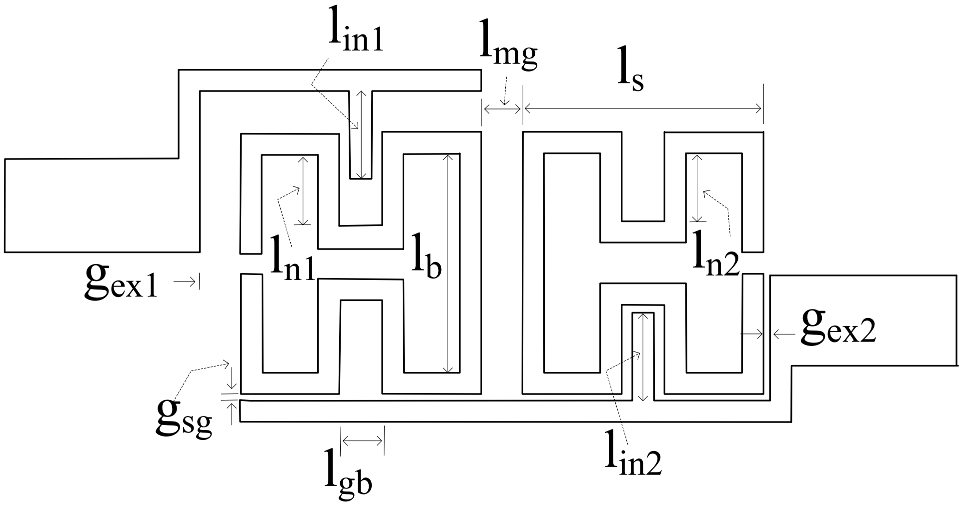

(a)

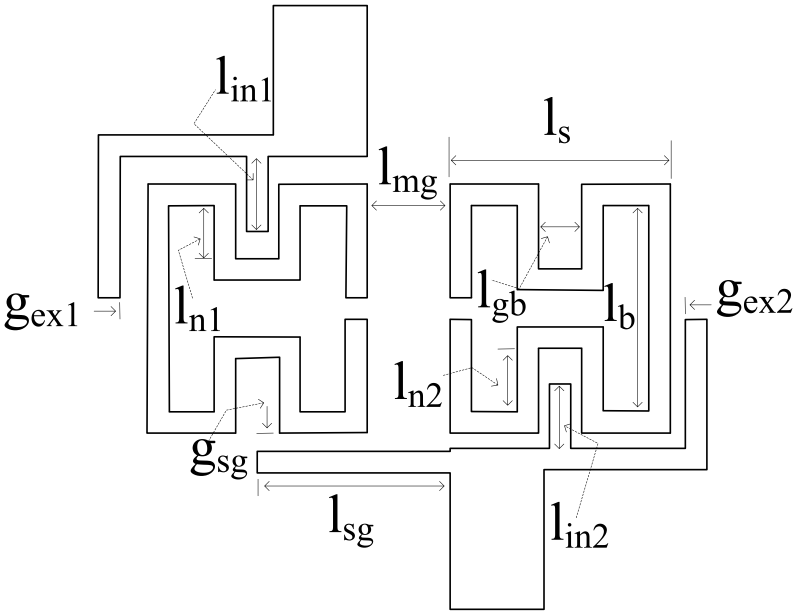

(b)

Figure 4.21: (a) Layout of the bandpass filter with a transmission zero in the higher stopband, (b) Layout of the bandpass filter with a transmission zero in the lower stopband

Tall microstrip conductors of thickness 0.22 mm were used in designs to avoid the extremely narrow coupling gaps which would be required were thin conductors used to realize direct and bypass couplings as evident from Fig. 3.15. The width of 50Ω lines is 0.875 mm.

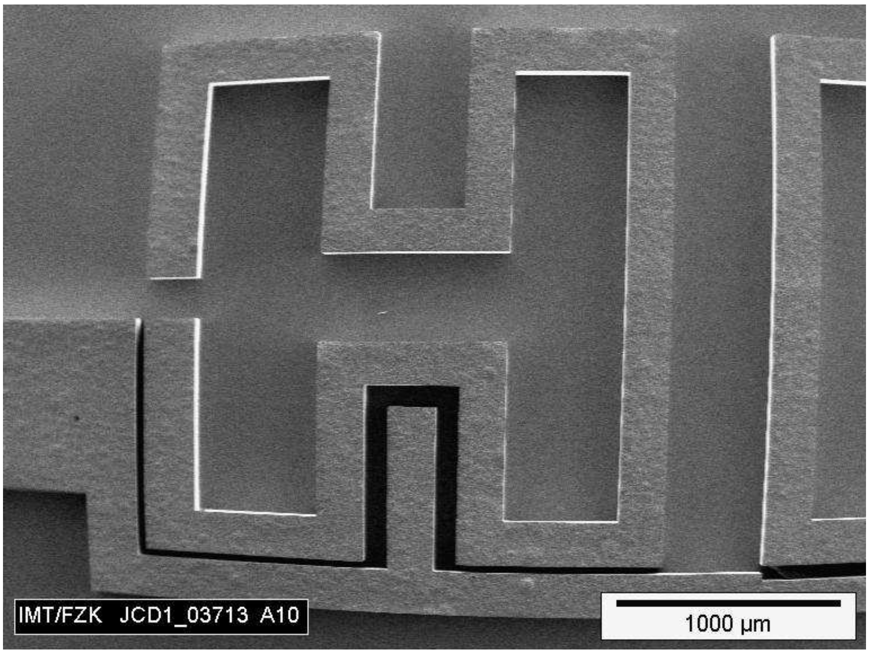

Figure 4.22: SEM micrograph of the microstrip bandpass filter with a transmission zero shown in Fig.4.21(a). (Courtesy of IMT)

The dimensions of the filter with the transmission zero in the higher stopband and 4.0 percent bandwidth centred at 10.5 GHz (Fig. 4.21(a)) are given in Table 4.1.

Table 4.1: Dimensions of the filter in Fig. 4.21(a)

Variable	Dimension (mm)	Variable	Dimension (mm)
l_s	2.250	l_b	2.050
l_{gb}	0.400	l_{in1}	0.820
l_{in2}	0.820	l_{n1}	0.678
l_{n2}	0.635	l_{mg}	0.385
g_{ex1}	0.380	g_{ex2}	0.060
g_{sg}	0.062	–	–

The width of resonator openings is 0.200 mm. The thickness of the high aspect ratio microstrip metal structure is 0.220 mm. This filter requires tight direct and bypass coupling for the second termination. It is interesting to note that very narrow coupling gaps for the second port (g_{ex2} and g_{sg}) are required, even with the use of high aspect ratio microstrip metal structures of thickness 0.220 mm. Extremely narrow coupling gaps which would be difficult to accurately fabricate using planar fabrication methods, would otherwise be required, were thin conductors used to realize these direct and bypass couplings. This filter was fabricated using the LIGA process with nickel electroplating [78]. The fabricated device was prepared for testing by adding coaxial connectors and the ground as described in Chapter 3. Fig. 4.22 shows a scanning electron microscope (SEM) micrograph of the second open loop resonator, external and bypass coupling of the second termination (right side of Fig. 4.21(a)) of deep X-ray lithography fabricated high-aspect-ratio microstrip bandpass filter with the transmission zero in the upper stopband, with 0.220 mm thick electroplated nickel on a 0.5 mm fused quartz substrate. Fig. 4.23(a) compares the prototype response with the simulated response obtained from *EM* simulation using an adaptive mesh with about 90000 tetrahedral elements and the simulated response is in good agreement with the prototype response. The minimum passband insertion loss and maximum passband return loss of the simulated response are 0.33 dB and 20 dB, respectively while the transmission zero at a finite frequency is located at 11.4 GHz in the upper stopband with at least -43.3 dB attenuation over 0.6 GHz frequency range, supported by an additional unintended transmission zero, in the vicinity of the intended transmission zero. The structure consisting the bypass coupling arm and the first half wave length resonator is responsible for creating this unintended transmission zero. This feature is not considered in the synthesis and design because of the difficulty of controlling both intended and unintended transmission zeros independently in the final structure. The experimental responses in Fig. 4.23(a) are in good agreement with simulated responses. There are two transmission zeros in the experimental S_{21} as in the simulated response. However, the experimental responses have shifted right along the frequency axis due to higher metal height of this fabricated filter. The measured metal heights near the first and second resonator openings are 0.286 mm and 0.264 mm where as the targeted height (h) is 0.22 mm. It was difficult to maintain uniform metal height in electroplating because of non uniform structures in the layout. An accurate simulation of the fabricated filter is difficult because of the difficulty of modeling these local height variations. Fig. 4.23(b) demonstrates the variation of this second order filter with a transmission zero in the upper stopband with h= 0.2 mm, 0.22 mm and 0.24 mm. Increasing metal height, h, results in higher resonant frequencies of open loop resonators in this filter shifting the response higher in frequency. However, lateral dimensions of this fabricated filter are in excellent agrement with designed dimensions. For an example, measured g_{ex2} near the bottom right hand corner in Fig. 4.21(a) is 0.059 mm where as designed g_{ex2} is equal to 0.06 mm. The fabrication accuracy of the lateral dimensions of filters is important to obtained the desired responses. For instance, approximately 7 percent change in the bypass coupling gap (g_{sg}) of this second order filter with the transmission zero in the upper stopband will result in approximately 4 percent change in the frequency of the transmission zero.

The filter with 3.6 percent bandwidth centred at 11.6 GHz and having a lower side transmission zero in its response at 10.66 GHz (Fig. 4.21(b)) has dimensions that are shown in Table 4.2. The width of the resonator openings is same as the previous filter.

Table 4.2: Dimensions of the filter in Fig. 4.21(b)

Variable	Dimension (mm)	Variable	Dimension (mm)
l_s	2.050	l_b	1.92
l_{gb}	0.400	l_{in1}	0.700
l_{in2}	0.600	l_{n1}	0.495
l_{n2}	0.590	l_{mg}	0.770
g_{ex1}	0.256	g_{ex2}	0.141
g_{sg}	0.170	l_{sg}	1.795

Fig. 4.24(a) shows photographs of the LIGA fabricated high aspect ratio bandpass filter with the one transmission zero in the lower stopband. Fig. 4.24(b) is an SEM micrograph of the region indicated by the circle in Fig. 4.24(a). Evident is the extremely smooth and vertical sidewalls, and thick narrow (approx. 0.25 mm)

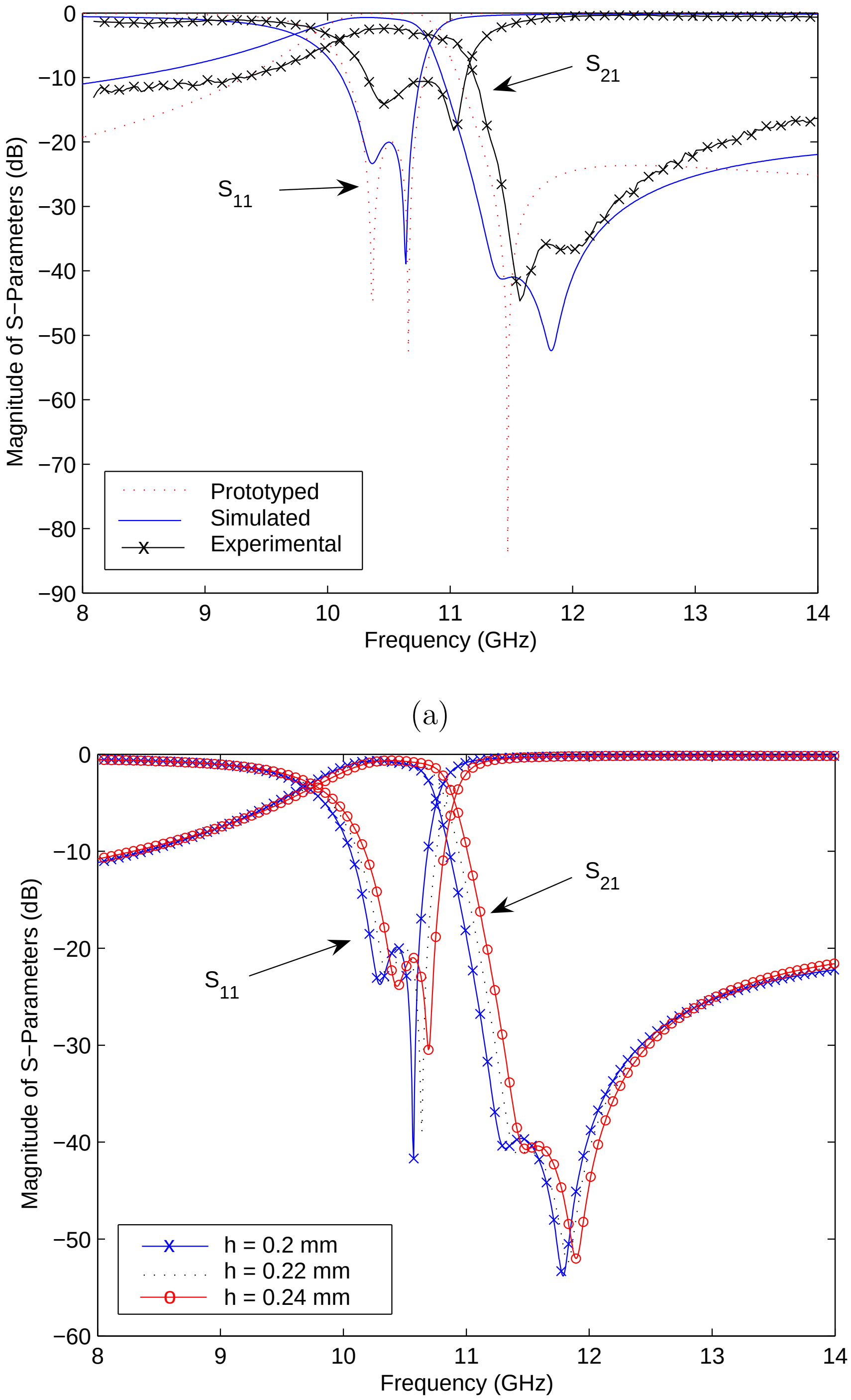

(a)

(b)

Figure 4.23: Filter with a transmission zero in upper stop band: (a) Comparison of simulated, prototyped and experimental responses; (b) Sensitivity due to metallic height variations.

coupling gaps. The experimental filter response is compared with the prototype and simulated responses obtained from EM simulation using an adaptive mesh

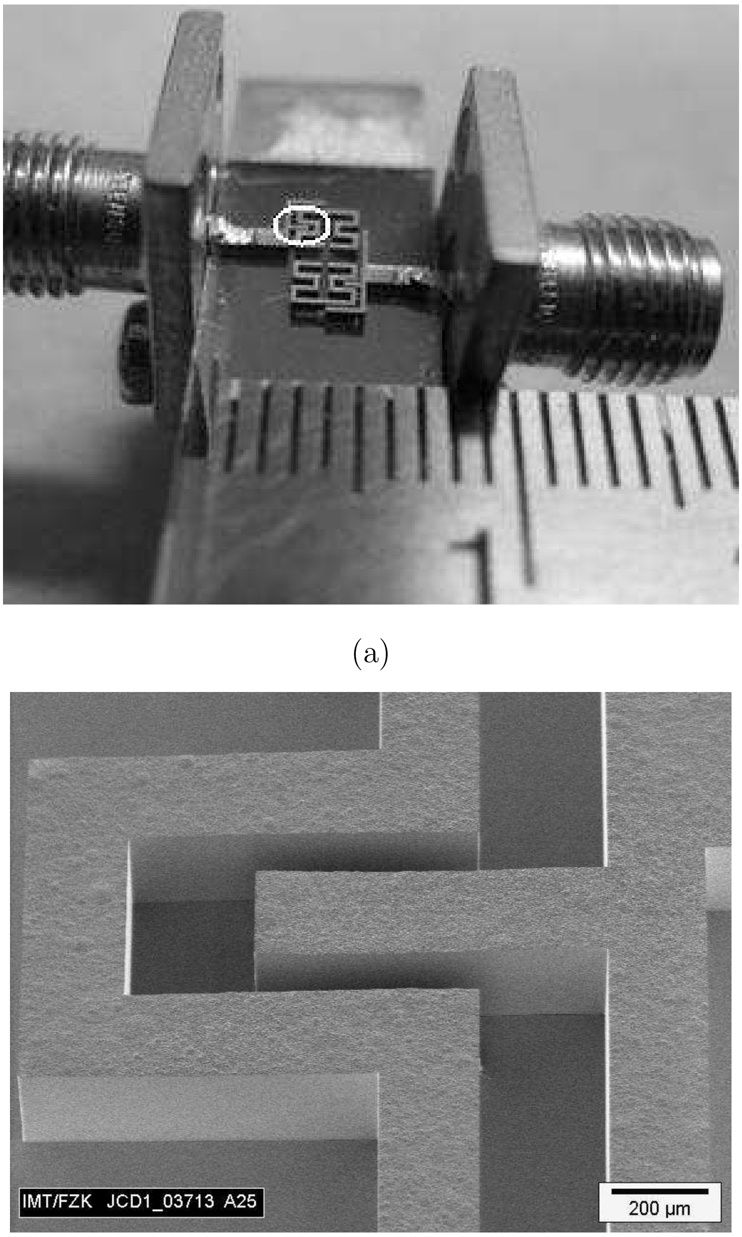

(a)

(b)

Figure 4.24: (a) Photograph of LIGA fabricated high aspect ratio bandpass filter with a transmission zero in upper stop band, (b) A SEM micrograph of the indicated area in (a), (Courtesy of IMT)

with about 90000 tetrahedral elements, in Fig. 4.25. The experimental response is in good agreement with the prototype and simulated responses. The minimum passband insertion loss and maximum passband return loss of the simulated response are in good match with the prototype response, and are 0.32 dB and 20 dB respectively. The transmission zero of the simulated response is located at

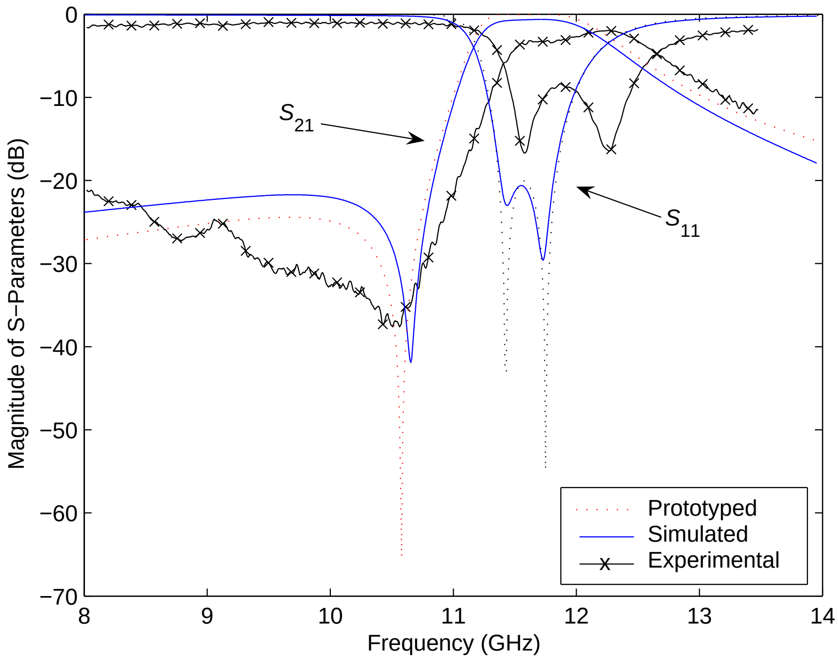

Figure 4.25: Comparison of simulated, prototyped and experimental responses of the microstrip bandpass filter with a transmission zero in lower stopband

10.65 GHz while that of the experimental response is located at 10.56 GHz. The experimental responses have shifted right along the frequency axis due to higher metal height of this fabricated filter.

Chapter 5

Half Wavelength Open Loop Higher Order LIGA Bandpass Filters with Transmission Zeros

5.1 Introduction

Second order bandpass filters with one transmission zero in either side of the stopband were discussed in the previous chapter. A ladder type synthesis procedure was adapted to obtain the prototype circuit. Not only is this synthesis procedure tedious for higher order networks but also there are limitations of this synthesis method for complex networks. Complex higher order networks with additional couplings are often used to generate transmission zeros in the stopband to increase the cutoff slope of the filter response. The filters with sharp cutoff slopes in their response are required to meet stringent frequency selectivity requirements that are imposed by efficient spectrum utilization for modern mobile communication systems.

Complex higher order networks with additional couplings can be effectively represented by a coupling matrix [79]. Off diagonal elements of the coupling matrix represent inter-node couplings while non zero diagonal elements generally represent asynchronously tuned resonant nodes. In the coupling matrix approach, the network synthesis is a matter of determining elements of the coupling matrix. Kurzrok [80] described how extra coupling between the first and last cavities of a direct coupled four coaxial cavity structure produces transmission zeros in the stopband. Design equations to calculate coupling coefficients of the coupling matrix have also been given for fourth order filters. Williams has given design equations for finding coupling coefficients for forth order elliptic filter with asymmetrically located transmission zeros [81]. The more general theory presented in [79] is widely used in synthesis of these type of structures. It is an analytical synthesis method. However, source/load multi-resonator coupling was not included because the order of the matrix is n(source and load are not considered as separate nodes). Extraction techniques applicable to folded canonical structures were given in [82], [83], [84].

Although the synthesis techniques mentioned at the end of the above paragraph produce a coupling matrix, which fulfills the filter specifications, they sometimes rely on similarity transformations to enforce a desired topology. There is no general and reliable algorithm to generate a coupling matrix with an arbitrarily chosen topology starting from the matrix encountered from the above synthesis procedure. The intended implementation method imposes constraints on the coupling matrix. There is inability of the above mentioned techniques to strictly enforce an arbitrary topology and constrain the coupling coefficients. A coupling matrix synthesis method based on gradient optimization has been given in [76] and [85]. This method allows to strictly enforce an arbitrary topology and constrain the coupling coefficients. Hence this method is used in this chapter for designing higher order filters for convenience.

The coupling matrix synthesis method based on gradient optimization is described in the first section. The cost function given in [85] is modified by introducing a real constant for fast convergence. The change of filter responses with the change of signs of certain coupling matrix elements are also described. Fourth order bandpass filters with two transmission zeros in the upper stopband and lower stopband, created by source and load multi-resonator coupling, are given in the next section. The fourth section is devoted to a third order bandpass filter with transmission zeros in both sides of the passband, again produced by source and load multi-resonator coupling. Third order filter structures with two transmission zeros in the upper stopband or lower stopband are given in the last section. All of these filter structures are designed to use the advantages of high aspect ratio structures.

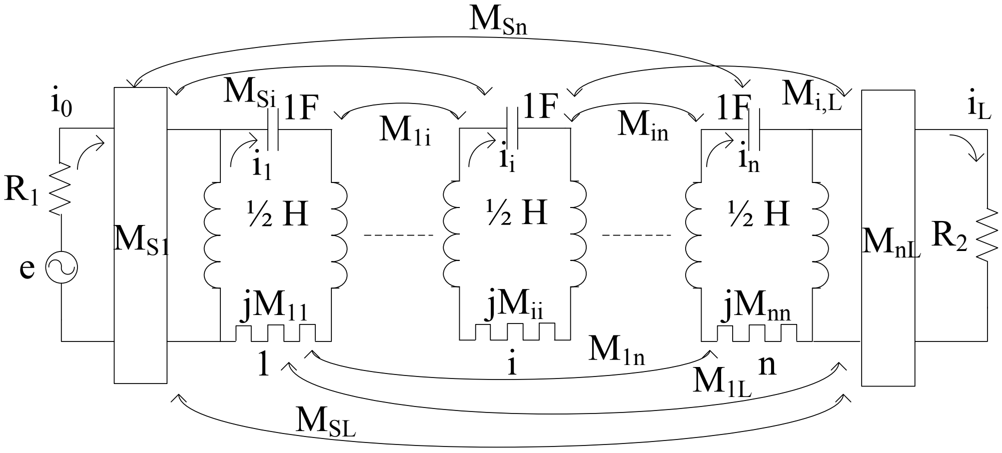

Figure 5.1: Coupling scheme of n coupled resonators with source/load multi-resonator coupling.

5.2 Coupling Matrix

A coupling scheme of n coupled resonators with source/load multi-resonator coupling is shown in Fig. 5.1. Lossless resonators have unity inductors and capacitors and are asynchronously tuned due to frequency invariant reactances (M_{ii}). The voltage source of internal resistance R_1 is coupled to the first resonator with a coupling coefficient of M_{S1} while the load with resistance, R_2, is coupled to the n^{th} resonator with a coupling coefficient of M_{nL}. Using Kirchchoff's voltage rule, which states that the algebraic sum of the voltage drops around any closed path in the network is zero, one can write the following loop equations in matrix form for the network in Fig. 5.1 and formulate an impedance matrix : $[Z][I] = [V]$.

$$\begin{pmatrix} R_1 & jM_{S1} & \cdots & jM_{Si} & \cdots & jM_{Sn} & jM_{SL} \\ jM_{S1} & j\omega' + jM_{11} & \cdots & jM_{1i} & \cdots & jM_{1n} & jM_{1L} \\ \vdots & \vdots & \vdots & \vdots & \vdots & \vdots & \vdots \\ jM_{Si} & jM_{1i} & \cdots & j\omega' + jM_{ii} & \cdots & jM_{in} & jM_{iL} \\ \vdots & \vdots & \vdots & \vdots & \vdots & \vdots & \vdots \\ jM_{Sn} & jM_{1n} & \cdots & jM_{in} & \cdots & j\omega' + jM_{nn} & jM_{nL} \\ jM_{SL} & jM_{1L} & \cdots & jM_{iL} & \cdots & jM_{nL} & R_2 \end{pmatrix} \times$$

$$\begin{pmatrix} i_0 \\ i_1 \\ \vdots \\ i_i \\ \vdots \\ i_n \\ i_L \end{pmatrix} = \begin{pmatrix} e \\ 0 \\ \vdots \\ 0 \\ \vdots \\ 0 \\ 0 \end{pmatrix} \tag{5.1}$$

where

$$\omega' = \omega - \frac{1}{\omega}$$

and

$$jM_{ij} \approx jM_{ij}\omega \approx jM_{ij}\omega_0, \qquad \omega_0 = 1 \quad \text{rad/s.}$$

The dimensions of the impedance matrix $[Z]$ are $(n+2) \times (n+2)$ such that it can accommodate source/load multi-resonator couplings. Taking the impedance matrix as $[Z] = [R] + j\omega'[W] + j[M]$, Equation 5.1 can be expressed in the form:

$$[-jR + \omega'[W] + M][I] = [A][I] = -j[e] \tag{5.2}$$

where [R] is a $(n+2) \times (n+2)$ matrix whose only nonzero entries are $R_{11} = R_1$ and $R_{n+2,n+2} = R_2$, [W] is similar to the $(n+2) \times (n+2)$ identity matrix except that $W_{11} = W_{n+2,n+2} = 0$, and $[M]$ is the $(n+2) \times (n+2)$ symmetric coupling matrix. $[e]$ and $[I]$ are voltage and current matrices respectively. Now the current matrix can be found from, $[I] = -j[A]^{-1}[e]$. The insertion loss and the return loss of the network are given as (Appendix C)

$$\begin{aligned} S_{21} &= \frac{2\sqrt{R_1 R_2} i_L}{e} \\ S_{11} &= 1 - \frac{2R_1 i_0}{e}. \end{aligned} \tag{5.3}$$

Assuming $R_1 = R_2 = 1$, $e^t = [1, 0...., 0]$ and using above relationships, S_{21} and S_{11} can be expressed as

$$\begin{aligned} S_{21} &= -2j[A]^{-1}_{n+2,1} \\ S_{11} &= 1 + 2j[A]^{-1}_{11}. \end{aligned} \tag{5.4}$$

The elements of the coupling matrix associated with $[A]$ in Equation 5.4 are denoted by m_{ij} since the normalized network is considered hereafter for the synthesis. The synthesis problem is associated with determining the coupling matrix $[M]$ such that the intended response is produced. The topology that is dictated by constraints imposed by the envisaged implementation, is defined with coupling coefficients in the coupling matrix. Unknown coupling matrix elements are found from using a gradient based optimization method. The problem of optimization may be formulated as the minimization of a scalar objective function or cost function. It represents the difference between the performance achieved at any stage and the desired specification.

Generalized Chebychev prototype functions are the filtering function under consideration and rational functions of frequency. They are uniquely specified by the location of poles and zeros and an additional scaling constant [76]. Since the zeros of the filtering function, $F_n(\omega')$, are identical to those of S_{11},

$$|S_{11}|^2 = \frac{\epsilon^2 F_n^2(\omega')}{1 + \epsilon^2 F_n^2(\omega')} \tag{5.5}$$

and its poles coincide with the zeros of S_{21}, the original network can be found from equating S_{11} and S_{21} to zero at the corresponding frequency points. The scaling constant is determined by equating the return loss at $\pm\omega'$ to $(\epsilon/\sqrt{1+\epsilon^2})$. Hence, the cost function which is used here is given as,

$$\begin{aligned} K \;=\; & \sum_{i=1}^{n} |S_{11}(\omega'_{zi})|^2 + \sum_{i=1}^{p} |S_{21}(\omega'_{pi})|^{\alpha} + \\ & \left(|S_{11}(\omega'=-1)| - \frac{\epsilon}{\sqrt{1+\epsilon^2}}\right)^2 + \left(|S_{11}(\omega'=1)| - \frac{\epsilon}{\sqrt{1+\epsilon^2}}\right)^2 \end{aligned} \tag{5.6}$$

where ω'_{zi} and ω'_{pi} are the zeros and poles of the filtering function $F_n(\omega')$, respectively, p is the total number of poles of $F_n(\omega')$ and $\alpha = 1$ or 2. The above cost function is similar to the cost function given in [85] and [76] except the order of the second term of the cost function in Equation 5.6 is selected as 1 or 2 whereas it is a second order term only in [85] and [76]. The contribution from the second term to K enhances by selecting $\alpha = 1$ since $|S_{21}(\omega')| \ll 1$ in the stopband. Hence the first order term would expedite the convergence in certain cases where transmission zeros are slowly converging to desired frequencies. Examples will be given later in this chapter.

The entries of the coupling matrix are used as independent variables in the optimization process. The gradient based optimization starts with assigning initial guessed values to the elements of the coupling matrix. The search for the minimum of the cost function can be based on the direction given by $-\nabla K(m_{ij})$. Hence, the updated M is given by $M - \lambda\nabla K(m_{ij})$ where λ is a scalar. It is suggested from the observation of Equation 5.6 that the gradient of the error function with respect to the independent elements of coupling matrix involves the derivatives $\partial|S_{11}|/\partial m_{ij}$ and $\partial|S_{21}|/\partial m_{ij}$. It can be shown that

$$\frac{\partial|S_{21}|}{\partial m_{ij}} = Re\left[\frac{|S_{21}|}{S_{21}}\frac{\partial S_{21}}{\partial m_{ij}}\right] \tag{5.7}$$

with a similar expression for S_{11}. Using Equation 5.3, partial derivatives of S_{21} and S_{11} can be obtained as,

$$\begin{aligned} \frac{\partial S_{21}}{\partial m_{ij}} &= 2\frac{\partial i_L}{\partial m_{ij}}, \\ \frac{\partial S_{11}}{\partial m_{ij}} &= -2\frac{\partial i_0}{\partial m_{ij}}. \end{aligned} \tag{5.8}$$

The derivatives of currents in the above equations can be found from

$$\frac{\partial [I]}{m_{ij}} = j[A^{-1}]\frac{\partial [A]}{m_{ij}}[A^{-1}][e], \tag{5.9}$$

which is obtained using equation, $[I] = -j[A^{-1}][e]$ and the derivatives of the identity $[A][A^{-1}] = [U]$, where $[U]$ is the identity matrix. The topology matrix, $[P]$, of the network is defined as $P_{ij} = 1$ if $m_{ij} \neq 0$ and $P_{ij} = 0$ if $m_{ij} = 0$. The topology of the network is specified in advance and will be enforced at each step in the optimization.

Simplifying Equation 5.9 further using the symmetry of $[A]$ and $[A^{-1}]$ and substituting it into Equation 5.8, the following expressions can be obtained [85];

$$\begin{aligned} \frac{\partial S_{11}}{\partial m_{ij}} &= -4jP_{ij}[A^{-1}]_{1i}[A^{-1}]_{j1} \qquad i \neq j \\ \frac{\partial S_{21}}{\partial m_{ij}} &= 2jP_{ij}\left([A^{-1}]_{n+2,i}[A^{-1}]_{j1} + [A^{-1}]_{n+2,j}[A^{-1}]_{i1}\right) \qquad i \neq j \end{aligned} \tag{5.10}$$

The gradient of S_{11} and S_{21} with respect to the diagonal elements of the coupling matrix can be obtained from the previous expressions by simply letting $i = j$ and dividing by a factor of 2 because diagonal elements of a symmetric matrix produces only one term in the intermediate column matrices in the matrix multiplication in Equation 5.10, where as off diagonal elements produces two similar terms in those intermediate matrices. Thus,

$$\begin{aligned}
\frac{\partial S_{11}}{\partial m_{ii}} &= -2jP_{ii}[A^{-1}]_{1i}[A^{-1}]_{i1} \\
\frac{\partial S_{21}}{\partial m_{ii}} &= jP_{ii}\left([A^{-1}]_{n+2,i}[A^{-1}]_{i1} + [A^{-1}]_{n+2,i}[A^{-1}]_{i1}\right).
\end{aligned} \tag{5.11}$$

The above gradient based optimization method for filter synthesis was applied for synthesizing the second order filter with a transmission zero in the upper stopband described in the previous chapter. The transmission zero is located at $\omega' = 4.42$. The return loss of the filter response is 20 dB. Poles of the filtering function, $F_n(\omega')$ are the same as transmission zeros according to Equation 4.3 while zeros of $F_n(\omega')$ are evaluated from Equation 4.4 and they are 0.7621 and -0.6475. To implement the transmission zero, the source or load is coupled to the non-adjacent resonator as realized in the previous chapter. To accommodate the above implementation, a coupling matrix of following form is enforced;

$$[M] = \begin{pmatrix} 0 & x_1 & x_3 & 0 \\ x_1 & x_5 & x_4 & 0 \\ x_3 & x_4 & x_6 & x_2 \\ 0 & 0 & x_2 & 0 \end{pmatrix}. \tag{5.12}$$

The initial guess for the optimization is set to x_1=-1, x_2=-1, x_3=-0.01, x_4=0.5, x_5 and x_6 =0. The signs of the initial guesses are chosen to enforce the coupling signs of the intended implementation. The above values were selected to match with the realization of the filter with one transmission zero in the upper stopband in the previous chapter. The order of the second term, α, was selected to be 2 because the convergence of $S_{11}(\omega')$ in the passband was slower than convergence of transmission zeros in this case. The optimization converged after 774 iterations. After the optimization, the obtained coupling matrix is,

$$\begin{pmatrix} 0 & x_1 & x_3 & 0 \\ x_1 & x_5 & x_4 & 0 \\ x_3 & x_4 & x_6 & x_2 \\ 0 & 0 & x_2 & 0 \end{pmatrix} = \begin{pmatrix} 0 & -1.1403 & -0.4397 & 0 \\ -1.1403 & -0.6157 & 1.4604 & 0 \\ -0.4397 & 1.4604 & 0.5053 & -1.2198 \\ 0 & 0 & -1.2198 & 0 \end{pmatrix}. \tag{5.13}$$

The transmission and reflection coefficients of the filter, calculated using the resultant coupling matrix and Equation 5.4, are shown from solid curves in Fig. 5.2. The responses formed by the Chebychev polynomial which are given by cross marks in the same figure, are coincident with the responses obtained from the coupling matrix synthesized by the optimization, thereby indicating the accuracy of the optimization method.

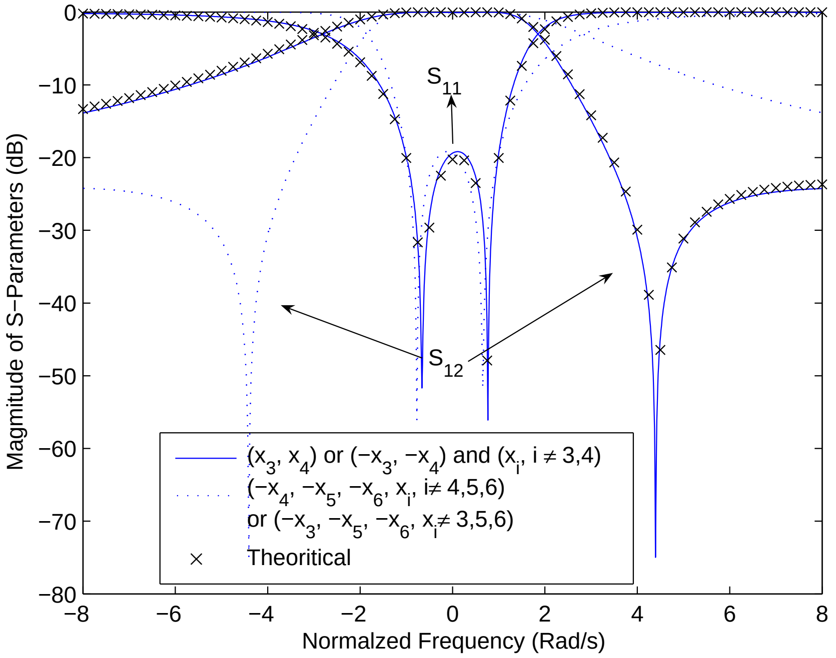

Figure 5.2: Responses of second order filters derived from the coupling matrix in Equation 5.13. Solid curves represent responses from the coupling matrix with $\pm x_3$ and $\pm x_4$; Dotted curves represent responses from the coupling matrix with (x_4=$-x_4$, x_5=$-x_5$ and x_6=$-x_6$) or (x_3=$-x_3$, x_5=$-x_5$ and x_6=$-x_6$).

The same responses given by the solid line can be obtained from the same coupling matrix when x_3 and x_4 take the opposite signs (i.e. x_3=$-x_3$ and x_4=$-x_4$) as illustrated in Fig. 5.2. This fact was taken into account in realizing the second order filter with a transmission zero in the lower stopband in the previous chapter. It is also interesting to point out that transmission zeros can be shifted into the lower stopband ($|S_{21}(\omega')|$=$|S_{21}(-\omega')|$ and $|S_{11}(\omega')|$=$|S_{11}(-\omega')|$), just by changing the signs of x_4, x_5 and x_6 or x_3, x_5 and x_6 into their opposite signs as illustrated in Fig. 5.2.

To prove the above observations, the insertion loss and return loss are found using Equation 5.4 and from the coupling matrix in Equation 5.12 as,

$$S_{21} = \frac{-2j}{d}\left[x_1x_2x_4 - x_2x_3x_5 - x_2x_3\omega'\right] \tag{5.14}$$

and

$$\begin{aligned} S_{11} \; = \; & \frac{1}{d}[\omega'^2 + \omega'(x_5 + x_6) - x_4^2 + x_1^2x_2^2 + x_5x_6 + j\{\omega'(x_1^2 + 3x_2^2 + x_3^2) + \\ & x_1^2x_6 - x_2^2x_5 + x_3^2x_5 - 2x_1x_3x_4\}] \end{aligned} \tag{5.15}$$

where

$$\begin{aligned} d \; = \; & -\omega'^2 + \omega'\{-x_5 - x_6 + j(x_1^2 + x_2^2 + x_3^2)\} + x_4^2 + x_2^2x_1^2 - x_5x_6 + \\ & j\{x_1^2x_6 + x_2^2x_5 + x_3^2x_5 - 2x_1x_3x_4\}. \end{aligned} \tag{5.16}$$

From the above equations, it is obvious that the magnitudes of denominators and numerators of S_{21} and S_{11} do not change with the shift of signs of both x_3 and x_4. Hence the magnitude responses are also invariant with changing the signs of x_3 and x_4. Equations 5.14 and 5.15 also suggest that changing the signs of x_4, x_5 and x_6 changes $|S_{21}(\omega')|$ and $|S_{11}(\omega')|$ into $|S_{21}(-\omega')|$ and $|S_{11}(-\omega')|$, respectively. Similar arguments can be made for changing the signs of x_3, x_5 and x_6.

The resultant coupling matrix from the optimization is a normalized matrix with respect to source, load, and frequency. To obtain a coupling matrix, Equation 5.1 was derived for a system with an unity fractional bandwidth, Δ, and an unity angular resonant frequency. To design a bandpass filter with a fractional bandwidth of Δ and angular center frequency of ω_0, off-diagonal elements are de-normalized as,

$$M_{ij}|_{i \neq j} = m_{ij}\Delta. \tag{5.17}$$

Diagonal m_{ii} offsets the resonant frequencies of the resonators. Using Equation 4.10, angular resonant frequencies of required resonators are found from,

$$\omega_{0i} = \omega_0 \sqrt{1 - \frac{m_{ii}}{\frac{1}{\Delta} + \frac{m_{ii}}{2}}} \tag{5.18}$$

Considering the fact that K^2/R is the impedance of a resistive load, R, seen by a resonator when the resistive load is coupled to the resonator through an impedance inverter K, and using an equation analogous to Equation 4.12, the external quality factors of the source/ load multi-resonator coupling are found from

$$Q_{ei} = \frac{\omega_{0i}}{\omega_0 {m_{S,L,i}}^2} \left(\frac{1}{\Delta} + \frac{m_{ii}}{2} \right) \tag{5.19}$$

where $m_{S,L,i} \equiv m_{S,i}$ or $m_{L,i}$.

5.3 Fourth Order Filters with Two Transmission Zeros

5.3.1 Transmission Zeros in Upper Stopband

The second order networks with coupling structures as in the above second order filter are cascaded to form a fourth order filter network with two transmission zeros in the upper stopband. The transmission zeros are located at $\omega' = 3.69$ and $\omega' = 5.197$ in the prototyped network. The return loss of the filter response is 19.6 dB. A higher targeted return loss is chosen in this filter design because of the difficulty in the optimization of higher order filters with lower return loss. The source and load are coupled to the non-adjacent resonator as realized in the previous chapter to implement the transmission zeros. The first and second, and third and fourth resonant nodes are positively coupled while second and third resonant nodes are negatively coupled. To accommodate the above implementation, a coupling matrix of following form is enforced;

$$[M] = \begin{pmatrix} 0 & m_{S1} & m_{S2} & 0 & 0 & 0 \\ m_{S1} & m_{11} & m_{12} & 0 & 0 & 0 \\ m_{S2} & m_{12} & m_{22} & m_{23} & 0 & 0 \\ 0 & 0 & m_{23} & m_{33} & m_{34} & m_{L3} \\ 0 & 0 & 0 & m_{34} & m_{44} & m_{L4} \\ 0 & 0 & 0 & m_{L3} & m_{L4} & 0 \end{pmatrix}. \tag{5.20}$$

The initial guess for the optimization is set as, m_{S1} =m_{L4} =-1, m_{S2}=-0.1, m_{11} =m_{22} =m_{33} =m_{44}= 0, m_{12} =m_{34} =0.5, m_{23} =-0.5 and m_{L3} =-0.05. The order of the second term in the error function, α, is selected to be 1 for fast convergence. The solid lowpass response and dotted lowpass response in Fig. 5.3 are given by coupling matrices obtained from optimization with α=1 and 2 respectively. The optimization with α=1 converged after 2096 iterations and the optimization with α=2 did not converge even after 10000 iterations. After the optimization with α=1, the following coupling matrix was obtained,

$$[M] = \begin{pmatrix} 0 & -0.9781 & -0.2425 & 0 & 0 & 0 \\ -0.9781 & -0.3854 & 0.8230 & 0 & 0 & 0 \\ -0.2425 & 0.8230 & 0.2293 & -0.6937 & 0 & 0 \\ 0 & 0 & -0.6937 & 0.184 & 0.8533 & -0.1715 \\ 0 & 0 & 0 & 0.8533 & -0.2633 & -0.9928 \\ 0 & 0 & 0 & -0.1715 & -0.9928 & 0 \end{pmatrix}. \tag{5.21}$$

The magnitudes of S-parameters are independent of the sign of the coupling coefficient, m_{23} (i.e. matrix elements $m(3,4)$ and $m(4,3)$). Negative coupling for m_{23} is chosen to realize it conveniently in the intended implementation.

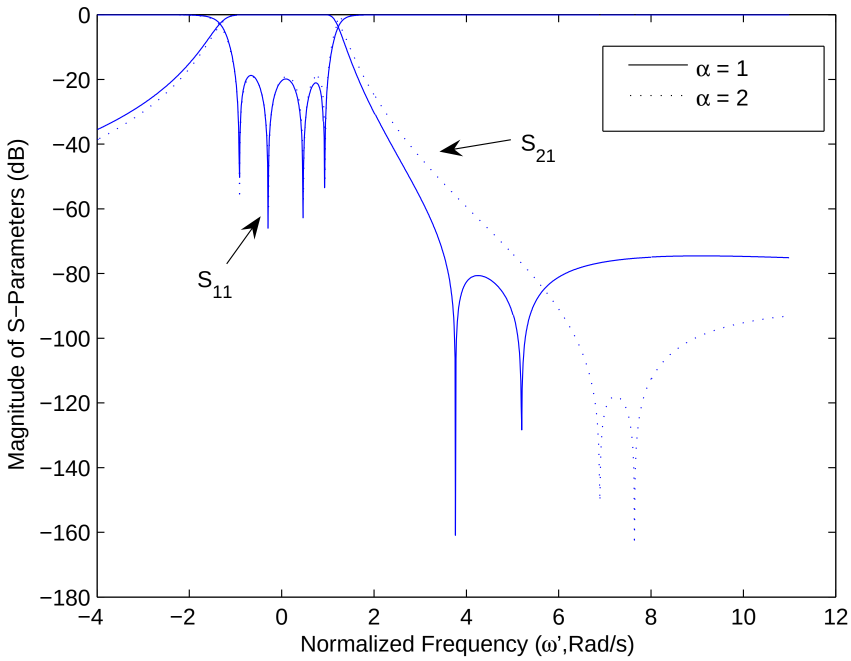

Figure 5.3: Responses of fourth order prototyped filters with transmission zeros in the upper stopband; Solid curves represent converged responses from the coupling matrix obtained from taking α=1, Dotted curves represent responses from the coupling matrix obtained from taking α=2, however this optimization did not converge.

A fourth order bandpass filter with a fractional bandwidth of 2.52 percent centred at 10.5 GHz is designed using the coupling matrix in Equation 5.21. Transmission zeros are located in the upper stopband at 11 GHz and 11.21 GHz. The filter is implemented using LIGA microstrip folded open loop resonators. The required resonant frequencies of the first, second, third, and fourth resonators are 10.55 GHz, 10.47 GHz, 10.48 GHz, 10.53 GHz, respectively. Inter-resonator couplings evaluated using Equation 5.17 are M_{12}= 0.0207, M_{23}= -0.0175, M_{34}= 0.0215. External quality factors of source/load multi-resonator couplings are found from Equation 5.19 and they are Q_{S1}= 41.47, Q_{S2}= 674.82, Q_{L3}= 1349.74, Q_{L4}= 40.24.

External quality factors of source/load coupling with adjacent resonators are

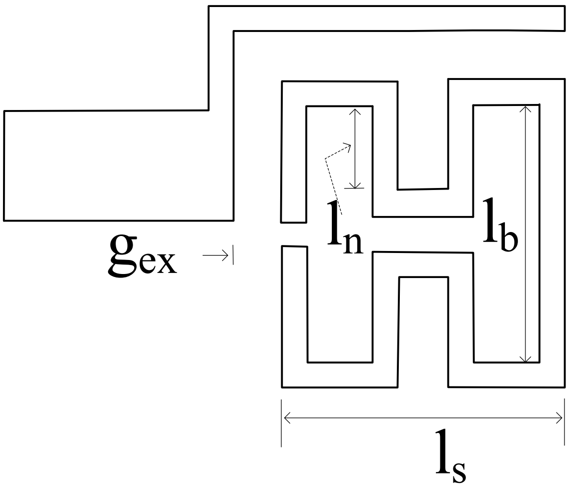

Figure 5.4: Structure for source/load coupling with adjacent resonators for filters with transmission zeros in higher stopband.

implemented as illustrated in Fig. 5.4. The only difference of this structure with the structure shown in Fig. 4.10 which was used to design the second order filter with transmission zero in the higher stopband, is that the short arm with a length of l_{in} is not present in the coupling structure in Fig. 5.4. Dimensions of the coupling structure on a 0.5 mm thick fused quartz substrate are l_s= 2.25 mm, l_b= 2.2 mm, and 0.22 mm wide resonator opening. The conductor width and height of resonators are 0.2 mm and 0.22 mm, respectively. Other dimensions of the external coupling structures are extracted from Fig. 5.5 which gives relationships of the independent variable, g_{ex} and the dependent variable l_n with external quality factors at resonant frequencies of 10.53 GHz and 10.55 GHz.

The above relationships were obtained from *EM* simulations. g_{ex} and l_n of the first resonator are 0.37 mm and 0.588 mm respectively. g_{ex} and l_n of the fourth resonator are 0.362 mm and 0.594 mm respectively. Now all dimensions of the first and fourth resonators are available. The dimensions, l_n of the other middle resonators (the second and third resonators) are obtained from a graphical relationship of resonant frequency vs l_n that is obtained from *HFSS EM* simulation. l_n of the second and third resonators are 0.627 mm and 0.622 mm respectively.

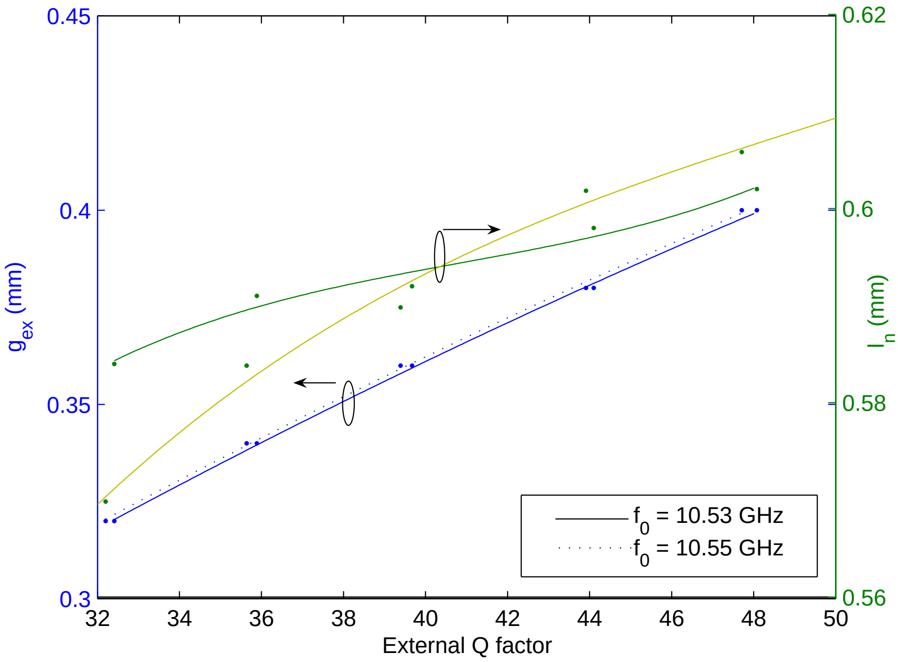

Figure 5.5: Variation of external quality factor with independent variable g_{ex} and dependant variable l_n. Solid lines correspond to the resonant frequency of 10.53 GHz and dotted curves correspond to the resonant frequency of 10.55 GHz.

Positive couplings between the first and second resonators and the third and fourth resonators are realized from similar resonator orientation used for implementing the second order filter with a transmission zero in higher stopband in the previous chapter while the negative coupling between the second and the third resonators are realized from similar resonator orientation used for implementing the second order filter with a transmission zero in the lower stopband in the previous chapter. Coupling gaps between resonators were determined from graphs in Fig. 5.6 that show variation of coupling coefficients with coupling gaps of previously designed resonators where the solid curve demonstrates the coupling coefficient of inductively coupled resonators and the dotted curve demonstrates the variation of coupling coefficient of capacitively coupled resonators. The inductive coupling gap between the first and second resonators and the third and fourth resonators are 1.49 mm and 1.45 mm respectively while the capacitive gap between the second and third resonators is 0.92 mm.

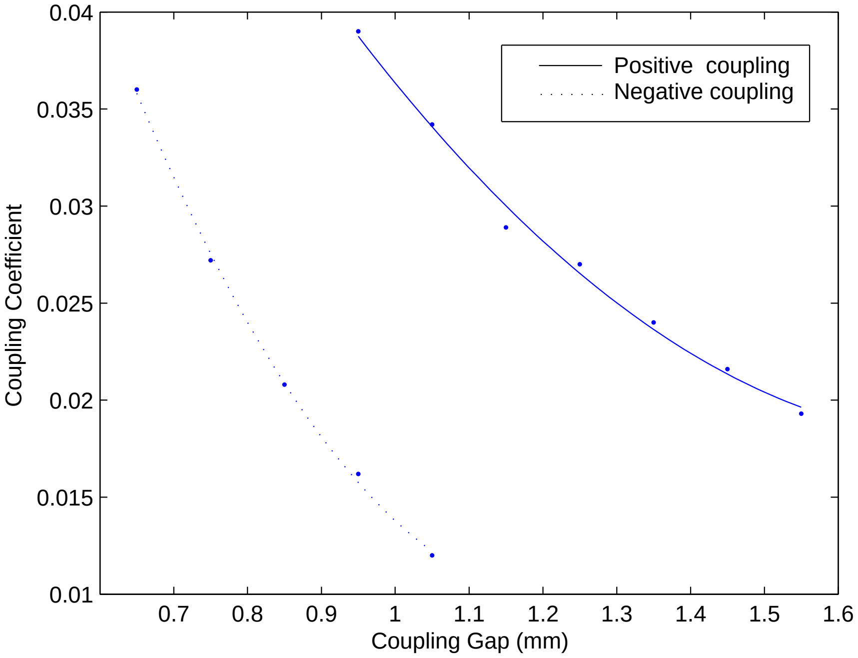

Figure 5.6: Variation of coupling coefficient with coupling gap. The solid curve corresponds to inductive coupling while the dotted line corresponds to capacitive coupling.

Source/load bypass coupling with nonadjacent resonators is implemented by extending the coupling arm connected to source or load up to the non adjacent resonator by a length of l_{sg} as shown in Fig. 5.7. The solid curve and the dotted curve in Fig. 5.8 demonstrate the relationships of the external quality factor with the coupling gap, g_{sg}, for the source/load bypass coupling of the second resonator and the third resonator with l_{sg1}= 2.615 mm and l_{sg2}= 1.731 mm respectively. The coupling gap, g_{sg} found from Fig. 5.8, between the side arm and the second resonator is 0.214 mm while g_{sg} between the side coupling arm and the third resonator is 0.146 mm.

Based on graphically extracted parameters, a microstrip structure for the above fourth order bandpass filter with two transmission zeros in the upper stopband was designed on a 0.5 mm thick fused quartz substrate as shown in Fig. 5.9. Both narrow side arms connected to the source and load have been extended up to their immediate non adjacent resonators (up to the second and third resonators)

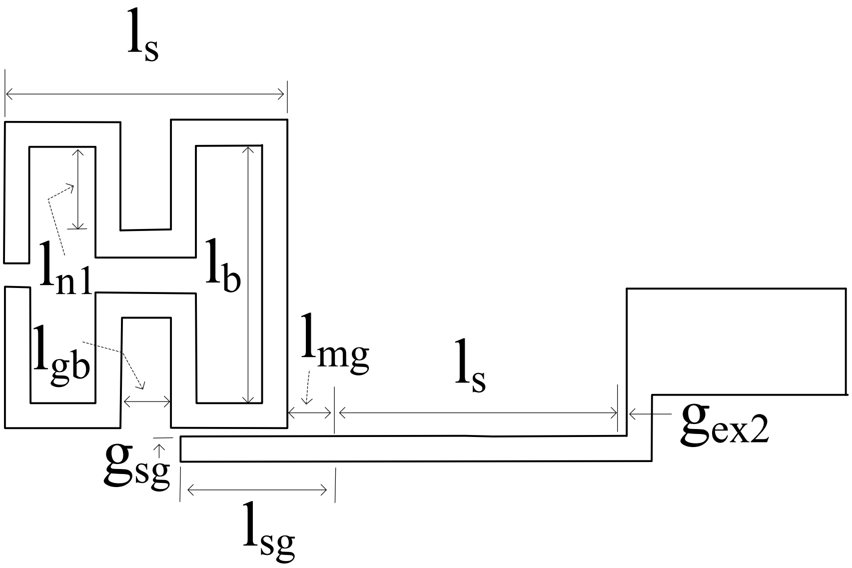

Figure 5.7: Bypass coupling structure for the filter with transmission zeros in the upper stopband.

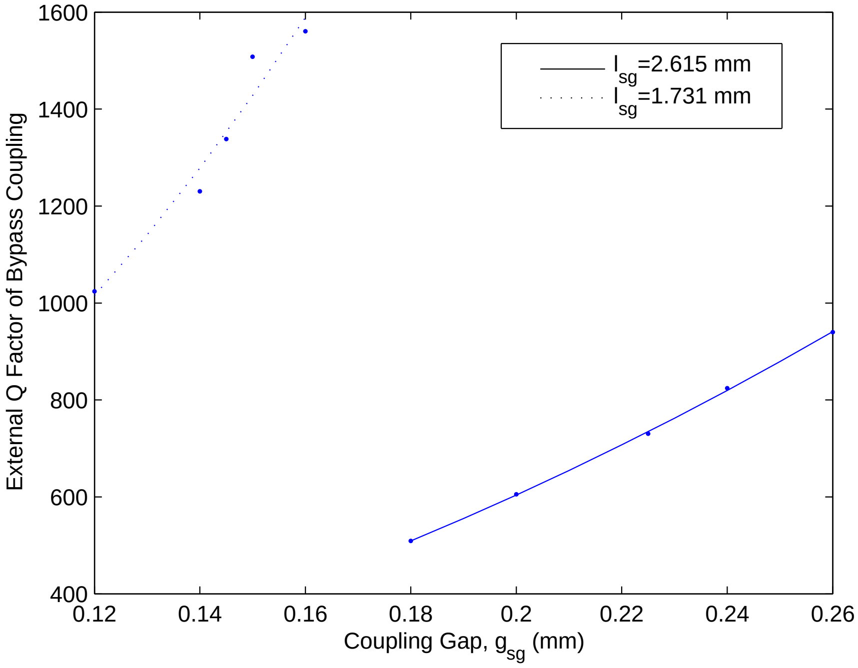

Figure 5.8: External Q factor of bypass coupling with l_{sg}= 2.615 mm (from the solid curve) and l_{sg}= 1.731 mm (from the dotted curve).

to realize bypass couplings, namely M_{S2} and M_{L3}. The structure was analyzed and optimized from *HFSS EM* simulation. Conductor height was selected to be 0.22 mm to reduce conductor losses. The width of 50Ω lines is 0.875 mm. The width of resonator openings is 0.22 mm. Dimensions of the fourth order filter with two transmission zeros in the upper stopband and a fractional bandwidth of 2.52 percent centered at 10.5 GHz are given in Table 5.1. The lengths of bypass coupling arms (l_{sg1} and l_{sg2}) are selected such that moderate coupling gaps (g_{sg1} and g_{sg2}) are required.

Table 5.1: Dimensions of the filter in Fig. 5.9.

Variable	Dimension (mm)	Variable	Dimension (mm)
l_s	2.250	l_b	2.200
l_{gb}	0.400	l_{n1}	0.641
l_{n2}	0.650	l_{n3}	0.653
l_{n4}	0.630	l_{mg1}	1.100
l_{mg2}	0.834	l_{mg3}	0.980
g_{ex1}	0.220	g_{ex2}	0.215
g_{sg1}	0.210	g_{sg2}	0.100
l_{sg1}	2.225	l_{sg2}	1.261

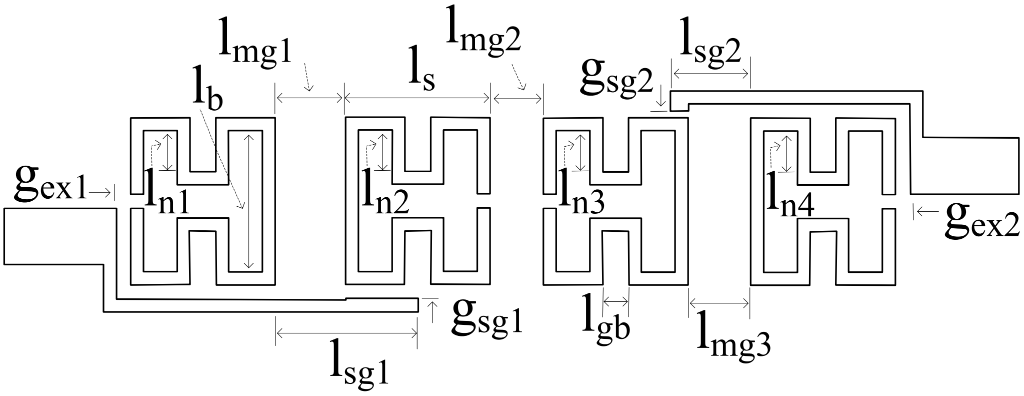

Figure 5.9: Layout of the 4th order bandpass filter with two transmission zeros in the higher stopband.

Fig. 5.10 compares the prototype response with the simulated response obtained from *EM* simulation using an adaptive mesh with about 90000 tetrahedral elements and the simulated response is in good agreement with the prototype response. The minimum passband insertion loss and maximum passband return loss of the simulated response are 2.77 dB and 19.8 dB, respectively while the intended transmission zeros at a finite frequencies are located at 11.05 GHz and

11.19 GHz in the upper stopband with at least -71.9 dB attenuation over a 0.2 GHz frequency band. Conductor loss and radiation loss are mainly responsible in passband loss. Due to an unintended resonance or cross coupling in the simulating structure, there is an additional unintended transmission zero in the upper stopband located at 12.39 GHz, as well.

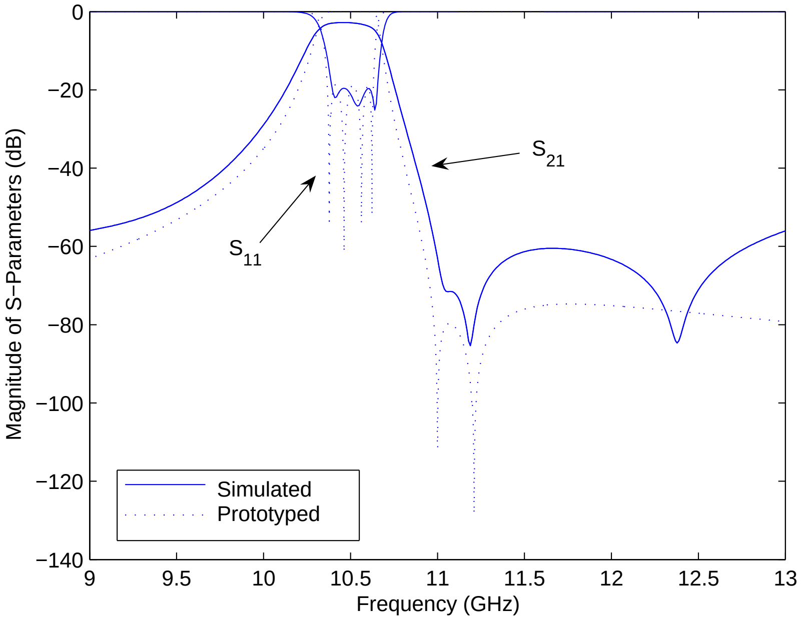

Figure 5.10: Responses of the fourth order bandpass filter with two transmission zeros in upper stopband.

5.3.2 Transmission Zeros in Lower Stopband

The second order filter with one transmission zero in the lower stopband in the previous chapter is cascaded with another similar network to form a forth order filter with two transmission zeros in the lower stopband. The transmission zeros are located at $\omega' = -2.38$ and $\omega' = -3.3$ in the prototyped response. The return loss of the filter response is 15.5 dB. The source and load are coupled to the non-adjacent resonator as realized for the second order filter in the previous chapter to implement the transmission zeros. The first and second, and third and fourth resonant nodes are negatively coupled while second and third resonant nodes are positively coupled. To accommodate the above implementation, a coupling matrix similar to the one in Equation 5.20 is enforced. The initial guess for the optimization is set as, m_{S1} $=m_{L4}$ =-1, m_{S2}=-0.1, m_{11} $=m_{22}$ $=m_{33}$ $=m_{44}$= 0, m_{12} $=m_{34}$ =-0.5, m_{23} =0.5 and m_{L3} =-0.05. The order of the second term in the error function, α, is selected to be 1 for fast convergence by increasing the weight of the second term in the error function. The optimization converged after 1317 iterations yielding the following coupling matrix,

$$[M] = \begin{pmatrix} 0 & -0.8737 & -0.3365 & 0 & 0 & 0 \\ -0.8737 & 0.5210 & -0.7028 & 0 & 0 & 0 \\ -0.3365 & 0.7028 & -0.2782 & 0.6697 & 0 & 0 \\ 0 & 0 & 0.6697 & -0.2281 & -0.7617 & -0.2380 \\ 0 & 0 & 0 & -0.7617 & 0.3612 & -0.9050 \\ 0 & 0 & 0 & -0.2380 & -0.9050 & 0 \end{pmatrix}. \tag{5.22}$$

For this filter also, magnitude responses of S-parameters are independent of the sign of coupling coefficient, m_{23}. The response is realized using mixed coupling in the intended implementation. In the previous section, it was mentioned that the transmission zero of the second order network can be shifted into the other side of the passband by changing the signs of x_4, x_5 and x_6. Similarly, the observation of coupling matrices in Equations 5.21 and 5.22 suggests that transmission zeros of these fourth order networks can also be shifted into the other side of the passband by changing signs of variables m_{11}, m_{22}, m_{12}, m_{33}, m_{44} and m_{34} in Equation 5.20.

The fourth order bandpass filter with transmission zeros in the lower stopband at 11 GHz and 11.21 GHz and a fractional bandwidth of 3.0 percent centered at 11.4 GHz is designed using the coupling matrix in Equation 5.22. The filter is implemented using LIGA microstrip folded open loop resonators. The required resonant frequencies of the first, second, third, and fourth resonators evaluated from Equation 5.18 are 11.311 GHz, 11.448 GHz, 11.439 GHz, 11.338 GHz, respectively. Inter-resonator couplings evaluated using Equation 5.17 are M_{12}= -0.0211, M_{23}=

0.020, M_{34}= -0.0228. External quality factors of source/load multi-resonator couplings found from Equation 5.19 are Q_{S1}= 43.66, Q_{S2}= 294.39, Q_{L3}= 588.46, Q_{L4}= 40.70.

External quality factors of source/load coupling with adjacent resonators for this filter are implemented as illustrated in Fig. 5.11. The short arm with a length of l_{in}, used to realize the external coupling in the second order filters in the previous chapter is not present in the coupling structure in Fig. 5.11. Dimensions of the coupling structure, on a 0.5 mm thick fuzed quartz substrate are l_s= 2.15 mm, l_b= 2.04 mm, and a 0.2 mm wide resonator opening. The conductor width and height of resonators are 0.2 mm and 0.22 mm, respectively. Fig. 5.12 shows relationships of the independent variable, g_{ex} and dependent variable l_n with external quality factors at resonant frequencies of 11.311 GHz and 11.338 GHz.

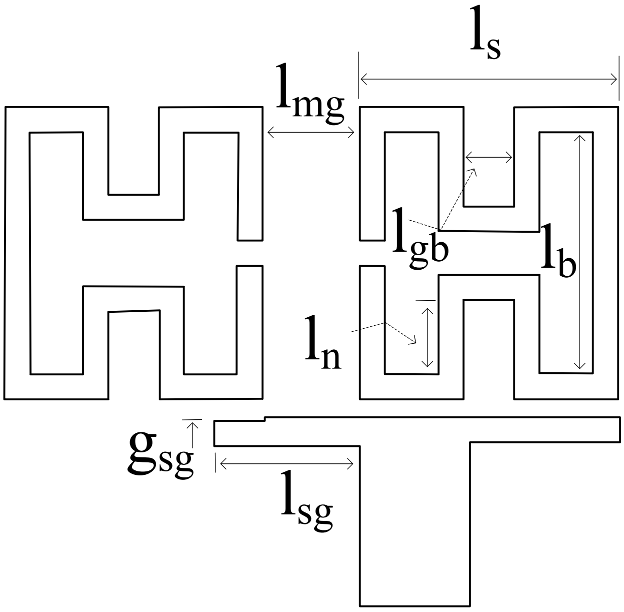

Figure 5.11: Structure for source/load coupling with adjacent resonators for filters with transmission zeros in lower stopband.

The lengths, g_{ex} and l_n, of the external coupling structures of this filter are extracted from the above graphs. g_{ex} and l_n of the first resonator are 0.189 mm and 0.49 mm respectively. g_{ex} and l_n of the fourth resonator are 0.18 mm and

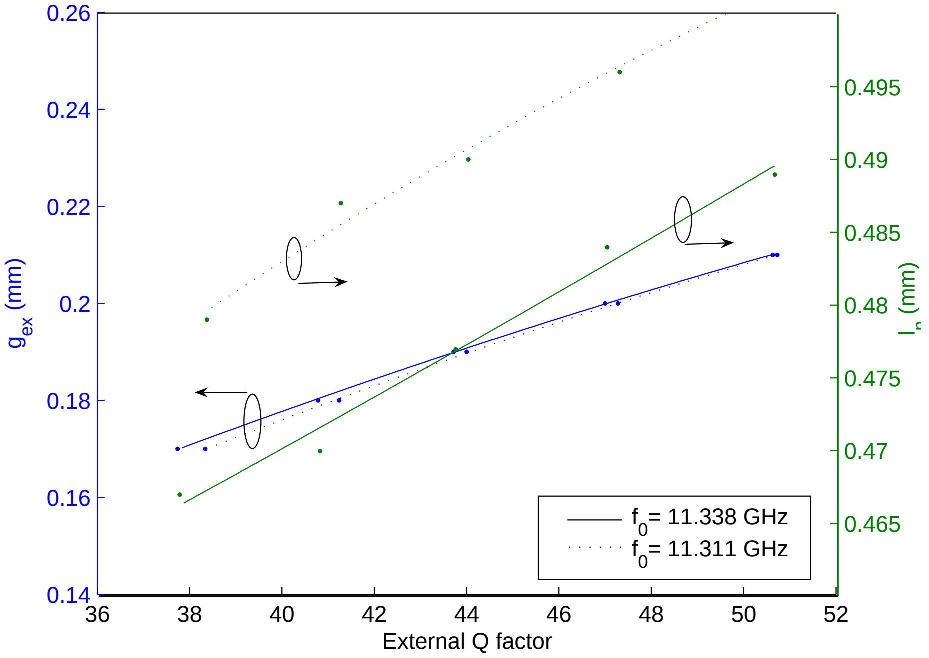

Figure 5.12: Variation of external quality factor with independent variable g_{ex} and dependant variable l_n. Solid lines correspond to the resonant frequency of 11.338 GHz and dotted curves correspond to the resonant frequency of 11.311 GHz.

0.471 mm respectively. l_n of the second and third resonators, extracted from *EM* simulations, are 0.504 mm and 0.507 mm respectively.

The negative coupling required between the first and second resonators and the third and fourth resonators are implemented as in the previous instances. The solid curve in Fig. 5.13 demonstrates coupling characteristics of the first and second resonator. The coupling characteristics of the third and fourth resonators are also approximately equal to that of the first and second resonators. The required coupling gaps of the first and second resonators and the third and fourth resonators extracted from the above graph are 0.843 mm and 0.808 mm respectively. The coupling between the second and third resonators is to be implemented from the mixed coupling orientation as illustrated in Fig. 5.14. The dotted curve in Fig. 5.13 shows the characteristics of mixed coupling. The gap between these resonators extracted from the dotted curve is 0.994 mm.

To implement source/load bypass coupling with nonadjacent resonators, the

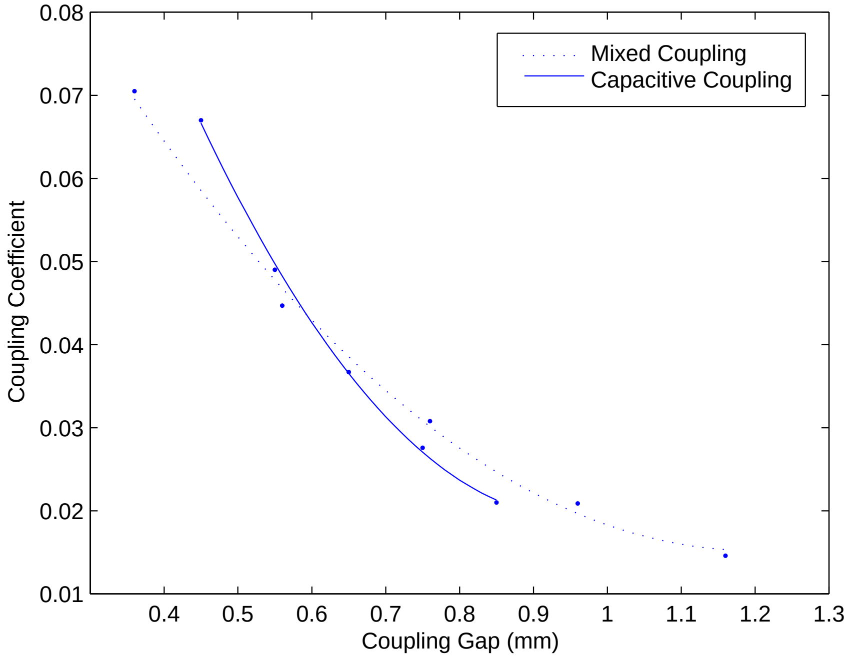

Figure 5.13: Variation of coupling coefficient with coupling gap. The solid curve corresponds to capacitive coupling while the dotted line corresponds to mixed coupling.

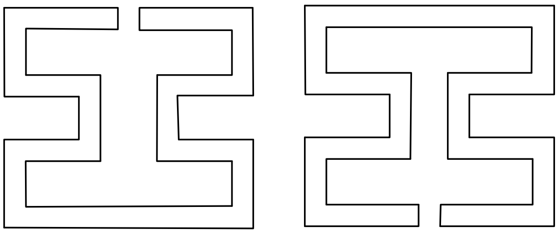

Figure 5.14: Mixed coupling.

narrow arms whose one end connected to the source and load, are extended towards the second and third resonators as indicated in Fig. 5.11. The length of extension of the narrow arm up to the second resonator is 1.15 mm. The bypass coupling gaps of coupling arms with the second resonator and the third resonator are 0.184 mm and 0.298 mm respectively.

A microstrip structure for the above fourth order bandpass filter with two transmission zeros in the lower stopband was designed, using parameters extracted above, on a 0.5 mm thick fuzed quartz substrate as shown in Fig. 5.16. Bypass

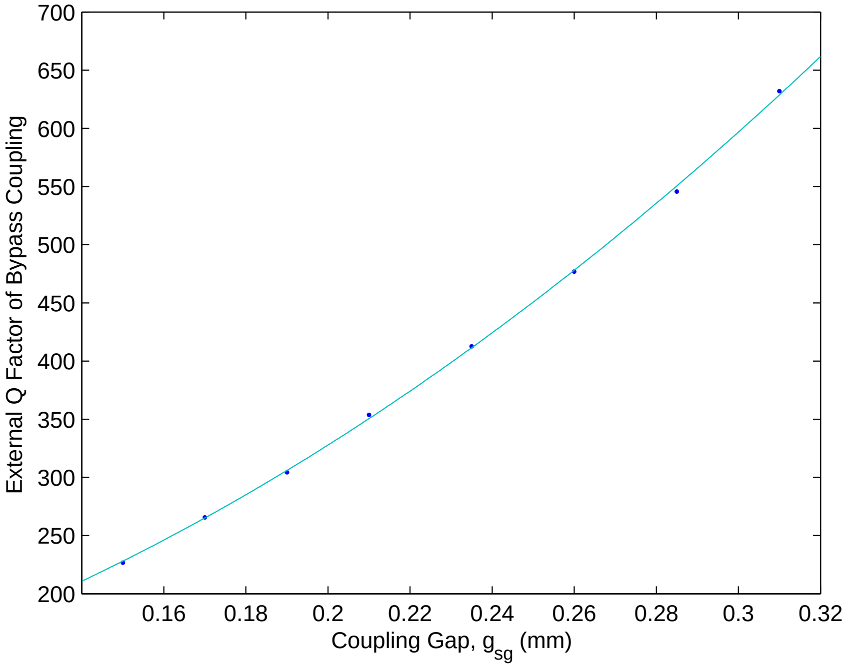

Figure 5.15: External Q factor of source/load bypass coupling with the second resonator of the 4th order filter with two transmission zeros in the lower stopband.

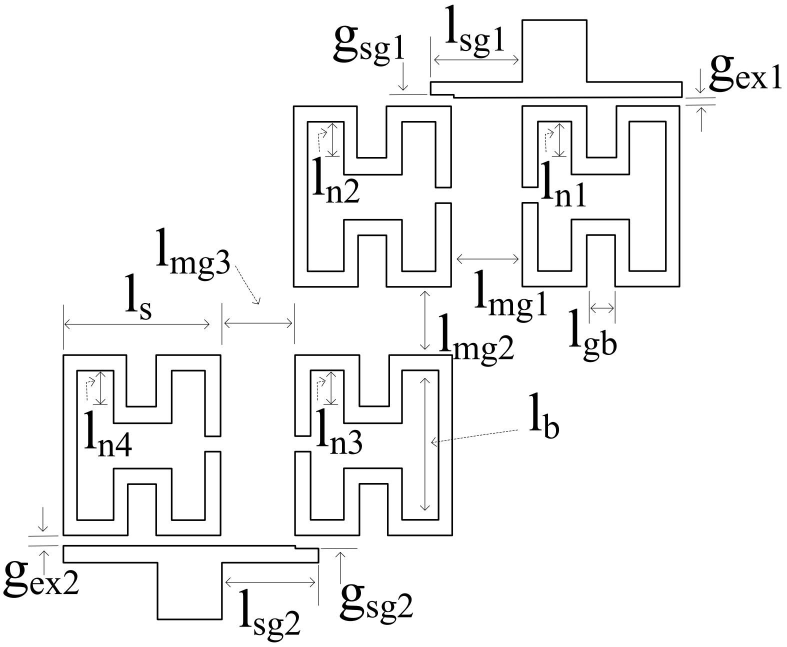

Figure 5.16: Layout of the 4th order bandpass filter with two transmission zeros in the lower stopband.

couplings, namely M_{S2} and M_{L3}, are realized using coupling arms extended up to the second and third resonators. The structure was analyzed and optimized from *HFSS EM* simulation. Copper was selected as the material of the structure. Conductor height was selected to be 0.22 mm to reduce conductor losses. The width of 50Ω lines are 0.875 mm. The width of resonator openings is 0.22 mm. The lengths of bypass coupling arms (l_{sg1} and l_{sg2}) are selected such that moderate coupling gaps (g_{sg1} and g_{sg2}) are required. The other dimensions of the fourth order filter with two transmission zeros in lower stopband and a fractional bandwidth of 3.00 percent centred at 11.4 GHz are given in Table 5.2.

Table 5.2: Dimensions of the filter in Fig. 5.16.

Variable	Dimension (mm)	Variable	Dimension (mm)
l_s	2.150	l_b	2.040
l_{gb}	0.400	l_{n1}	0.510
l_{n2}	0.505	l_{n3}	0.509
l_{n4}	0.508	l_{mg1}	0.952
l_{mg2}	0.125	l_{mg3}	0.980
g_{ex1}	0.160	g_{ex2}	0.153
g_{sg1}	0.165	g_{sg2}	0.180
l_{sg1}	1.259	l_{sg2}	1.287

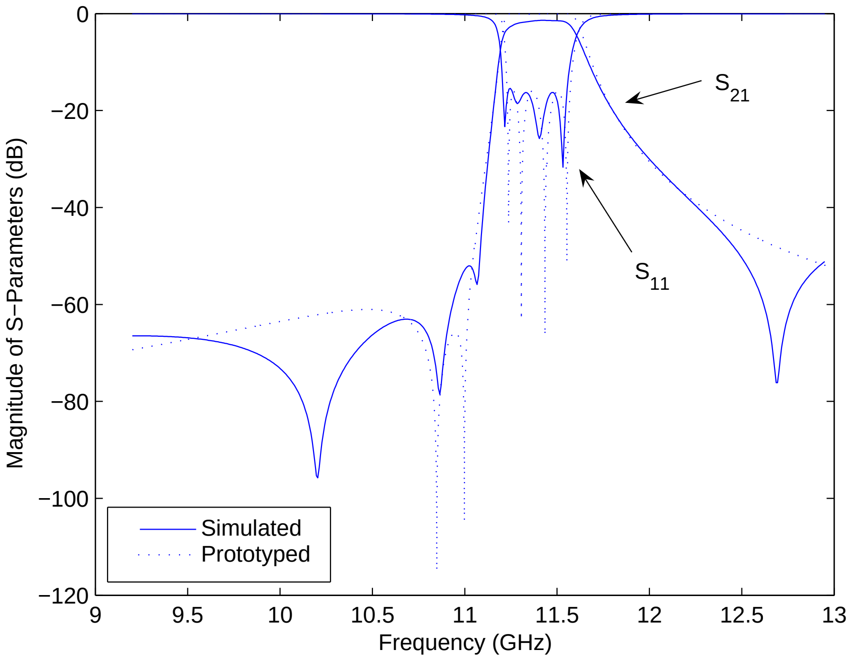

Figure 5.17: Responses of the fourth order bandpass filter with two transmission zeros in lower stopband.

Fig. 5.17 compares the prototype response with the simulated response obtained from *EM* simulation using an adaptive mesh with about 90000 tetrahedral elements and the simulated response is in good agreement with the prototype response. The minimum passband insertion loss and maximum passband return loss of the simulated response are 1.39 dB and 15.5 dB, respectively while the intended transmission zeros at a finite frequencies are located at 11.07 GHz and 10.87 GHz in the lower stopband with at least -52.1 dB attenuation below 11.08 GHz frequency range, supported by an additional unintended transmission zero, in the vicinity of the intended transmission zero. There is an additional unintended transmission zero in the upper stopband as well. Passband loss of this filter is less than the passband loss of the fourth order filter with transmission zeros in the upper stopband given in the previous section due mainly to the different metals in the structures.

5.4 Third Order Filter with Two Transmission Zeros in Both Sides of Passband

The previous sections presented filters with $n-2$ transmission zeros. This section presents a filter with $n-1$ tramsmission zeros. A third order bandpass filter network that creates two transmission zeros in both lower and upper stopbands is described. Both source and load are coupled to the middle resonant node to create bypass coupling paths that produces two transmission zeros. The transmission zeros of the prototyped response are located at $\omega' = -3.925$ and $\omega' = 3.7$. It is interesting to note that transmission zeros are located asymmetrically in both sides of the passband. The proposed filter network has the capability to place them symmetrically in both sides of the passband should necessity arise. The return loss of the filter response is 18 dB. The source and load are coupled to the non-adjacent resonant node as realized in previous sections. The first and second resonant nodes are positively coupled while second and third resonant nodes are negatively coupled. To accommodate the above implementation, the following coupling matrix is obtained:

$$[M] = \begin{pmatrix} 0 & -0.9903 & -0.2724 & 0 & 0 \\ -0.9903 & -0.4931 & 0.8957 & 0 & 0 \\ -0.2724 & 0.8957 & 0.0150 & -0.9062 & -0.2636 \\ 0 & 0 & -0.9062 & 0.4802 & -0.9926 \\ 0 & 0 & -0.2636 & -0.9926 & 0 \end{pmatrix}. \quad (5.23)$$

In this filter, the couplings between the source, the first resonant node and the second resonant node are similar to the coupling paths that created transmission zeros in higher stopbands in previous filters. The couplings between the load, the third resonant node and the second resonant node are similar to the coupling paths that created transmission zeros in lower stopbands in previous filters.

A third order bandpass filter with a fractional bandwidth of 3.0 percent centred at 10.5 GHz is designed using the coupling matrix in Equation 5.23. Transmission zeros are located in the upper stopband at 11.1 GHz and in the lower stopband at 9.9 GHz. The filter is implemented using LIGA microstrip folded open loop resonators. The required resonant frequencies of the first, second and third resonators are 10.578 GHz, 10.498 GHz and 10.423 GHz, respectively. Inter-resonator couplings evaluated using Equation 5.17 are M_{12}= 0.0269 and M_{23}= -0.0272. External quality factors of source/load multi-resonator couplings are found from Equation 5.19 and they are Q_{S1}= 33.99, Q_{S2}= 449.22, Q_{L3}= 479.71, Q_{L4}= 33.83.

External quality factor of the first resonator for this filter is implemented as in previous filters with transmission zeros in the upper stopband and as illustrated in Fig. 5.4. The dimensions of the coupling structure, on a 0.5 mm thick fuzed quartz substrate are l_s= 2.25 mm, l_b= 2.2 mm, l_{gb}= 0.4 mm, and 0.2 mm wide resonator opening. The conductor width and height of resonators are 0.2 mm and 0.22 mm, respectively. The required coupling gap, g_{ex}, evaluated from *EM* simulation, is

0.31 mm while l_n is 0.649 mm. External quality factor of the third resonator for this filter is implemented as in previous filters with transmission zeros in the lower stopband and as illustrated in Fig. 5.11. The required g_{ex} and l_n found again from *EM* simulations are 0.337 mm and 0.635 mm respectively while the other dimensions are same as those of the first resonator. l_n of the second resonator to resonate at 10.498 GHz is 0.565 mm. The first and second resonators are oriented similar to the resonator orientation used for implementing the filters with transmission zeros in higher stopband. A 1.17 mm wide inductive coupling gap is necessary to obtained the coupling coefficient of 0.0269. The negative coupling between the second and the third resonators are realized from a similar resonator orientation used for implementing filters with a transmission zeros in the lower stopband and the negative coupling gap is found to be 0.575 mm. The bypass coupling of the first port with the second resonator is implemented extending the coupling arm connected to the first port up to the second resonator by a length of l_{sg}= 1.735 mm as shown in Fig. 5.7. The required coupling gap is 0.11 mm. To implement bypass coupling of the second port with the second resonator, a narrow arm whose one end is connected to the second port, is extended towards the second resonator, as indicated in Fig. 5.11. The length of extension of the narrow arm up to the second resonator is 1.545 mm. The bypass coupling gap of coupling arm connected to the second port with the second resonator is 0.187 mm.

A microstrip structure for the above third order bandpass filter with two transmission zeros in both upper and lower stopband was designed, using parameters given above, on a 0.5 mm thick fused quartz substrate as shown in Fig. 5.18. Bypass couplings, namely M_{S2} and M_{L2}, are realized using coupling arms extended up to the second resonator. The structure was analyzed and optimized from *HFSS EM* simulation. Nickel conductor height was selected to be 0.2 mm to reduce conductor losses. The width of 50Ω lines is 0.875 mm. The width of resonator openings is 0.22 mm. Dimensions of the third order filter with two

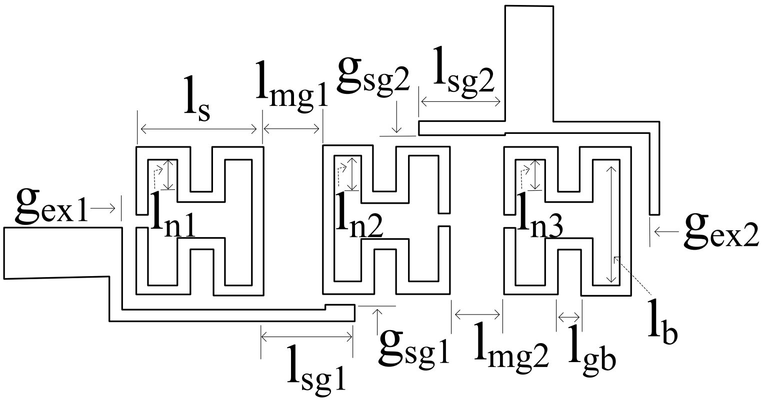

Figure 5.18: Layout of the 3rd order bandpass filter with two transmission zeros in both upper and lower stopbands.

transmission zeros in both upper and lower stopbands and a fractional bandwidth of 3.0 percent centred at 10.5 GHz are given in Table 5.3.

Table 5.3: Dimensions of the filter in Fig. 5.18.

Variable	Dimension (mm)	Variable	Dimension (mm)
l_s	2.260	l_b	2.200
l_{gb}	0.400	l_{n1}	0.612
l_{n2}	0.575	l_{n3}	0.587
l_{mg1}	1.040	l_{mg2}	0.980
g_{ex1}	0.270	g_{ex2}	0.270
g_{sg1}	0.130	g_{sg2}	0.210
l_{sg1}	1.605	l_{sg2}	1.545

Fig. 5.19 compares the prototype response with the simulated response obtained from *EM* simulation using an adaptive mesh with about 90000 tetrahedral elements and the simulated response is in good agreement with the prototype response. The minimum passband insertion loss and maximum passband return loss of the simulated response are 1 dB and 19 dB, respectively while the finite transmission zeros are located closely to the passband at 9.91 GHz and 11.08 GHz increasing stopband attenuation.

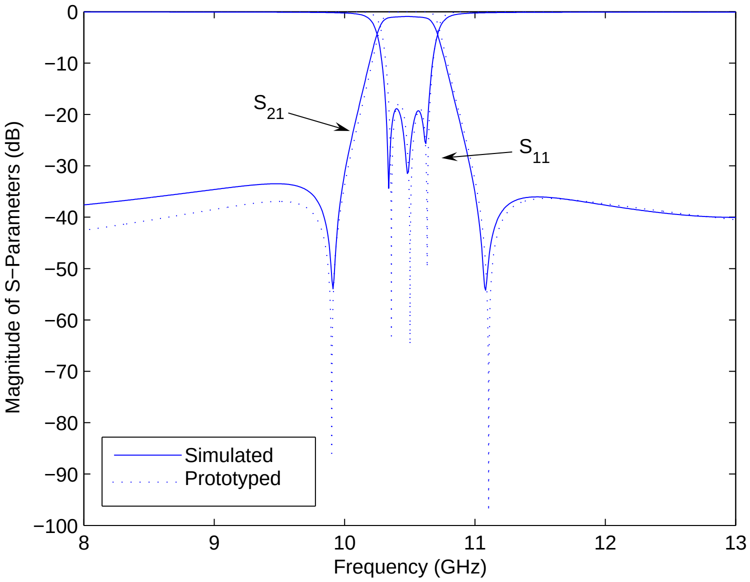

Figure 5.19: Responses of the third order bandpass filter with two transmission zeros in lower and upper stopbands.

5.5 Third Order Filters with Two Transmission Zeros in One Side of Passband

5.5.1 Transmission Zeros in Upper Stopband

Fourth order filter networks that create two transmission zeros $(n-2)$ in one side of the passband and a third order filter network that creates two transmission zeros $(n-1)$ in both sides of the passband were appended in previous sections. A third order filter network that creates two transmission zeros $(n-1)$ in the upper stopband is elaborated in this section. The resonator orientation of the filter given in this section will be different from the previous filters. Both source and load are coupled to the middle resonant node to create bypass coupling paths that produces two transmission zeros. The transmission zeros of the prototyped response are located at $\omega' = 3.19$ and $\omega' = 4.778$. The return loss of the filter response is 20 dB. The first and second resonant nodes are positively coupled while second and third resonant nodes are also positively coupled. Bypass couplings of source and load to the middle resonant node are negative. To accommodate the above implementation, the following coupling matrix is formed from the gradient based optimization (with $\alpha = 1$,converged after 8604 iterations):

$$[M] = \begin{pmatrix} 0 & -1.0318 & -0.3560 & 0 & 0 \\ -1.0318 & -0.5238 & 0.9220 & 0 & 0 \\ -0.3560 & 0.9220 & 0.5510 & 0.9996 & -0.2400 \\ 0 & 0 & 0.9996 & -0.3112 & -1.0653 \\ 0 & 0 & -0.2400 & -1.0653 & 0 \end{pmatrix}. \tag{5.24}$$

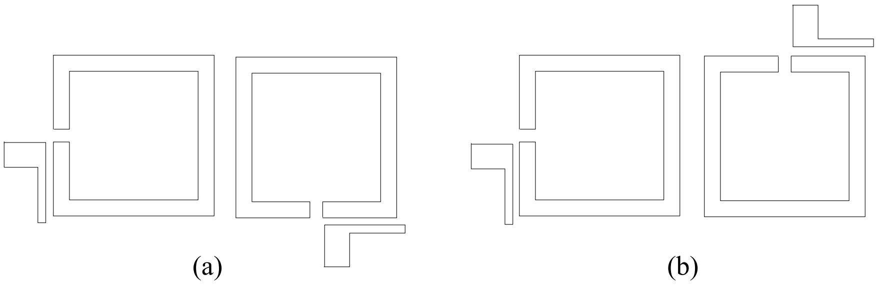

Figure 5.20: Different coupling configurations of half wavelength open loop resonators.

Inter resonator coupling is implemented differently from the previous implementations. Fig. 5.20 illustrates two different open loop resonator coupling methods. Their phase and magnitude responses are given in Fig. 5.21. The phase responses of these two configurations take the opposite signs. The phase response of the structure in Fig. 5.20 (a) has same shape as that of the magnetically coupled structure in Fig. 4.3 (c). Hence, the resonator configuration in Fig. 5.20 (a) can be used to implement positive coupling since the configuration in 4.3 (c) was used to implement positive coupling in a coupling matrix. The phase response of the structure in Fig. 5.20 (b) has same shape as that of the capacitively coupled structure in Fig. 4.3 (a). Hence, the resonator configuration in Fig. 5.20 (b) can be used to implement negative couplings in a coupling matrix.

A third order bandpass filter with a fractional bandwidth of 2.5 percent centred at 10.57 GHz is designed using the coupling matrix in Equation 5.24. Transmission

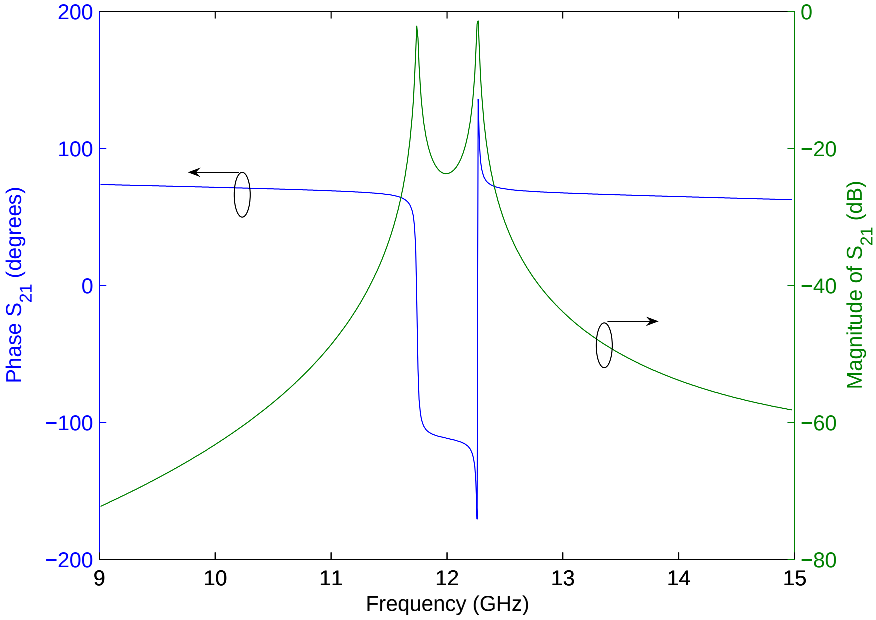

(a)

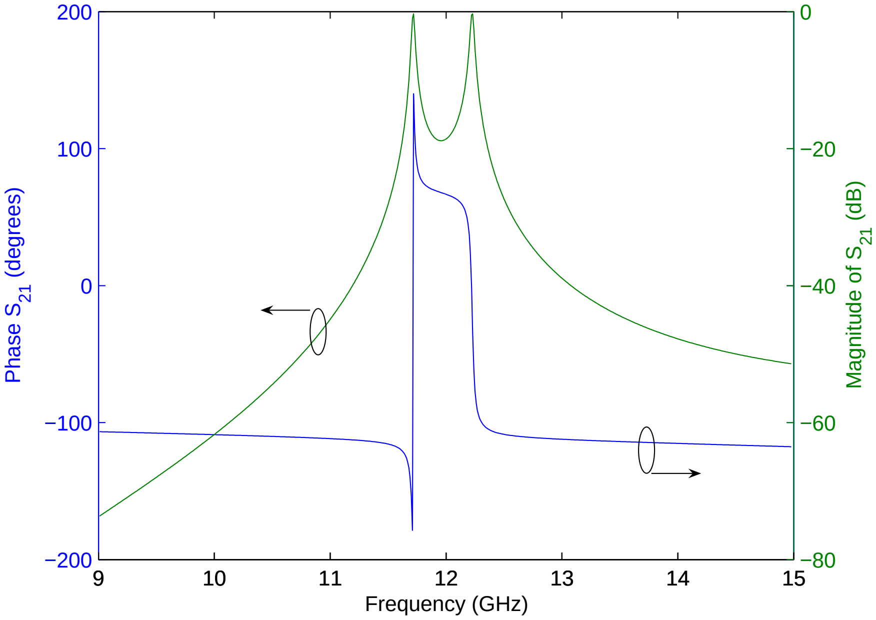

(b)

Figure 5.21: (a) Typical resonance responses of the configuration in Fig. 5.20(a), (b) typical resonance responses of the configuration in Fig. 5.20(b).

zeros are located in the upper stopband at 11.0 GHz and 11.22 GHz. The filter is implemented using high aspect ratio microstrip folded open loop resonators. The required resonant frequencies of the first, second and third resonators are 10.639

GHz, 10.497 GHz and 10.611 GHz, respectively. Inter-resonator couplings evaluated using Equation 5.17 are M_{12}= 0.0230 and M_{23}= 0.0250. External quality factors of source/ load multi-resonator couplings are found from Equation 5.19 and they are Q_{S1}= 37.57, Q_{S2}= 315.61, Q_{L3}= 694.42, Q_{L4}= 35.24.

External quality factor of the first resonator for this filter is implemented as in previous filters with transmission zeros in the upper stopband and as illustrated in Fig. 5.4. The dimensions of the coupling structure, on a 0.5 mm thick fused quartz substrate are l_s= 2.23 mm, l_b= 2.22 mm, l_{gb}= 0.4 mm, and 0.2 mm wide resonator opening. The conductor width and height of the resonators are 0.2 mm and 0.22 mm, respectively. The required coupling gap of the first resonator, g_{ex}, evaluated from *EM* simulation, is 0.359 mm while l_n is 0.526 mm. The external quality factor of the third resonator for this filter is also implemented as for the first resonator. Required g_{ex} and l_n are found again from *EM* simulations as 0.346 mm and 0.524 mm respectively while the other dimensions are the same as those of the first resonator. l_n of the second resonator, extracted from *EM* simulations, is 0.62 mm.

The positive couplings required between the first and second resonators and the second and third resonators are implemented using a coupled resonator configuration similar to Fig. 5.20 (a). Fig. 5.22 demonstrates coupling characteristics of the first and second resonator. The required coupling gaps of the first and second resonators and the second and third resonators are 0.802 mm and 0.750 mm respectively.

To implement source/load bypass coupling with nonadjacent resonators, narrow arms with one end connected to the source and load, are extended towards the second resonator, as indicated in Fig. 5.23. The length of the extension of the narrow arm up to the second resonator to realize M_{S2} is 1.36 mm while the length of extension of the narrow arm up to the second resonator to realize M_{L2} is 0.909 mm. Source/load bypass coupling characteristics are shown in Fig. 5.24. The dotted curve in Fig. 5.24 gives external quality factor of the second resonator

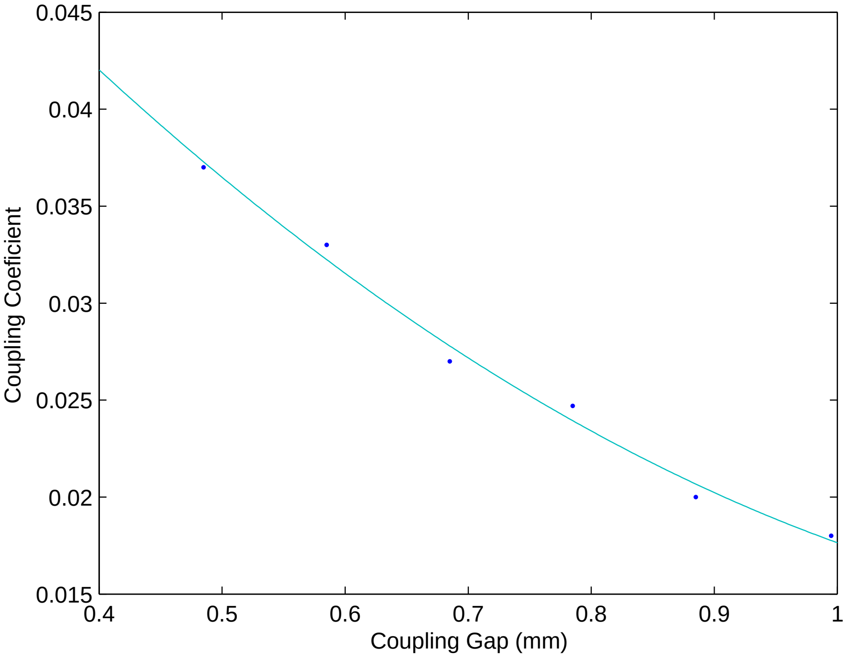

Figure 5.22: Variation of coupling coefficient with coupling gap of the first and second resonators coupled as in Fig. 5.20 (a).

with the bypass coupling arm with $l_{sg} = 0.909$ mm. The solid curve illustrates the variation of the external quality factor with g_{sg} for a bypass coupling arm with $l_{sg} = 1.36$ mm. The required coupling gaps for realizing M_{S2} and M_{L2} are 0.409 mm and 0.405 mm respectively.

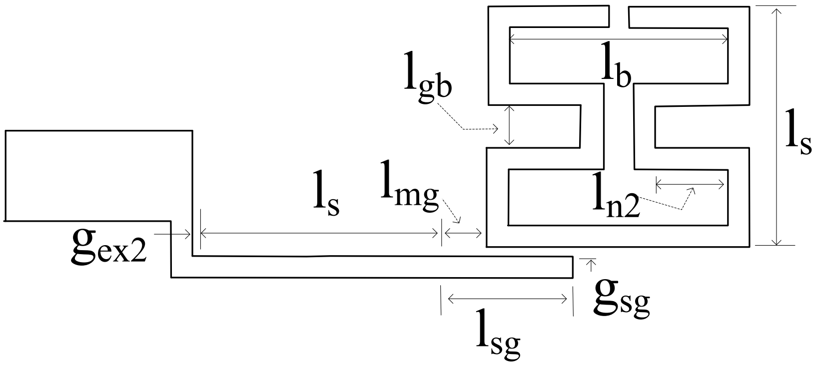

Figure 5.23: Bypass coupling structure of the 3rd order filter with two transmission zeros in the upper stopband.

A microstrip structure for the above third order bandpass filter with two transmission zeros in the upper stopband was designed, using parameters extracted

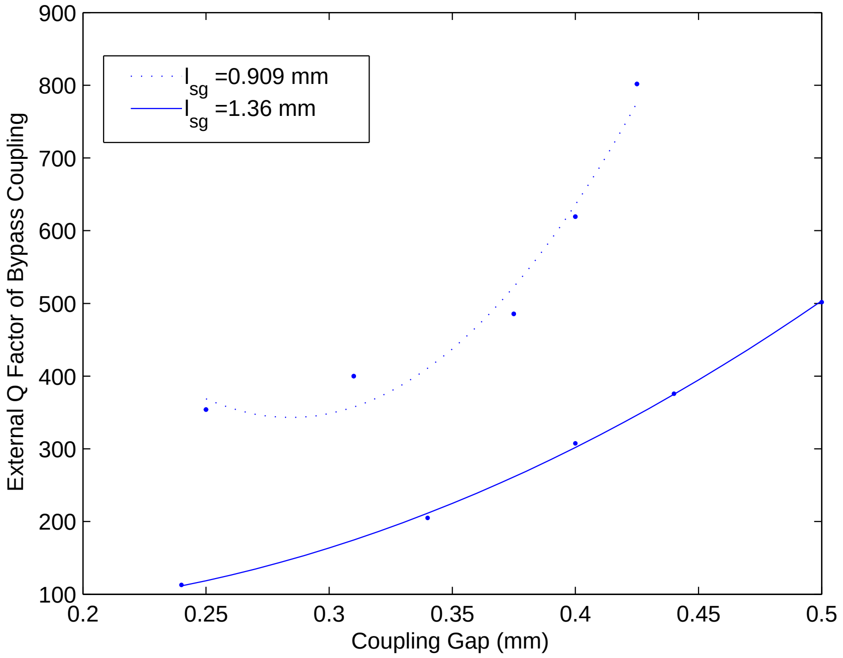

Figure 5.24: External Q factor of source/load bypass coupling with the second resonator of the 3$^{\text{rd}}$ order filter with two transmission zeros in the higher stopband.

above, on a 0.5 mm thick fused quartz substrate as shown in Fig. 5.25. Bypass couplings, namely M_{S2} and M_{L2}, are realized using coupling arms extended up to the second resonator. The structure was analyzed and optimized from *HFSS EM* simulation, assuming lossless conditions. Conductor height is 0.22 mm. The width of 50Ω lines are 0.875 mm. Dimensions of the third order filter with two transmission zeros in upper stopband and a fractional bandwidth of 2.5 percent centred at 10.57 GHz are given in Table 5.4.

Table 5.4: Dimensions of the filter in Fig. 5.25.

Variable	Dimension (mm)	Variable	Dimension (mm)
l_s	2.230	l_b	2.220
l_{gb}	0.400	l_{n1}	0.600
l_{n2}	0.637	l_{n3}	0.604
l_{mg1}	0.690	l_{mg2}	0.660
g_{ex1}	0.350	g_{ex2}	0.360
g_{sg1}	0.240	g_{sg2}	0.540
l_{sg1}	1.247	l_{sg2}	0.819

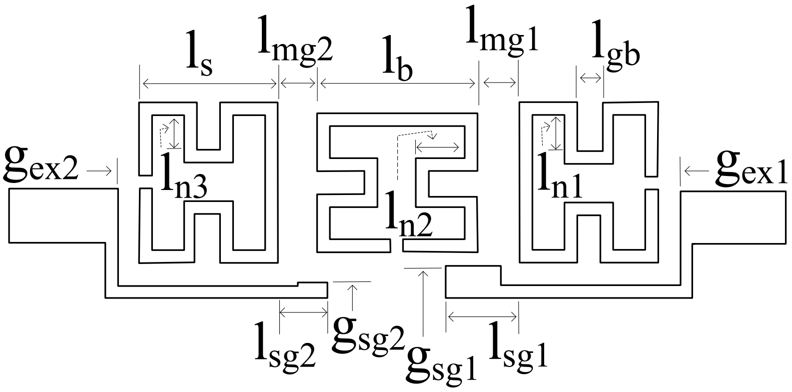

Figure 5.25: Layout of the 3rd order bandpass filter with two transmission zeros in the upper stopbands.

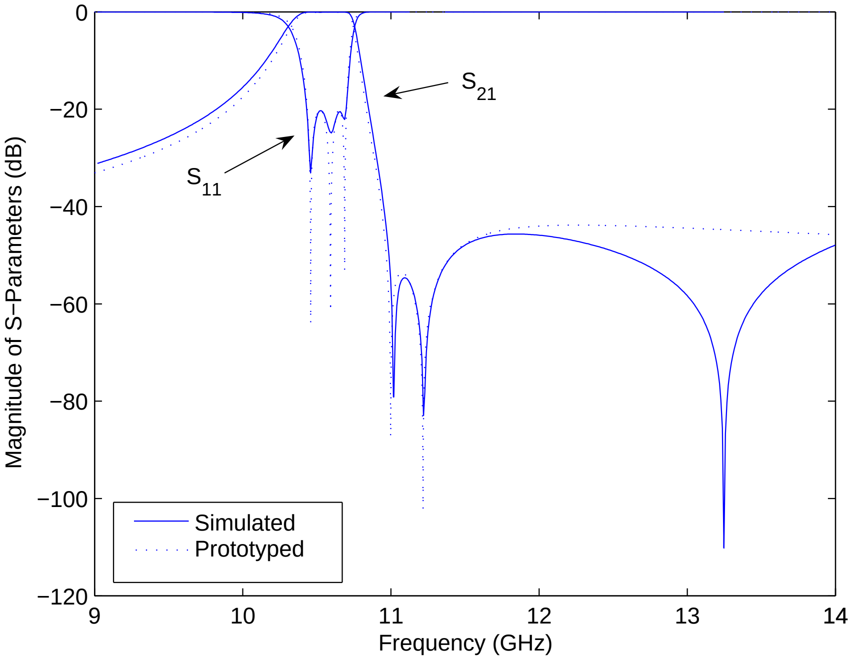

Figure 5.26: Responses of the third order bandpass filter with two transmission zeros in upper stopband.

Fig. 5.26 compares the prototype response with the simulated response of the above filter assuming lossless conditions, obtained from *EM* simulation using an adaptive mesh with about 90000 tetrahedral elements and the simulated response is in good agreement with the prototype response. The maximum passband return loss of the simulated response is 20.03 dB, while the intended transmission zeros at a finite frequencies are located at 11.02 GHz and 11.22 GHz in the upper stopband with at least -54.7 dB attenuation over 0.3 GHz frequency range. There is an additional unintended transmission zero in the upper stopband as well.

5.5.2 Transmission Zeros in Lower Stopband

A third order filter network that creates two transmission zeros $(n-1)$ in the lower stopband is described in this section. It is characterized by a coupling matrix with similar sparsity to that of the above filter but with different coupling signs. The transmission zeros of the prototyped response of this network are located at $\omega' = 3.19$ and $\omega' = 4.778$. The return loss of the filter response is 20 dB. The first and second resonant nodes are negatively coupled while second and third resonant nodes are also negatively coupled. Bypass couplings of source and load to the middle resonant node are negative. The following coupling matrix is obtained (the optimization with $\alpha = 1$, converged after 11416 iterations).

$$[M] = \begin{pmatrix} 0 & -1.0028 & -0.5141 & 0 & 0 \\ -1.0028 & 0.7373 & -0.8238 & 0 & 0 \\ 0.5141 & -0.8238 & -0.7474 & -1.0190 & -0.3000 \\ 0 & 0 & -1.0190 & -0.3112 & -1.0653 \\ 0 & 0 & -0.3000 & -1.0871 & 0 \end{pmatrix} \tag{5.25}$$

A third order bandpass filter with a fractional bandwidth of 2.75 percent centered at 11.15 GHz is designed using the coupling matrix in Equation 5.25. Transmission zeros are located in the lower stopband at 10.55 GHz and 10.8 GHz. The filter is implemented using high aspect ratio microstrip folded open loop resonators. The required resonant frequencies of the first, second and third resonators are 11.04 GHz, 11.264 GHz and 11.095 GHz, respectively. Inter-resonator couplings are M_{12}= -0.0220 and M_{23}= -0.0280. External quality factors of source/load multi-resonator couplings are Q_{S1}= 36.429, Q_{S2}= 138.58, Q_{L3}= 406.97, Q_{L4}= 30.99.

The external quality factor of the first resonator for this filter is realized as in the previous filter with transmission zeros in the upper stopband. The dimensions of the coupling structure, on a 0.5 mm thick fuzed quartz substrate are l_s= 2.15 mm, l_b= 2.13 mm, l_{gb}= 0.4 mm, and 0.2 mm wide resonator opening. The conductor width and height of the resonators are 0.2 mm and 0.22 mm, respectively. The required coupling gap of the first resonator, g_{ex}, is 0.337 mm while l_n is 0.568 mm. The external quality factor of the third resonator for this filter is also implemented as for the first resonator. The required g_{ex} and l_n are 0.326 mm and 0.545 mm respectively while the other dimensions are the same as those of the first resonator. l_n of the second resonator is 0.495 mm.

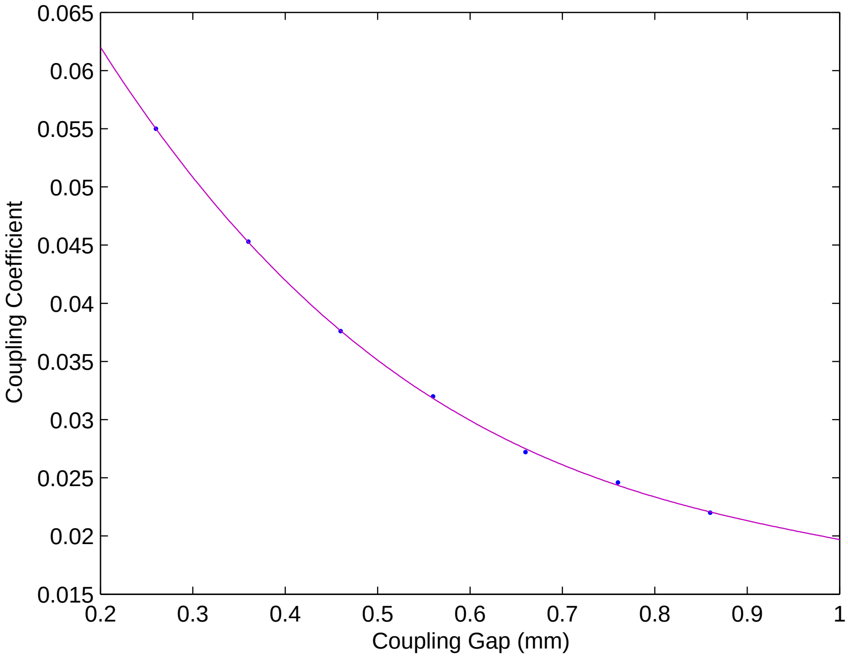

Figure 5.27: Variation of coupling coefficient with coupling gap of the first and second resonators coupled as in Fig. 5.20 (b).

The negative couplings required between the first and second resonators and the second and third resonators are implemented using a coupled resonator configuration similar to Fig. 5.20 (b). Fig. 5.27 demonstrates coupling characteristics of the first and second resonator. The required coupling gaps of the first and second resonators and the second and third resonators are 0.839 mm and 0.666 mm respectively.

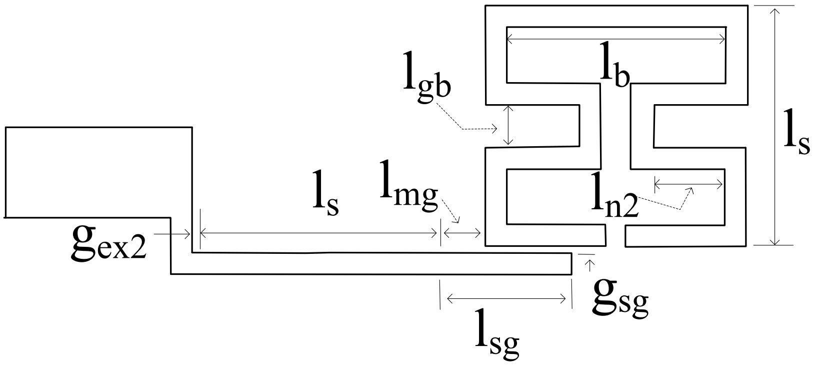

Figure 5.28: Bypass coupling structure of the 3rd order filter with two transmission zeros in the lower stopband.

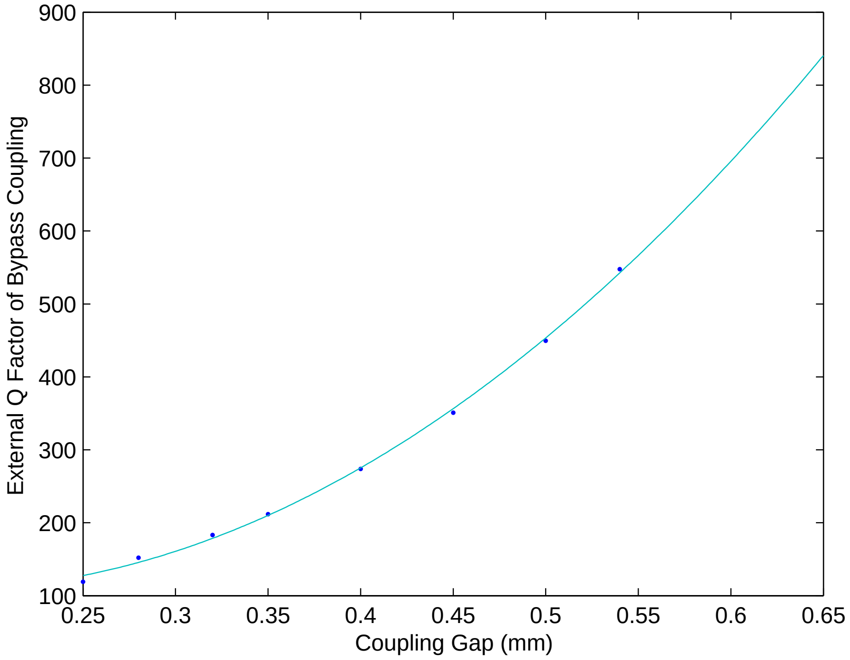

Figure 5.29: External Q factor of source/load bypass coupling with the second resonator of the 3rd order filter with two transmission zeros in the lower stopband.

Source/load bypass couplings with nonadjacent resonators are implemented by extending narrow arms that are used to realize external quality factors of the first and third resonators, towards the second resonator, as indicated in Fig. 5.28. The length of extension of the narrow arm up to the second resonator to realize M_{S2} (l_{sg}) is 1.3075 mm while the length of extension of the narrow arm up to the second resonator to realize M_{L2} is 1.3125 mm. However, lengths of the portions of narrow arms overlapped with the second resonator are the same. Fig. 5.29 illustrates the variation of external quality factor of the second resonator due to the bypass coupling, with the coupling gap between this arm and the second resonator. The required coupling gaps for realizing M_{S2} and M_{L2} are 0.272 mm and 0.485 mm respectively.

A microstrip structure for the above third order bandpass filter with two transmission zeros in the lower stopband was designed, using parameters extracted above, on a 0.5 mm thick fused quartz substrate as shown in Fig. 5.30. Bypass couplings, namely M_{S2} and M_{L2}, are realized using coupling arms extended up to the second resonator. The structure was analyzed and optimized from *HFSS EM* simulation. The width of 50Ω lines are 0.875 mm. The width of resonator openings is 0.2 mm. The dimensions of the third order filter with two transmission zeros in upper stopband and a fractional bandwidth of 2.75 percent centred at 11.15 GHz are given in Table 5.5.

Table 5.5: Dimensions of the filter in Fig. 5.30.

Variable	Dimension (mm)	Variable	Dimension (mm)
l_s	2.150	l_b	2.130
l_{gb}	0.400	l_{n1}	0.618
l_{n2}	0.525	l_{n3}	0.614
l_{mg1}	0.770	l_{mg2}	0.780
g_{ex1}	0.334	g_{ex2}	0.360
g_{sg1}	0.470	g_{sg2}	0.540
l_{sg1}	1.307	l_{sg2}	1.312

Fig. 5.31 compares the prototype response with the simulated response of the above filter assuming lossless conditions, obtained from *EM* simulation using an adaptive mesh with about 90000 tetrahedral elements and the simulated response is in good agreement with the prototype response. The maximum passband return loss of the simulated response is 19 dB, while the intended transmission zeros at a finite frequencies are located at 10.53 GHz and 10.78 GHz in the lower stopband with at least -41.9 dB attenuation over 0.5 GHz frequency range.

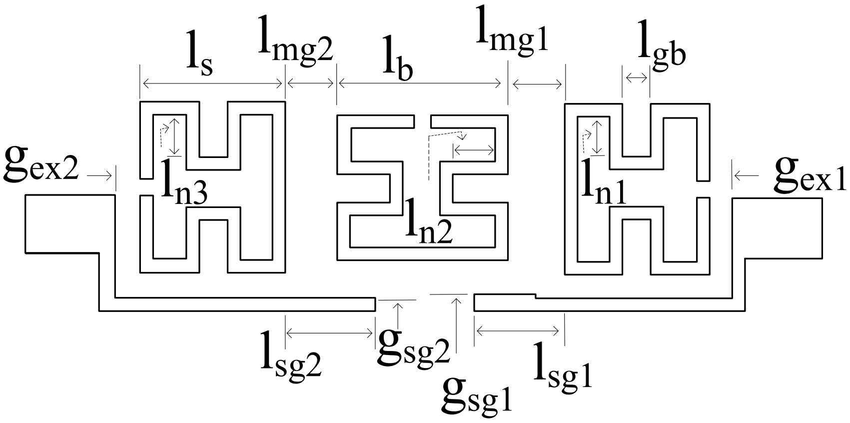

Figure 5.30: Layout of the 3rd order bandpass filter with two transmission zeros in the lower stopband.

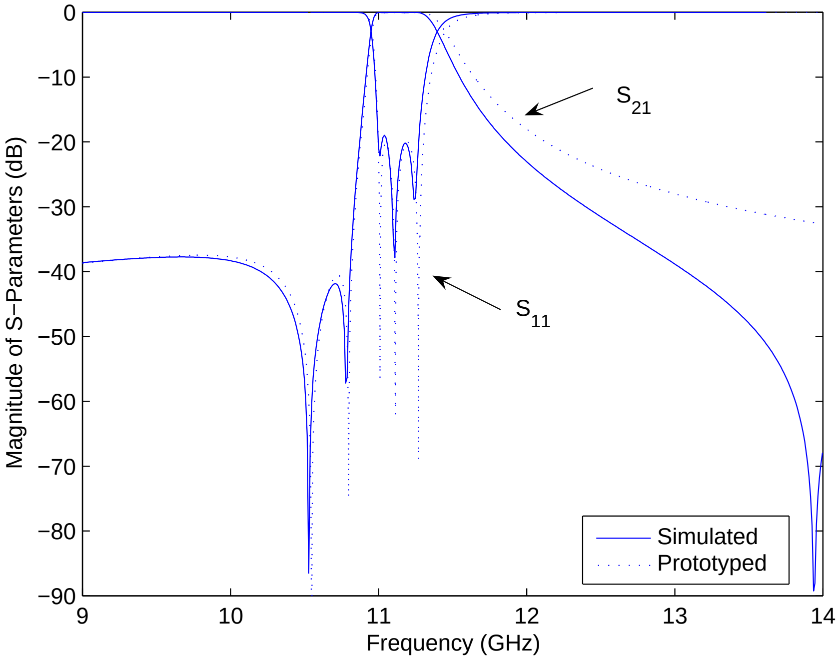

Figure 5.31: Responses of the third order bandpass filter with two transmission zeros in lower stopband.

Chapter 6

High Aspect Ratio Diplexers

6.1 Introduction

Modern wireless and mobile communication systems demand compact diplexers with low power loss and high port isolation. In the literature, there are several approaches in designing diplexers [9], [86]. The synthesis of diplexers classically starts from two port filters and a three port junction that are separately designed and combined in such a way as to maximize the performance.

Directional filters can be used to combine two port filters to form a diplexer [9]. The use of directional filters for multiplexing is a conceptually simple and elegant way of solving multiplexing problems, though by no means always the most practical way. The combining junction consumes larger space. For narrow band diplexers and multiplexers whose passbands are separated by guard bands, various relatively simple decoupling techniques are available [9]. One method is to connect channel filters using approximately quarter wavelength transmission lines [87], [88]. Another technique has been proposed by Cline et al. using decoupling resonators. This decoupling resonator located a quarter wavelength away from the adjacent filter short circuits the rest of the network at the passband frequency of the adjacent filter. The decoupling resonator is loosely coupled to the network such that the effect of its presence is minimum to filter performance. More recently, a similar technique has been adapted using the properties of tap connected stepped impedance resonators in triplexer design [89]. However, these additional decoupling resonators consume larger space. In designing diplexers and multiplexers with contiguous band, a susceptance-annulling network is added in shunt when channels are connected in parallel and a reactance-annulling network is added in series when channels are connected in series to compensate for the loading effects. Elements of the channels are adjusted for improved performance. Rhodes et al. have proposed a theory for designing adjusted elements of channels and the annulling network [9]. Recently, Chen et al have proposed a method of designing diplexers using a dual mode resonator which is common for both channels eliminating the requirement of junctions [86]. Instead of designing diplexers from combining individually designed channel filters, complicated and rigorous design approaches of three port networks considering junction effects are also available in recent literature [90], [91], [92], [93].

Diplexers in modern communication systems demand minimal adjacent channel interference. When designing diplexers combining two adjacent channels, minimal channel interference can be achieved by introducing transmission zeros to the response of one channel at the passband of the other channel and vise versa. The second order and third order filters elaborated in the previous chapters are combined to form diplexers in this chapter. Tight coupling, lower loss, and higher fabrication accuracy of the LIGA micromachining method are utilized in designing these diplexers. T-junctions are used in combining individual filter channels. Reactance or susceptance annulling networks are not used. Only simple matching lines are used. Fig. 6.1 illustrates a block diagram of a diplexer that contains individual bandpass filters in the receiving and transmission channel. Each branch length (l_1 and l_2) of the T-junction line and their characteristic impedances (Z_{01} and Z_{02}) are designed by the following procedure. Y_{in1}, Y_{in2} are the input admittances of each channel at the junction including the bandpass filters. The matching condition can be obtained if $Y_{in02} = 0$ at the centre frequency of the passband of the first channel and $Y_{in01} = 0$ at the centre frequency of the passband of the second channel.

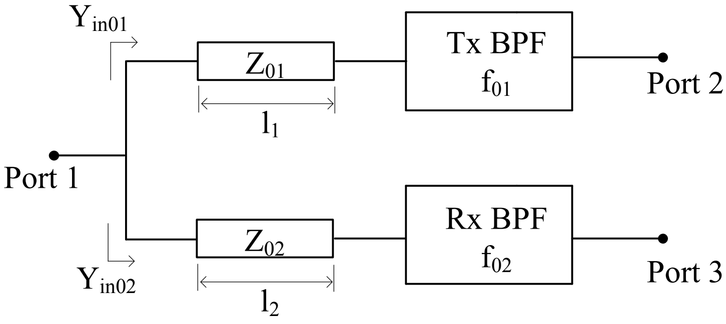

Figure 6.1: A block diagram of a diplexer containing individual bandpass filters in each channel.

6.1.1 A Second Order Diplexer

A second order asymmetric bandpass filter with a centre frequency of 10.5 GHz, 4 percent bandwidth and with a transmission zero located at 11.4 GHz (in the upper stopband) was designed in Chapter 4 using advantages of LIGA fabricated high aspect ratio structures, especially the tight coupling required to realize lower external quality factor and the bypass coupling. In addition, a second order asymmetric filter with 3.6 percent bandwidth centered at 11.6 GHz and having a lower side transmission zero in its response at 10.66 GHz was also designed in Chapter 4. A second order diplexer is designed combining these two filters and using the tight coupling advantage of LIGA structures in this section. Greater isolation is to be achieved due to the transmission zeros in the stopband of the individual filters.

Fig. 6.2 illustrates a sketch of the second order diplexer designed combining second order filters with transmission zeros. The first channel bridging the first and second ports contains the second order filter with the transmission zeros located at its upper stopband and the passband centered around 10.5 GHz while the second channel bridging the first and third ports contains the second order filter with the transmission zero in its lower stopband and the passband centred around 11.6 GHz. The impedance of the matching line with length l_2 is increased in order to minimize the coupling of the second channel in its stopband. The

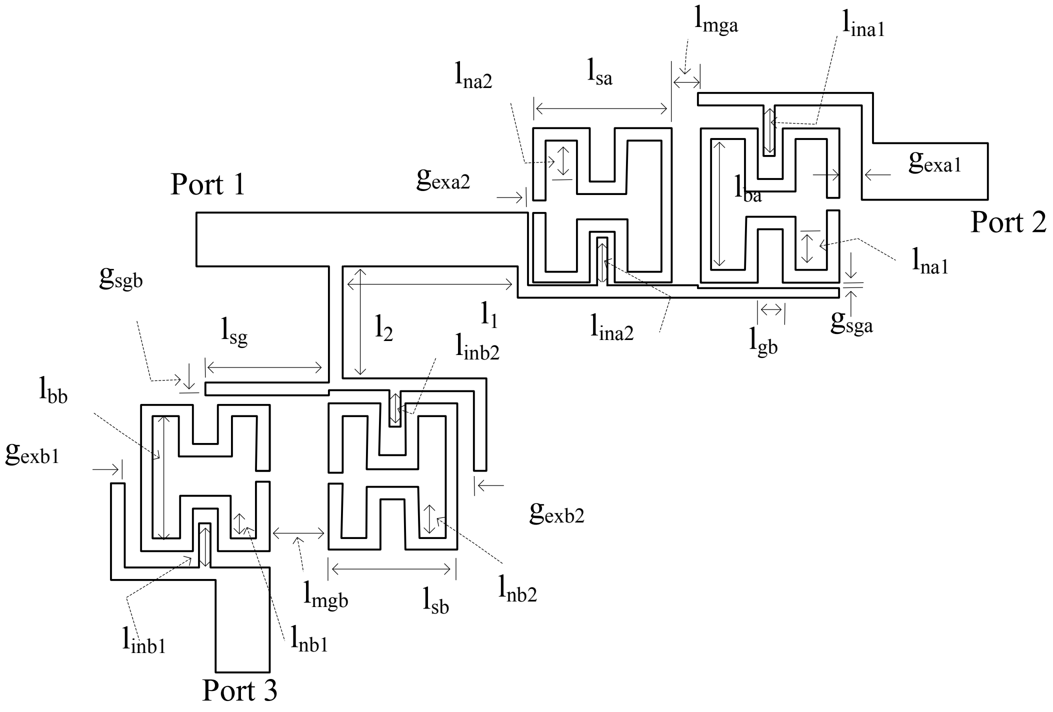

Figure 6.2: The layout of the second order diplexer.

lengths of matching lines (l_1, l_2) were selected such that coupling of each channel in their stopband is minimum and there is enough physical space to separate channels with minimum interference. Some dimensions of the second order filters with transmission zeros given in the fourth chapter were optimized to improve the diplexer responses. The diplexer circuit is designed on 0.5 mm thick substrate. The width of 50Ω lines are 0.875 mm while the width of narrow conductors comprising the open loop resonators and coupling arms is 0.2 mm. The width of the resonator openings is 0.22 mm. The other dimensions are listed in Table 6.1.

This diplexer was fabricated using LIGA deep X-ray lithography. Fig. 6.3 shows photographs of the fabricated high-aspect-ratio microstrip diplexer, with 0.220 mm thick electroplated nickel. Fig. 6.3(b) is an SEM micrograph of the region indicated by the circle in Fig. 6.3(a). It is evident that the required tight coupling gap g_{exa2} (refer to Fig. 6.2) with the targeted gap of 35 μm has been realized very accurately.

In Fig. 6.4, the experimental filter response is compared with the simulated

Table 6.1: Dimensions of the diplexer in Fig. 6.2.

Variable	Dimension (mm)	Variable	Dimension (mm)
g_{exa1}	0.370	l_{na1}	0.678
l_{gb}	0.400	l_{ina1}	0.820
g_{sga}	0.071	l_{ba}	2.050
l_{mga}	0.438	l_{sa}	2.200
l_{na2}	0.618	l_{ina2}	0.750
g_{exa2}	0.035	l_1	2.790
l_2	1.755	l_{sg}	1.975
g_{sgb}	0.130	l_{bb}	1.920
g_{exb1}	0.256	l_{inb1}	0.700
l_{nb1}	0.450	l_{mgb}	0.950
l_{sb}	2.050	l_{nb2}	0.618
l_{inb2}	0.600	g_{exb2}	0.210

responses obtained from EM simulation for the diplexer, using an adaptive mesh with about 90000 tetrahedral elements. The experimental response is in good agreement with the prototype and simulated responses. In the simulated response, the transmission zero of S_{21} is aligned with the passband of S_{31} (insertion loss between port 1 and 3) at 11.35 GHz and the transmission zero of S_{31} is aligned with the passband of S_{21} at 10.51 GHz, increasing channel isolation S_{23}. In the experimental response, the transmission zero of S_{21} is located at 11.21 GHz while the transmission zero of S_{31} is located at 10.87 GHz. The channel isolation is over 25 dB across both filter bands, over 30 dB in the region of the transmission zeros.

6.1.2 A Third Order Diplexer

A third order asymmetric bandpass filter with the centre frequency of the passband 10.57 GHz, 2.5 percent bandwidth and with two transmission zero located at 11 GHz and 11.22 GHz (in the upper stopband) was designed using an effective coupling scheme as described in Chapter 5. In addition, an asymmetric filter with 2.73 percent bandwidth centred at 11.15 GHz and having lower side transmission zeros in its response at 10.55 GHz and 10.8 GHz was also designed using a slightly

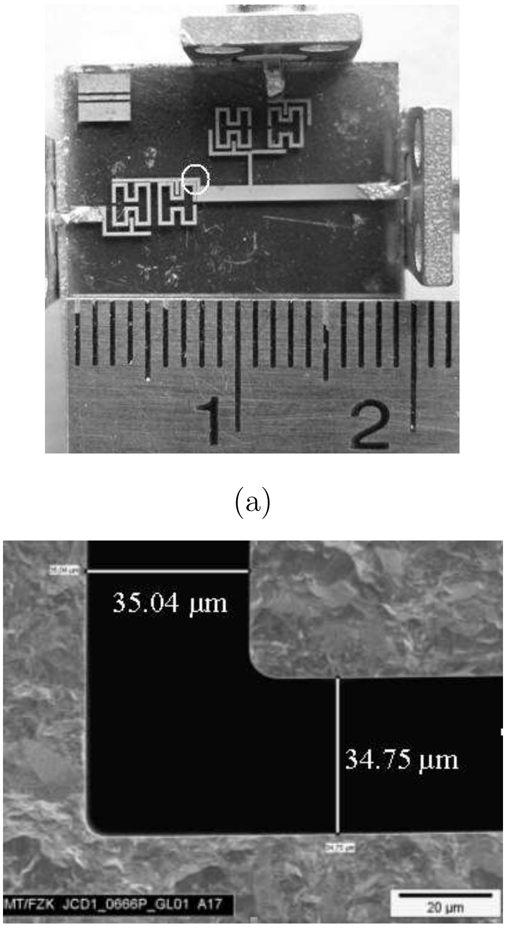

(a)

(b)

Figure 6.3: (a) Photograph of LIGA fabricated high aspect ratio second order diplexer with transmission zeros. (b) SEM micrograph of the indicated area by a circle in (a), (Courtesy of IMT).

different effective coupling scheme as in Chapter 5. A third order diplexer is designed combining these two filters in this section. Greater isolation is expected due to the transmission zeros in the stopband of the individual filters.

Fig. 6.5 depicts the third order diplexer designed combining third order filters with transmission zeros. The first channel bridging the first and second ports contains the third order filter with two transmission zeros located in its upper stopband and the passband centred around 10.57 GHz while the second channel bridging the first and third ports contains the third order filter with the transmission zero in its lower stopband and the passband centred around 11.15 GHz. The

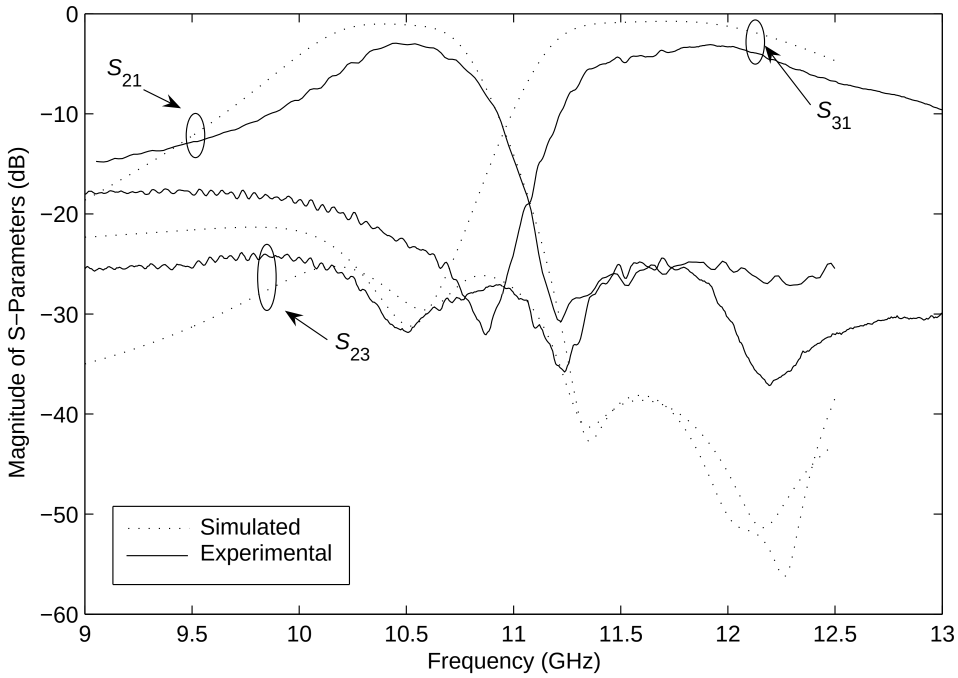

Figure 6.4: Responses of the second order diplexer with two transmission zeros.

lengths of matching lines (l_1, l_2) were selected such that coupling of each channel in their stopband is minimum and there is enough physical space to separate channels with minimum interference. Some dimensions of the third order filters with two transmission zeros given in the fifth chapter were optimized to improve the diplexer responses. The diplexer circuit is designed on 0.5 mm thick substrate. The width of 50Ω lines are 0.875 mm while the width of narrow conductors for open loop resonators and coupling arms is 0.2 mm. The width of the resonator openings is 0.2 mm. The other dimensions are listed in Table 6.2.

Fig. 6.6 gives the simulated response of the above filter assuming lossless conditions, obtained from *EM* simulation using an adaptive mesh with about 90000 tetrahedral elements. The maximum passband return loss of the simulated response is 19 dB, while the intended transmission zeros at a finite frequencies are located at 10.53 GHz and 10.78 GHz in the lower stopband with at least -41.9 dB attenuation over 0.5 GHz frequency range. There is an additional unintended transmission zero in the upper stopband that supports to increase the attenuation in the upper stopband.

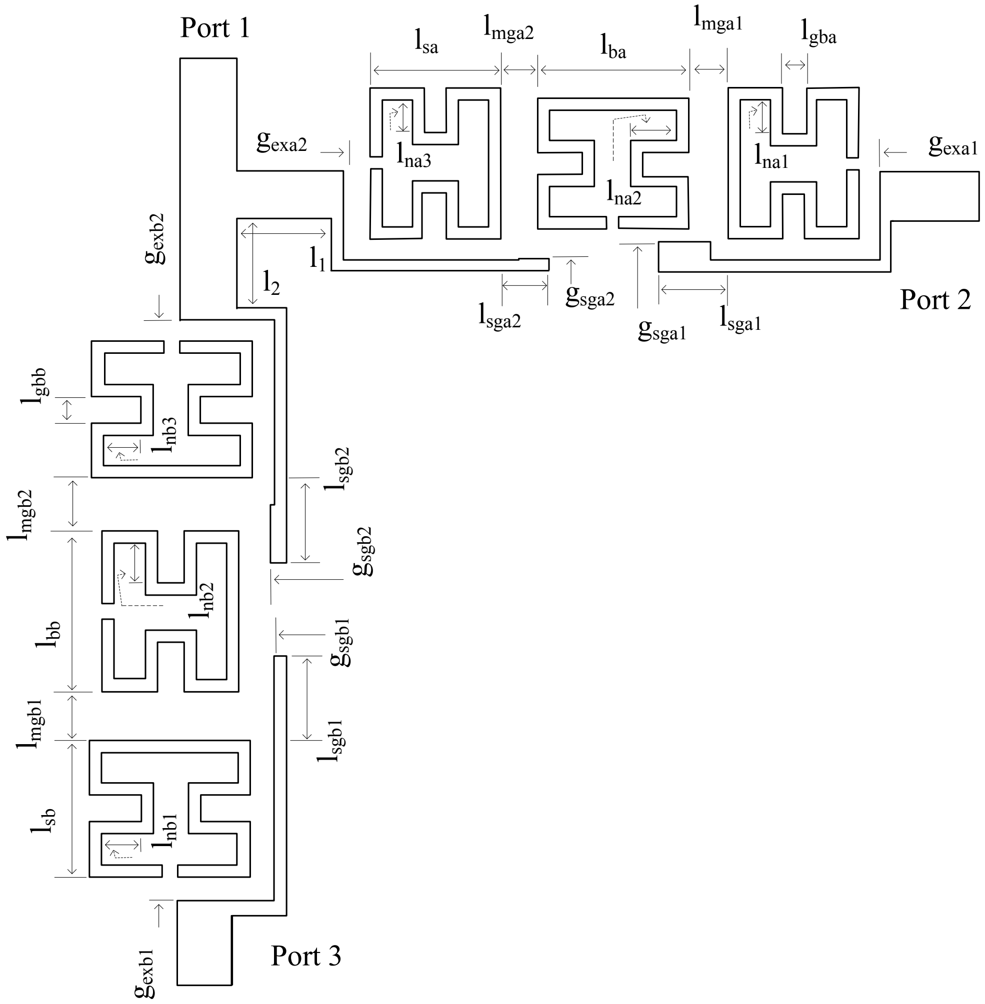

Figure 6.5: Diagram of the third order diplexer.

From the comparison of responses of second order and third order diplexers, it is evident that the stopband attenuation of the third order diplexer is greater than the stopband attenuation in the second order diplexer. Two transmission zeros have contributed in creating increased channel isolation (> -45 dB) over wider frequency range.

Table 6.2: Dimensions of the diplexer in Fig. 6.5.

Variable	Dimension (mm)	Variable	Dimension (mm)
g_{exa1}	0.350	l_{na1}	0.600
l_{gba}	0.400	l_{na2}	0.640
g_{sga1}	0.240	l_{ba}	2.210
l_{mga1}	0.730	l_{sa}	2.220
l_{na3}	0.604	l_{mga2}	0.670
l_{mga3}	0.730	l_{sga1}	1.285
g_{exa2}	0.350	l_1	4.625
l_2	2.291	l_{sga2}	0.828
g_{sga2}	0.540	l_{bb}	2.130
g_{exb1}	0.360	l_{nb1}	0.628
l_{nb2}	0.518	l_{mgb1}	0.780
l_{sb}	2.150	l_{nb3}	0.612
l_{mgb2}	0.760	g_{exb2}	0.324
g_{sgb1}	0.520	g_{sgb}	0.470
l_{sgb1}	1.312	l_{sgb2}	1.298

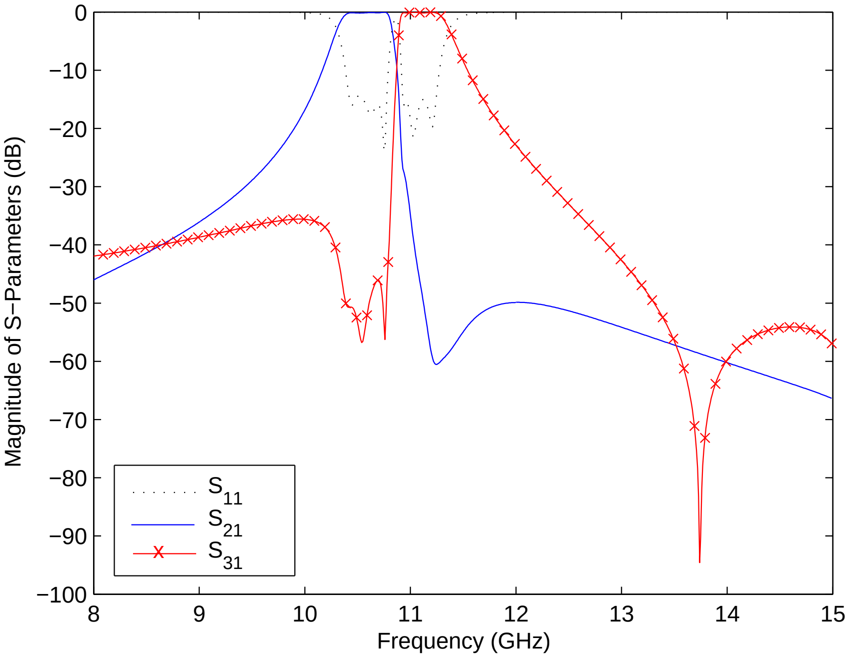

Figure 6.6: Responses of the third order diplexer with four transmission zeros.

Chapter 7

Application of LIGA Process into Periodic Structures

7.1 Introduction

Periodic structures have attracted a growing research interest in the microwave and millimeter-wave regime. For example, planar periodic structures have been utilized to realize high performance filters, high efficiency power amplifiers, and antennas [22], [94]. Key to this interest is the capability of these structures to inhibit signal propagation in certain frequency bands. A slow wave transmission line can be obtained by introducing periodic perturbations into the conventional transmission structure itself [18]. For example, these perturbations can be made on the ground, signal trace or in the substrate of microstrip lines and CPWs as detailed in [22]. The slow wave nature of periodic structures has also been exploited to reduce circuit component size [95], [21]. Periodically loaded transmission lines are also used for performance improvement of passive microwave devices as mentioned in [19]. On the other hand, periodic-like structures have been designed to obtain materials with negative permeability and permittivity which has also been exploited to realize microwave and millimeter-wave devices [96].

Electromagnetic band gap (EBG) structures have attracted much attention recently and are essentially a slow wave periodic structure. EBG structures can be introduced on the ground plane or into the substrate of microstrip lines or CPWs. A widely used EBG structure for microstrip substrates that contains

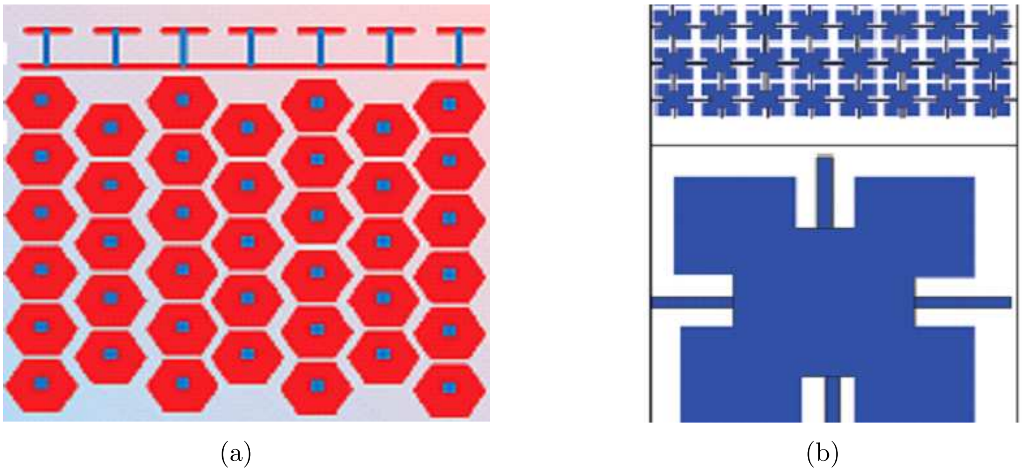
(a) (b)

Figure 7.1: Two types of widely used EBG structures (a) A mushroom like structure [1] (b) Planar EBG structure [2].

mushroom like EBG unit cells as shown in Fig. 7.1 (a) has been proposed by Sievenpiper et al. recently in [1]. Metal pads on top of the substrate connected to the ground become resonant when the EBG structure made of them is in the stopband. An uni-planar EBG lattice made of unit cells which consist of square pad having a capacitive effect and narrow branches having an inductive effect that is further enhanced by insets as shown in Fig. 7.1 (b) has also been proposed by Yang et al. in [2]. These EBG structures form a distributed LC network with specific resonant frequency at which periodic loading becomes an open circuit and an equivalent magnetic surface is created. EBG structures have been used in microwave engineering in many ways. Low noise oscillators are designed using high Q resonators based on EBG defect effects [97]. The planar EBG lattice depicted in Fig. 7.1 has been used for suppression of leakage from the local oscillator to intermediate frequency (IF) side in mixers [98]. The achievement of broadband harmonic tuning of power amplifiers is cumbersome and a wider stopband of an EBG patterned ground plane may be used for harmonic tuning. EBG structures are also used in antennas, specially in microstrip patch antennas, for gain improvement by making image currents in the same phase, for reducing back radiation from finite ground plane, for suppressing surface waves that cause side lobes in the radiation pattern and for suppressing coupling between antennas when they share a same ground plane [94].

On the other hand, EBG typed periodic structures have been used to realize filters with several approaches. Much research has focused on realizing high performance low pass filters directly using the first passband of EBG structures [23], [99]. Passband ripple level and losses are relatively high because small resonant elements are used. However, the filter structure is more compact and the stopband may also be wider. In this type of low pass filters, passband and out-of-band is coincident with its EBG passband and stopband. The ground plane or the dielectric substrate of conventional planar low pass filters and bandpass filters are EBG engineered to suppress spurious passbands in stopbands [2]. Here, the EBG stopband is made coincident with the spurious passband that may arise due to higher order resonant modes. Narrow-band bandpass filters can also be realized using EBG defect resonators where a defect is introduced in the EBG structure to obtain a high Q defect mode as it is used in oscillators [24].

Recently, narrow-band bandpass filters designed by cascading left handed coplanar waveguide unit cells based on split ring resonators have been reported in [100], while periodic bandpass filters using a microstrip line series loaded with split ring resonators have been given in [101]. Slow-wave periodic bandpass filters using microstrip transmission lines shunt loaded with open loop resonators or stepped impedance hairpin resonators have been reported in [20]. However, a detailed design methodology for controlling passband edge frequencies or passband ripple level has not been reported in the above previous work. In an another approach, a wide-band bandpass filter has been proposed by cascading a low pass EBG structure and a high pass EBG structure [102].Though sharp roll off at passband edge is demonstrated, the insertion loss is high.

Two unit cell topologies shown in Fig. 7.2 which were proposed for a periodic structure suitable for realizing novel wide-band compact filters by the author in [103], [104] are detailed here. Shunt and series loaded unit cells shown in Fig. 7.2 are cascaded separately in order to realize shunt loaded bandpass filters

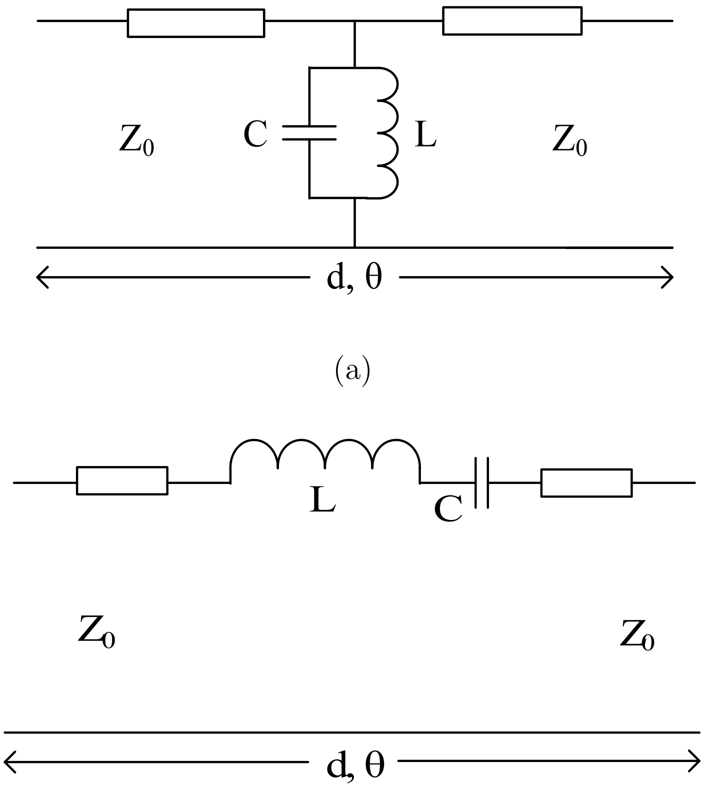

(a)

(b)

Figure 7.2: (a) Shunt LC loaded unit cell (b) Series LC loaded unit cell.

and series loaded bandpass filters respectively. The main difference of the proposed filter structures from the conventional coupled resonator bandpass filter is that the filter response is determined by the electromagnetic passbands and stopbands as explained in succeeding sections in this chapter rather than the resonator impedances. Periodic structures consisting of proposed unit cells are analyzed and filter designing equations are also presented. A method for controlling the passband ripple level is also discussed in Section 7.2. Wave propagation characteristics of a shunt loaded passband type EBG model are also discussed in the next section. Sample circuit and electromagnetic (EM) simulation results are included to demonstrate the performance of the proposed wideband filters. The main advantage of this type of bandpass filter is that the electrical length of the EBG unit cell can be somewhat arbitrarily selected. Hence the final filter structure becomes small in size, compared to conventional ultra wideband (UWB) bandpass filters made, for instance, with grounded quarter wavelength resonators, connected by quarter wavelength admittance inverters. In Section 7.4, the physical size of the EBG-based 60 percent bandwidth microstrip bandpass filter is also compared with a conventional bandpass filter giving similar performance. Finally a miniaturized EBG based CPW bandpass filter with 50 percent bandwidth is appended. Both EBG concept and advantages of high aspect ratio LIGA structures are exploited for the miniaturization of the above CPW bandpass filter.

7.2 Bandpass Type EBG Concept

7.2.1 Parallel LC Shunt Loaded EBG Structure

Fig. 7.2 (a) shows a parallel connected inductance, L , and capacitance, C, shunt loaded on a transmission line segment of physical length d and electrical length θ with characteristic impedance Z_0. One can resort to the transmission matrix or in other words *abcd* matrix of the above circuit in order to determine electrical behavior, especially when it is cascaded with any number of unit cells. The *abcd* matrix of the above unit cell is,

$$\begin{pmatrix} a & b \\ c & d \end{pmatrix} = \begin{pmatrix} \cos\frac{\theta}{2} & jZ_0\sin\frac{\theta}{2} \\ \frac{j\sin\frac{\theta}{2}}{Z_0} & \cos\frac{\theta}{2} \end{pmatrix} \begin{pmatrix} 1 & 0 \\ jB & 1 \end{pmatrix} \begin{pmatrix} \cos\frac{\theta}{2} & jZ_0\sin\frac{\theta}{2} \\ \frac{j\sin\frac{\theta}{2}}{Z_0} & \cos\frac{\theta}{2} \end{pmatrix} \tag{7.1}$$

where $B = \omega C - 1/\omega L$ is the parallel susceptance, ω being the angular frequency. The unit cell in Fig. 7.2 (a) is cascaded in order to obtain an EBG structure showing frequency bands for which propagation can take place separated by frequency bands in which the wave does not propagate. The propagation constant $\gamma = \alpha + j\beta$ of infinite cascaded unit cells is given as, (Refer to the Appendix D)

$$\cosh\gamma = \frac{a+d}{2} \tag{7.2}$$

where α and β are the attenuation and phase constants of the propagating wave in the EBG structure. Assuming negligible attenuation in the passband (i.e. $\alpha \simeq 0$), one can obtain the well known relation (Appendix D)

$$\cos \beta d = \cos k_0 d - \frac{B}{2} Z_0 \sin k_0 d \tag{7.3}$$

where k_0 is the propagation constant in the unloaded transmission line. Fig. 7.3 (a) illustrates the variation of the right hand side of Equation 7.3 with frequency for a representative EBG structure with lower and upper band edge frequencies of 3.75 GHz and 6.75 GHz, respectively. The dotted lines of Fig. 7.3(b) show real and imaginary parts of βd, obtained by numerically solving Equation 7.3. The phase constant, β should have only real values for unattenuated wave propagation in the cascaded structure. Hence, wave propagation is allowed in the frequency band between 3.75 GHz and 6.75 GHz, according to Fig. 7.3 (b). Generally, the velocity of wave propagation, v, is given by

$$v = \frac{2\pi f}{\beta}. \tag{7.4}$$

The solid line in Fig. 7.3(b) depicts the variation of $k_0 d$ with frequency. According to Equation 7.4, one can deduce that wave propagation is slow in the passband of the representative EBG structure over the wave propagation in the unloaded transmission line because the phase constant of the EBG structure, β is higher than the phase constant of the unloaded line, k_0 from the frequency slightly above the lower bandedge frequency which is 3.75 GHz. It is evident from the figure that the phase constant of the representative EBG structure, β has real values only if the magnitude of the right hand side of Equation 7.3 falls within -1 and +1. According to the Foster reactance theorem [18], B in Equation 7.3 is continuously increasing from negative infinity to positive infinity. As a result, the right hand side of Equation 7.3 decreases from positive to negative. Hence, with the increase of frequency, the right hand side of Equation 7.3 approaches to +1 at the lower

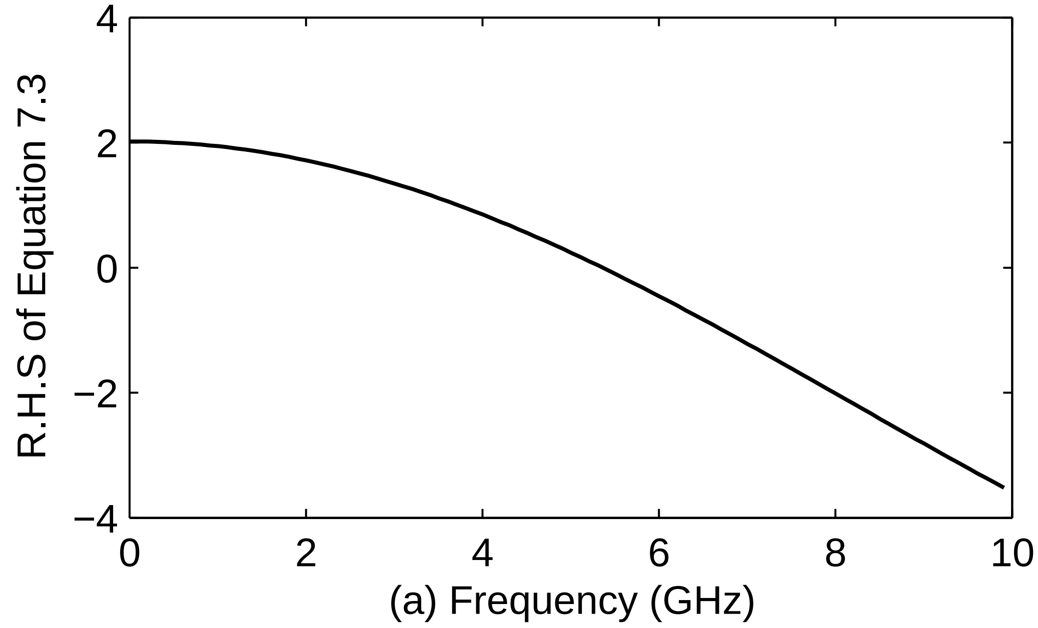

(a) Frequency (GHz)

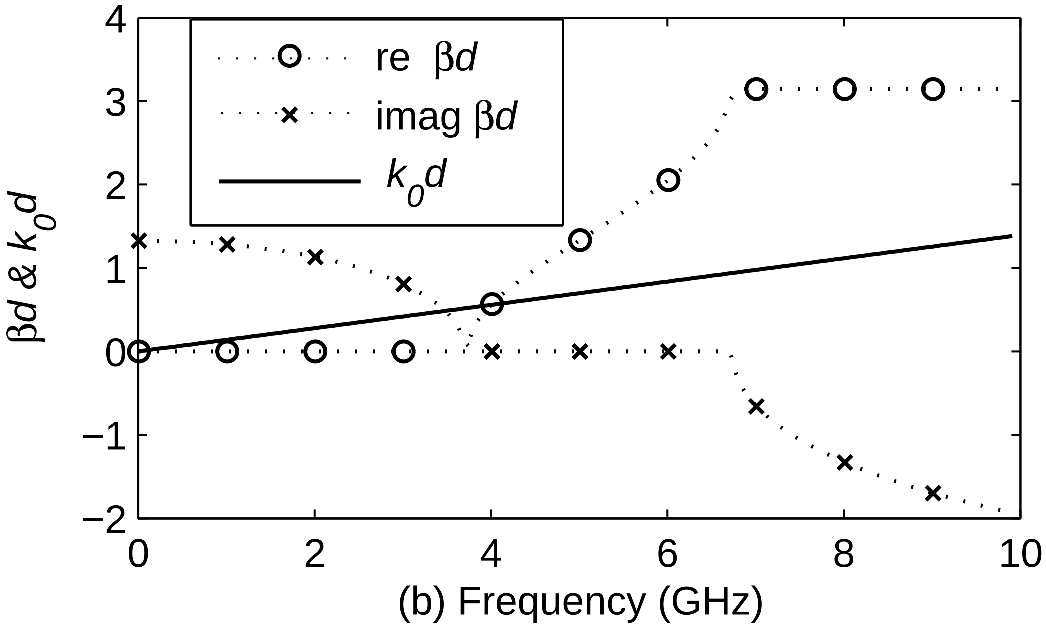

(b) Frequency (GHz)

Figure 7.3: (a) Variation of the right hand side of Equation 7.3 with frequency, (b) Variation of phase constants of bandpass type representative EBG structure and unloaded transmission line with frequency.

edge of the passband when,

$$\tan\frac{k_0 d}{2} = -\frac{B}{2}Z_0, \tag{7.5}$$

or

$$\sin\frac{k_0 d}{2} = 0. \tag{7.6}$$

With the further increase of frequency, the right hand side of the Equation 7.3 approaches to -1 at the upper edge of the passband or lower edge of the next stopband and it can be shown that,

$$\cot\frac{k_0 d}{2} = \frac{B}{2} Z_0, \tag{7.7}$$

or

$$\cos\frac{k_0 d}{2} = 0, \tag{7.8}$$

at the upper edge of the passband.

Equations 7.6 and 7.8 are satisfied when $k_0 d$ is a multiple of 2π and π, respectively. The latter equation is related to Bragg's condition. They are satisfied for particular frequencies and d and hence, these two conditions cannot be used efficiently to control the passband of the loaded transmission line independent of the physical parameter d. But Equations 7.5 and 7.7 can be used to determine L and C for a specified bandwidth of the first passband of the proposed shunt LC loaded EBG structure consisting of unit cells of length d. Expressing B in Equations 7.5 and 7.7 in terms of L and C, we obtain

$$C\omega_1 - \frac{1}{L\omega_1} = -\frac{2}{Z_0}\tan\frac{k_0' d}{2}, \tag{7.9}$$

and

$$C\omega_2 - \frac{1}{L\omega_2} = \frac{2}{Z_0}\cot\frac{k_0'' d}{2}, \tag{7.10}$$

where ω_1 and ω_2 are the angular frequency of the lower band edge and the upper band edge of the first pass band in the EBG structure, respectively where, k' and k'' are the propagation constants of the unloaded line at ω_1 and ω_2. Solving above two equations for L and C, it can be shown that,

$$C = \frac{2[\frac{1}{\omega_2}\tan\frac{k_0'd}{2} + \frac{1}{\omega_1}\cot\frac{k_0''d}{2}]}{Z_0[\frac{\omega_2}{\omega_1} - \frac{\omega_1}{\omega_2}]}, \tag{7.11}$$

$$L = \frac{Z_0[\frac{\omega_2}{\omega_1} - \frac{\omega_1}{\omega_2}]}{2[\omega_2\tan\frac{k_0'd}{2} + \omega_1\cot\frac{k_0''d}{2}]}. \tag{7.12}$$

The EBG structure inhibits wave propagation below ω_1. It exhibits wave propagation between ω_1 and ω_2. Again, wave propagation is inhibited above ω_2 until the next passband appears. Eventually B is large enough to suppress repeated passbands. Hence parallel LC shunt loaded periodic structures can be used as a bandpass filter. The transverse physical length of unit cells, d, can be arbitrarily selected and hence compact unit cells can be realized.

7.2.2 LC Series Loaded Periodic Structure

An EBG structure with bandpass characteristics can also be achieved by cascading unit cells consisting of LC series loaded transmission line segments of electrical length θ as shown in Fig. 7.2 (b). The *abcd* matrix of the above unit cell is,

$$\begin{pmatrix} a & b \\ c & d \end{pmatrix} = \begin{pmatrix} \cos\frac{\theta}{2} & jZ_0\sin\frac{\theta}{2} \\ \frac{j\sin\frac{\theta}{2}}{Z_0} & \cos\frac{\theta}{2} \end{pmatrix} \begin{pmatrix} 1 & jX \\ 0 & 1 \end{pmatrix} \begin{pmatrix} \cos\frac{\theta}{2} & jZ_0\sin\frac{\theta}{2} \\ \frac{j\sin\frac{\theta}{2}}{Z_0} & \cos\frac{\theta}{2} \end{pmatrix} \tag{7.13}$$

where $X = (\omega L - 1/\omega C)$ is the series reactance. As in the previous case for shunt loaded unit cells, the propagation constant is expressed in terms of parameters of the *abcd* matrix, a and b , as $\cosh\gamma = (a + d)/2$. Again assuming unattenuated wave propagation in the representative EBG structure, a dispersion relation is obtained as,

$$\cos\beta d = \cos k_0 d - \frac{X}{2Z_0}\sin k_0 d. \tag{7.14}$$

Here also, a real value for β exists only if the right hand side of Equation 7.14 is between -1 and +1. X is continuously increasing from negative infinity to positive infinity. Hence, with increase of frequency, the right hand side of Equation 7.14 approaches to +1 at the lower edge of passband, ω_1, when

$$\tan\frac{k_0 d}{2} = -\frac{X}{2Z_0}, \tag{7.15}$$

or

$$\sin\frac{k_0 d}{2} = 0. \tag{7.16}$$

With further increase of frequency, the right hand side of the Equation 7.14 approaches to -1 at the upper edge of the passband or lower edge of the next stopband and it can be shown that

$$\cot\frac{k_0 d}{2} = \frac{X}{2Z_0}, \tag{7.17}$$

or

$$\cos\frac{k_0 d}{2} = 0, \tag{7.18}$$

at the upper edge of the passband, ω_2. Equations 7.15 and 7.17 can be used for obtaining expressions to determine L and C for controlling band edge frequencies. Expanding X in above equation in terms of series L and C, the following equations are obtained:

$$L\omega_1 - \frac{1}{C\omega_1} = -2Z_0\tan\frac{k_0' d}{2}, \tag{7.19}$$

and

$$L\omega_2 - \frac{1}{C\omega_2} = 2Z_0\cot\frac{k_0'' d}{2} \tag{7.20}$$

where ω_1, ω_2, k' and k'' have similar definitions as in the case of shunt LC loaded representative EBG structure. Using Equations 7.19 and 7.20, expressions for L and C are derived as

$$C = \frac{[\frac{\omega_2}{\omega_1} - \frac{\omega_1}{\omega_2}]}{2Z_0[\omega_2\tan\frac{k_0' d}{2} + \omega_1\cot\frac{k_0'' d}{2}]}, \tag{7.21}$$

and

$$L = \frac{2Z_0[\frac{1}{\omega_2}\tan\frac{k_0'd}{2} + \frac{1}{\omega_1}\cot\frac{k_0''d}{2}]}{[\frac{\omega_2}{\omega_1} - \frac{\omega_1}{\omega_2}]}. \tag{7.22}$$

In this series LC loaded EBG structure, wave propagation is inhibited below ω_1 and there exists wave propagation between ω_1 and ω_2. Another stopband appears for angular frequencies above ω_2. This EBG structure can also be used as a bandpass filter.

7.3 LC Shunt Loaded Bandpass Filters

7.3.1 Circuit Simulated Results

The EBG structure realized from cascading shunt LC loaded unit cells can be used as a bandpass filter. Based on the above relationships, bandpass filters with wideband characteristics have been simulated at upper microwave frequencies using *Agilent* ADS$^{\text{TM}}$ [105] circuit simulator and representative LC loaded cascaded transmission line unit cells. Fig. 7.4 shows the magnitude responses, $|S_{21}|$, of bandpass filters with f_1 = 18 GHz and f_2 = 22 GHz, where f_1 and f_2 are the band edge frequencies, realized by cascading three and four shunt LC loaded unit cells. The lower side transition band ratio, f_s/f_p , is 0.866 for the bandpass filter with three cascaded cells where f_s and f_p are defined as the frequencies giving -30 dB attenuation and -3 dB attenuation respectively. The upper transition band ratio is 1.150. The transition band ratios of a same order Chebyshev bandpass filter are approximately similar to this filter. The transition band ratio of an ideal filter is one. The filters with four cascaded unit cells provides 0.925 and 1.077 transition band ratios defined as above in the lower side and the upper side of the passband respectively. Maximum pass-band ripple of the filter with four sections is around 1 dB and located closer to the passband edges. The unit cells have been designed to have an electrical length of 90^0 at 20 GHz and with 50 Ω transmission line sections. The values of L and C calculated from Equations

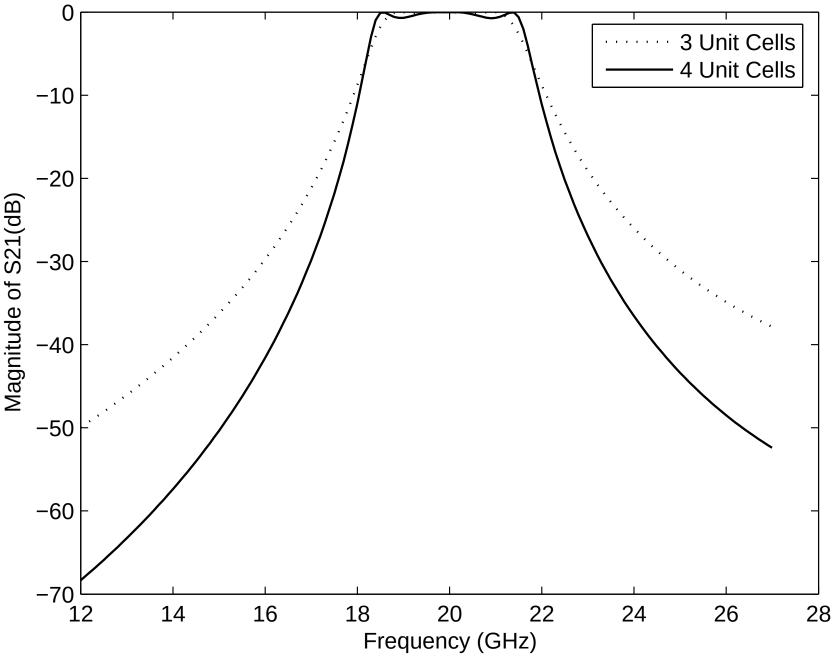

Figure 7.4: Magnitude response of the filter with $f_1 = 18$ GHz, $f_2 = 22$ GHz, $Z_0 = 50\Omega$ and $\theta = 90^0$.

7.11 and 7.12 are 0.047 nH and 1.359 pF respectively. It is evident from Equation 7.11 that C increases further if the electrical length of unit cells is increased or decreased considerably. Using Equation 7.11, the electrical length of unit cells for minimum capacitance can be evaluated and C is around its minimum when the electrical length of unit cells is 90^0 at the mid of the passband. On the other hand, the electrical length of unit cells can be further reduced at the expense of higher shunt capacitance if the transmission line impedance is kept constant as discussed in a later part of this section. The required susceptance slope parameter of shunt LC resonators is higher when shunt capacitance of the shunt resonator is higher. Shunt resonators with high susceptance slope parameters can be realized by fabricating high aspect ratio structures. Hence, the overall physical size of unit cells can potentially be reduced since the required shunt inductance is lesser for shortened unit cells. The phase responses of the above filters are shown in Fig. 7.5.

Fig. 7.6 illustrates the bandpass responses of wide-band filters with four and

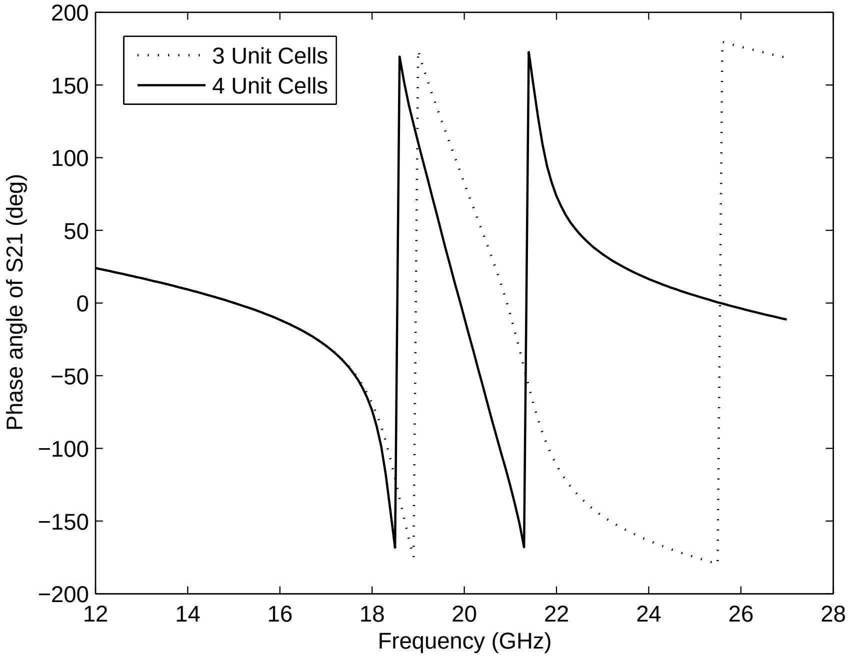

Figure 7.5: Phase response of the filter with $f_1 = 18$ GHz, $f_2 = 22$ GHz, $Z_0 = 50\Omega$ and $\theta = 90^0$.

five cascaded shunt LC unit cells with $f_1 = 16$ GHz and $f_2 = 24$ GHz. The bandwidth based on f_1 and f_2 is forty percent with the centre frequency of 20 GHz. The calculated L and C values are 0.114 nH and 0.578 pF respectively for a unit cell of 90^0 electrical length and having 50 Ω transmission line segments. The lower side transition band ratio, defined as above, of the filter with four cascaded unit cells is 0.840 where as the transition band ratio in the upper side is 1.18. The maximum passband ripple is 0.5 dB. Transition bands are improved with five cascaded unit cells such that transition band ratios are 0.90 and 1.10 in the lower and upper transition bands respectively, at the expense of the maximum passband ripple level of 1 dB.

Evaluated L and C values for a unit cell of 90^0 electrical length and having 50 Ohm transmission line segments are 1.974 pF and 0.272 nH respectively for a bandpass filter with forty percent bandwith based on f_1 and f_2 centred at 8 GHz. The filter characteristics obtained from a filter with four cascaded shortened LC shunt unit cells of 90^0 in electrical length with $f_1 = 16$ GHz and $f_2 = 24$

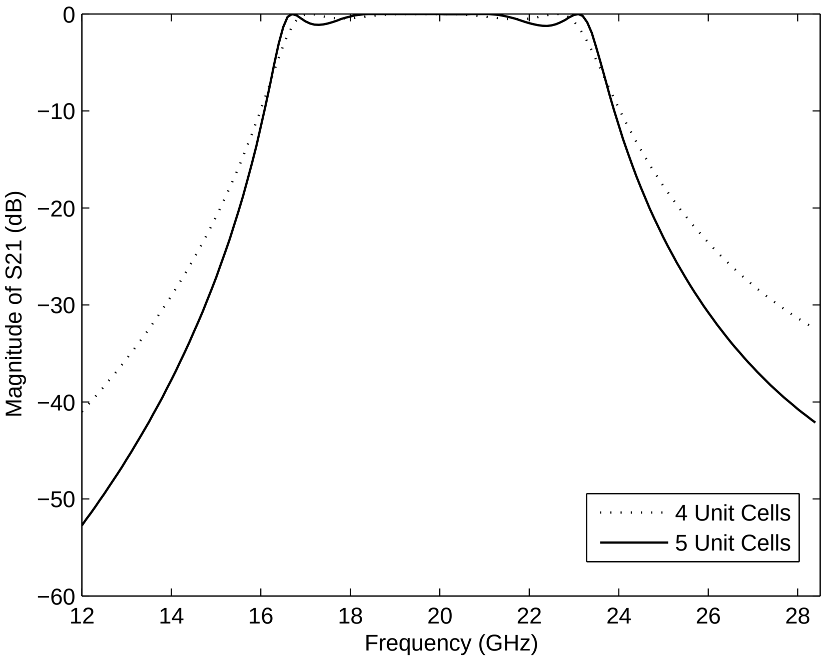

Figure 7.6: Magnitude response of the filter with $f_1 = 16$ GHz, $f_2 = 24$ GHz, $Z_0 = 50\Omega$ and $\theta = 90^0$.

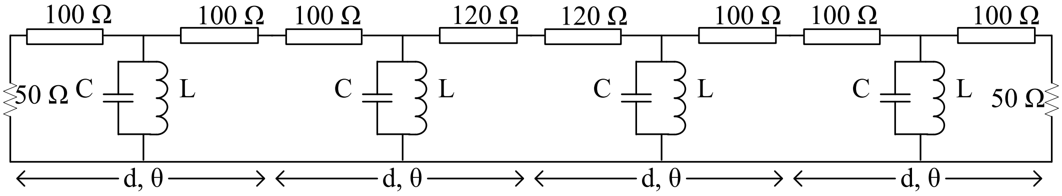

Figure 7.7: Schematic diagram of a bandpass filter with four unit cells. Characteristic impedance of the transmission line segment connecting two middle shunt resonators has been increased.

GHz is depicted by the dotted curve in the Fig. 7.8. Values for L and C have been calculated taking the characteristic impedance of transmission line sections as 100 Ohm and they are 0.17 nH and 0.52 pF respectively. The maximum passband ripple located near the edge of passband is about 1.5 dB. The filter can be optimized to minimize the passband ripple such that the transmission line segment connecting the middle two shunt resonant tanks in the filter is having characteristic impedance of 120 Ω while the other transmission line segments being 100 Ω and optimized filter response is shown by the continuous curve in Fig. 7.8. Maximum ripple level has been reduced to around -0.25 dB.

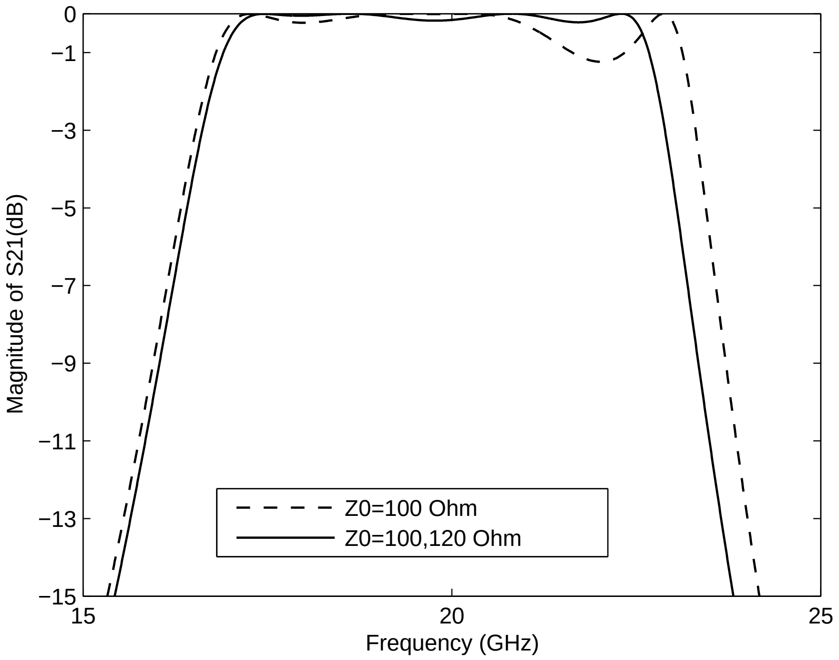

Figure 7.8: Magnitude response of the filter with $f_1 = 16$ GHz, $f_2 = 24$ GHz, $Z_0 = 50\Omega$ and $\theta = 90^0$.

Wide-band bandpass filters based on EBG principle for different bandwidth at 20 GHz centre frequency were analyzed and a design methodology was discussed. Ultra-wideband and compact bandpass filters consisting of small unit cells can potentially be realized based on this principle. With the shortening of the unit cell with the shunt resonator, the required capacitance in the shunt resonator increases and shunt resonators with this increased capacitance might be realizable using high aspect ratio CPW structure as discussed later in this chapter. The transition band can be improved by increasing the number of unit cells in the filter at the expense of higher ripples at the band edges. This increased ripple could potentially be improved by using tapered reactance loading or by using tapered characteristic impedances for transmission line sections.

7.4 Wideband Microstrip Bandpass Filter Based on EBG Concept

7.4.1 Filter Design

Shunt lumped LC resonators, used in designing bandpass filters in the previous section are relatively difficult to realize in practice. In addition, these resonators are lossy though they consume relatively small space. The EBG based bandpass filter design concept is verified adapting a different approach in this section.

Distributed elements can be used to realize the shunt reactance instead of using lumped elements. For instance, using a grounded quarter wavelength transmission line segment is a one method of substituting the shunt lumped elements with distributed elements. Unlike in narrow band filter design, the equivalent transmission line parameters cannot be evaluated considering a single frequency. If an equivalent transmission line resonator was designed considering a single frequency, band edge frequencies of the final bandpass filter would be different from those in the response of the lumped element filter because the shunt susceptances of equivalent transmission line resonators and lumped resonators at the band edge frequencies would be different. In order to determine the characteristic impedance and resonant frequency of the equivalent shunt transmission line, the following equations are obtained by equating susceptances of the shunt transmission line and LC loading at ω_1 and ω_2 as,

$$\frac{1}{Z_s}\cot\left(\frac{\pi\omega_1}{2\omega_r}\right) = -\left(C\omega_1 - \frac{1}{L\omega_1}\right) \tag{7.23}$$

and

$$\frac{1}{Z_s}\cot\left(\frac{\pi\omega_2}{2\omega_r}\right) = -\left(C\omega_2 - \frac{1}{L\omega_2}\right) \tag{7.24}$$

where Z_s and ω_r are characteristic impedance and quarter wavelength resonant frequency of the equivalent shunt transmission line, respectively. Dividing Equation

7.23 by Equation 7.24, Z_s is eliminated and one nonlinear function, $F(\omega_r)$ with an unknown variable, ω_r, is obtained for solving it using Newton's iterative technique. Taking the angular resonant frequency of lumped resonators as an initial guess for ω_r, the unknown ω_r is found using the equation $\omega_{r,i+1} = \omega_{r,i} + F(\omega_{r,i})/F'(\omega_{r,i})$ where $F'(\omega_{r,i})$ is the derivative of $F(\omega_{r,i})$ and $\omega_{r,i}$ is the value of the angular frequency of the i^{th} iteration.

A 60 percent bandwidth (with respect to EBG band edge frequencies f_1 and f_2) UWB EBG-based bandpass filter with $f_1 = 3.75$ GHz and $f_2 = 6.75$ GHz and four cascaded unit cells was designed to show the capability of this EBG based filter designing method. For the above frequency specifications, the lumped element parameters were obtained first using Equations 7.11 and 7.12, assuming 40^0 long unit cells. Evaluated lumped parameter values of CZ_0 and L/Z_0 for the above specifications are 144.78 pFΩ and 10.926 pHΩ^{-1} respectively. The characteristic impedance of the transmission line to be loaded with shunt resonators, Z_0, was selected to be 110 Ω. Z_0 is chosen to avoid unrealizable susceptance slope parameters (because the calculated C depends on selected Z_0) and unrealizable transmission line sections possibly encountered when optimized to reduce passband ripple as describe subsequently. The response of four cascaded unit cells modeled with ideal elements in a 50 Ω system was obtained using the *Agilent* ADS$^{\text{TM}}$ [105] circuit simulator and it was optimized to reduce passband ripples. Passband ripple level was minimized by increasing the characteristic impedance of the transmission line segment connecting the middle two shunt resonators, to 128.6 Ω as shown in Fig. 7.9 (b). Shunt resonators were realized with grounded quarter wavelength transmission lines. The characteristic impedance and the resonant frequency of equivalent shunt quarter wavelength resonators were evaluated using Equations 7.23 and 7.24, as described previously, to obtain approximately equivalent characteristics to the required lumped shunt resonators. The evaluated characteristic impedance and resonant frequency of required shunt resonators are 38.3 Ω and 4.2 GHz. The resonant frequency of the equivalent quarter wavelength resonator is different from the resonant frequency of the lumped shunt resonator in the representative EBG unit cell. Furthermore, the resonant frequencies of both lumped and distributed shunt resonators are not similar to the center frequency of the passband of the final UWB bandpass filter.

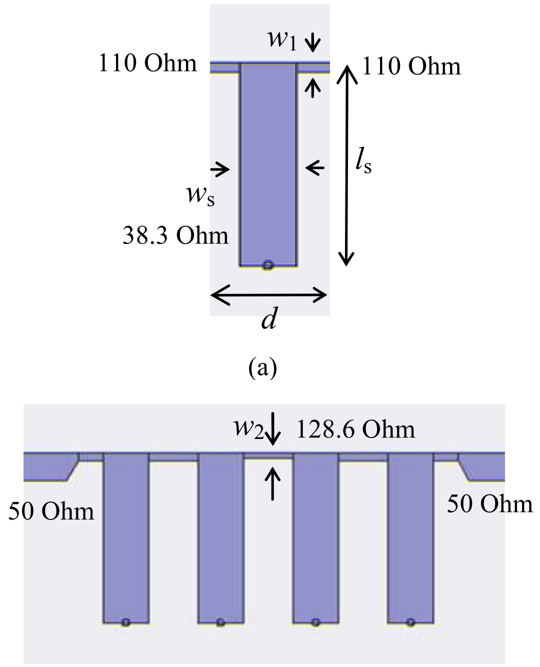

(a)

(b)

Figure 7.9: (a) A unit cell-110 Ω transmission line shunt loaded with a quarter wave length transmission line with via hole grounding and resonating at 4.2 GHz, (b) Wide-band filter (60 percent bandwidth with respect to EBG band edge frequencies) with $f_1 = 3.75$ GHz and $f_2 = 6.75$ GHz.

7.4.2 Experimental Results

A real thin metal layer microstrip structure on a 0.7874 mm thick RT/duroid 5880$^{\text{TM}}$ substrate with dielectric constant of 2.2 was designed for the above EBG-based UWB bandpass filter. An unit cell of the filter structure has been illustrated in Fig. 7.9 along with dimensional variables. For obtaining physical dimensions of the filter given in Fig. 7.9, the LineCalc tool in ADS was used and dimensions of the unit cell before EM simulation, obtained in above manner, are $w_s = 3.542$ mm, $l_s = 12.82$ mm and $d = 8.618$ mm. The width of the middle transmission line segment connecting the middle two shunt resonators is 0.369 mm. The real microstrip UWB bandpass filter was analyzed and optimized using the electromagnetic full-wave finite element simulator HFSS [52]. Some parameters, especially d and l_s, were changed to improve filter performance. Dimensions of the unit cell in the final structure are $w_s = 3.56$ mm, $l_s = 12.2$ mm and $d = 6.485$ mm. The width of the middle transmission line segment connecting the middle two shunt resonators is the same as in the initial structure obtained from the ADS LineCalc tool and the length is 3.025 mm. The width of the 50 Ω transmission line sections leading to external ports is 2.42 mm while the radius of via holes made to ground the one end of quarter wavelength transmission line resonators is 200 μm. The discrepancies between dimensions evaluated from ADS circuit simulation and dimensions of the final optimized EM simulated structure mainly arise because of the effects of the via hole; the widths of the shunt resonators and the widths of resonator connecting transmission lines were not taken into account in designing their lengths (i.e. d, and l_s). The minimum passband insertion loss and the maximum passband return loss of the filter obtained from EM simulation using an adaptive mesh with approximately 25000 tetrahedral elements are 0.7 dB and 12 dB as depicted in Fig. 7.11. Fig. 7.11 also shows measurement results of the filter shown in Fig. 7.10 (top) fabricated using a standard printed circuit board fabrication method. As evident from Fig. 7.11, excellent agreement has been found between measured and EM simulated responses of the EBG-based UWB filter. The number of unit cells determines the steepness of the band edges of the filter.

A conventional UWB thin metal layer microstrip bandpass filter with similar performance to the above EBG-based UWB filter, consisting of quarter wavelength resonators connected with quarter wavelength admittance inverters (proximity coupling is not practical for realizing admittance inverters of UWB bandpass filters with quarter wavelength resonators with one end grounded) was also designed in order to compare the physical size of the EBG-based UWB bandpass

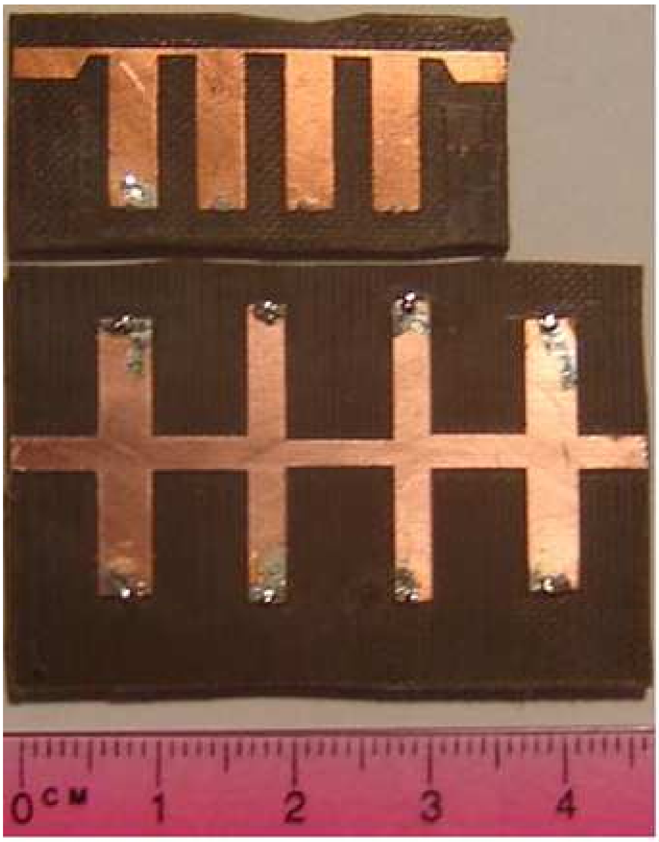

Figure 7.10: Photograph of the EBG-based UWB thin metal layer microstrip bandpass filter and conventional thin metal layer microstrip UWB filter with quarter wavelength admittance inverters.

filter with its conventional counterpart. Wideband design equations given by Matthaei et al [9] quoted in Appendix D were used since use of narrowband design formulas causes bandwidth contraction. Admittance inverters connecting external source and load to the wideband filter have been eliminated from the above wideband design method unlike in narrowband design. Evaluated impedance of the quarter wavelength transmission lines connecting first two resonators and last two resonators is 47.96 Ω. Transmission line with characteristic impedance of 58.58 Ω is needed for connecting the middle two resonators. The characteristic impedance of the first and fourth resonator is 17.69 Ω while the impedance of second and third resonators is 23.09 Ω. Physical parameters were obtained first with the ADS LineCalc tool and the structure was EM simulated and optimized subsequently. The length of transmission line connecting between the first and

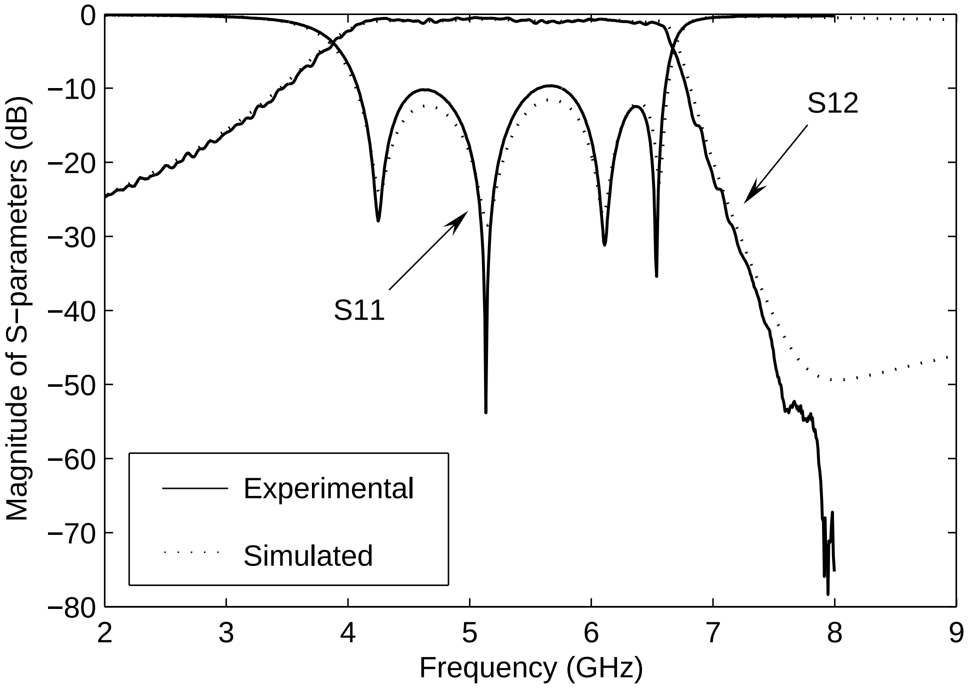

Figure 7.11: Experimental and simulated responses of the EBG based UWB bandpass filter with quarter wavelength shunt resonators.

second resonators in the final structure is 7.3 mm, while width is 2.4 mm. The width and length of the transmission line segment connecting the middle two resonators are 1.763 mm and 8.2 mm respectively. The end to end distance of the first set of resonators is 20.14 mm and the width is 3.73 mm. The dimensions of the last set of resonators are same as the first set of resonators. The end to end distance of the middle set of resonators is 21.948 mm while their width is 2.608 mm. Dimensions of 50 Ω transmission lines are same as the previous EBG microstrip UWB bandpass filter.

The conventional UWB thin metal layer bandpass filter was also fabricated on the same substrate using a standard printed circuit board fabrication method. Fig. 7.10 compares the physical sizes of the EBG-based UWB thin metal layer microstrip bandpass filter and a conventional UWB thin metal layer microstrip filter with quarter wavelength admittance inverters. Experimental and simulated responses of conventional UWB bandpass filter with quarter wavelength admittance inverters are given in Fig. 7.12 in order to compare to the EBG counterpart. Bandwidths and the passband ripple levels of both filters are similar. The steepness of the EBG-based filter response in the upper side of the passband is considerably higher compared to the conventional counterpart, while the filter response of the conventional filter is more symmetric in this particular example. The spacing between resonators of the EBG-based UWB filter is about $\lambda_g/14$ while, the spacing between resonators of the conventional UWB filter is about $\lambda_g/5.6$ where λ_g is the wavelength of the unloaded 50 Ω microstrip line at the centre frequency. Therefore, the EBG-based filter is about 30 percent more compact length-wise. The area of the EBG-based UWB filter is $0.627\ \lambda_g \times 0.295\lambda_g$ while that of the conventional UWB bandpass filter is $0.858\ \lambda_g \times 0.531\lambda_g$. Therefore, the total size reduction with respect to the conventional UWB filter with quarter wavelength admittance inverters is approximately 60 percent.

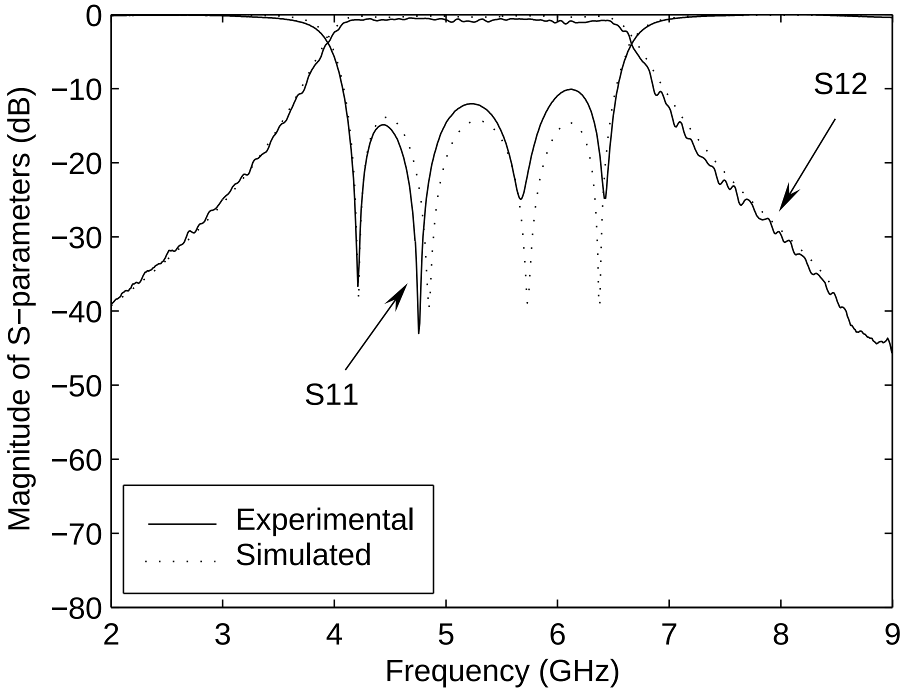

Figure 7.12: Experimental and simulated responses of conventional UWB bandpass filter with quarter wavelength admittance inverters.

7.5 Wideband CPW Bandpass Filter Based on EBG Concept

In the previous section shunt resonators in unit cells were realized with planar microstrip quarter wavelength resonators. Via holes were made in the substrate to allow the grounding of one end of the quarter wavelength resonators. CPW EBG structure is proposed as an alternative to microstrip EBG structure, eliminating via holes. Shunt resonators in unit cells are again realized from CPW distributed elements. However, quarter wavelength type resonance of nonuniform CPW transmission lines are used to obtain the shunt resonator characteristics of EBG unit cells required to miniaturize passband type EBG unit cells. The nonuniform CPW transmission line resonator is made by cascading two pieces of transmission lines having different charcteristic impedances, namely the stepped impedance resonator (SIR). Advantages of high aspect ratio LIGA CPWs are exploited to miniaturize SIRs.

7.5.1 Theory of SIRs

A circuit diagram of an SIR is illustrated in Fig. 7.13. A one open ended piece of transmission line with the characteristic impedance of Z_2, electrical length of θ_2 and physical length of d_2 is cascaded to another piece of one end grounded transmission line with the characteristic impedance of Z_1, electrical length of θ_1 and physical length of d_1. The *abcd* parameters of the cascaded two uniform transmission line sections can be expressed as [12],

$$\begin{aligned}
a &= \cos\theta_1\cos\theta_2 - \frac{\sin\theta_1\sin\theta_2}{K} \\
b &= j\left(Z_2\cos\theta_1\sin\theta_2 + Z_1\sin\theta_1\cos\theta_2\right) \\
c &= j\left(\frac{\sin\theta_1\cos\theta_2}{Z_1} + \frac{\cos\theta_1\sin\theta_2}{Z_2}\right) \\
d &= \cos\theta_1\cos\theta_2 - K\sin\theta_1\sin\theta_2
\end{aligned} \tag{7.25}$$

where $K = Z_1/Z_2$ is the impedance ratio. Since the transmission line segment with characteristic impedance Z_1 is shorted to ground and the load impedance at the shorted end is $Z_L = 0$, the admittance of the SIR from the open end is given as

$$Y_{in} = \frac{cZ_L + d}{aZ_L + b} = \frac{d}{b}. \tag{7.26}$$

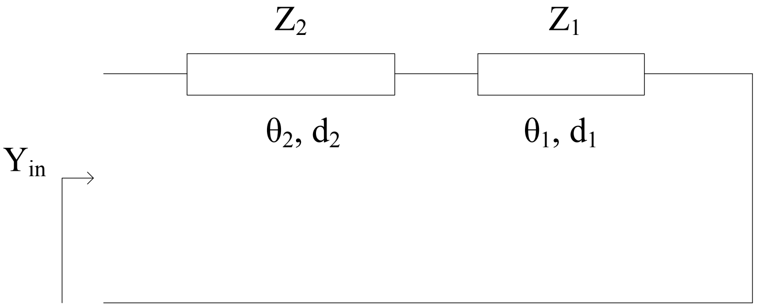

Figure 7.13: Circuit diagram of a one end short circuited SIR.

The condition for the fundamental resonance of the above SIR is $Y_{in} = 0$ [11], and Equation 7.26 suggests that the parameter $d = 0$ for the fundamental resonance, is expressed by

$$K \tan\theta_1 \tan\theta_2 = 1. \tag{7.27}$$

Assuming the phase constant of both transmission lines is the same and equal to β, the total length of the SIR at resonance can be found using Equation 7.27 and is given by

$$d = d_1 + d_2 = \frac{\theta_1 + \theta_2}{\beta} = \frac{\left\{\theta_1 + \tan^{-1}\left(\frac{1}{K\tan\theta_1}\right)\right\}}{\beta}. \tag{7.28}$$

The above equation suggests that the physical length of the resonator becomes minimum when the total electrical length $\theta = \theta_1 + \theta_2$ is minimum. In the resonator depicted in Fig. 7.13, $Z_1 > Z_2$, and θ has a minimum value when the differentiation of Equation 7.28 by θ_1 is equal to zero, which results in

$$\theta_1 = \theta_2 = \tan^{-1}\left(\sqrt{\frac{1}{K}}\right). \qquad (7.29)$$

It is evident from Equation 7.29 that the greater the impedance ratio K, the shorter the whole length of the resonator, and for a fixed K, the length of the resonator is minimum when the two transmission lines have the same electrical length. Table 7.1 shows a comparison of the impedance ratio K for CPW structures (given in Chapter 3) with $w = 0.5$ mm on 0.5 mm thick fused quartz substrate. As evident from Table 7.1, high aspect ratio CPW is especially useful for realizing SIR with large impedance ratio.

Table 7.1: Comparison of impedance ratio (K) with metal height (h)

h (mm)	Impedance, Z_2 (Ω) ($s = 0.05$ mm)	Impedance, Z_1 (Ω) ($s = 0.95$ mm)	K
0.01	45.87	109.40	2.38
0.22	20.83	94.15	4.52
0.80	9.45	70.55	7.47

7.5.2 EBG Based CPW Filter Design

Shunt lumped resonators in the proposed representative EBG unit cells can be realized as SIRs in CPW structures. EBG unit cells are made more compact by reducing the physical length of equivalent shunt distributed resonators using SIRs, unlike in microstrip unit cells used in UWB filter design in the previous section. In designing SIRs in EBG unit cells used in wideband filter design, parameters of equivalent SIRs cannot be evaluated considering a single frequency as in designing the microstrip EBG unit cells in the previous section, unlike with the narrow band filter design. Hence, the admittance of equivalent SIR equates to the admittance of lumped resonators which was evaluated from Equations 7.11 and 7.12 for a particular bandpass filter, at band edge angular frequencies ω_1 and ω_2 in designing the equivalent SIR.

The input admittance of the SIR in Fig. 7.13 can be determined from

$$Y_{in} = -j\frac{1 - K\tan\theta_1\tan\theta_2}{Z_2\left(\tan\theta_2 + K\tan\theta_1\right)}. \tag{7.30}$$

Earlier it was mentioned that the total length of SIR is minimum when individual electrical lengths of transmission line segments are equal. Hence, the physical length of the transmission line segments are kept constant, assuming the propagation constants of both lines are equal. Electrical length of a transmission line segment can be expressed in terms of angular resonant frequency of the SIR, ω_r as $\theta_1 = \theta_2 = \alpha\omega/\omega_r$ where $\alpha = \tan^{-1}\sqrt{1/K}$. In order to determine the characteristic impedances and resonant frequency of the equivalent SIR for a given K, the following equations are obtained using Equation 7.30 and by Equating the susceptances of the SIR line and LC loading at ω_1 and ω_2 as,

$$\frac{1 - K\tan^2\left(\frac{\alpha\omega_1}{\omega_r}\right)}{Z_2\left(K+1\right)\tan\left(\frac{\alpha\omega_1}{\omega_r}\right)} = -\left(C\omega_1 - \frac{1}{L\omega_1}\right) \tag{7.31}$$

and

$$\frac{1 - K\tan^2\left(\frac{\alpha\omega_2}{\omega_r}\right)}{Z_2\left(K+1\right)\tan\left(\frac{\alpha\omega_2}{\omega_r}\right)} = -\left(C\omega_2 - \frac{1}{L\omega_2}\right), \tag{7.32}$$

respectively. Dividing Equation 7.31 by Equation 7.32, Z_2 is eliminated and one nonlinear function, $F(\omega_r)$ with unknown variable, ω_r, is obtained for solving using Newton's iterative technique. Taking the angular resonant frequency of lumped resonators as an initial guess for ω_r, the angular resonant frequency ω_r is found following the same procedure given for designing microstrip quarter wavelength shunt resonator in the previous section. Z_1 and Z_2 are determined subsequently for a given K. SIR design equations obtained in an different approach is given in [106].

From Equations 7.11 and 7.12, it is evident that the values of the right hand sides of Equation 7.31 and 7.32 increase with further decrease of physical length,

d from the length that results in minimum C around $k_0d/2 \approx \pi/4$. Hence, the required Z_2 for SIR decreases. Fig. 7.14 shows the required Z_2 of the shunt SIR normalized to Z_0 (characteristic impedance of the unloaded transmission line) versus the SIR impedance ratio, K, for 45^0 and 60^0 electrically long unit cells in 50 percent and 70 percent bandwidth filters. It is evident that the required Z_2 in the SIR with higher K for a smaller unit cell in both lateral and transverse directions decreases. The required low impedance CPW line which would be considerably difficult to realize in planar transmission lines can be effectively realized using high aspect ratio LIGA fabricated structures, without requiring prohibitively narrow conductor to ground spacing.

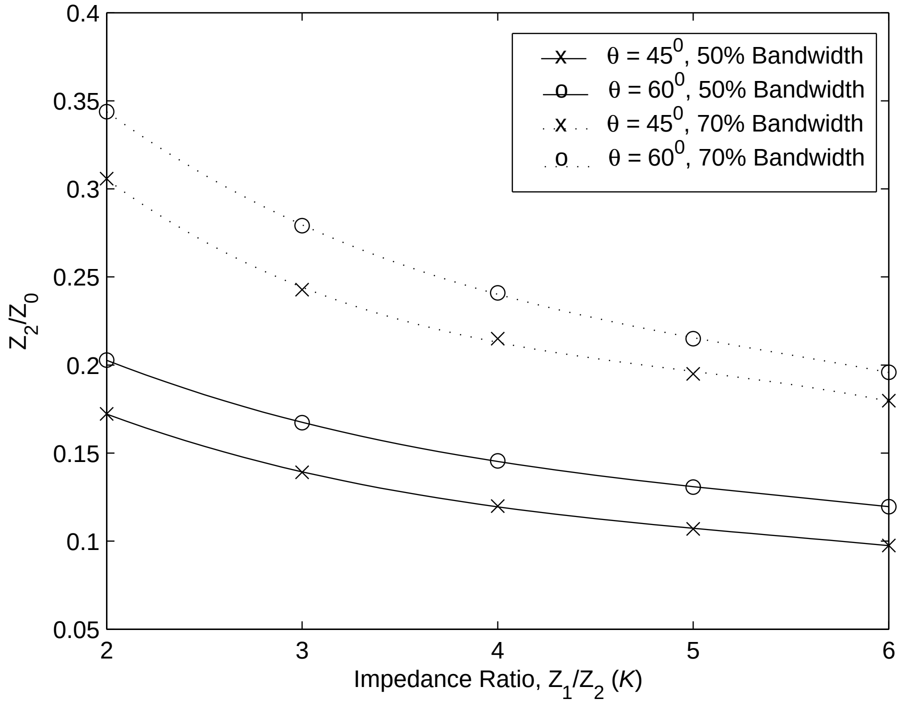

Figure 7.14: Required normalized Z_2 of SIR vs. impedance ratio Z_1/Z_2 $(K)$for 50 percent and 70 percent bandwidth bandpass filters with 45^0 and 60^0 long unit cells.

A 50 percent bandwidth (with respect to EBG band edge frequencies f_1 and f_2) UWB EBG-based CPW bandpass filter with $f_1 = 6.246$ GHz and $f_2 = 10.246$ GHz and four cascaded unit cells was designed to demonstrate an EBG based

UWB filter miniaturized using the advantages of high aspect ratio LIGA structures. For the above frequency specifications, the lumped element parameters were obtained first using Equations 7.11 and 7.12, assuming 40^0 long unit cells. Evaluated lumped parameter values of CZ_0 and L/Z_0 for the above specifications are 111.53 pFΩ and 5.162 pHΩ^{-1} respectively. The characteristic impedance of the transmission line to be loaded with shunt resonators, Z_0, was selected to be 110 Ω. The response of four cascaded unit cells modeled with ideal elements in a 50 Ω system was obtained using the ADS$^{\text{TM}}$ circuit simulator and was optimized to reduce passband ripples. Passband ripple level was minimized by increasing the characteristic impedance of the transmission line segment connecting the middle two shunt resonators, to 132.88 Ω. The prototyped responses of the optimized filter network is illustrated in Fig. 7.15. Shunt resonators were realized with grounded SIRs as shown in Fig. 7.16. The characteristic impedances and the resonant frequency of equivalent shunt SIRs were evaluated using Equations 7.31

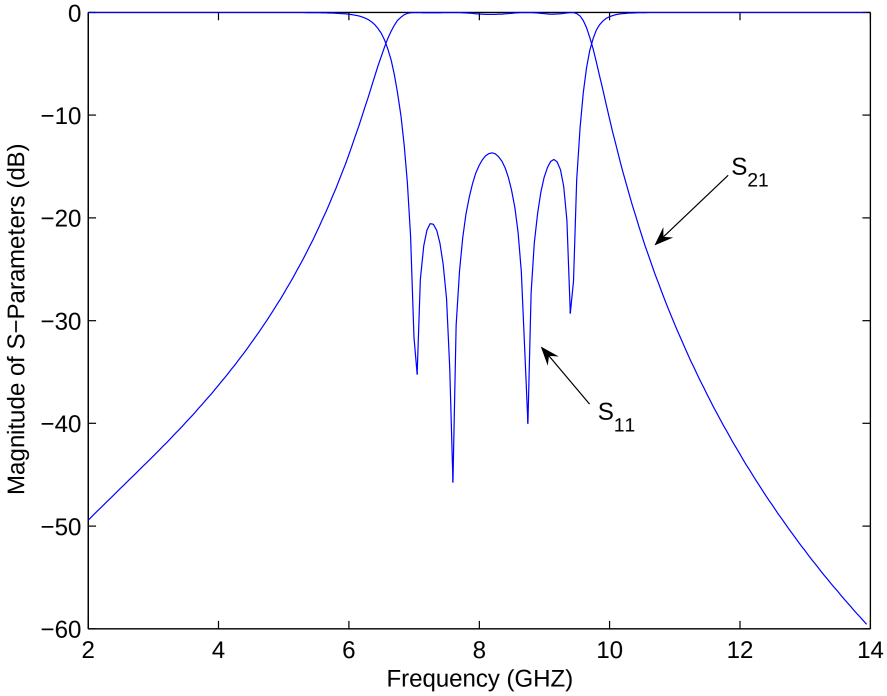

Figure 7.15: Prototyped responses of the EBG based UWB CPW bandpass filter with $f_1 = 6.246$ GHZ and $f_2 = 10.246$ GHZ.

and 7.32, as described previously, to obtain approximately equivalent characteristics to the required lumped shunt resonators. The impedance ratio of SIRs was selected as $K = 5$. The evaluated characteristic impedances, Z_1, Z_2 and the resonant frequency of the required SIRs are 53.65 Ω, 10.73 Ω, and 6.667 GHz. Since CPW structures are usually symmetrical around the signal trace, each EBG CPW unit cell contains two SIRs connected in shunt to the main signal trace. Hence, impedances of SIRs in CPW unit cells are double the required impedances for SIRs in unit cells that contain a single SIR, in other words, Z_1 and Z_2 of SIRs in CPW unit cells are 107.3 Ω and 21.46 Ω respectively. Choosing the impedance ratio of SIRs, K, as high as possible is important for achieving a greater degree of SIR miniaturization. However, K should be chosen carefully not to come across unrealizable impedances (Z_1 and Z_2) with the selected structure.

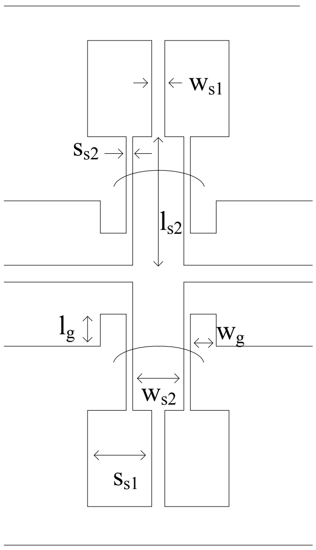

Figure 7.16: A tall metal CPW EBG unit cell-110 Ω transmission line shunt loaded with SIRs with $Z_1 = 107.3\Omega$ and $Z_2 = 21.46\Omega$.

7.5.3 Experimental Results

A real tall metal CPW structure on a 0.5 mm thick fused quartz substrate with dielectric constant of 3.78 was designed for the above EBG-based UWB bandpass filter. A unit cell of the filter structure has been illustrated in Fig. 7.16 along with dimensional variables. Physical parameters of the EBG based CPW filter with $f_1 = 6.246$ GHz and $f_2 = 10.246$ GHz shown in Fig. 7.17, were found initially using some CPW characteristics which were obtained from EM simulation and appended in Chapter 3. Next, the above EBG-based UWB bandpass filter was analyzed and filter performance optimized using HFSS. Dimensions of the unit cell are $w_{s1} = 0.15$ mm, $s_{s1} = 0.806$ mm, $w_{s2} = 0.5$ mm, $s_{s2} = 0.051$ mm, $l_{s2} = 2.36$ mm, $l_g = 1.039$ mm, and $w_g = 0.35$ mm. The length of the high impedance transmission line is 2.17 mm. The width of the signal trace of 110 Ω transmission line is 0.268 mm and signal to ground spacing is 1.2 mm. The normal length of unit cells, d, is 2.95 mm. However, the length of the transmission line segment whose width of the signal trace is 0.08 mm and the signal to ground spacing is 1.344 mm, connecting the two middle SIRs is 2.355 mm. The width of signal traces of 50 Ω transmission line sections leading to external ports is 0.25 mm and their signal to ground spacing is 0.17 mm. The ground in both side of SIRs are wire bonded as shown in Fig. 7.16 in order to keep the ground in same potential thereby not introducing series inductance. Conductive epoxy glue is used to connect the bonding wire to the nickel ground. The ultra sonic wirebonding is not successful on nickel structures. TRL calibration lines were also designed to calibrate the Agilent$^{\text{TM}}$ 8722 ES VNA in order to measure the CPW filter performance with better accuracy (Refer Appendix E).

Fig. 7.17 shows the LIGA fabricated EBG based UWB CPW bandpass filter with $f_1 = 6.246$ GHz and $f_2 = 10.246$ GHz. An SEM micrograph of the region indicated by the circle in Fig. 7.17 is shown in Fig. 7.18 to illustrate precise structure, extremely smooth and vertical sidewalls, and tall narrow (approx. 50 μm) coupling gaps.

Scattering parameters of this filter were measured using Cascade$^{\text{TM}}$ coplanar air probes with a signal to ground pitch of 0.75 mm. LIGA fabricated TRL standard transmission lines were used for the calibration of Agilent$^{\text{TM}}$ 8722 ES VNA. The minimum passband insertion loss and the maximum passband return loss

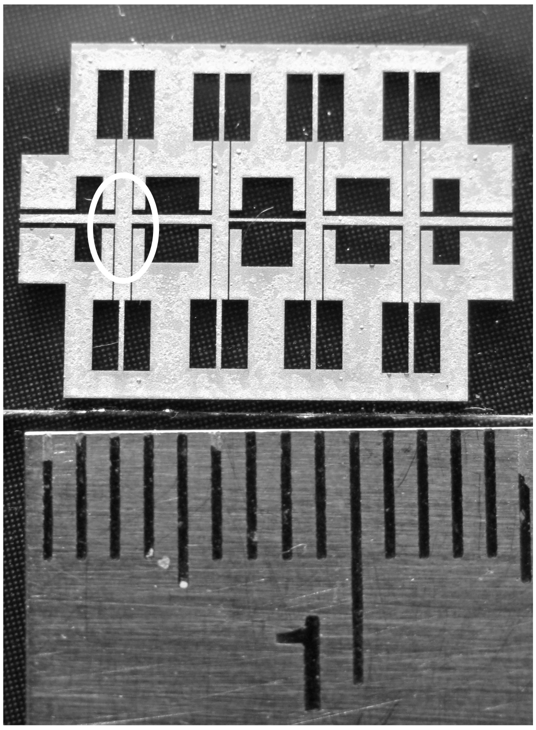

Figure 7.17: EBG based UWB CPW bandpass filter (before addition of bondwires) with $f_1 = 6.246$ GHz and $f_2 = 10.246$ GHz.

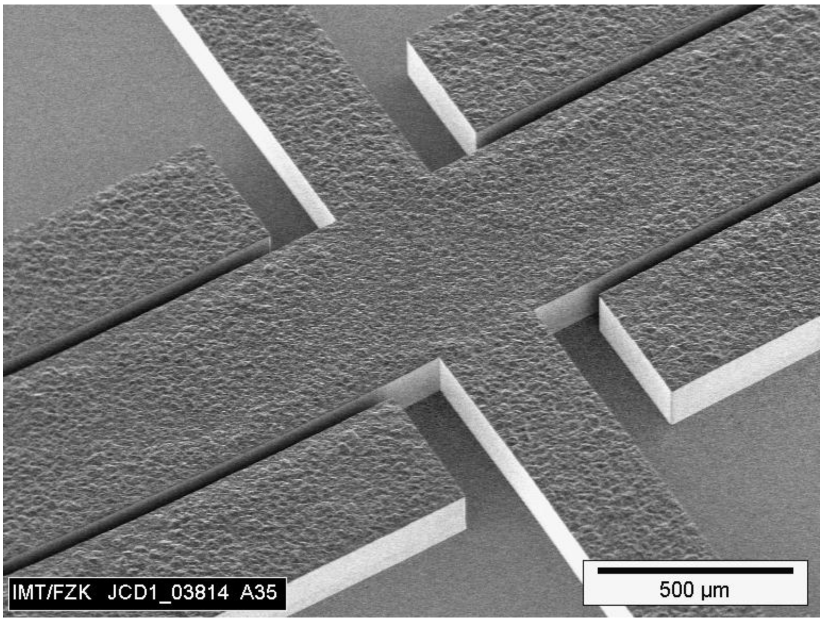

Figure 7.18: SEM micrograph of the region indicated by circle in Fig. 7.17. The 110 Ω CPW transmission line runs from top-left to bottom-right and the 21.5 Ω low-impedance portions of the shunt SIRs run from bottom-left to top-right. (Courtesy of IMT).

of the filter obtained from EM simulation using an adaptive mesh with approximately 85000 tetrahedral elements are 0.4292 dB and 13.02 dB as depicted in Fig. 7.19. Fig. 7.19 also shows measurement results of the fabricated EBG-based CPW filter. As evident from Fig. 7.19, good agreement has been found between measured and EM simulated responses of the EBG-based CPW UWB filter. The fabricated filter has slightly higher minimum passband insertion loss (1.2 dB) and slightly better return loss (14 dB). The experimental response has also slightly shifted upward in the frequency axis because the nickel height of the fabricated filter is higher than the designed value. The group delay of this filter is shown in Fig. 7.20.

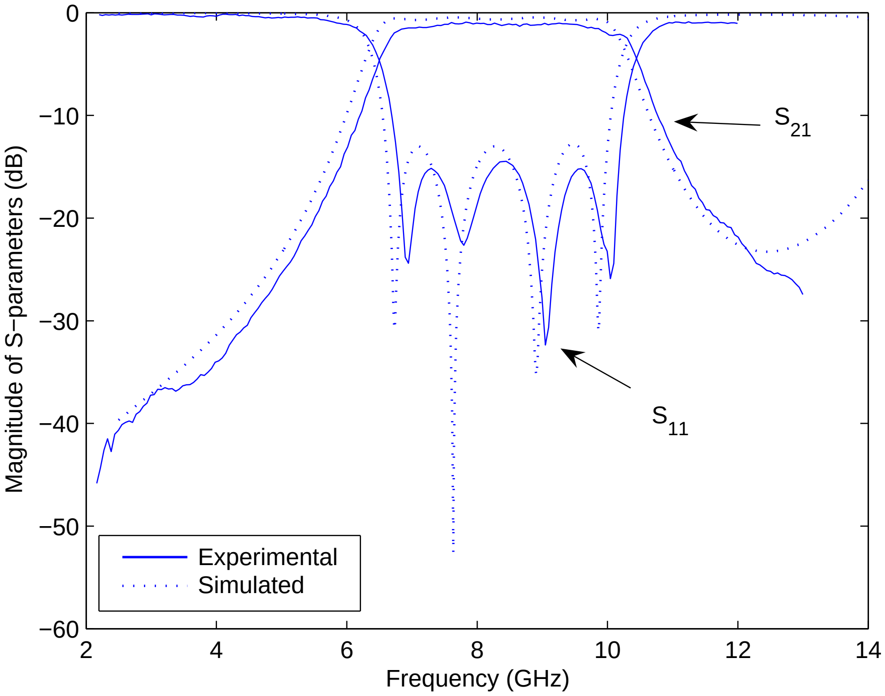

Figure 7.19: Experimental and simulated responses of the EBG based UWB CPW bandpass filter with $f_1 = 6.246$ GHz and $f_2 = 10.246$ GHz.

A conventional UWB CPW bandpass filter with similar performance to the above EBG-based miniaturized UWB CPW filter, consisting of quarter wavelength resonators connected with quarter wavelength admittance inverters (proximity coupling is not practical for realizing admittance inverters of UWB bandpass

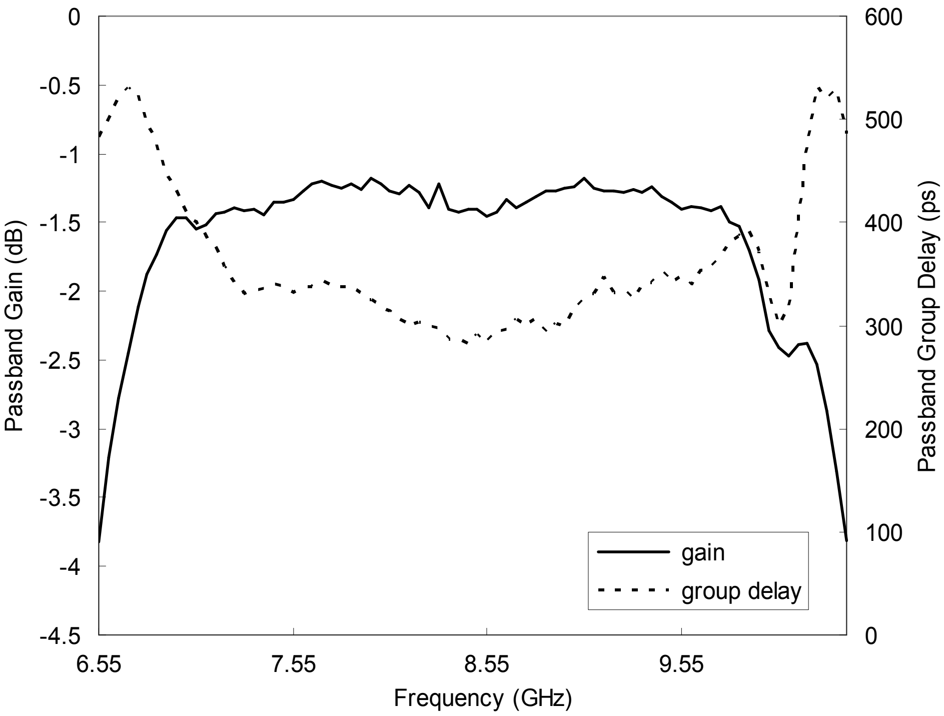

Figure 7.20: Group delay of the EBG based UWB CPW pandpass filter with $f_1 = 6.246$ GHz and $f_2 = 10.246$ GHz.

filters with quarter wavelength resonators with one end grounded) was also designed in order to compare the physical size of the EBG-based UWB bandpass filter with its conventional counterpart. Wideband design equations in Appendix D were used here as well since use of narrowband design formulas cause bandwidth contraction. Evaluated impedance of the quarter wavelength transmission lines connecting the first two sets of resonators and last two sets of resonators is 48.8 Ω. Transmission line with characteristic impedance of 59.86 Ω is needed for connecting the middle two resonators. The evaluated characteristic impedance of the first and fourth resonator is 15.28 Ω while the impedance of second and third resonators is 23.09 Ω. Since these resonators are realized with the symmetrical CPW structure, two quarter wavelength shunt transmission lines with double the required impedances were used for these resonators (i.e. 30.56 Ω lines for first and fourth resonators and 46.18 Ω lines for second and third resonators).

A physical structure for the conventional CPW UWB bandpass filter was also designed on the same substrate. Conductor height, h, is selected to be same as

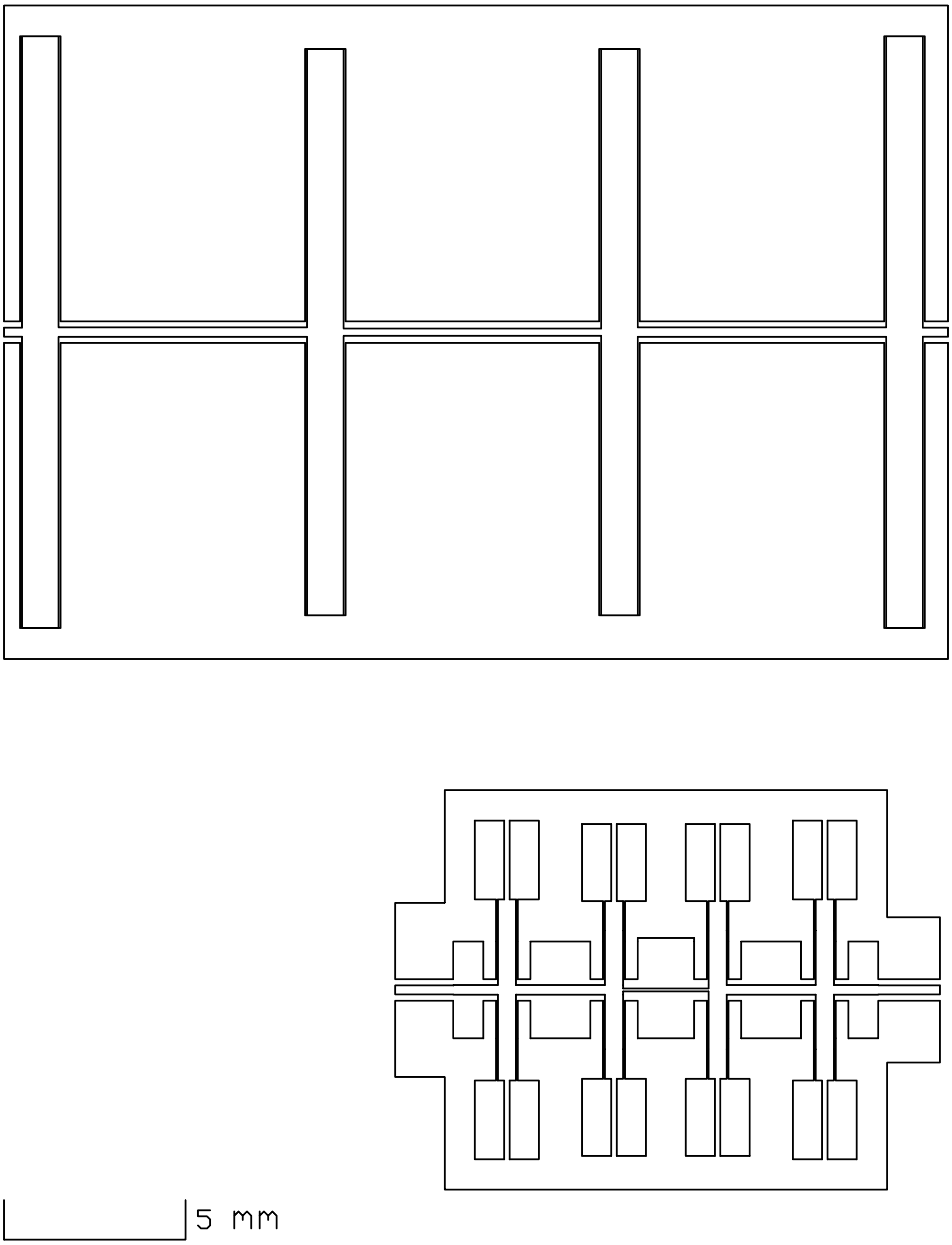

Figure 7.21: Comparison of physical sizes of the EBG-based CPW UWB bandpass filter and a conventional CPW UWB filter with quarter wavelength admittance inverters; Top: Sketch of conventional CPW UWB filter, Bottom: Sketch EBG based CPW UWB pandpass filter. Both sketches are drawn in the same scale.

that of the EBG-based CPW filter because low impedance shunt resonators are difficult to realize with its planar version. The structure was EM simulated and optimized to reduce passband return loss. The signal trace width and signal to ground spacing of all shunt quarter wavelength resonators are 1 mm and 0.06 mm respectively, while the length of first and fourth set of resonators and the length of middle two set of resonators are 8.019 mm and 7.669 mm, respectively. The signal trace width and the signal to ground spacing of CPW sections (admittance inverters) connecting the first and second sets of resonators and CPW sections connecting the third and fourth sets of resonators are 0.262 mm and 0.164 mm respectively while the length of these admittance inverters is 6.85 mm. The width of the signal trace, signal to ground spacing and the length of the admittance inverter in between the middle two sets of resonators are 0.2 mm, 0.195 mm and 7.1 mm, respectively. Ground planes in both sides of shunt resonators are connected with bond wires near to the common junction.

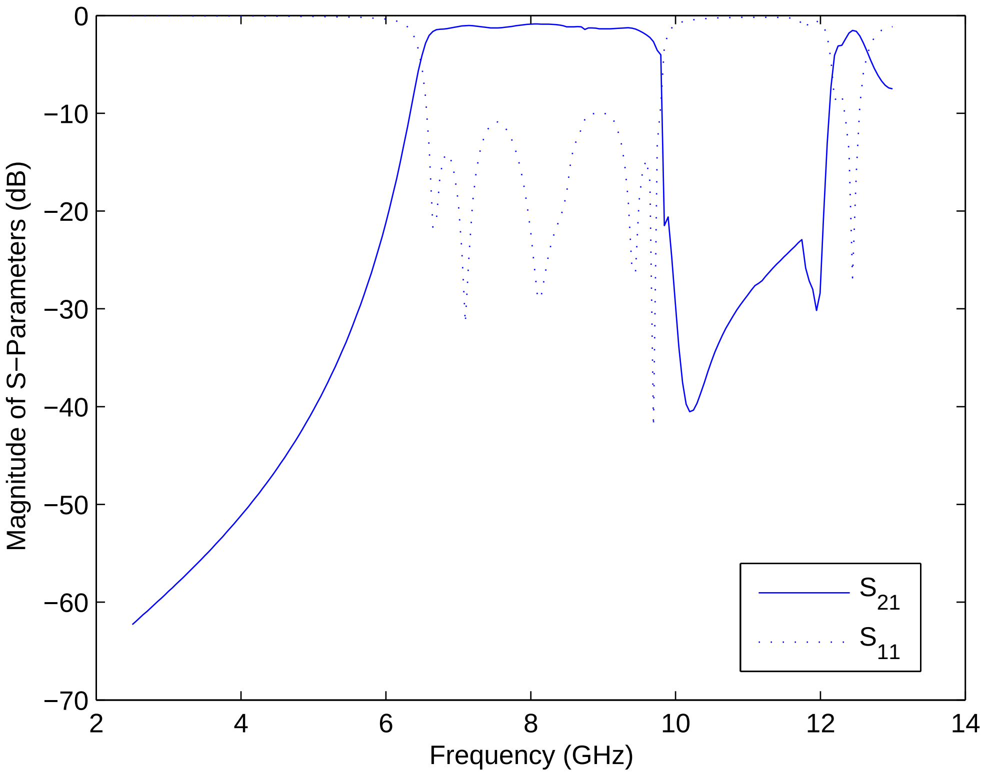

Figure 7.22: Simulated responses of the conventional UWB CPW bandpass filter depicted in Fig. 7.21.

Fig. 7.21 compares the physical sizes of the EBG-based CPW UWB bandpass filter and a conventional CPW UWB filter with quarter wavelength admittance inverters. The simulated responses of the conventional CPW UWB bandpass filter with quarter wavelength admittance inverters are given in Fig. 7.22 in order to compare to the EBG counterpart. The bandwidths of both filters are similar. The passband ripple level of the return loss curve of the conventional CPW UWB bandpass filter is higher than that of the EBG counterpart whose response is more symmetric. The spacing between resonators of the EBG-based UWB CPW filter is about $\lambda_g/12$ while, the spacing between resonators of the conventional UWB filter is about $\lambda_g/4$ where λ_g is the wavelength of the unloaded 50 λ_g microstrip line at the centre frequency. Therefore, the EBG-based CPW filter is about 47 percent more compact length-wise. The normal length of SIRs in EBG-based CPW bandpass filter is about $\lambda_g/6.5$ while, the length of resonators of conventional CPW bandpass filter is about $\lambda_g/3.6$. Hence, SIRs are 55 percent more compact length-wise. The area of the EBG-based UWB CPW filter is $0.406\lambda_g \times 0.323\lambda_g$ while that of the conventional UWB bandpass filter is $0.864\lambda_g \times 0.565\lambda_g$. Therefore, the total size reduction with respect to the conventional UWB filter with quarter wavelength admittance inverters is approximately 73 percent.

Chapter 8

Conclusions

8.1 Summary

The motivation behind this work was to exploit the advantages of high aspect ratio (tall) structures of high precision into microwave transmission lines and filters to achieve good performance and miniaturization in novel ways. The LIGA process allows the fabrication of very accurately patterned high aspect ratio metal structures with optical quality side walls. These high aspect ratio structures are useful in realizing low impedance and low loss transmission lines and tightly coupled structures for microwave circuits. In response to this motivation, high aspect ratio microstrip folded open loop resonator filters and diplexers and high aspect ratio CPW wideband filters based on EBG concepts were mainly presented.

Characteristics of high aspect ratio microstrip and CPW transmission lines were investigated. The characteristic impedances of high aspect ratio microstrip and CPW lines are relatively low compared with their planar counterparts. It was demonstrated that high aspect ratio CPW with characteristic impedance 10-20 Ω can be realized with relatively narrow ground to ground spacing. Similarly, the high aspect ratio microstrip line with a certain impedance is narrower than its planar line of the same impedance. The attenuation of these high aspect ratio lines is also relatively low compared with planer lines with the same dimensions.

A high aspect ratio microstrip folded half wavelength open loop resonator was introduced. Two effective configurations for external gap coupling with the open loop resonator were given. It was found that high aspect ratio external gap coupling structures are better coupled with high aspect ratio open loop resonators than with planer coupling structures. The unloaded quality factor of high aspect ratio open loop resonators is higher than the unloaded quality factor of thin open loop resonators. It was found that there can be a difference of unloaded quality factors between high aspect ratio and planar open loop resonators as high as 100.

A second order filter with a transmission zero in the upper stopband, consisting of high aspect ratio single mode open loop resonators was presented to demonstrate the advantages of high aspect ratio structures in realizing lower external quality factors or tight coupling. The transmission zero was created by bypass coupling realized from extending the side couplings arms to the non adjacent single mode open loop resonator. A second order filter with a transmission zero in the lower stopband was also synthesized and designed changing the orientation of open loop resonators. The simulated results of these second order filters were experimentally verified.

Higher order filters with transmission zeros in their stopband were also synthesized manipulating a coupling matrix based optimization technique and designed using high aspect ratio half wavelength folded microstrip resonators. Network topologies with both source and load coupled with adjacent and immediate non-adjacent resonant nodes were given for fourth order filters with two transmission zeros in the upper or lower stopband. These fourth order networks were designed on high aspect ratio microstrip structures. A third order high aspect ratio microstrip bandpass filter consisting of open loop resonators with a transmission zero in both stopbands was designed by extending the coupling arms of both source and load up to the non adjacent resonator. High aspect ratio folded half wavelength open loop resonator based third order coupling structures to produce bandpass filter responses with two transmission zeros in the upper or lower stopband using source/load multi-resonator coupling were also presented.

A second order high aspect ratio diplexer with appropriately located two transmission zeros was designed combining the above mentioned second order bandpass filters. The required tight direct and bypass couplings were effectively realized from high aspect ratio coupling gaps in LIGA structures. It was experimentally verified. A third order high aspect ratio diplexer with appropriately located four transmission zeros was also designed combining the above mentioned third order bandpass filters to produce higher channel isolation.

An ultra wideband (60 percent with respect to EBG band edge frequencies) EBG-based bandpass filter with four 80^0 electrically long unit cells was realized in microstrip form with quarter wavelength resonators and EM simulated results and experimental results were compared to verify the design method. Finally, about 30 percent in length and 60 percent in overall size reductions were obtained with the EBG-based filter over a representative conventional counterpart. To achieve further size reduction, applications of LIGA fabrication method in wideband filter design were demonstrated by designing and fabricating a high-aspect-ratio CPW wideband electromagnetic bandgap filter with 3-dB bandwidth of 47 percent. The EBG-based filter was miniaturized by reducing the EBG unit cell width effectively, through realization of high-aspect-ratio CPW stepped impedance resonators. The resultant SIR low impedance line sections, which might be prohibitive to fabricate with traditional planar methods, were accurately and effectively realized using deep X-ray lithography fabrication. Finally, 53 percent reduction in transverse length using the EBG concept in filter design, 43 percent reduction in width using high-aspect-ratio SIRs, and 73 percent reduction in overall size were obtained with the high-aspect-ratio CPW EBG-based filter over a representative conventionally designed counterpart.

8.2 Contributions

A number of unique contributions to the field have been made during the course of this work, including the followings.

- Unloaded quality factor and external quality factor of high aspect ratio microstrip folded half wave length resonators were investigated.
- An effective method of achieving source/load bypass coupling with non adjacent microstrip folded resonators was established. Second order high aspect ratio microstrip filters with half wavelength resonators were designed and realized to demonstrate this source/load bypass coupling method and tight coupling capabilities of high aspect ratio structures. An expression to calculate external quality factor for the resonators coupled to source/load via a reactance was established to use in the above filter design.
- Higher order filter topologies for creating transmission zeros were presented. An optimization technique was used in design these higher order filters. The convergence of two optimization functions was compared.
- A passband type EBG based filter design method was developed to realize compact filters. This method was verified by fabricating microstrip wideband bandpass filters. Employing this EBG based filter design method, further size reduction of a wideband bandpass filter was achieved in a high aspect ratio CPW structure using SIRs with very low impedance transmission line sections.

8.3 Future Work

Although filtering structures with very accurate lateral dimensions and very smooth side walls (near optical quality) were realized utilizing the LIGA process, there is room for improving the uniformity of vertical metal height. A suitable top surface polishing technique can be investigated to maintain smooth top metal surface of

LIGA structures. Instead of Nickel as the electroplating metal for LIGA structures with a thickness applied in this work, a metal with higher conductivity should be used to reduce losses in microwave devices.

EBG based highpass and lowpass filters in high aspect ratio structures can be exploited to achieve size reduction and better performance. Applying high aspect ratio LIGA fabricated structures in realizing meta materials is an another potential research area.

Appendix A

Layout

Fig. A.1 illustrates the layout of devices that are fabricated using the LIGA process. Blue (or dark) and green (or light) straight lines indicate paths for dicing. The substrate is diced first along the blue (or dark) lines. Then the diced pieces in the first stage are again diced along the green (or light) lines in the second and third stages of dicing.

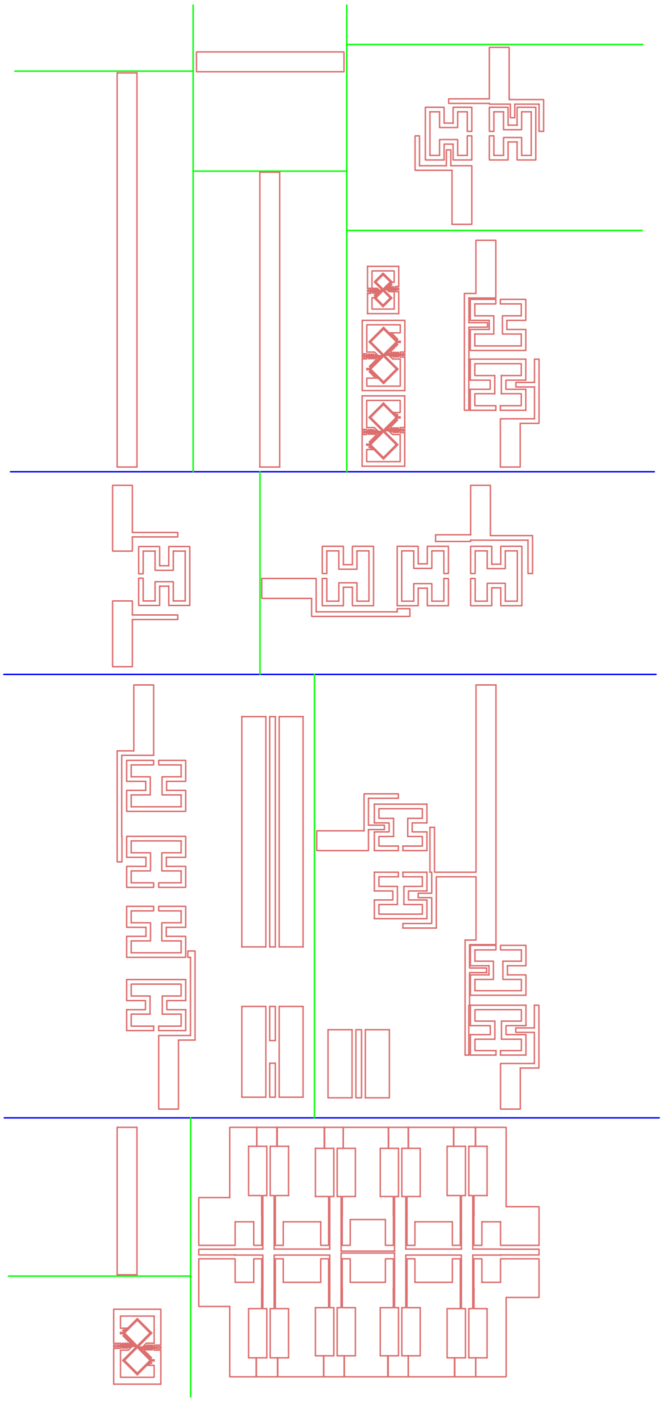

Figure A.1: Device layout.

Appendix B

More Details on Network Synthesis

B.0.1 Asymmetric Filter with One Transmission Zero in the Higher Stopband

Filter specifications given in Section 4.3.1 are $R = -20$ dB and $\omega' = 4.42$. Using $\epsilon = (10^{R/10} - 1)^{1/2}$, ϵ is found to be 0.1. Using Equations 4.3 and 4.4, we obtain

$$F_2(\omega') = -8.7254 \frac{\omega'^2 - 0.1146\omega' - 0.4934}{\omega' - 4.42}. \tag{A.1}$$

Hence,

$$\begin{aligned} |S_{11}(\omega')|^2 &= \frac{\epsilon^2 F_2^2(\omega')}{1 + \epsilon^2 F_2^2(\omega')} \\ & \frac{(\omega'^2 - 0.1146\omega' - 0.4934)^2}{\omega'^4 - 0.2292\omega'^3 + 0.3398\omega'^2 - 11.4982\omega' + 25.9045} \end{aligned} \tag{A.2}$$

Taking $\omega' = jp$, poles of of $|S_{11}(\omega')|^2$ are found to be, $2.1278 - j1.551$, $-2.1278 - j1.551$, $0.9817 + j1.6652$ and $-0.9817 + j1.6652$. From left half plane poles, $S_{11}(p)$ is formulated as,

$$S_{11}(p) = \alpha \frac{-p^2 + j0.1146p - 0.4934}{p^2 + 3.1095p - j0.1146p + 4.6771 - j2.0211}. \tag{A.3}$$

where α is an unknown constant. When $p \rightarrow \alpha$, $S_{11}(p) \rightarrow 1$. To satisfy this condition, α should be equal to -1. Now, the input admittance function is formed as,

$$\begin{aligned} Y(p) &= \frac{1+S_{11}(p)}{1-S_{11}(p)} \\ & \frac{2p^2+3.1095p+5.1646-j1.7919}{3.1095p+4.1778-j2.0211}. \end{aligned} \tag{A.4}$$

The variables encountered in the synthesis cycle are shown in Fig. B.1. $Y(p)$ has a pole at $p=\infty$. Thus we can extract capacitor C_1 as

$$C_1 = \left.\frac{Y(p)}{p}\right|_{p=\infty} = 0.6432. \tag{A.5}$$

Hence, the remaining admittance

$$\begin{aligned} Y_1(p) &= Y(p) - C_1 p \\ & \frac{0.4223p + j1.0708p + 5.1646 - j2.0211}{3.1095p + 4.1778 - 2.0211j}. \end{aligned} \tag{A.6}$$

Frequency invariant susceptance may now be extracted from Y_1 such that the remaining admittance after the extraction, Y_2 possesses a transmission zero at $p = j4.42$ (i.e. $Y_2(j4.42) = 0$). If a susceptance, jB_1, equal to $Y_1(j4.42)$ is extracted, then the remaining admittance at $p = j4.42$, $Y_2(j4.42)$, should be equal to zero. Hence,

$$\begin{aligned} Y_1(p) &= jB_1 + Y_2(p) \\ & -j0.0368 + \frac{(p-j4.42)(A+jD)}{3.1095p+4.1778-2.0211j} \end{aligned} \tag{A.7}$$

where A and D are unknown constants. Equating coefficients of p, A is found to be 0.4223 while, equating coefficients of *jp*, D is found to be equal to 1.1852. $Z_2(p)$ $(1/Y_2(p))$ may be synthesized into a series bandstop resonator (to produce the transmission zero) and the remaining impedance by using a partial fraction expansion as given below,

$$Z_2(p) = \frac{K}{p-j4.42} + \frac{E}{0.4223+j1.1852} \tag{A.8}$$

where

$$K = \left. Z_2(P)(p-j4.42)\right|_{p=j4.42} = 9.8913 \tag{A.9}$$

and E is found to be 3.1095 by equating coefficients of p. The first term in Equation A.8 consists of a capacitor, $C_2 = 1/9.8913 = 0.101$ and a frequency invariant susceptance, $B'_2 = -4.42/9.8913 = -0.4469$. The second term consists of a frequency invariant susceptance, $B'_3 = 0.4296$, in series with a resistor, $r_{02} = 0.8295$.

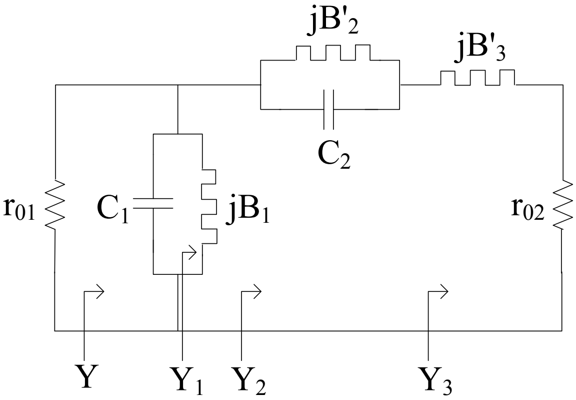

Figure B.1: Synthesis cycle.

Appendix C

Two Port Network

A two port network connected to a voltage source, e, with internal resistance R_1 and to a load R_2 is shown in Fig. C.1. V_1^+ and V_2^+ are voltages of incident waves a_1 and a_2 respectively while V_1^- and V_2^- are voltages of reflected waves b_1 and b_2 respectively. Hence, $a_i = V_i^+/\sqrt{R_i}$ and $b_i = V_i^-/\sqrt{R_i}$. I_0 and I_L are currents at the first and second ports.

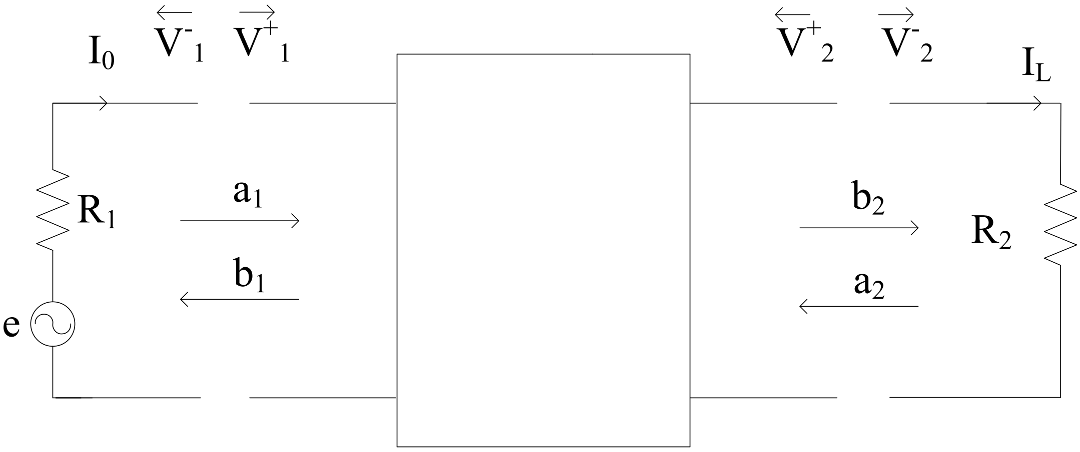

Figure C.1: Two port network.

In order to calculate S_{21} and S_{11}, the load should be matched (i.e. a_2, $V_2^+ = 0$). Hence,

$$\begin{aligned} V_2 &= V_2^+ + V_2^- = V_2^- = I_L R_2 \\ b_2 &= I_L\sqrt{R_2}. \end{aligned} \tag{A.1}$$

Similarly for the input side, following relationships can be obtained;

$$\begin{aligned}
I_0 &= \frac{V_1^+}{R_1} - \frac{V_1^-}{R_1} \\
V_1 &= V_1^+ + V_1^- = e - I_0 R_1 \\
a_1 + b_1 &= \frac{e}{\sqrt{R_1}} - I_0\sqrt{R_1} \\
& \frac{e}{\sqrt{R_1}} - \left(\frac{a_1}{\sqrt{R_1}} - \frac{b_1}{\sqrt{R_1}}\right)\sqrt{R_1} \\
a_1 &= \frac{e}{2\sqrt{R_1}} \\
b_1 &= \frac{e - 2I_0R_1}{2\sqrt{R_1}}.
\end{aligned} \tag{A.2}$$

Now using Equations A.1 and A.2, S_{21} and S_{11} can be found as,

$$\begin{aligned}
S_{21} &= \left.\frac{b_2}{a_1}\right|_{a_2=0} = \frac{2\sqrt{R_1R_2}I_L}{e} \\
S_{11} &= \left.\frac{b_1}{a_1}\right|_{a_2=0} = 1 - \frac{2R_1I_0}{e}.
\end{aligned} \tag{A.3}$$

Appendix D

Dispersion Relation for Periodically Shunt *LC* Loaded Transmission Line and Wideband Filter Design Equations

D.1 Dispersion Relation

The dispersion relation for the structure obtained cascading the shunt LC loaded unit cell shown in Fig. 7.2(a) is determined. V_n, I_n are the voltage and the current respectively at the input terminal of n^{th} the unit cell while V_{n+1}, I_{n+1} are those at the output terminal. Terminal voltages and currents can be related as,

$$\begin{pmatrix} V_n \\ I_n \end{pmatrix} = \begin{pmatrix} \cos\frac{\theta}{2} & jZ_0\sin\frac{\theta}{2} \\ \frac{j\sin\frac{\theta}{2}}{Z_0} & \cos\frac{\theta}{2} \end{pmatrix} \begin{pmatrix} 1 & 0 \\ jB & 1 \end{pmatrix} \begin{pmatrix} \cos\frac{\theta}{2} & jZ_0\sin\frac{\theta}{2} \\ \frac{j\sin\frac{\theta}{2}}{Z_0} & \cos\frac{\theta}{2} \end{pmatrix} \begin{pmatrix} V_{n+1} \\ I_{n+1} \end{pmatrix} \tag{A.1}$$

where θ, jB and Z_0 are as defined in chapter 4. The *abcd* matrix of the unit cell is found to be,

$$\begin{pmatrix} a & b \\ c & d \end{pmatrix} = \begin{pmatrix} \cos\theta - \frac{Z_0 b}{2}\sin\theta & jZ_0(\sin\theta - Z_0 b\sin^2\frac{\theta}{2}) \\ j(\frac{\sin\theta}{Z_0} + b\cos^2\frac{\theta}{2}) & \cos\theta - \frac{Z_0 b}{2}\sin\theta \end{pmatrix}. \tag{A.2}$$

If the periodic structure is supporting a propagating wave, the relations, $V_{n+1} = e^{-\gamma d}V_n$ and $I_{n+1} = e^{-\gamma d}I_n$ should hold, where $\gamma = \alpha + j\beta$ is the propagation constant for the periodic structure. In terms of transmission matrix, it can be given as,

$$\left(\begin{pmatrix} a & b \\ c & d \end{pmatrix} - \begin{pmatrix} e^{\gamma d} & 0 \\ 0 & e^{\gamma d} \end{pmatrix}\right)\begin{pmatrix} V_{n+1} \\ I_{n+1} \end{pmatrix} = 0. \tag{A.3}$$

This equation is a matrix eigenvalue equation for γ. A nontrivial solution for V_{n+1}, I_{n+1} exists only if the determinant vanishes. Hence, $ad - bc + e^{2\gamma d} - e^{\gamma d}(a + d) = 0$. For a reciprocal network the determinant $ad - bc$ of a transmission matrix should be unity. So, it is evident that

$$\cosh \gamma d = \frac{a+d}{2}. \tag{A.4}$$

Hence, from (A.2) and (A.4), the dispersion relation is obtained as,

$$\cosh \gamma d = \cos k_0 d - \frac{B}{2} Z_0 \sin k_0 d \tag{A.5}$$

since $\theta = k_0 d$ as defined in chapter 4. For unattenuated wave propagation, $\alpha = 0$. When unattenuated wave propagation exists in the periodic structure, the dispersion relation becomes,

$$\cos \beta d = \cos k_0 d - \frac{B}{2} Z_0 \sin k_0 d. \tag{A.6}$$

D.2 Wideband Design Equations

Good results are insured not only for wideband filters but also for narrow and moderate bandwith filters by the design equations presented below for filters with shunt quarter wavelength resonators and quarter wavelength connecting lines as shown in Fig. D.1.

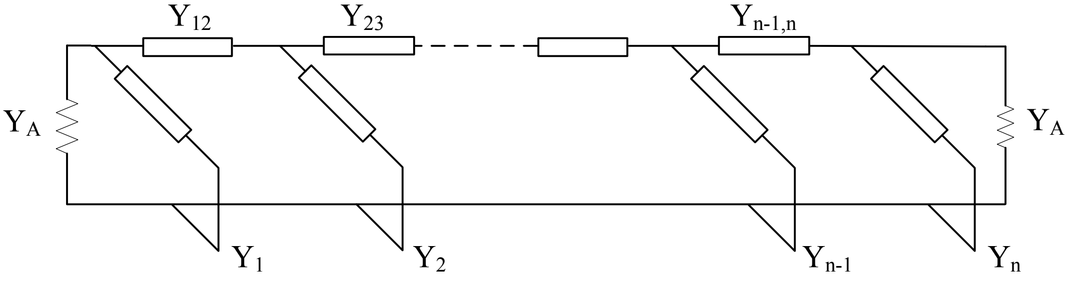

Figure D.1: Bandpass filter with quarter wavelength

The following equations are given in [107], [9].

$$\begin{aligned}
\frac{J_{12}}{Y_A} &= g_0\sqrt{\frac{C_A}{g_2}} \\
\frac{J_{k,k+1}}{Y_A} &= \frac{g_{0C_a}}{\sqrt{g_k g_{k+1}}} \qquad \text{For } k = 2 \text{ to } n-2 \\
\frac{J_{n-1,n}}{Y_A} &= g_0\sqrt{\frac{C_a g_{n+1}}{g_0 g_{n-1}}} \qquad \text{(A.7)}
\end{aligned}$$

where $C_a = 2dg_1$, and d is a dimensionless constant which can be chosen so as to give a convenient admittance level in the interior of the filter.

$$N_{k,k+1} = \sqrt{\left(\frac{J_{k,k+1}}{Y_a}\right)^2 + \left(\frac{g_0\omega_1' C_a \tan\theta_1}{2}\right)} \qquad \text{(A.8)}$$

where $\theta_1 = (\pi\omega_1)/(2\omega_0)$ and ω_1 being lower band edge angular frequency. The characteristic admittances of the shunt stubs are,

$$\begin{aligned}
Y_1 &= g_0 Y_A \omega_1'(1-d)g_1\tan\theta_1 + Y_A\left(N_{12} - \frac{J_{12}}{Y_A}\right) \\
Y_k &= Y_A\left(N_{k-1,k} + N_{k,k+1} - \frac{J_{k-1,k}}{Y_A} - \frac{J_{k,k+1}}{Y_A}\right) \qquad \text{For } k = 2 \text{ to } k = n-1 \\
Y_n &= Y_A\omega_1'\left(g_n g_{n+1} - dg_0 g_1\right)\tan\theta_1 + Y_A\left(N_{n-1,n} - \frac{J_{n-1,n}}{Y_A}\right). \qquad \text{(A.9)}
\end{aligned}$$

Appendix E

TRL Calibration

The fabricated structures are tested using the Agilent$^{\mathrm{TM}}$ 8722 ES vector network analyzer (VNA), which is usually connected to tested device via co-axial cables. A test fixture is required to connect circuits to VNA. With a test fixture inserted between the tested device and VNA, the S-parameters obtained by VNA contain errors. The fixture characteristic must be known and taken into account during the measurement in order to eliminate the influence of the test fixture. Suitable calibration procedure help to eliminate the errors. In general, systematic errors which are repeatable errors can be removed from the calibration. Mismatch and leakage in the test setup, fixture losses and finite isolation between input and output are among these errors [108]. Drift errors and random errors are also among the other measurement errors, while the latter is due to instrument noise and connection repeatability [108]. Though they cannot be eliminated from calibration, They are generally reduced with three different noise reduction techniques facilitated by the VNA, namely sweep to sweep averaging and variable IF bandwidth.

Among different calibration techniques, the Thru, Reflect, Line (TRL) two port calibration method is used here because of its advantages such as convenience of design, fabrication and characterization of standards [109]. All TRL standards are based on the same transmission line as that used in the device under test. 50 Ω LIGA transmission lines (with same the dimensions of 50 Ω lines in the CPW LIGA filter in Chapter 7) designed from simulation are taken as the measurement reference.

The Reflect standards should optimally provide reflection coefficient of unity and here, it is achieved by open ended lines [108]. Reflection coefficients must be same at both ports and should be known within ± 90 degrees. Two pieces of 1.5 mm long 50 Ω LIGA CPW lines are designed for this purpose. Half wavelength or its integer multiple lengths at the centre frequency are avoided.

The Thru standard can be a non-zero length transmission line whose characteristic impedance is equal to that of the Line standard. Its insertion loss does not have to be known. A 50 Ω LIGA transmission line with the length of 3 mm is designed as the Thru standard.

The Line standard is a piece of the same transmission line as used in the Thru. By default calibration impedance is defined to be equal to the characteristic impedance of the Line. However, if the characteristic impedance of the Line is not of the desired value (ie system impedance of devices under test), the difference between calibration and measurement impedances can be set in the VNA manually. In this research, the same design of LIGA CPW line is used for both line standards and the microwave filter device. All the structures undergo same fabrication process. Therefore, the above default setting (calibration impedance set the same as the impedance of Line) is kept intact. The electrical length of the Line must be longer than the Thru, optimally, the Line should be longer than the Thru by a quarter wavelength at the centre frequency or electrical length of 90 degrees. Hence, the length of Line is designed to be 10.15 mm. The TRL calibration is valid for the frequency band where the additional electrical length of Line relatively to Thru stays within 20 to 160 degrees [108].

Bibliography

[1] D. Sievenpiper, L. Zhang, and R. Broas, "High impedance electromagnetic surfaces with a forbidden frequency band," *IEEE Trans. Microwave Theory Tech.*, vol. 47, no. 11, pp. 2059–2074, Nov. 1999.

[2] F. Yang, K.P.Ma, Y. Qian, and T. Itoh, "A uniplanar compact photonic-bandgap (UC-PBG) structure and its applications for microwave circuits," *IEEE Trans. Microwave Theory Tech.*, vol. 47, no. 8, pp. 1509–1514, Aug. 1999.

[3] M. Hella, S. Devarajan, J. Lu, K. Rose, and R. Gutmann, "Die-on-wafer and wafer-level 3D integration for millimeter-wave smart antenna transceivers," *IEEE Annual Conf. on wireless and Microwave Tech.*, pp. 21–21, April 2005.

[4] R. Malmqvist, A. Ouacha, and R. Erickson, "Multi-band and reconfigurable front-ends for flexible and multi-functional RF systems," *Asia-Pacific Microwave Conf.*, pp. 1–4, Dec. 2007.

[5] I. Robertson and S. Lucyszyn, *RFIC and MMIC Design and Technology*, First ed. London: IEE, 2001.

[6] L. Athukorala and D. Budimir, "Miniaturized microstrip diplexers for wimax applications," *Int. Symp. on Antennas and Prop.*, pp. 5–11, July 2008.

[7] K. Gupta, R. Grag, and I. Bahl, *Microstrip Lines and Slotlines*, First ed. Norwood: Artech House, 1979.

[8] D. Pozar, *Microwave Engineering*, First ed. New York: Addison-Wesly, 1990.

[9] G. Matthaei, L. Young, and E. Jones, *Microwave Filters, Impedance Matching Networks and Coupling Structures*, First ed. New York: McGraw-Hill, 1964.

[10] T. Yang, R. Xiu, L. Xiao, and S. Wang, "An improved SIR filter designed using LTCC technology," *Int. Conf. on Microwave and Millimeter Wave Tech.*, vol. 2, pp. 587–590, April 2008.

[11] M. Makimoto and S. Yamashita, "Bandpass filters using parallel coupled stripline stepped impedance resonators," *IEEE Trans. Microwave Theory Tech.*, vol. 28, no. 12, pp. 1413–1417, Dec. 1980.

[12] J. Zhou and M. Lancaster, "Coplanar quarter-wavelength quasi-elliptic filters without bond-wire bridges," *IEEE Trans. Microwave Theory Tech.*, vol. 52, no. 4, pp. 1150–1156, April 2004.

[13] K. Shum, T. Mo, Q. Xue, and C. Chan, "A compact bandpass filter with two tuning transmission zeros using a CMRC resonator," *IEEE Trans. Microwave Theory Tech.*, vol. 53, no. 3, pp. 895–900, March 2005.

[14] A. Batmanov, A. Baoutejdar, J. Machac, and A. Omar, "New compact coplanar bandpass filter composed of serpentine shape shunt-stubs," 14th *Conf. on Microwave Tech.*, pp. 23–24, April 2008.

[15] S. Jenei, S. Decoutere, K. Maex, , and B. Nauwelaers, "Add-on Cu/SiLK."

[16] Y. Konishi, *Microwave Integrated Circuits*, First ed. New York: Marcel Dekker, 1991.

[17] I. Hunter, *Theory and Design of Microwave Filters*, First ed. London: IEE, 2001.

[18] R. Collin, *Foundations for Microwave Engineering*, First ed. New York: McGraw-Hill, 1966.

[19] B. Kim, J. Lee, and M. Song, "An implementation of harmoic-suppression microstrip filters with periodic grooves," *IEEE Microwave and Wireless Comp. Lett.*, vol. 14, no. 9, pp. 413–416, Sept. 2004.

[20] L. Hsieh and K. Chang, "Slow wave bandpass filters using ring or stepped-impedance hairpin resonators," *IEEE Trans. Microwave Theory Tech.*, vol. 50, no. 7, pp. 1795–1800, July 2002.

[21] Y. Kuo, C. Wang, and C. Chen, "Novel reduced size coplanar waveguide bandpass filters," *IEEE Microwave and Wireless Comp. Lett.*, vol. 11, no. 2, pp. 65–67, Feb. 2001.

[22] N. Karmakar and M. Mollah, "Potential applications of PBG engineered structures in microwave engineering: part I," *Microwave Journal*, vol. 5, pp. 22–44, July 2004.

[23] J. Sor, Y. Qian, and T. Itoh, "Miniature low-loss CPW periodic structures for filter applications," *IEEE Trans. Microwave Theory Tech.*, vol. 49, no. 12, pp. 2336–2341, Dec. 2001.

[24] W. Chapple, M. Little, and L. Katehi, "High isolation, planar filters using EBG substrates," *IEEE Microwave and Wireless Comp. Lett.*, vol. 11, no. 6, pp. 246–248, June 2001.

[25] D. Kim and J. Lee, "Partial h- plane filters with multiple transmission zeros," *IEEE Trans. Microwave Theory Tech.*, vol. 56, no. 7, pp. 1693–1669, July 2008.

[26] J. Hong and M. Lancaster, *Microstrip Filters for RF/Microwave Applications*, First ed. New York: Wiley, 2001.

[27] H. Jayatilaka and D. Klymyshyn, “Half wavelength open loop bandpass filters with transmission zeros,” *Asia-Pacific Microwave Conf., APMC 2007*, pp. 2213–2217, Dec. 2007.

[28] J. Kiang, *Novel Technologies for Microwave and Millimeterwave Applications*, First ed. Boston: Kluwer Academic Publishers, 2004.

[29] C. Nguyen and L. Katehi, “Micromachined devices for wireless communications,” *IEEE Proc.*, vol. 86, no. 8, pp. 1756–1768, Aug. 1998.

[30] K. Rambabu and J. Bornemann, “Simlified analysis technique for the initial design of LTCC filters with all capacitive coupling,” *IEEE Trans. Microwave Theory Tech.*, vol. 53, no. 5, pp. 1787–1791, May 2005.

[31] Z. Ma, D. Klymyshyn, S. Achenbach, M. Borner, N. Dambrowsky, and J. Mohr, “An ultra deep high- Q microwave cavity resonator fabricated using deep X-ray lithography,” *IEICE Trans. on Electron.*, vol. E90-C, no. 12, pp. 2192–2197, Dec. 2007.

[32] S. Achenbach, D. Klymyshyn, T. Mappes, A. Kachayev, V. Subramanian, G. Wells, and J. Mohr, “Submicron-scale surface acoustic wave resonators fabricated by high aspect ratio X-ray lithography Aluminum lift-off,” *Microsystem Technologies*, vol. 14, no. 9-11, pp. 1715–1719, Oct. 2008.

[33] A. Kachayev, D. Klymyshyn, S. Achenbach, and V. Saile, “High vertical aspect ratio LIGA microwave 3 dB coupler,” *Proc. of ICMENS*, pp. 38–43, July 2003.

[34] D. Klymyshyn, D. Haluzan, M. Borner, S. Achenbach, J. Mohr, and T. Mappes, “High aspect ratio vertical cantilever RF- MEMS variable capacitor,” *IEEE Microwave and Wireless Comp. Lett.*, vol. 17, no. 2, pp. 127–129, Feb. 2007.

[35] D. Haluzan, S. Achenbach, D. Klymyshyn, T. Mappes, A. Kachayev, V. Subramanian, G. Wells, and J. Mohr, “Stiction issues and actuation of RF

LIGA-MEMS variable capacitors," *Microsystem Technologies*, vol. 14, no. 9-11, pp. 1709–1714, Oct. 2008.

[36] T. Willke and S. Gearhart, "LIGA micromachined planar transmision lines and filters," *IEEE Trans. Microwave Theory Tech.*, vol. 45, no. 10, pp. 1681–1688, Oct. 1997.

[37] K. Park and J. Lee, "A new three dimensional 30 GHz bandpass filter using the LIGA micromachining process," *Microwave and Opt. Tech. Lett.*, vol. 30, no. 3, pp. 199–201, March 2001.

[38] E. Becker, W. Ehrfeld, P. Hagman, A. Maner, and D. Munchmeyer, "Fabrication of microstructures with high-aspect ratios and great structural heights by synchrotron radiation lithography, galvanoformimg and plastic moulding (LIGA process)," *Microelectron. ENG4*, pp. 35–36, 1986.

[39] J. Mohr, W. Ehrfeld, D. Munchmeyer, and A. Stutz, "Resist technology for deep-etch synchrotron radiation lithography," *Proc. Macromel Chem. Machromol Symp.*, vol. 24, pp. 231–251, 1989.

[40] W. Menz, J. Mohr, and O. Paul, *Microsystem Technology*, First ed. Verlag Gmbh: Wiley-vch, 2001.

[41] F. Pantenburg and J. Mohr, "Influence of secondary effects on the structure quality in deep X-ray lithography," *Nuclear instruments and methods in physics research*, vol. B 97, pp. 551–556, 1995.

[42] F. Pantenburg, S. Achenbach, and J. Mohr, "Characterisation of defects in very high deep-etch X-ray lithography microstructures," *Microsystem Technologies*, vol. 4, no. 2, pp. 89–93, 1998.

[43] M. Medley, *Microwave and RF Circuits: Analysis, Synthesis and Design*, First ed. Norwood: Artech House, 1993.

[44] C. Montgomery, R. Dicke, and E. Purcell, *Principle of Microwave Circuits*, First ed. New York: McGrow-Hill, 1948.

[45] D. Kajfez, *Q Factor*, First ed. Oxford: MS:Vector Forum, 1994.

[46] E. Ginzton, *Microwave Measurements*, First ed. New York: McGrow-Hill, 1957.

[47] R. Goyal, *Monolithic Microwave Circuits*, First ed. Norwood: Artech House, 1989.

[48] H. Wheeler, "Transmission-line properties of parrallel strips seperated by a dielectric sheet," *IEEE Trans. Microwave Theory Tech.*, vol. 13, no. 2, pp. 172–185, March 1965.

[49] ——, "Transmission-line properties of a strip on a dielectric sheet on a plane," *IEEE Trans. Microwave Theory Tech.*, vol. 25, no. 8, pp. 631–647, Aug. 1977.

[50] E. Hammerstad, "Accurate models for microstrip computer-aided design," *Int. Microwave. Symp. Dig.*, vol. 80, no. 1, pp. 407–409, May 1980.

[51] M. Sadiku, *Numerical Techniques in Electromagnetics*, Second ed. Norwood: CRC Press, 2000.

[52] "Ansoft $HFSS^{TM}$ 9.1 reference manual."

[53] C. Wen, "Coplanar waveguide: a surface strip transmission line suitable for non reciprocal gyromagnetic device application." *IEEE Trans. Microwave Theory Tech.*, vol. 17, no. 12, pp. 1087–1090, Dec. 1969.

[54] M. Davis, "Finite boundry corrections to the co-planar waveguide analysis," *IEEE Trans. Microwave Theory Tech.*, vol. 21, no. 9, pp. 594–596, Sept. 1973.

[55] M. Goano, F. Bertazzi, P. Caravelli, G. Ghione, and T. Driscoll, “A general conformal mapping approach to the optimum electrode design of coplanar waveguides with arbitrary cross section,” *IEEE Microwave and Wireless Comp. Lett.*, vol. 49, no. 9, pp. 1573–1580, Sept. 2001.

[56] I. Bahl and P. Bhartia, *Microwave Solidstate Circuit Design*, Second ed. New Jersy: Wiley-Interscience, 2003.

[57] E. cristal and S. Frankel, “Hairpin-line and hybrid hairpin-line/ half-wave parallel-coupled line filters,” *IEEE Trans. Microwave Theory Tech.*, vol. 20, no. 11, pp. 719–728, Nov. 1972.

[58] J. Hong and M. Lancaster, “Cross coupled microstrip hairpin-resonator filters,” *IEEE Trans. Microwave Theory Tech.*, vol. 46, no. 1, pp. 118–122, Jan. 1998.

[59] I. Wolf and S. Frankel, “The microstrip open-ring resonator,” *IEEE Trans. Microwave Theory Tech.*, vol. 32, no. 1, pp. 102–107, Jan. 1984.

[60] J. Hong and M. Lancaster, “Compact microwave elliptic function filter using novel microstrip meander open-loop resonators,” *Electronic Lett.*, vol. 32, no. 6, pp. 563–564, March 1996.

[61] C. Mobbs and J. Rhodes, “A generalized chebyshev suspended substrate stripline bandpass filters,” *IEEE Trans. Microwave Theory Tech.*, vol. 31, no. 5, pp. 397–402, May 1983.

[62] K. Wada and I. Awai, “A $\lambda/2$ CPW resonator BPF with multiple attenuation poles and its miniaturization,” *IEEE Int. Microwave Symp. Digest*, vol. 3, pp. 1139–1142, June 1999.

[63] R. Kurzrok, “General three-resonator filters in waveguide,” *IEEE Trans. Microwave Theory Tech.*, vol. 14, no. 1, pp. 46–47, Jan. 1966.

[64] R. Cameron and J. Rhodes, “Asymmetric realization of dual-mode bandpass filters,” *IEEE Trans. Microwave Theory Tech.*, vol. 29, no. 1, pp. 51–58, Jan. 1981.

[65] J. S. Hong and M. Lancaster, “Design of highly selective microstrip bandpass filters with a single pair of attenuation poles at finite frequencies,” *IEEE Trans. Microwave Theory Tech.*, vol. 48, no. 7, pp. 1098–1107, July 2000.

[66] R. Levy, “Filters with single transmission zeros at real and imaginary frequencies,” *IEEE Trans. Microwave Theory Tech.*, vol. 24, no. 4, pp. 172–181, April 1976.

[67] C. Wu, Y. Lin, C. Wang, and C. Chen, “Novel microstrip coupled-line bandpass filters with shortened coupled sections for stopband extension,” *IEEE Trans. Microwave Theory Tech.*, vol. 54, no. 2, pp. 540 – 546, Feb. 2006.

[68] J. Lee, J. Cho, and S. Yun, “New compact bandpass filter using microstrip $\lambda/4$ resonators with open stub inverters,” *IEEE Microwave and Wireless Comp. Lett.*, vol. 10, no. 12, pp. 526–527, Dec. 2000.

[69] S. Amari, Y. Antar, and A. Freundorfer, “New elliptic microstrip $\lambda/4$-resonator filters,” *Proc. of APMC2001*, pp. 755–758, 2006.

[70] U. Rosenberg and S. Amari, “Novel design possibilities for dual mode filters without intracavity couplings,” *IEEE Microwave and Wireless Comp. Lett.*, vol. 12, no. 8, pp. 296–298, Aug. 2002.

[71] Y. Kolmokov, A. Savin, and I. Vendik, “Quasi-elliptic two pole microstrip filter with source-load coupling,” *Proc. MSMW’04 Symp.*, pp. 695–696, 2004.

[72] U. Rosenberg and S. Amari, “Novel coupling schemes for microwave resonator filters,” *IEEE Trans. Microwave Theory Tech.*, vol. 50, no. 12, pp. 2896–2902, Dec. 2002.

[73] I. Hunter, J. Rhodes, and V. Dassonville, "Dual mode filters with conductor-loaded dielectric resonators," *IEEE Trans. Microwave Theory Tech.*, vol. 47, no. 12, pp. 2304–2311, Dec. 1999.

[74] Accatino, G. Bertin, M. Mongiardo, and G. Resnati, "A new dielectric loaded dual-mode cavity for mobile communication filters," *Proc.* 31st *EM Con.*, pp. 37–40, 2001.

[75] R. Wu and S. Amari, "New triangular microstrip loop resonators for band-pass dual-mode filter applications," *IEEE Int. Microwave Symp. Digest*, vol. 53, pp. 941–944, June 2005.

[76] S. Amari, "Synthesis of cross-coupled resonator filters using an analytical gradient-based optimization technique," *IEEE Trans. Microwave Theory Tech.*, vol. 48, no. 9, pp. 1559–1564, Sept. 2000.

[77] R. Cameron, "General prototype network synthesis methods for microwave filters," *ESA Journal*, vol. 6, pp. 193–206, 1982.

[78] H. Jayatilaka, D. Klymyshyn, M. Boerner, and J. Mohr, "Compact thick metal bandpass filters and diplexers with tall folded half wavelength multi-coupled resonators," *IEEE Trans. Microwave Theory Tech.- Under Review*, vol. 58, 2010.

[79] A. Atia and A. Williams, "Narrow-bandpass waveguide filters," *IEEE Trans. Microwave Theory Tech.*, vol. 20, no. 4, pp. 258–265, April 1972.

[80] R. Kurzrok, "General four-resonator filters at microwave frequencies," *IEEE Trans. Microwave Theory Tech.*, vol. 14, no. 6, pp. 295–296, June 1966.

[81] A. Williams, "A four cavity elliptic waveguide filters," *IEEE Trans. Microwave Theory Tech.*, vol. 18, no. 12, pp. 1109–1114, Dec. 1970.

[82] J. Montejo-Garai, “Synthesis of n-even order symetric filters with n transmission zeros by means of source-load cross coupling,” *Electron. Lett.*, vol. 36, no. 3, pp. 232–233, Feb. 2000.

[83] S. Amari, “Direct synthesis of folded symmetric resonator filters with source-load coupling,” *IEEE Microwave and Wireless Comp. Lett.*, vol. 11, no. 6, pp. 264–266, June 2001.

[84] R. Cameron, “Advance coupling matrix synthesis techniques for microwave filters,” *IEEE Trans. Microwave Theory Tech.*, vol. 51, no. 1, pp. 1–10, Jan. 2003.

[85] S. Amari, U. Rosenberg, and J. Bornemann, “Adaptive synthesis and design of resonator filters with source/load-multiresonator coupling,” *IEEE Trans. Microwave Theory Tech.*, vol. 50, no. 8, pp. 1969–1978, Aug. 2002.

[86] C. Chen, T. Huang, C. Chou, and R. Wu, “Microstrip diplexers design with common resonator sections for compact size, but high isolation,” *IEEE Trans. Microwave Theory Tech.*, vol. 54, no. 5, pp. 1945–1952, May 2006.

[87] T. Ohno, K. Wada, and O. Hashimoto, “Design methodologies of planar duplexers and triplexers by manipulating attenuation poles,” *IEEE Trans. Microwave Theory Tech.*, vol. 53, no. 6, pp. 2088–2095, June 2005.

[88] C. Tang and S. You, “Design methodologies of LTCC bandpass filters, diplexers, and triplexer with transmisson zeros,” *IEEE Trans. Microwave Theory Tech.*, vol. 54, no. 2, pp. 717–723, Feb. 2006.

[89] P. Deng, M.I.Lai, S. Jeng, and C. Chen, “Design of matching circuits for microstrip triplexers based on stepped impedance resonators,” *IEEE Trans. Microwave Theory Tech.*, vol. 54, no. 12, pp. 4185–4192, Dec. 2006.

[90] A. Morini, T. Rozzi, M. Farina, and G. Venanzoni, “A new look at the practical design of compact diplexers,” *IEEE Trans. Microwave Theory Tech.*, vol. 54, no. 9, pp. 3515–3520, Sept. 2006.

[91] A. Morini and T. Rozzi, “Design of optimum three port symmetrical junctions for diplexer applications,” *IEEE Int. Microwave Symp. Digest*, vol. 2, pp. 739–742, May 1994.

[92] G. Macchiarella and S. Tamiazzo, “Novel approach to the synthesis of microwave diplexers,” *IEEE Trans. Microwave Theory Tech.*, vol. 54, no. 12, pp. 4281–4290, Dec. 2006.

[93] D. Traina, G. Macchiarella, and T. Sarkar, “Robust formulation of the cauchy method suitable for microwave diplexers modeling,” *IEEE Trans. Microwave Theory Tech.*, vol. 55, no. 5, pp. 974–982, May 2007.

[94] N. Karmakar and M. Mollah, “Potential applications of PBG engineered structures in microwave engineering: part II,” *Microwave Journal*, vol. 5, pp. 45–52, July 2004.

[95] J. Sor, Y. Qian, and T. Itoh, “Miniature low-loss CPW periodic structures for filter applications,” *IEEE Trans. Microwave Theory Tech.*, vol. 49, no. 1, pp. 2336–2341, Dec. 2001.

[96] A. Lai, C. Caloz, and T. Itoh, “Composite right/left-handed transmission line metamaterials,” *Microwave Journal*, vol. 5, no. 3, pp. 34–50, Sept. 2004.

[97] Y. Qian, R. Coccioli, F. Yang, and T. Itoh, “Passive and active component design using PBG,” *IEEE Sixth Int. Conf. on Terahertz Electronics Proc.*, pp. 42–45, Sept. 1998.

[98] F. Yang, Y. Qian, and T. Itoh, “A novel uniplanar compact PBG structure for filter and mixer applications,” *IEEE Int. Microwave Symp. Digest*, vol. 3, pp. 919–922, June 1999.

[99] B. Karyamapudi and J. Hong, “Coplanar waveguide periodic structures with resonant elements and their application in microwave filters,” *IEEE Int. Microwave Symp. Digest*, vol. 3, pp. 1619–1622, June 2003.

[100] F. Falcone, F. Martin, J. Bonache, R. Marques, T. Lopetegi, and M. Sorolla, "Left handed coplanar waveguide bandpass filters based on bi-layer split ring resonators," *IEEE Microwave and Wireless Comp. Lett.*, vol. 14, no. 1, pp. 10–12, Jan. 2004.

[101] J. Martel, R. Marques, F. Falcone, J. Baena, F. Medina, F. Martin, and M. Sorolla, "A new LC series element for compact bandpass filter design," *IEEE Microwave and Wireless Comp. Lett.*, vol. 14, no. 5, pp. 210–212, May 2004.

[102] Y. Lin, W. Ku, C. Wang, and C. Chen, "Wideband coplanar-waveguide bandpass filters with good stopband rejection," *IEEE Microwave and Wireless Comp. Lett.*, vol. 14, no. 9, pp. 422–424, Sept. 2004.

[103] H. Jayatilaka and D. Klymyshyn, "Periodically loaded wideband bandpass filters," *Proc. of the IASTD Int. Conf. on Antennas, Radar and Wave Propa.*, pp. 11–16, 2006.

[104] ——, "Wideband microstrip bandpass filter based on EBG concept," *IEICE Trans. Electron.*, vol. E90-C, no. 12, pp. 2212–2217, Dec. 2007.

[105] "Agilent ADS^{TM} 2003A reference manual."

[106] D. Klymyshyn, H. Jayatilaka, M. Boerner, and J. Mohr, "High-aspect-ratio coplanar waveguide wideband bandpass filter with compact unit cells," *IEEE Trans. Microwave Theory Tech.*, vol. 57, no. 11, pp. 2753–2760, Nov. 2009.

[107] G. L. Matthaei, "Design of wide-band (and narrow-band) band-pass microwave filters on the insertion loss basis," *IRE Trans. Microwave Theory Tech.*, vol. 8, no. 11, pp. 580–593, Nov. 1960.

[108] A. Technologies, "In-fixture measurements using vector network analyzers," *Application Note, AN 1287-9*, pp. 1–32, 2000.

[109] G. Engen and C. Hoer, "Thru-reflect-line: An improved technique for calibrating the dual six-port automatic network analyzer," *IEEE Trans. Microwave Theory Tech.*, vol. 27, no. 12, pp. 987–992, Dec. 1979.